PROGRESS IN THEORETICAL CHEMISTRY AND PHYSICS

Advances in the Theory of Atomic and Molecular Systems

Dynamics, Spectroscopy, Clusters, and Nanostructures

P. Piecuch, J. Maruani,
G. Delgado-Barrio,
and S. Wilson (Eds.)

Springer

ADVANCES IN THE THEORY OF ATOMIC
AND MOLECULAR SYSTEMS

Progress in Theoretical Chemistry and Physics

VOLUME 20

For other titles published in this series, go to
www.springer.com/series/6464

Advances in the Theory of Atomic and Molecular Systems

Dynamics, Spectroscopy, Clusters, and Nanostructures

Edited by

PIOTR PIECUCH
Michigan State University, East Lansing, MI, USA

JEAN MARUANI
CNRS, Paris, France

GERARDO DELGADO-BARRIO
CSIC, Madrid, Spain

and

STEPHEN WILSON
University of Oxford, UK

Springer

Editors
Piotr Piecuch
Department of Chemistry
Michigan State University
East Lansing, MI 48824
USA
piecuch@chemistry.msu.edu

Jean Maruani
Laboratoire de Chimie Physique
CNRS and UPMC
11 Rue Pierre et Marie Curie
F-75005 Paris
France
jean.maruani@upmc.fr
jemmaran@gmail.com

Gerardo Delgado-Barrio
Instituto de Física Fundamental
CSIC
Serrano 123
E-28006 Madrid
Spain
gerardo@imaff.cfmac.csic.es

Stephen Wilson
Physical & Theoretical Chemistry Laboratory
University of Oxford
South Parks Road
Oxford OX1 3QZ
United Kingdom
quantumsystems@gmail.com

ISSN 1567-7354
ISBN 978-90-481-2984-3 e-ISBN 978-90-481-2985-0
DOI 10.1007/978-90-481-2985-0
Springer Dordrecht Heidelberg London New York

Library of Congress Control Number: 2009929297

Progress in Theoretical Chemistry and Physics

A series reporting advances in theoretical molecular and materials sciences, including theoretical, mathematical and computational chemistry, physical chemistry, and chemical physics

Aim and Scope

Science progresses by a symbiotic interaction between theory and experiment: theory is used to interpret experimental results and may suggest new experiments; experiment helps to test theoretical predictions and may lead to improved theories. Theoretical Chemistry (including Physical Chemistry and Chemical Physics) provides the conceptual and technical background and apparatus for the rationalization of phenomena in the chemical sciences. It is, therefore, a wide ranging subject, reflecting the diversity of molecular and related species and processes arising in chemical systems. The book series *Progress in Theoretical Chemistry and Physics* aims to report advances in methods and applications in this extended domain. It will comprise monographs as well as collections of papers on particular themes, which may arise from proceedings of symposia or invited papers on specific topics as well as initiatives from authors or translations.

The basic theories of physics – classical mechanics and electromagnetism, relativity theory, quantum mechanics, statistical mechanics, quantum electrodynamics – support the theoretical apparatus which is used in molecular sciences. Quantum mechanics plays a particular role in theoretical chemistry, providing the basis for the valence theories which allow to interpret the structure of molecules and for the spectroscopic models employed in the determination of structural information from spectral patterns. Indeed, Quantum Chemistry often appears synonymous with Theoretical Chemistry: it will, therefore, constitute a major part of this book series. However, the scope of the series will also include other areas of theoretical chemistry, such as mathematical chemistry (which involves the use of algebra and topology in the analysis of molecular structures and reactions), molecular mechanics, molecular dynamics and chemical thermodynamics, which play an important role in rationalizing the geometric and electronic structures of molecular assemblies and polymers, clusters and crystals, surface, interface, solvent and solid-state effects, excited-state dynamics, reactive collisions, and chemical reactions.

Recent decades have seen the emergence of a novel approach to scientific research, based on the exploitation of fast electronic digital computers. Computation provides a method of investigation which transcends the traditional division between

theory and experiment. Computer-assisted simulation and design may afford a solution to complex problems which would otherwise be intractable to theoretical analysis, and may also provide a viable alternative to difficult or costly laboratory experiments. Though stemming from Theoretical Chemistry, Computational Chemistry is a field of research in its own right, which can help to test theoretical predictions and may also suggest improved theories.

The field of theoretical molecular sciences ranges from fundamental physical questions relevant to the molecular concept, through the statics and dynamics of isolated molecules, aggregates and materials, molecular properties and interactions, and the role of molecules in the biological sciences. Therefore, it involves the physical basis for geometric and electronic structure, states of aggregation, physical and chemical transformations, thermodynamic and kinetic properties, as well as unusual properties such as extreme flexibility or strong relativistic or quantum-field effects, extreme conditions such as intense radiation fields or interaction with the continuum, and the specificity of biochemical reactions.

Theoretical chemistry has an applied branch – a part of molecular engineering, which involves the investigation of structure–property relationships aimed at the design, synthesis, and application of molecules and materials endowed with specific functions, now in demand in such areas as molecular electronics, drug design, or genetic engineering. Relevant properties include conductivity (normal, semi- and supra-), magnetism (ferro- or ferri-), optoelectronic effects (involving nonlinear response), photochromism and photoreactivity, radiation and thermal resistance, molecular recognition and information processing, and biological and pharmaceutical activities, as well as properties favouring self-assembling mechanisms and combination properties needed in multifunctional systems.

Progress in Theoretical Chemistry and Physics is made at different rates in these various research fields. The aim of this book series is to provide timely and in-depth coverage of selected topics and broad-ranging yet detailed analysis of contemporary theories and their applications. The series will be of primary interest to those whose research is directly concerned with the development and application of theoretical approaches in the chemical sciences. It will provide up-to-date reports on theoretical methods for the chemist, thermodynamicist or spectroscopist, the atomic, molecular or cluster physicist, and the biochemist or molecular biologist who wish to employ techniques developed in theoretical, mathematical, or computational chemistry in their research programmes. It is also intended to provide the graduate student with a readily accessible documentation on various branches of theoretical chemistry, physical chemistry, and chemical physics.

Preface

These two volumes, which share the common title *Advances in the Theory of Atomic and Molecular Systems*, contain a representative selection of some of the most outstanding papers presented at the *Thirteenth International Workshop on Quantum Systems in Chemistry and Physics* (QSCP-XIII). The QSCP-XIII workshop, which ran from 6 to 12 July 2008, was held at the impressive site of the James B. Henry Center for Executive Development of Michigan State University, East Lansing, Michigan, USA, and was coordinated with the *Sixth Congress of the International Society for Theoretical Chemical Physics* (ISTCP-VI) that took place a week later in Vancouver, British Columbia, Canada. As a mark of the close collaboration which underpinned the scientific agendas of both meetings, three of the thirty three papers included in the present two volumes have been written by scientists who contributed in person at the ISTCP-VI Congress.

The QSCP-XIII workshop continued the series that was initiated by Roy McWeeny in April 1996 with a meeting held at San Miniato, near Pisa, Italy. Held every year, QSCP meetings bring together, in an informal atmosphere and with the aim of fostering collaboration, chemists and physicists who share interests in such areas as Novel Concepts and Methods in Quantum Chemistry, Molecular Structure and Spectroscopy, Atoms and Molecules in Electric and Magnetic Fields, Condensed Matter, Complexes and Clusters, Surfaces and Interfaces, Nano-Materials and Molecular Electronics, Reactive Collisions and Chemical Reactions, Computational Chemistry, Physics, and Biology, and Biological Modeling. The emphasis of the QSCP workshops is on broadly defined quantum-mechanical many-body methods, i.e., the development of innovative theory and its computational realization, along with their application to a broad range of scientific problems of relevance to chemistry, physics, biochemistry, and related fields.

The QSCP-XIII workshop, which was the first in the series held in North America, was truly international in nature. We welcomed more than 100 participants from 22 countries from North and South America, Europe, Africa, Asia, and Australia. The workshop was divided into 19 plenary sessions, during which a total of 64 scientific lectures were delivered in accordance with the usual QSCP "democratic" allocation of about 30 minutes for each lecture. These lectures were complemented by two 45-minute long keynote plenary talks which focused on science and relevant historical overviews, constituting a special session that was held on 6 July, as well as by a welcome presentation by Vice President for Research and Graduate Studies at Michigan State University, J. Ian Gray, given on 7 July, and 36 poster presentations divided into two poster sessions.

Following a tradition of QSCP workshops, the scientific programme of QSCP-XIII was accompanied by a social programme including a musical concert, a trip to the Henry Ford Museum in Dearborn, Michigan, and an award ceremony that took place at the banquet dinner. The musical concert, coordinated by Charles Ruggiero of Michigan State University, was performed by Danilo Mezzadri and Susan Ruggiero-Mezzadri, a flute and soprano duo who were accompanied by Judy Kabodian at the piano. The ceremony of the award honored five nominees and recipients of the *QSCP Promising Scientist Prize of the Centre de Mécanique Ondulatoire Appliquée* (CMOA). The first Prize was presented to Garnet K.-L. Chan from Cornell University, USA, and the second Prize was shared by David A. Mazziotti from the University of Chicago, USA, and Ágnes Szabados from Eötvös University, Hungary. T. Daniel Crawford from Virginia Tech, USA, and Stéphane Carniato from Université Pierre et Marie Curie, France, received certificates of nomination. For further details of the QSCP-XIII events and programme, including the abstracts of all lectures and poster presentations, we refer the reader to the workshop webpages at

www.chemistry.msu.edu/qscp13

The thirty three papers in the proceedings of QSCP-XIII are divided between the present two volumes in the following manner. The first volume, with the subtitle *Conceptual and Computational Advances in Quantum Chemistry*, contains twenty papers and is divided into six parts. The first part focuses on historical overviews of significance to the QSCP workshop series and quantum chemistry. The remaining five parts, entitled "High-Precision Quantum Chemistry," "Beyond Nonrelativistic Theory: Relativity and QED," "Advances in Wave Function Methods," "Advances in Density Functional Theory," and "Advances in Concepts and Models," address different aspects of quantum mechanics as applied to electronic structure theory and its foundations. The second volume, with the subtitle *Dynamics, Spectroscopy, Clusters, and Nanostructures*, contains the remaining thirteen papers and is divided into three parts: "Quantum Dynamics and Spectroscopy," "Complexes and Clusters," and "Nanostructures and Complex Systems."

We hope that together the present two volumes, with thirty three authoritative papers that are either of the advanced review type or original research articles, will provide readers with a good idea of the range of stimulating topics which made QSCP-XIII such a success. We thank both the contributors to these proceedings, who sent us their outstanding manuscripts, and the referees, who were willing to invest time in the unacknowledged effort of reviewing the work submitted. We greatly appreciate the help and advice they gave to authors and editors alike. We also thank Jeffrey R. Gour, Jesse J. Lutz, and Wei Li for their assistance with technical aspects of the manuscripts.

We are grateful to the participants of QSCP-XIII, not only for the high standard of the lectures and posters presented at the workshop, which is reflected in these proceedings, but also for the friendly and constructive atmosphere throughout the formal and informal sessions. Thanks to the participants, the QSCP workshops con-

tinue to provide a unique forum for the presentation and appraisal of new ideas in the broadly defined area of quantum systems in chemistry and physics.

We are grateful to the Honorary Chairs of QSCP-XIII for their support, encouragement, and advice. Specifically, we thank (in alphabetical order): Ernest R. Davidson of the University of Washington, USA, Zohra Ben Lakhdar of the University of Tunis, Tunisia, Raphael D. Levine of the Hebrew University of Jerusalem, Israel and the University of California, Los Angeles, USA, Rudolph A. Marcus of the California Institute of Technology, Pasadena, USA, and Roy McWeeny of the University of Pisa, Italy. We also express our gratitude to other members of the International Scientific Committee of QSCP-XIII, including Vincenzo Aquilanti of the University of Perugia, Italy, Erkki J. Brändas of the University of Uppsala, Sweden, Lorenz S. Cederbaum of the University of Heidelberg, Germany, Souad Lahmar of the University of Tunis, Tunisia, Aristides Mavridis of the National University of Athens, Greece, Hiroshi Nakatsuji of the Quantum Chemistry Research Institute, Kyoto, Japan, Josef Paldus of the University of Waterloo, Canada, Alia Tadjer of the University of Sofia, Bulgaria, Carmela Valdemoro of CSIC, Madrid, Spain, Oleg Vasyutinskii of the Ioffe Institute, St. Petersburg, Russia, and Y. Alexander Wang of the University of British Columbia, Vancouver, Canada, for their invaluable suggestions and collective wisdom.

We thank the Local Organizing Committee of QSCP-XIII, particularly several members of the Department of Chemistry at Michigan State University, including Thomas V. Atkinson, Thomas P. Carter, Jeffrey R. Gour, Janet K. Haun, and Paul A. Reed, for their dedication and hard work at all stages of the workshop preparation and organization, which resulted in the smooth running of the meeting.

Finally, no scientific meeting can be successful without sponsors, and QSCP-XIII was no different in this regard. We are grateful for the financial support provided to the organizers of QSCP-XIII by several offices and units at Michigan State University: the Office of the Vice President for Research and Graduate Studies, the Office of the Vice Provost for Libraries, Computing, and Technology, the AT&T Lectureships in Information Technology Endowment, the Colleges of Natural Science and of Engineering, the Office of International Studies and Programs, the Departments of Chemistry and of Biochemistry and Molecular Biology, and the Quantitative Biology Initiative, as well as corporate sponsors: SGI, JRT, and Dell.

It is the editors' hope that the present two volumes will not only convey the breadth, depth, and dynamism of the QSCP-XIII workshop itself, but also seed innovative ideas in the wider research community.

April 2009

Piotr Piecuch
Jean Maruani
Gerardo Delgado-Barrio
Stephen Wilson

Contents

Part I
Quantum Dynamics and Spectroscopy

Quantum Theory in Terms of Cumulant Variables

Yasuteru Shigeta, Hideaki Miyachi, Toru Matsui, Norisuke Yokoyama, and Kimihiko Hirao

Abstract We have formulated the quantal cumulant dynamics (QCD) method as an extension of the quantized Hamilton dynamics (QHD) method, first proposed by Prezhdo. In particular, we have derived the coupled equation of motion (EOM) for the position, momentum, and second-order cumulants of the product of the momentum and position fluctuation operators. The EOM for second-order approximation to QCD (QCD2) consists of classical and cumulant variables and of a quantal potential and its derivatives, where the quantal potential is expressed as an exponential function of the differential operator acting on a given potential or as a Gaussian convolution integral. We demonstrated exactly soluble models in the QCD2 framework, whose solutions are the same as the ground states of corresponding solution derived from quantum mechanics. We have applied the QCD2 method to (1) one-dimensional Morse potential, (2) molecular vibrations, (3) quantum

Y. Shigeta (✉)
Department of Physics, Graduate School of Pure and Applied Sciences, Tsukuba University, Tennodai 1-1-1, Ibaraki 305-0006, Japan
Institute of Picobiology, Graduate School of Life Science, University of Hyogo, Koto 3-2-1, Hyogo 678-1297, Japan
Core Research for Evolutional Science and Technology, Japan Science and Technology Agency (CREST, JST), Japan

H. Miyachi
Department of Applied Chemistry, School of Engineering, The University of Tokyo, Hongo 7-3-1, Tokyo 113-8656, Japan

T. Matsui
Department of Applied Chemistry, School of Engineering, The University of Tokyo, Hongo 7-3-1, Tokyo 113-8656, Japan

N. Yokoyama
Department of Applied Chemistry, School of Engineering, The University of Tokyo, Hongo 7-3-1, Tokyo 113-8656, Japan

K. Hirao
Core Research for Evolutional Science and Technology, Japan Science and Technology Agency (CREST, JST), Japan
Department of Applied Chemistry, School of Engineering, The University of Tokyo, Hongo 7-3-1, Tokyo 113-8656, Japan

P. Piecuch et al. (eds.), *Advances in the Theory of Atomic and Molecular Systems*, Progress in Theoretical Chemistry and Physics 20, DOI 10.1007/978-90-481-2985-0_1,

tunneling in quantum well, and (4) proton-transfer reactions in DNA base pairs. The results are quite useful for understanding underlying quantum nature of these systems of interests.

Keywords: Quantum dynamics · Cumulant expansion · Quantum isotope effects · Zero point vibration · Quantum confinement

1 Introduction

Quantum effects, such as zero-point energy, tunneling, and resonance, are essential, and cannot be avoided, in molecules and even in mesoscopic sciences. For example, to characterize reactions in mesoscopic systems, it is essential to take into consideration both dynamical fluctuation and quantum effects. Nevertheless, the many-body dynamics of these chemical reactions are too complicated and demanding to be simulated using full quantum dynamics methods. Therefore, the full quantum dynamics method is limited to a few degrees of freedom, i.e., to small systems.

The quantum tunneling is one of the most important phenomena of quantum mechanics, which is one of the greatest discoveries in the twentieth century, and it has given us a wide variety of phenomena crucial for both science and technologies. A particle can tunnel through a potential barrier by the overlap between initial and final state wave functions, although such motion cannot be observed in classical mechanics [1]. Quantum mechanical tunneling has given us a great number of new scientific knowledge such as the origin of α decay in nuclear physics [2] and it has enabled us to realize modern semiconductor technologies. The zero-point motion is also quite remarkably different from the classical mechanics, since any classical object with no velocity does not move at zero temperature. The resonance is a consequence of the wave nature of the quantum particle so that the quantum object exhibits two different characteristics (quantum duality).

There are a number of approaches that can be used to treat these quantum effects, at least approximately. The Schrödinger equation is solved to investigate the quantum effects often by introducing basis sets. As an alternative, the path integral-based methods are sometimes adopted [3]. For an update on the recent developments in this field, the reader should refer to the original reviews [4–8]. One of the recent remarkable progresses in this field is that development of quantized Hamilton dynamics (QHD) approach by Prezhdo and co-workers derived using a different route, i.e., Heisenberg's equations of motion [9–11], because the QHD approach is a general approach and is widely used. The advantages of the QHD approach are (i) it is not necessary to reconstruct the full quantum wave function or the density matrix as in the semiclassical WKB-based method and (ii) it requires less computational effort than the full quantum dynamics approach does. On the other hand, the drawbacks of the QHD method are that the truncation of the potential energy entails an error in the energy evaluation, where the remaining energy is assumed to be a classical one and that laborious calculations are required to formulate the higher-order approximations in decompositions of given moments, where an nth moment

$\langle \hat{Q}^n \rangle$ is approximated by a function of a set of given moments $\langle \hat{Q}^n \rangle \sim \sum_{m<n} c_{m,n} \langle \hat{Q}^m \rangle$, where $c_{m,n}$ is expansion coefficient. The decomposition schemes for higher-order moments are intractable. Therefore, it is desirable to construct a systematic method without truncation of the potential and the decomposition scheme.

We have utilized the cumulant rather than the moment as a dynamical variable [11–18]. The cumulant expansion techniques were introduced by Mayer for classical problems [19] and by Kubo [20] for quantum mechanical problems to evaluate averages of exponential functions. The advantages of the cumulant expansion over the moment expansion are as follows: (i) one can avoid the tedious derivation in the decomposition so that there is no need to truncate the given potential and (ii) less terms appear than in the moment expansion do as shown later. Recently, the cumulant expansion techniques have been applied by several groups to quantum chemistry problems in relation to higher-order density matrices [21–24] and to multireference-coupled cluster methods [25]. The cumulant-based theory is also given by Mukherjee for thermal averages [26].

In this review, we derive the coupled equations of motion of cumulants that consist of symmetric-ordered products of the position and the momentum fluctuation operators in one dimension as an extension of the QHD method. Hereafter, we will refer to our method as the quantal cumulant dynamics (QCD) method. The key idea is to use a position shift operator acting on a potential operator. Due to the shift operator, the dependence of the quantum position operator on the given potential formally disappears, and the expectation value of the shift operator can be evaluated using cumulant expansion techniques. The basic theory and definitions are given in Sect. 2. In Sect. 3, we demonstrate several applications to physically and chemically interesting problems, where the quantum effect plays an essential role. Section 4 provides our conclusions.

2 Theoretical Background

Here we first give basic formulation of cumulant-based theory for one-dimensional systems and then generalize it for multi-dimensional systems.

2.1 Cumulant Representation of Energy for One-Dimensional Case

Hamiltonian of one-dimensional systems is given by

$$\hat{H}\left(\hat{P}, \hat{Q}\right) = \frac{\hat{P}^2}{2M} + V\left(\hat{Q}\right), \tag{1}$$

where the first and second terms are kinetic and potential energy operators, respectively. By introducing the shift operator, the potential energy operator is rewritten as [12]

$$V\left(\hat{Q}\right) = \exp\left(\delta\hat{Q}\frac{\partial}{\partial q}\right) V(q)\Big|_{q=\langle\hat{Q}\rangle}, \tag{2}$$

where $\delta\hat{A} = \hat{A} - \langle\hat{A}\rangle$ is a definition of a fluctuation operator of a given operator $\hat{A}$ and $\langle\hat{A}\rangle$ is an expectation value of $\hat{A}$. The expectation value of the potential is written as

$$\langle V\left(\hat{Q}\right)\rangle = \left\langle \exp\left(\delta\hat{Q}\frac{\partial}{\partial q}\right)\right\rangle V(q)\Big|_{q=\langle\hat{Q}\rangle}. \tag{3}$$

It should be stressed here that the expectation value of the exponential function is universal and is independent of the Hamiltonian. Alternatively we need to evaluate the expectation value of the exponential function of the operators which is defined as

$$C\left(\frac{\partial}{\partial q}\right) \equiv \left\langle \exp\left(\delta\hat{Q}\frac{\partial}{\partial q}\right)\right\rangle. \tag{4}$$

By means of the cumulant expansion technique [19, 20], one yields

$$\ln C\left(\frac{\partial}{\partial q}\right) \equiv \sum_n \frac{\lambda_{n,0}}{n!}\frac{\partial^n}{\partial q^n}. \tag{5}$$

For example, lower-order cumulants are expressed by means of expectation values of functions of fluctuation operators as $\lambda_{1,0} = 0$, $\lambda_{2,0} = \langle\delta\hat{Q}^2\rangle$, $\lambda_{3,0} = \langle\delta\hat{Q}^3\rangle$, and $\lambda_{4,0} = \langle\delta\hat{Q}^4\rangle - \langle\delta\hat{Q}^2\rangle^2$. The expectation value of the potential energy operator is clearly expressed by means of position cumulants as

$$\langle V\left(\hat{Q}\right)\rangle = \exp\left[\sum_n \frac{\lambda_{n,0}}{n!}\frac{\partial^n}{\partial q^n}\right] V(q)\Big|_{q=\langle\hat{Q}\rangle}. \tag{6}$$

If we retain all cumulant variables, we can evaluate the potential energy exactly. In the following, we retain it up to second order:

$$\langle V\left(\hat{Q}\right)\rangle_2 = \exp\left[\frac{\lambda_{2,0}}{2}\frac{\partial^2}{\partial q^2}\right] V(q) \equiv \tilde{V}_2\left(q, \lambda_{2,0}\right), \tag{7}$$

where we hereafter refer it as a second-order quantal potential.

So far, we have treated an expectation value of an arbitrary function of the position operators. Here we generalize the above procedure in order to treat an arbitrary function of the position and momentum operators,

$$A_s\left(\hat{P},\hat{Q}\right)=\sum_{m,n}a_{m,n}\left(\hat{P}^m\hat{Q}^n\right)_s, \tag{8}$$

where s denotes a symmetric-ordered product defined as

$$\left(\hat{P}^m\hat{Q}^n\right)_s=\frac{\hat{P}^m\hat{Q}^n+\hat{Q}^n\hat{P}^m}{2}. \tag{9}$$

The expectation value of the above operator is given by

$$\left\langle A_s\left(\hat{P},\hat{Q}\right)\right\rangle=\left\langle\left[\exp\left(\delta\hat{Q}\frac{\partial}{\partial q}\right)\exp\left(\delta\hat{P}\frac{\partial}{\partial p}\right)\right]_s\right\rangle A\left(p,q\right). \tag{10}$$

The problem is to evaluate the following expectation value of the symmetric-ordered product of the position and momentum shift operators as

$$D\left(\frac{\partial}{\partial p},\frac{\partial}{\partial q}\right)\equiv\left\langle\left[\exp\left(\delta\hat{Q}\frac{\partial}{\partial q}\right)\exp\left(\delta\hat{P}\frac{\partial}{\partial p}\right)\right]_s\right\rangle. \tag{11}$$

The exponential function is also universal and independent of the Hamiltonian. By applying the expansion techniques for two variables

$$\ln D\left(\frac{\partial}{\partial p},\frac{\partial}{\partial q}\right)\equiv\sum_{m+n=2}\frac{\lambda_{n,m}}{m!n!}\frac{\partial^{m+n}}{\partial p^m\partial q^n}, \tag{12}$$

we have

$$\left\langle A_s\left(\hat{P},\hat{Q}\right)\right\rangle=\exp\left[\sum_{m+n=2}\frac{\lambda_{n,m}}{m!n!}\frac{\partial^{m+n}}{\partial p^m\partial q^n}\right]A\left(p,q\right), \tag{13}$$

where we have defined the two-variable cumulant, $\lambda_{n,m}$. For example, by neglecting higher order rather than second order, the second-order expectation values are given by

$$\left\langle A_s\left(\hat{P},\hat{Q}\right)\right\rangle_2=\exp\left[\frac{\lambda_{2,0}}{2}\frac{\partial^2}{\partial q^2}+\lambda_{1,1}\frac{\partial^2}{\partial q\partial p}+\frac{\lambda_{0,2}}{2}\frac{\partial^2}{\partial p^2}\right]A\left(p,q\right). \tag{14}$$

The second-order energy is approximated as

$$\left\langle H\left(\hat{P},\hat{Q}\right)\right\rangle_2=\frac{p^2+\lambda_{0,2}}{2M}+\tilde{V}_2\left(q,\lambda_{2,0}\right)\equiv E_2\left(p,q,\lambda_{2,0},\lambda_{0,2}\right). \tag{15}$$

The energy is a function of the four variables, i.e., the classical momentum, position, the second-order position, and momentum cumulant variables. Hereafter we refer the second-order approximation with respect to the cumulant variables as QCD2.

2.2 Equations of Motion

The quantum mechanical equations of motion for operators are derived from the Heisenberg's equation of motion (EOM), which is equivalent to the time-dependent Schrödinger equation. The operator in the Heisenberg representation is given by [12]

$$\hat{A}(t) = \exp\left(i\hat{H}t/\hbar\right)\hat{A}\exp\left(-i\hat{H}t/\hbar\right). \tag{16}$$

The Heisenberg's EOM of the above operator is expressed as

$$i\hbar\frac{d}{dt}\hat{A}(t) = \left[\hat{A}(t), \hat{H}\right]_{-}. \tag{17}$$

The EOM for the expectation value of $\hat{A}(t)$ becomes

$$i\hbar\frac{d}{dt}\left\langle\hat{A}(t)\right\rangle = \left\langle\left[\hat{A}(t), \hat{H}\right]_{-}\right\rangle. \tag{18}$$

The EOMs of the coordinate, momentum, and cumulant variables in the QCD2 framework are

$$\dot{q}(t) = \frac{1}{i\hbar}\left\langle\left[\hat{Q}(t), \hat{H}\right]_{-}\right\rangle = \frac{p(t)}{M}, \tag{19}$$

$$\dot{p}(t) = \frac{1}{i\hbar}\left\langle\left[\hat{P}(t), \hat{H}\right]_{-}\right\rangle = -\tilde{V}_2^{(1,0)}\left(q(t), \lambda_{2,0}(t)\right), \tag{20}$$

$$\dot{\lambda}_{2,0}(t) = \frac{1}{i\hbar}\left\langle\left[\delta\hat{Q}^2(t), \hat{H}\right]_{-}\right\rangle = \frac{2\lambda_{1,1}(t)}{M}, \tag{21}$$

$$\begin{aligned}\dot{\lambda}_{1,1}(t) &= \frac{1}{i\hbar}\left\langle\left[\left[\delta\hat{Q}(t)\,\delta\hat{P}(t)\right]_s, \hat{H}\right]_{-}\right\rangle \\ &= \frac{\lambda_{0,2}(t)}{M} - \lambda_{2,0}(t)\,V_2^{(2,0)}\left(q(t), \lambda_{2,0}(t)\right)\end{aligned}, \tag{22}$$

and

$$\dot{\lambda}_{0,2}(t) = \frac{1}{i\hbar}\left\langle\left[\delta\hat{P}^2(t), \hat{H}\right]_{-}\right\rangle = -2\lambda_{1,1}(t)\,V_2^{(2,0)}\left(q(t), \lambda_{2,0}(t)\right). \tag{23}$$

Note that the second-order position–momentum cumulant, $\lambda_{1,1}(t)$, has been introduced, though the energy is independent of $\lambda_{1,1}(t)$. It is easily shown that the time

derivative of the energy is zero, $\dot{E}_2(t) = 0$, so that the energy conserves during the dynamics. Here we have the other conservation law among the cumulant variables.

The time derivative of $\gamma(t) = \lambda_{2,0}(t)\lambda_{0,2}(t) - \lambda_{1,1}^2(t)$ is zero, $\dot{\gamma}(t) = 0$, i.e., $\gamma(t)$ is a constant. This indicates that the actual variables in the above five EOMs are reduced to be four. Nevertheless, in this study we use all the EOMs for simplicity.

2.3 Quantal Potential and Effective Quantal Potential in QCD2

Hereafter, we demonstrate three different schemes to evaluate the quantal potential and its derivative as follows: (1) a truncation (decoupling), (2) a series summation of an analytic derivative, and (3) a convolution scheme. Note that (1) is an approximation scheme also used in the QHD method, while (2) and (3) are in principle exact.

In most cases, the potential operator can be expanded into Taylor series. It is assumed that the potential can be truncated at some order like as in the well-known normal mode analysis. We adopt the present method to the case of a quartic potential (or quartic force field (QFF)), which can describe anharmonic vibrations and is an approximation to the general potential as a finite series by truncating it at fourth order, defined as

$$V_{\mathrm{QFF}}(q) = v_0 + gq + \frac{h}{2}q^2 + \frac{t}{6}q^3 + \frac{u}{24}q^4, \tag{24}$$

where g, h, t, and u are the coefficients of the approximate Taylor series. In this case, we can evaluate the quantal potential explicitly as

$$\tilde{V}_{\mathrm{QFF},2}\left(q, \lambda_{2,0}\right) = V_{\mathrm{QFF}}(q) + \frac{\lambda_{2,0}}{2}\left(h + tq + \frac{u}{2}q^2\right) + \frac{\lambda_{2,0}^2}{8}u. \tag{25}$$

Therefore, the second-order total energy is expressed as

$$E_{\mathrm{QFF}} = \frac{p^2 + \lambda_{0,2}}{2M} + V_{\mathrm{QFF}}(q) + \frac{\lambda_{2,0}}{2}\left(h + tq + \frac{u}{2}q^2\right) + \frac{\lambda_{2,0}^2}{8}u. \tag{26}$$

The total energy terminates at the fourth order, because derivatives of higher order than the fourth order will vanish in the QFF approximation, i.e., $V_{\mathrm{QFF}}^{(n)} = 0 \quad (n > 4)$. In the EOM of the momentum operator, we retain the term up to third order in the differential operators to give

$$\dot{p}(t) = -\frac{\partial V_{\mathrm{QFF}}(q)}{\partial q} - \frac{\lambda_{2,0}(t)}{2}\frac{\partial^3 V_{\mathrm{QFF}}(q)}{\partial q^3}. \tag{27}$$

The other EOMs that include the quantal potential become

$$\dot{\lambda}_{0,2}(t) = -2\lambda_{1,1}(t)\left[\frac{\partial^2 V_{\mathrm{QFF}}(q)}{\partial q^2} + \frac{\lambda_{2,0}(t)}{2}\frac{\partial^4 V_{\mathrm{QFF}}(q)}{\partial q^4}\right], \tag{28}$$

$$\dot{\lambda}_{1,1}(t) = \frac{\lambda_{0,2}(t)}{M} - \lambda_{2,0}(t)\left[\frac{\partial^2 V_{\mathrm{QFF}}(q)}{\partial q^2} + \frac{\lambda_{2,0}}{2}\frac{\partial^4 V_{\mathrm{QFF}}(q)}{\partial q^4}\right]. \tag{29}$$

The inconsistency in order of the differential operators in the above EOMs results in violation of the energy conservation law for the truncated potential.

So far, we approximate the exponential function of the differential operators as a finite series. There is no guarantee that ensures its accuracy in actual computations. In particular, the energy is not conserved if we truncate the potential as in the QHD method presented by Prezhdo [9].

We therefore suggest a more rigorous way to evaluate the quantal potential by summing the series of the analytic derivatives over infinite order. Hereafter we refer to the scheme as an analytic summation. As a typical example, we adopt the method to the EOMs of the Morse potential. The Morse potential is given by

$$V_M(q) = D_e\left(e^{-2\alpha q} - 2e^{-\alpha q}\right), \tag{30}$$

where D_e, α, and q_0 are three fundamental parameters. In the QCD method, we have to evaluate the exponential function of the differential operator, so we first derive an expression of the derivative at a general order. The nth derivative of the Morse potential ($D_e = 1$) is given by

$$V_M^{(n)}(q) = (-2\alpha)^n e^{-2\alpha(q-q_0)} - 2(-\alpha)^n e^{-\alpha(q-q_0)}. \tag{31}$$

Using this expression, the second-order quantal potential of the Morse potential is evaluated as

$$\tilde{V}_{M,2}\left(q, \lambda_{2,0}\right) = e^{-2\alpha(q-q_0)+2\alpha^2\lambda_{2,0}} - 2e^{-\alpha(q-q_0)+\alpha^2\lambda_{2,0}/2}. \tag{32}$$

Once the analytic form of the quantal potential is obtained, its higher-order derivatives are easily evaluated. These potentials and their derivatives can be calculated at any points $q$and $\lambda_{2,0}$ as in a standard classical dynamics simulation..

Thirdly, we exploit a convolution technique in order to deal with the exponential function of the differential operators that become a function with respect to k. In this work, we use the Fourier transformation as a first step. This procedure is quite convenient, since one does not need to consider an infinite series of a potential as in Eq. (32) and there is no need to truncate it to some order as in Eq. (24). We again consider the Morse potential. The Fourier transformation of the Morse potential is described as

$$V_M(k) = \sqrt{2\pi}\left(\delta(2i\alpha + k)\, e^{2\alpha q_0} - 2\delta(i\alpha + k)\, e^{\alpha q_0}\right). \tag{33}$$

Thus, the Fourier transform of the second-order Morse quantal potential becomes

$$\tilde{V}_{M,2}\left(q,\lambda_{2,0}\right)=\int_{-\infty}^{\infty}\frac{dk}{\sqrt{2\pi}}\exp\left(-ikq-\frac{\lambda_{2,0}}{2}k^{2}\right)V_{M}\left(k\right). \tag{34}$$

Integrating the right hand side of the above equation leads to the same result as in the right hand side of Eq. (32). In general, rearranging the definition of the Fourier transform of $V\left(k\right)$ leads to

$$\tilde{V}_{2}\left(q,\lambda_{2,0}\right)=\int\frac{ds}{\sqrt{2\pi\lambda_{2,0}}}\exp\left(-\frac{\left(q-s\right)^{2}}{2\lambda_{2,0}}\right)V\left(s\right). \tag{35}$$

This expression is the Gaussian transformation of the given potential.

Since the position and momentum cumulant variables depend mutually on themselves via Heisenberg's uncertainty relation and $\gamma\left(t\right)=\hbar^{2}\big/4$, one may delete one of them by introducing an assumption for the variables. By using the Heisenberg's uncertainty relation [1], we have

$$\left\langle\left(\delta\hat{Q}\left(t\right)\delta\hat{P}\left(t\right)\right)_{s}^{2}\right\rangle=\lambda_{2,0}\left(t\right)\lambda_{0,2}\left(t\right)+2\lambda_{1,1}^{2}\left(t\right)\geq\frac{\hbar^{2}}{4}. \tag{36}$$

We assume a least uncertainty relation and $\gamma\left(t\right)=\hbar^{2}\big/4$. The momentum cumulant is now expressed by means of the position cumulant as

$$\lambda_{0,2}\left(t\right)=\frac{\hbar^{2}}{4\lambda_{2,0}\left(t\right)}. \tag{37}$$

The kinetic energy is reduced to be

$$T_{2}=\frac{p^{2}\left(t\right)}{2M}+\frac{\hbar^{2}}{8M\lambda_{2,0}\left(t\right)}. \tag{38}$$

The total energy is then expressed by means of three variables as

$$E_{2}^{LU}\left(p,q,\lambda_{2,0}\right)=\frac{p^{2}}{2M}+\frac{\hbar^{2}}{8M\lambda_{2,0}}+\tilde{V}_{2}\left(q,\lambda_{2,0}\right). \tag{39}$$

This implies that the least uncertainty relation reduces the actual variables from four to three. We here define an effective quantal potential energy hyper surface (EQPES) as

$$V_{2}^{\text{eff}}\left(q,\lambda_{2,0}\right)=\frac{\hbar^{2}}{8M\lambda_{2,0}}+\tilde{V}_{2}\left(q,\lambda_{2,0}\right), \tag{40}$$

which is an analog of the potential energy surface (PES) in the classical dynamics. The first term originates from a quantum correction to the kinetic energy, which is inversely proportional to the position cumulants and masses. On the other hand, the second term contains a quantum correction to the potential energy, which is a function of both classical positions and position cumulant variables. Thus, the quantum effects are consequences due to a competition between the first mass-dependent and the second mass-independent terms. Owing to the first term and the definition of $\lambda_{2,0}$, $\lambda_{2,0}$ is always greater than zero, $\lambda_{2,0} > 0$. If we assume $M\lambda_{2,0}/\hbar^2 \to \infty$ and $\lambda_{2,0} \to 0$, the EQPES agrees with the ordinary PES (classical limit).

2.4 Density and Joint Density [16]

As Wigner pointed out in his first paper about a distribution function in quantum mechanics [27], the Wigner distribution function cannot be considered a proper probability distribution, because it may take on negative values. For this reason the function has a poor correspondence to the classical distribution function and is sometimes called a quasi-probability. The Husimi function is the simplest class of Gaussian smoothing of the Wigner distribution and leads to a non-negative distribution [28–30]. Although the Husimi function reveals a better correspondence to the probability distribution function in classical mechanics than the Wigner function does, the former loses the property of the marginal distribution [31]. There are a few distribution functions, which fulfill both the non-negativity and the marginal conditions as summarized in Table 2 of [30]. Here we derive a distribution function (joint density) based on the QCD2 framework that fulfills both conditions. This enables one to evaluate Shannon entropy, and the density is regarded as the proper probability distribution.

The density is given as an expectation value of a delta function as

$$\rho(s) = \left\langle \delta\left(\hat{Q} - s\right)\right\rangle. \tag{41}$$

By means of the Gaussian convolution, the second-order density is estimated to be

$$\rho_2\left(s, q, \lambda_{2,0}\right) = \frac{1}{\sqrt{2\pi\lambda_{2,0}}} \exp\left(-\frac{1}{2\lambda_{2,0}}(s-q)^2\right). \tag{42}$$

This indicates that the density appearing in the QCD is the Gaussian centered at the classical position, q, and its width is related to the position cumulant, $\lambda_{2,0}$. The second-order momentum density is also expressed as the Gaussian, $\pi_2\left(t, p, \lambda_{0,2}\right) = \rho_2\left(t, p, \lambda_{0,2}\right)$.

We also define a joint density, which is a function of position and momentum, as

$$\Delta(s,t) = \left\langle \left[\delta\left(\hat{Q} - s\right)\delta\left(\hat{P} - t\right)\right]_s\right\rangle. \tag{43}$$

The second-order joint density is given by

$$\Delta_2\left(s,t,q,p,\lambda_{2,0},\lambda_{1,1},\lambda_{0,2}\right)=\frac{1}{2\pi\gamma^{1/2}}\exp\left(-\frac{G\left(r-p,s-q\right)}{2\gamma}\right)\equiv\Delta_2\left(s,t\right), \tag{44}$$

where

$$G\left(r-p,s-q\right)=\lambda_{0,2}\left(q-s\right)^2+2\lambda_{1,1}\left(q-s\right)\left(p-t\right)+\lambda_{2,0}\left(p-t\right)^2. \tag{45}$$

The joint density fulfills following conditions as

$$1=\int\int\Delta_2\left(s,t\right)dsdt, \tag{46}$$

$$\rho_2\left(s\right)=\int\Delta_2\left(s,t\right)dt, \tag{47}$$

$$\pi_2\left(t\right)=\int\Delta_2\left(s,t\right)ds, \tag{48}$$

$$\Delta\left(s,t\right)\geq 0, \tag{49}$$

where the first one is the normalization, the second and third ones are marginal, and the last one is the positive definiteness conditions.

Finally, we consider the entropy of the present distribution function. Since the joint density devised here is positive definite, one can define entropy by means of the joint density. The Shannon entropy is given by

$$\begin{aligned}S_2^{\text{Shannon}}&=-\int\int\Delta\left(s,t\right)\ln\Delta\left(s,t\right)dsdt\\&=2.837877+\frac{1}{2}\ln\gamma\end{aligned}. \tag{50}$$

Since γ is constant with time, the Shannon entropy is time independent in this study.

2.5 Exactly Solvable Models

Here we show the exactly soluble models in the QCD2, which are also soluble in the classical dynamics. The first model is a free particle and the other is the harmonic oscillator. In the following, we derive the solutions for the global minima of the EQPES and of the EOMs.

Hamiltonian of the free particle is given by

$$\hat{H}_{\text{FP}}\left(\hat{P},\hat{Q}\right)=\frac{\hat{P}^2}{2M}. \tag{51}$$

Note here that there is no position-dependent term in the Hamiltonian. The second-order energy is written in terms of the momentum and momentum cumulant variables as

$$E_2\left(p, \lambda_{0,2}\right) = \frac{p^2 + \lambda_{0,2}}{2M}, \tag{52}$$

Therefore, the EQPES is given by

$$E_2^{LU}\left(p, \lambda_{2,0}\right) = \frac{p^2}{2M} + \frac{\hbar^2}{8M\lambda_{2,0}}. \tag{53}$$

The variational minimization of the energy leads to the solution $\left(p, \lambda_{2,0}\right) = (0, \infty)$ or equivalently $\left(p, \lambda_{0,2}\right) = (0, 0)$, where it is stressed that the position is undetermined. The corresponding energy minimum is zero, $E_2^{LU}(0, \infty) = 0$, where the zero-point energy is zero (k=0 state for the plane wave solution).

The solutions of EOMs are

$$\begin{pmatrix} q(t) \\ p(t) \end{pmatrix} = \begin{pmatrix} \frac{p(0)}{M} t \\ p(0) \end{pmatrix} \tag{54}$$

for the classical variables and

$$\begin{pmatrix} \lambda_{2,0}(t) \\ \lambda_{1,1}(t) \\ \lambda_{0,2}(t) \end{pmatrix} = \begin{pmatrix} \frac{\lambda_{0,2}(0)}{M^2} t^2 \\ \frac{\lambda_{0,2}(0)}{M} t \\ \lambda_{0,2}(0) \end{pmatrix} \tag{55}$$

for the cumulant variables. The solutions for the classical variables are the same as those obtained by the classical mechanics. The particle moves without any change in velocity and its position is linear with respect to time. On the other hand, the second-order position cumulant and the mixed position–momentum cumulant are quadratic and linear, respectively, with respect to the time. The second-order momentum cumulant is also time independent and keeps the initial value. Since both the momentum and momentum cumulant variables are time independent, the energy conserves, though the position changes with time.

Next is the harmonic oscillator, where the Hamiltonian is given by

$$\hat{H}_{HO}\left(\hat{P}, \hat{Q}\right) = \frac{\hat{P}^2}{2M} + \frac{M\omega^2 \hat{Q}^2}{2}, \tag{56}$$

where ω is a frequency of the oscillator. The second-order energy is evaluated as

$$E_2\left(p, q, \lambda_{2,0}, \lambda_{0,2}\right) = \frac{p^2 + \lambda_{0,2}}{2M} + \frac{M\omega^2\left(q^2 + \lambda_{2,0}\right)}{2}. \tag{57}$$

Note again that the energy is independent of $\lambda_{1,1}$. The EQPES is expressed as

$$E_2^{LU}\left(p, q, \lambda_{2,0}\right) = \frac{p^2}{2M} + \frac{\hbar^2}{8M\lambda_{2,0}} + \frac{M\omega^2\left(q^2 + \lambda_{2,0}\right)}{2}. \tag{58}$$

The variational minimization leads to the solution $\left(p, q, \lambda_{2,0}\right) = \left(0, 0, \hbar/2M\omega\right)$. The corresponding energy minimum is

$$E_2^{LU}\left(0, 0, \hbar/2M\omega\right) = \frac{\hbar\omega}{2}. \tag{59}$$

The energy minimum exactly agrees with the zero-point energy of the harmonic oscillator.

The solutions of the EOMs are given as

$$\begin{pmatrix} q\left(t\right) \\ p\left(t\right) \end{pmatrix} = \begin{pmatrix} q\left(0\right)\cos\left(\omega t\right) + \frac{p(0)}{m\omega}\sin\left(\omega t\right) \\ p\left(0\right)\cos\left(\omega t\right) - m\omega q\left(0\right)\sin\left(\omega t\right) \end{pmatrix} \tag{60}$$

and

$$\begin{pmatrix} \lambda_{2,0}\left(t\right) \\ \lambda_{1,1}\left(t\right) \\ \lambda_{0,2}\left(t\right) \end{pmatrix} = \begin{pmatrix} \lambda_{2,0}\left(0\right)\cos^2\left(\omega t\right) + \frac{\lambda_{0,2}(0)}{2M^2\omega^2}\sin^2\left(\omega t\right) + \frac{\lambda_{1,1}(0)}{M\omega}\sin\left(2\omega t\right) \\ \lambda_{1,1}\left(0\right)\cos\left(2\omega t\right) + \frac{1}{2}\left(\frac{\lambda_{0,2}(0)}{M\omega} - M\omega\lambda_{2,0}\left(0\right)\right)\sin\left(2\omega t\right) \\ \lambda_{0,2}\left(0\right)\cos^2\left(\omega t\right) + \frac{M^2\omega^2\lambda_{2,0}(0)}{2}\sin^2\left(\omega t\right) - M\omega\lambda_{1,1}\left(0\right)\sin\left(2\omega t\right) \end{pmatrix}. \tag{61}$$

Again the solutions of the classical variables are the same as those obtained by the classical mechanics, where the period of the oscillation depends on ω. On the other hand, the period of the oscillation of all the cumulant variables depends on 2ω, where we note that both $\cos^2\omega t$ and $\sin^2\omega t$ can be rewritten by functions of $\cos 2\omega t$.

When ω^2 is negative ($\omega^2 < 0$), the bound state energy of Eq. (59) becomes imaginary. In this case, there is no bound state any more. Nevertheless the solutions of EOMs can be obtained by introducing following changes: $\omega \to i\left|\omega\right|$, $\cos\omega t \to \cosh\left|\omega\right| t$, and $\sin\omega t \to -i\sinh\left|\omega\right| t$. The results are not shown here to avoid verbose expressions.

In above cases, the classical and cumulant variables are separated from each other and the solutions of the classical variables coincide with those obtained by the classical mechanics. In the general cases, all the classical and cumulant variables couple with each other and it is difficult to solve the EOMs analytically. In the

proceeding section, we will show the numerical solutions of the QCD-EOMs and its applicability for the physically and chemically interesting problems.

2.6 Extension to Multi-dimensional Systems

The Hamiltonian of N spinless particles interacting with $V\left(\left\{\hat{\mathbf{Q}}_\mathbf{i}\right\}\right)$ is

$$\hat{H} = \sum_i \frac{\hat{\mathbf{P}}_i^2}{2M_i} + V\left(\left\{\hat{\mathbf{Q}}_i\right\}\right), \tag{62}$$

where the operators fulfill the commutation relation as

$$\begin{aligned} \left[\hat{Q}_{ik}, \hat{P}_{jl}\right] &= i\hbar\delta_{ij}\delta_{kl} \\ \left[\hat{Q}_{ik}, \hat{Q}_{jl}\right] &= \left[\hat{P}_{ik}, \hat{P}_{jl}\right] = 0 \end{aligned}. \tag{63}$$

i and j denote for the particle and k for the Cartesian elements ($k = x$, y, and z). We again adopted the cumulant expansion of the multi-dimensional systems, which leads to

$$\left\langle V\left(\left\{\hat{\mathbf{Q}}_i\right\}\right)\right\rangle = \exp\left(\sum_i \sum_{\mathbf{m}} \lambda_{\mathbf{m}_i,\mathbf{0}_i} \cdot \frac{\partial^{\mathbf{m}_i}}{\partial \mathbf{q}_i^{\mathbf{m}_i}}\right) V\left(\{\mathbf{q}_i\}\right), \tag{64}$$

where $\mathbf{q}_i = \left\langle \hat{\mathbf{Q}}_i \right\rangle$ and $\mathbf{p}_i = \left\langle \hat{\mathbf{P}}_i \right\rangle$. The second-order approximation of it for three-dimensional systems leads to

$$V_2\left(\{\mathbf{q}_i\}, \left\{\lambda_{\mathbf{2}_i,\mathbf{0}}\right\}\right) = \exp\left(\sum_i \sum_{k=x,y,z} \lambda_{2_{ik},0_{ik}} \frac{\partial}{\partial q_{ik}^{m_{ik}}}\right) V\left(\{\mathbf{q}_i\}\right). \tag{65}$$

Note that the cumulant variables couple with each other via $V\left(\{\mathbf{q}_i\}\right)$. According to the Gaussian transform, we have the $3N$-dimensional integral as

$$V_2\left(\{\mathbf{q}_i\}, \left\{\lambda_{\mathbf{2}_i,\mathbf{0}}\right\}\right) = \int d\mathbf{s}_1 \cdots \int d\mathbf{s}_N \exp\left(\sum_i \sum_{k=x,y,z} \frac{(q_{ik} - s_{ik})}{\lambda_{2_{ik},0_{ik}}}\right) V\left(\{\mathbf{s}_i\}\right). \tag{66}$$

The total energy is

$$E_2\left(\{\mathbf{q}_i\}, \{\mathbf{p}_i\}, \left\{\lambda_{\mathbf{2}_i,\mathbf{0}}\right\}, \left\{\lambda_{\mathbf{0},\mathbf{2}_i}\right\}\right) = \sum_i \frac{\mathbf{p}_i^2 + \lambda_{\mathbf{0},\mathbf{2}_i} \cdot \mathbf{1}}{2M_i} + V_2\left(\{\mathbf{q}_i\}, \left\{\lambda_{\mathbf{2}_i,\mathbf{0}}\right\}\right). \tag{67}$$

We have used the cumulant variables as

$$\lambda_{\mathbf{2}_i,\mathbf{0}} = \left\langle \delta\hat{\mathbf{Q}}_i^2 \right\rangle, \tag{68}$$

$$\lambda_{\mathbf{0},\mathbf{2}_i} = \left\langle \delta\hat{\mathbf{P}}_i^2 \right\rangle, \tag{69}$$

and

$$\lambda_{\mathbf{1}_i,\mathbf{1}_i} = \left\langle \left(\delta\hat{\mathbf{Q}}_i \delta\hat{\mathbf{P}}_i \right)_s \right\rangle. \tag{70}$$

The EOMs are $15N$ set of the following equations as

$$\begin{aligned}
\dot{\mathbf{q}}_i(t) &= \mathbf{p}_i, \\
\dot{\mathbf{p}}_i(t) &= -\frac{\partial}{\partial \mathbf{q}_i} V_2\left(\{\mathbf{q}_i(t)\}, \left\{\lambda_{\mathbf{2}_i,\mathbf{0}}(t)\right\}\right), \\
\dot{\lambda}_{\mathbf{2}_i,\mathbf{0}}(t) &= 2\lambda_{\mathbf{1}_i,\mathbf{1}_i}(t), \\
\dot{\lambda}_{\mathbf{1}_i,\mathbf{1}_i}(t) &= \lambda_{\mathbf{0},\mathbf{2}_i}(t) - \lambda_{\mathbf{2}_i,\mathbf{0}} \frac{\partial^2}{\partial \mathbf{q}_i^2} V_2\left(\{\mathbf{q}_i(t)\}, \left\{\lambda_{\mathbf{2}_i,\mathbf{0}}(t)\right\}\right), \\
\dot{\lambda}_{\mathbf{0},\mathbf{2}_i}(t) &= -2\lambda_{\mathbf{1}_i,\mathbf{1}_i}(t) \frac{\partial^2}{\partial \mathbf{q}_i^2} V_2\left(\{\mathbf{q}_i(t)\}, \left\{\lambda_{\mathbf{2}_i,\mathbf{0}}(t)\right\}\right).
\end{aligned} \tag{71}$$

Again we have the conserved energy and N-conserved variables defined as

$$\gamma_{ik}(t) = \lambda_{2_{ik},0}(t)\,\lambda_{0,2_{ik}}(t) - \lambda^2_{1_{ik},1_{ik}}(t). \tag{72}$$

By using the least uncertainty relation for all axis, $\lambda_{0,2_{ik}} = \hbar^2 \big/ 4\lambda_{2_{ik},0}$, we have

$$E_2^{LU}\left(\{\mathbf{q}_i\}, \{\mathbf{p}_i\}, \left\{\lambda_{\mathbf{2}_i,\mathbf{0}}\right\}\right) = \sum_i \frac{\mathbf{p}_i^2}{2M_i} + \sum_i \frac{1}{8M_i\lambda_{\mathbf{2}_i,\mathbf{0}}} \cdot \mathbf{1} + V_2\left(\{\mathbf{q}_i\}, \left\{\lambda_{\mathbf{2}_i,\mathbf{0}}\right\}\right). \tag{73}$$

We also define multi-dimensional EQPES as

$$\tilde{V}_2^{eff}\left(\{\mathbf{q}_i\}, \left\{\lambda_{\mathbf{2}_i,\mathbf{0}}\right\}\right) = \sum_i \frac{1}{8M_i\lambda_{\mathbf{2}_i,\mathbf{0}}} \cdot \mathbf{1} + V_2\left(\{\mathbf{q}_i\}, \left\{\lambda_{\mathbf{2}_i,\mathbf{0}}\right\}\right). \tag{74}$$

3 Applications

Here we demonstrate four applications of physically and chemically interesting problems and one performance of a suggested algorithm for integrators.

3.1 Numerical Tests for One-Dimensional Morse Oscillator [12]

We here show the difference between two of the schemes, i.e., the analytic summation and the truncation methods, in order to measure the accuracy of the latter method. The parameters of the Morse potential are $\alpha = 0.1$ and De = 1.0 in this simulation. The time interval is $\delta t = 0.05$; a fourth-order Runge–Kutta integrator is used for the simulation; and total time of the simulation is $T = 10,000$. The initial conditions used in the simulation are $p(0) = 0$, $q(0) = 1$, $\lambda_{1,1}(0) = 0$, $\lambda_{2,0}(0) = 3.33885$, and $\lambda_{0,2}(0) = 1/4\lambda_{2,0}(0)$. The energy of the Morse potential is evaluated exactly, $E_{\text{exact}} = -0.930539$. On the other hand, energies obtained by the present schemes are $E_2 = -0.927174$ for full EQPES and $E_{2,\text{QFF}} = -0.927223$ for approximate EQPES, as a quartic potential expanded around $q = 0$.

In relation to the truncation scheme in dynamics, there exist two possible methods. One is the truncation at fixed-point (say $q = 0$) and the other is the truncation on-the-fly ($q = q(t)$). In order to see the error due to truncation of the Morse potential, we depicted phase space of trajectories obtained by analytic and truncation schemes in Fig. 1, where the potential is expanded around $q = q(t)$ (on-the-fly approach). The truncation scheme gives wrong trajectory around $(q, p) \sim (1, 0)$, where the deviation between the Morse and approximate quartic potential is evident. The relative error is defined as Error $= \frac{1}{T}\int_0^T \ln|E_2(t) - E_{2.av}|\,dt$, where $E_{2.av}$ is an averaged energy over T. Both the analytic and truncation schemes conserve the total energy throughout the simulations, so the energy conservation problem does not matter for this case. Actually, the energy conservation is almost fulfilled. The error of the truncation scheme for fixed-point and for on-the-fly is less than 12 and 4 decimals, respectively. Thus one needs to adopt smaller time step for the on-the-fly methods than that for the fixed-point truncation and analytic methods.

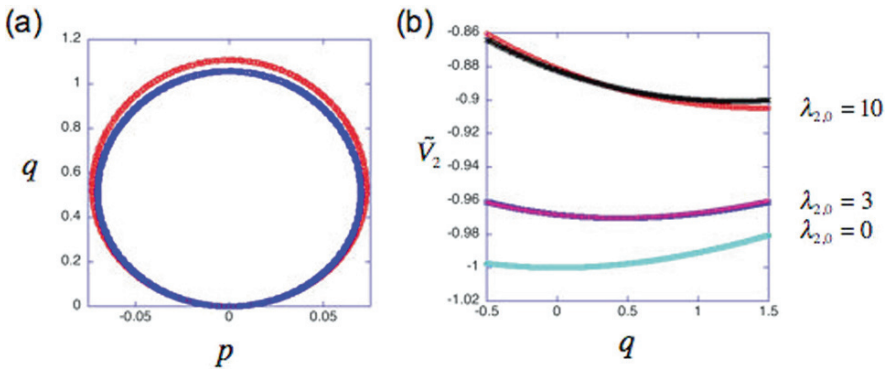

Fig. 1 (**a**) Phase space of trajectory obtained by analytic (*red*) and on-the-fly truncation (*blue*) schemes. (**b**) Second-order quantal potential of the Morse potential for analytic (*red, blue, and green*) and on-the-fly truncation (*black, pink, and sky-blue*) schemes

3.2 Time-Reversible Integrator [13]

3.2.1 Algorithms

An efficient time-reversible integrator was initially proposed by Yoshida for Hamiltonian dynamics and is well known as higher-order symplectic integrators [32, 33]. Independently Suzuki established the basics of a Lie-algebraic construction of a decomposed time evolution operator [34]. In the following, we give a time-reversible integrator for the QCD derived in a consistent manner. The time evolution of the above variables is described in terms of a propagator from $t = 0$ to $t = \delta t$ as

$$\mathbf{a}(\delta t) = e^{iL\delta t}\mathbf{a}(0), \tag{75}$$

where $\mathbf{a}(\delta t)$ is a vector that consists of the above five variables defined above at $t = \delta t$ and L is the Liouville operator of the QCD. A variety of integrators exist, which differ from one another in the way of approximating the time evolution operator. According to the EOMs, the Liouville operator in a vector form is expressed as

$$iL = \mathbf{X}(t) \cdot d\mathbf{Z}^{+} = \sum_{i} X_i(t)\, dZ_i, \tag{76}$$

where

$$\mathbf{X}^{+}(t) = \begin{pmatrix} X_q(t) \\ X_p(t) \\ X_{\lambda_{2,0}}(t) \\ X_{\lambda_{0,2}}(t) \\ X_{\lambda_{1,1}}(t) \end{pmatrix} = \begin{pmatrix} p(t) \\ -\tilde{V}^{(1)}\left(q(t), \lambda_{2,0}(t)\right) \\ 2\lambda_{1,1}(t) \\ -2\lambda_{1,1}(t)\,\tilde{V}^{(2)}\left(q(t), \lambda_{2,0}(t)\right) \\ -\lambda_{2,0}(t)\,\tilde{V}^{(2)}\left(q(t), \lambda_{2,0}(t)\right) + \lambda_{0,2}(t) \end{pmatrix}, \tag{77}$$

and

$$d\mathbf{Z}^{+}(t) = \begin{pmatrix} dZ_q(t) \\ dZ_p(t) \\ dZ_{\lambda_{2,0}}(t) \\ dZ_{\lambda_{0,2}}(t) \\ dZ_{\lambda_{1,1}}(t) \end{pmatrix} = \begin{pmatrix} \partial / \partial q(t) \\ \partial / \partial p(t) \\ \partial / \partial \lambda_{2,0}(t) \\ \partial / \partial \lambda_{0,2}(t) \\ \partial / \partial \lambda_{1,1}(t) \end{pmatrix}. \tag{78}$$

The time-reversible integrators can be derived in the following manner: The Liouville operator is decomposed into three non-commutative operators as

$$iL = iL_1 + iL_2 + iL_3. \tag{79}$$

Since there are several ways to decompose the Liouvillian, we here adopt three of them so as to require the least number of force evaluations. The definitions of L_k

Table 1 Operators appearing in decomposed Liouvillian

	L_1	L_2	L_3
Scheme A	$q,\ \lambda_{2,0}$	$p,\ \lambda_{1,1},\ \lambda_{0,2}$	
Scheme B	$q,\ \lambda_{2,0}$	$\lambda_{1,1}$	$p,\ \lambda_{0,2}$
Scheme C	$q,\ \lambda_{2,0}$	$p,\ \lambda_{0,2}$	$\lambda_{1,1}$

are listed in Table 1. By decomposing the time evolution operator into three parts, one can obtain a sequential time evolution operator as

$$e^{iL\delta t} \approx \prod_{j=1}^{n} \left[e^{ic_{j,1}L_1\delta t} e^{ic_{j,2}L_2\delta t} e^{ic_{j,3}L_3\delta t} \right], \tag{80}$$

where a set of real coefficients $c_{j,k}$ (k=1, 2, and 3) are determined by comparing the Taylor expansion of the partitioned time evolution operator with that of the whole time evolution operator. For example, a second-order approximation to the time evolution operator is given by

$$e^{iL\delta t} \approx e^{iL_3\delta t/2} e^{iL_2\delta t/2} e^{iL_1\delta t} e^{iL_2\delta t/2} e^{iL_3\delta t/2} \equiv S_2(\delta t). \tag{81}$$

This decomposition is corrected for third order with respect to the time step. The fourth-order integrator is constructed from a product of second-order evolution operators with different time steps as

$$S_4(\delta t) = S_2(s\delta t)\, S_2(s\delta t)\, S_2((1-4s)\,\delta t)\, S_2(s\delta t)\, S_2(s\delta t), \tag{82}$$

where $s = 1 \Big/ \left(4 - \sqrt[3]{4}\right)$. In this work, we adopt S_4 for actual calculations.

3.2.2 Performance

Numerical simulations of the QCD were performed with the Runge–Kutta integrator and the time-reversible integrators devised here. The parameter of the Morse potential is the same as adopted in the previous section.

The accuracy of the QCD was evaluated in terms of the conservation of the total energy. Figure 2 depicts time series of the maximum error of the total energy against the number of gradient and Hessian updates per 1,000 unit time, N. Here the number of updates and the error are defined as

$$\begin{aligned} N &= 1,000 n_x/\delta t \\ \text{Error} &= \max \log_{10}\left(|E_2(t) - E_2(0)|\right)' \end{aligned} \tag{83}$$

where n_x is the number of the updates for a unit time step, required in the algorithm x. Since one of the most time-consuming steps in a molecular dynamics simulation

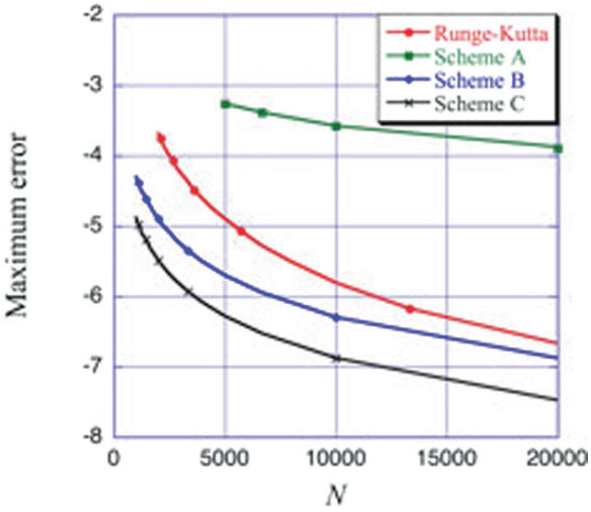

Fig. 2 Maximum error vs. number of Hessian update for different algorithms

is the update of the gradient and Hessian, it is instructive to measure the error against N rather than δt in order to estimate the efficiency in actual calculations. It is necessary to update the gradient and Hessian of the quantal potential once for the second-order time-reversible integrator, twice for the second-order Runge–Kutta, five times for the fourth-order time-reversible integrator, and four times for the fourth-order Runge–Kutta.

Comparing the time-reversible integrators, Scheme A is the least accurate and Scheme C is the most accurate of the three schemes. Since the EOMs of $\lambda_{1,1}$ and $\lambda_{0,2}$ depend mutually on each other, the error becomes critically large with Scheme A. In particular, the error in the fourth-order Scheme A is very similar to that in the second-order method (not shown in the figure). It is thus concluded that the partition of p, $\lambda_{0,2}$, and $\lambda_{1,1}$ cannot be disregarded. Scheme C is more accurate than that of B by one order of magnitude and Schemes B and C differ in the order of the time evolution operators of p, $\lambda_{0,2}$, and $\lambda_{1,1}$. This fact tells us that the equations of motion of the QCD are sensitive to the order in the time-reversible integrator. Judging from the figures, the time-reversible integrator (Scheme C) is always superior to the Runge–Kutta method at the same order.

3.3 Application to Molecular Vibration [11, 17]

3.3.1 Extended Normal Mode Analysis

Since we have defined a new effective potential (EQPES), which includes quantum effect through extended variables, we can consider vibrational analysis on

the EQPES. According to the ordinary normal mode analysis (NMA), a set of N vectors, which consist of only classical coordinates, are evaluated by diagonalizing a Hessian matrix (second derivative matrix) of the PES at equilibrium geometry. In analogy to the ordinary procedure, we may define normal modes, which consist of both classical coordinates and coordinate cumulant variables, by diagonalizing the Hessian matrix evaluated from the EQPES. Because the actual variables in the present theory are $2N$, we result in $2N$ normal modes, which are different from those in the ordinary NMA.

For example, we apply the extended NMA to the one-dimensional Morse oscillator based on QCD. Since the dimensions of the cumulant variables are different from those of classical ones, we should introduce alternative variables in order to consider the combined normal coordinates that consist of q and$\lambda_{2,0}$. The coordinate and conjugate momentum are given by

$$q_\lambda = \sqrt{\lambda_{2,0}}, \tag{84}$$

$$p_\lambda = \lambda_{1,1} \Big/ \sqrt{\lambda_{2,0}}\,, \tag{85}$$

where the dimensions of q_λ and p_λ are the same as those of q and p. The effective energy for the one-dimensional system is rewritten as

$$\tilde{E}_{eff}\left(q,\, p, q_\lambda,\, p_\lambda\right) = \frac{p^2}{2M} + \frac{p_\lambda^2}{2M} + \frac{1}{8Mq_\lambda^2} + \exp\left(\frac{q_\lambda^2}{2}\frac{\partial^2}{\partial q^2}\right) V_M\left(q\right). \tag{86}$$

By means of the Taylor series expansion, the effective energy is approximately given by second order with respect to q and q_λ as

$$\tilde{E}_{eff}\left(q,\, p, q_\lambda,\, p_\lambda\right) = \frac{1}{2M}\begin{pmatrix} p & p_\lambda \end{pmatrix}\begin{pmatrix} p \\ p_\lambda \end{pmatrix} + \frac{1}{2}\begin{pmatrix} \bar{q} & \bar{q}_\lambda \end{pmatrix}\begin{pmatrix} \tilde{V}_{qq} & \tilde{V}_{q\lambda} \\ \tilde{V}_{\lambda q} & \tilde{V}_{\lambda\lambda} \end{pmatrix}\begin{pmatrix} \bar{q} \\ \bar{q}_\lambda \end{pmatrix}, \tag{87}$$

where we have used the following abbreviations as

$$\bar{q} = q - q_{\text{opt}}, \tag{88}$$

$$\bar{q_\lambda} = q_\lambda - q_{\lambda,\text{opt}}\,, \tag{89}$$

and

$$\tilde{V}_{qq} = \frac{\partial^2 \tilde{V}_{\text{eff}}\left(q, q_\lambda\right)}{\partial q^2}, \tag{90}$$

$$\tilde{V}_{q\lambda} = \frac{\partial^2 \tilde{V}_{\text{eff}}\left(q, q_\lambda\right)}{\partial q\, \partial q_\lambda}, \tag{91}$$

$$\tilde{V}_{\lambda\lambda} = \frac{\partial^2 \tilde{V}_{\text{eff}}\left(q, q_\lambda\right)}{\partial q_\lambda^2}, \tag{92}$$

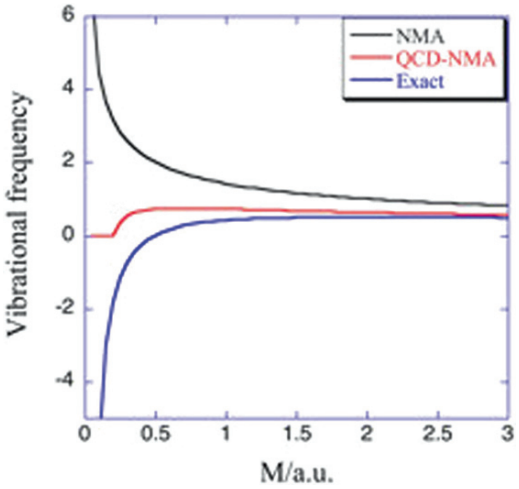

Fig. 3 First excitation energy obtained by normal mode analysis (NMA), QCD-NMA, and exact solution, where negative energy means no solution

where $\tilde{V}_{\text{eff}}(q, q_\lambda)$ is EQPES of the Morse potential. The optimized coordinates, q_{opt} and $q_{\lambda,\text{opt}}$, are obtained from the variational solutions of EQPES as done in Sects. 2, 3, 4, and 5. By diagonalizing the matrix in Eq. (87), one yields vibrational frequencies based on the extended NMA on EQPES, where lower energy solution corresponds to the corrected vibrational frequency over that obtained from the ordinary NMA. Figure 3 depicts frequencies obtained from the ordinary NMA on PES and from the extended NMA on EQPES as a function of the mass. We also plotted the energy gap between the ground and the first excited state estimated from the exact solution. The behavior of the exact solution is that (i) there exists a peak around $M/\text{a.u.} \approx 1$ and (ii) the energy gap becomes negative for $M/\text{a.u.} < 0.5$ which is a lower bound for the existence of the first excited state. The extended NMA gives more accurate results than the ordinary NMA does. Although the result by the extended NMA is unfortunately inaccurate for $M/\text{a.u.} < 1.5$ by comparing with the exact result, its behavior is similar. The frequency becomes complex for $M/\text{a.u.} < 0.2$. This behavior corresponds to the inexistence of the first excited state (c.f. Sect. 2.5). On the other hand, the ordinary NMA does not have any peak the first excited state always exists. Therefore, the extended NMA gives reasonable correction to the results obtained from the ordinary NMA as expected.

3.3.2 *n*-Mode Coupling Representation for Ab Initio Quartic Force Field (*n*MR-QFF)

In the previous section we consider the extension of the normal mode analysis for the extended phase space. Here we evaluate the vibrational modes from the results obtained from molecular dynamics (MD) simulations. Since the force field-based

model potentials, which are often used in molecular dynamics simulations, are empirical they sometimes lead to poor results for molecular vibrations. For quantitative results in any MD study, the accuracy of the PES is the other important requirement as well as the treatment of the nuclear motion. Here we use an efficient representation of the PES derived from ab initio electronic structure methods, which is suitable for both molecular vibration and the QCD scheme in principle. In order to include anharmonic effects, multi-dimensional quartic force field (QFF) approximation [35] is applied as

$$V_{\mathrm{QFF}}\left(\left\{\hat{Q}_i\right\}\right) = V_0 + \sum_i \frac{h_i}{2}\hat{Q}_i^2 + \sum_{ijk} \frac{t_{ijk}}{6}\hat{Q}_i\hat{Q}_j\hat{Q}_k + \sum_{ijkl} \frac{u_{ijkl}}{24}\hat{Q}_i\hat{Q}_j\hat{Q}_k\hat{Q}_l, \quad (93)$$

where V_0, h_i, t_{ijk}, u_{ijkl} denote the potential energy and its second-, third-, and fourth-order derivatives, respectively, with respect to a set of normal coordinates $\left\{\hat{Q}_i\right\}$, at the equilibrium geometry. To further reduce the computational cost for multi-dimensional cases, an n-mode coupling representation of QFF (nMR-QFF) was applied [35], which includes mode couplings up to n modes.

3.3.3 QCD2 with *n*MR-QFF for Molecular Vibrational Analysis

By taking each normal mode as the degree of freedom in the dynamics simulation, the Hamiltonian for QCD2 with nMR-QFF as the potential energy is

$$\hat{H}\left(\left\{\hat{P}_i\right\},\left\{\hat{Q}_i\right\}\right) = \sum_i \frac{\hat{P}_i^2}{2} + V_{\mathrm{QFF}}^{n-\mathrm{mode}}\left(\left\{\hat{Q}_i\right\}\right), \quad (94)$$

where $V_{\mathrm{QFF}}^{n-\mathrm{mode}}$ denotes nMR-QFF. In this Hamiltonian we neglected the Watson term, which represents the vibrational–rotational coupling. Mass does not appear in the equations since the QFF normal coordinate is mass weighted. Therefore, the time evolution of variables of QCD2 with 1MR-QFF (general expressions are not shown for simplicity) is derived as

$$\begin{aligned}
\dot{Q}_i &= P_i \\
\dot{P}_i &= -h_i Q_i + \frac{t_{iii}}{2}\left(Q_i^2 + \lambda_{2i,0i}\right) + \frac{u_{iiii}}{6}Q_i\left(Q_i^2 + 2\lambda_{2i,0i}\right) \\
\dot{\lambda}_{2i,0i} &= 2\lambda_{1i,1i} \\
\dot{\lambda}_{1i,1i} &= \lambda_{0i,2i} - \lambda_{2i,0i}\left[h_i + t_i Q_i + \frac{u_{iiii}}{2}\left(Q_i^2 + \lambda_{2i,0i}\right)\right] \\
\dot{\lambda}_{0i,2i} &= -2\lambda_{1i,1i}\left[h_i + t_i Q_i + \frac{u_{iiii}}{2}\left(Q_i^2 + \lambda_{2i,0i}\right)\right]
\end{aligned} \quad . \quad (95)$$

For molecules with more than 1 degree of freedom, we applied 3MR-QFF, because it has been shown by various examples that the 3MR-QFF is sufficient to describe fundamental modes as well as more complex overtone modes. The QCD2 and

classical simulations were performed numerically with a fourth-order Runge–Kutta integrator. For formaldehyde (CH_2O) and formic acid (HCOOH), 3MR-QFF PES was generated at the level of MP2/aug-cc-pVTZ [36, 37] using GAMESS [38] and Gaussian03 [39] program packages. In this work, the results obtained by our method are compared with those by vibrational self-consistent field method (VSCF) with second-order perturbation correction (VPT2), which is based on the quantum mechanics and accurate enough to treat molecular vibrations. We adopted the cc-VSCF method with the 3MR-QFF approximation to the ab initio potential implemented in the GAMESS program package for the VPT2 calculations.

We here present results of the spectral analysis of trajectories obtained from the simulation that can be compared with other theoretical calculations and experimental results. The Fourier transform of any dynamical variables obtained from the trajectories of MD simulations is related to spectral densities. In particular, Fourier transform of velocity autocorrelation function gives the density of vibrational states [33]. In addition, the power spectrum of the time series or autocorrelation function of each normal coordinate shows the contribution to frequency peaks of the spectrum obtained from velocity autocorrelation. Here we adopted the latter procedure. The time interval used was 0.1fs and total time is 1ps for all MD and QCD simulations. The resolution in the frequency domain is less than 1 cm^{-1}, which is an enough accuracy for the analysis of the molecular vibrations of interest. If a longer time trajectory is obtained, the resolution of the Fourier spectrum becomes fine.

Since each normal mode is taken as the degree of freedom explicitly in the present dynamics simulation, the interpretation and analysis of the results can directly be related with each normal mode. The results are shown in Table 2. The table indicates that the harmonic and QFF approximation of the PES results in a large deviation between each other. Therefore, anharmonicity of the potential must

Table 2 Vibrational frequency of H_2CO and HCOOH molecules, where NMA means normal mode analysis, MD does classical dynamics, QCD does the recent results, and VPT2 does the second-order vibrational perturbation theory. N/A means that there are no clear peaks in power spectrum around corresponding experimental values

	Mode	NMA	MD	QCD	VPT2	Exp.
H_2CO	ν_1	3,040	2,901	2,843	2,866	2,843
	ν_2	2,997	2,868	2,838	2,849	2,782
	ν_3	1,766	1,764	1,723	1,734	1,746
	ν_4	1,548	1,504	1,509	1,515	1,500
	ν_5	1,268	1,247	1,250	1,251	1,250
	ν_6	1,202	1,166	N/A	1,189	1,167
HCOOH	ν_1	3,739	N/A	3,527	3,554	3,570
	ν_2	3,126	N/A	2,980	2,989	2,943
	ν_3	1,794	N/A	1,761	1,761	1,770
	ν_4	1,409	N/A	1,377	1,385	1,387
	ν_5	1,302	N/A	1,270	1,231	1,229
	ν_6	1,130	N/A	1,120	1,097	1,105
	ν_7	626	N/A	631	620	625
	ν_8/ν_9	1,058/676	N/A	N/A	1,036/642	1,033/638

be considered to perform reliable simulations. The table shows that for the analysis of fundamental frequencies, the QCD2 has higher accuracy than the classical results, which can be compared with the VPT2 results in all cases. In spite of the high accuracy, the computational cost of the QCD2 remains low even when applied to larger systems. For HCOOH molecule, the QFF is so anharmonic that the classical simulation does not give clear vibrational frequencies due to the chaotic behavior of the power spectrum. The QCD may suppress the chaotic motion as seen in the full quantum mechanics.

3.4 Application to Magnetic Field-Induced Tunneling [15]

Recent advances in semiconductor technology enable us to fabricate lower-dimensional nano-structure. The particles are locally confined by an artificial confinement potential that can be controlled by its heterostructure. The properties are adjusted by applying the electro-magnetic field as observed in the bulk systems [40–44]. More recently, the electronic properties in the quantum dots and rings have received much attention. Especially, the quantum ring nano-structure is synthesized and the magnetic field-induced phenomena in the ring structure are observed [45]. The properties and possible mechanism of the electron tunneling in the ring structure are considered here.

Models are the two-dimensional (i) harmonic and (ii) double well potential as

$$V_q\left(q_x, q_y\right) = \frac{\omega}{2}\sum_{i=x,y} q_i^2 \quad (\omega = 0.2)\,, \tag{96}$$

$$V_w\left(q_x, q_y\right) = \sum_{i=x,y}\left(2q_i^4 - q_i^2\right), \tag{97}$$

where the first one is a model for quantum dot and the second is a model for a two-dimensional quantum well.

We performed the QCD2 simulations in a parabolic potential under the magnetic field. For the system (i), we choose $q_x = 0,\ q_y = -0.1,\ p_x = 0.1,$ and $p_y = 0$ for classical variables. On the other hand, for the system (ii), we set $q_x = q_y = 0.5$ and $p_x = p_y = 0$. The cumulant variables are estimated from the variational solutions on the EQPES with fixed classical positions. The initial total energy is $E(0) = 0.447214$ for (i) and $E(0) = -0.0573793$ for (ii). It should be stressed here that the initial energy for case (ii) is slightly higher than the energy of quantal transition state $E^{\mathrm{TS}}_{\mathrm{eff},q} = -0.0574275$ of the effective potential. On the other hand, a classical component of the total energy with zero-point energy correction ($E^{\mathrm{ZPVE}} = 0.02602$) $E_c(0) = -0.22398$ is much lower than corresponding classical transition state $E^{\mathrm{TS}}_{\mathrm{c}} = -0.125$. Thus, the trajectory obtained by the QCD may reflect quantum nature of the motion and is likely to exhibit transitions from one well to others.

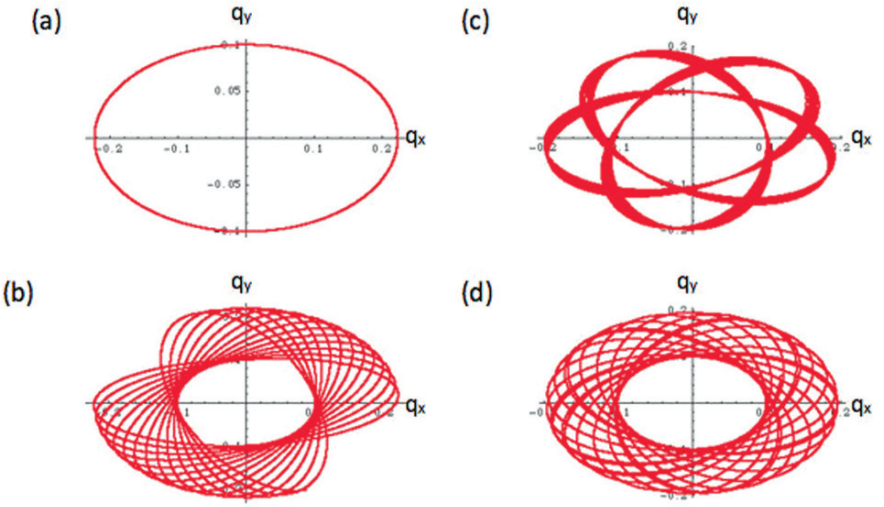

Fig. 4 Trajectory of $q_x - q_y$ for quantum well (**a**) $B = 0$, (**b**) $B = 0.02$, (**c**) $B = 0.18$, and (**d**) $B = 2.0$

The Fig. 4 illustrates the trajectories of q_x–q_y at a various magnitude of the magnetic field. At $B = 0$, since the potential is merely a harmonic oscillator, the trajectory is regular and draws an elliptic orbit on the q_x–q_y plane (see Fig. 4(a)). At weak magnetic field, the axis of the elliptic orbit rotates as shown in Fig. 4(b). As the magnitude of the magnetic field increases, the trajectory deviates from elliptic orbit (see Fig. 4(c)) and becomes differently closed orbit from the elliptic one (see Fig. 4(d)). The trajectory as illustrated in Fig. 4(d) is a first Landau level. If we apply stronger magnetic field, $B = 0.20$, we again observe the regular and elliptic orbit like as that appears in Fig. 4(b). Here the magnitude of the magnetic field $B = 0.20$ is comparable with the force constant of the parabolic potential $\omega = 0.2$. It is possible that the trajectory may reflect some resonances.

Next, we also performed the QCD2 simulation in the double well potential under the magnetic filed. Here we found two characteristics as follows: (i) a magnetic field-induced transition from a well to the others and (ii) a magnetic confinement. At weak magnetic field, $B = 0.001$, the particle is confined in the first quadrant as depicted in Fig. 5(a), where the particle does not move from a well at the first quadrant to the other. This reflects potential confinement as observed in the previous example at the weak magnetic field. As the magnitude of the magnetic field increases, the particle moves from a well to the others as shown in Fig. 4(b) and (c), where it involves the tunneling motion. At $B = 0.16$, the situation is completely different from the other cases. Although the particle is confined in a first quadrant as well as the case (a), the trajectory of the case (d) is different from that of the case (a). In particular, the trajectory of the case (d) has a "chink" that may reflect a Landau level as mentioned in the first example. This is an indication of the magnetic field-induced confinement, which should be distinguished from the potential confinement in the

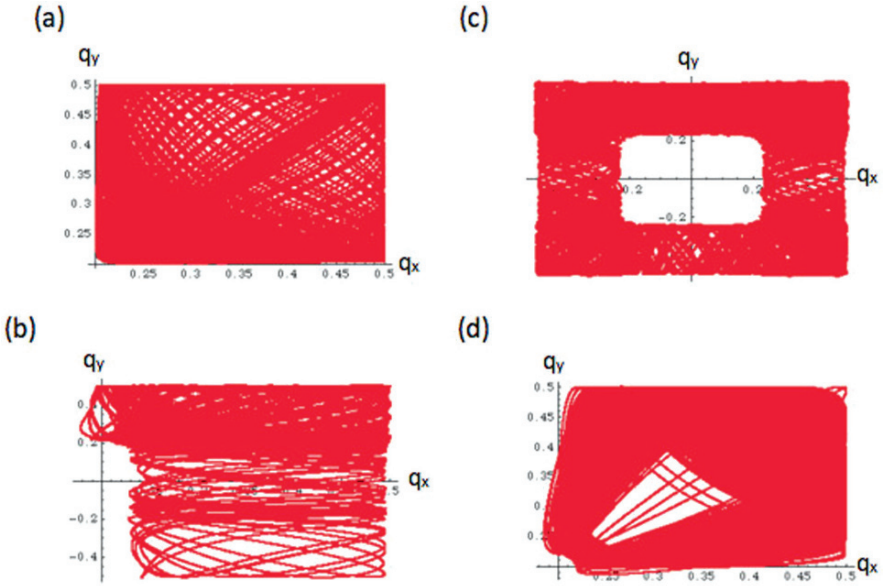

Fig. 5 Trajectory of $q_x - q_y$ in quantum ring nano-structure at magnetic field (**a**) $B = 0.001$, (**b**) $B = 0.07$, (**c**) $B = 0.12$, and (**d**) $B = 0.16$ (a.u.). Note that (**a**) and (**d**) only show first quadrant of the trajectory and (**b**) does both first and fourth quadrant in order to make the differences among them clear

case of (a). Note here that the simulation depends on the initial conditions we have chosen. Nevertheless, the observed phenomena were also found by changing initial conditions appropriately.

3.5 Application to Proton-Transfer Reaction [17]

In this section we consider multiple proton/hydrogen-transfer reactions in DNA bases. The multiple proton-transfer reactions in these systems were investigated by Florián et al. by density functional calculations [46, 47]. Later, quantum mechanical treatments for the system were performed by Villani [48, 49]. We also investigated influences of the metal binding to the base pairs and of the stacking effects on multiple proton-transfer reactions [50, 51]. We here adopt a model for Guanine–Cytosine (GC) base pair as depicted in Fig. 6.

In order to investigate dynamical stability of proton-transferred structures of the model system, we here perform QCD2 simulations of a model GC pair. The model potential is given by

$$V^{\mathrm{GC}}(x, y, z) = \sum_{i,j,k} h'_{i,j,k} x^i y^j z^k, \tag{98}$$

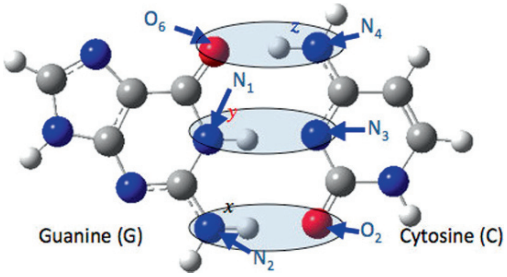

Fig. 6 Models for multiple proton-transfer reactions in GC pairs. x, y, and z are reaction coordinates of the proton-transfer reactions

where parameters in the model potential are given by Villani's paper [48, 49], which are fifth-order polynomials with respect to the coordinates for GC pairs and determined by the first principle calculations (B3LYP/cc-pVDZ). The reaction coordinates x, y, and z are shown in the Fig. 6. The corresponding quantal potentials are explicitly given by

$$\tilde{V}_2^{\mathrm{GC}}(x, y, z, \xi, \eta, \zeta) = \sum_{l,m,n=0}^{2} \sum_{i=0}^{5-2l} \sum_{j=0}^{5-2m} \sum_{k=0}^{5-2n} H_{i,j,k}^{l,m,n} x^i y^j z^k \left(\frac{\xi}{2}\right)^l \left(\frac{\eta}{2}\right)^m \left(\frac{\zeta}{2}\right)^n, \tag{99}$$

$$H_{i,j,k}^{l,m,n} = \frac{(i+2l)!}{i!l!} \frac{(j+2m)!}{j!m!} \frac{(k+2n)!}{k!n!} h'_{i+2l,j+2m,k+2n}, \tag{100}$$

where Greek characters denote the position cumulant variables. In order to avoid the particles escaping from the bottoms, we have added the well-like potential, which gives small influence on minima and transition states in the potential. In the actual calculations, the time interval used was 0.1fs, total time is 2ps, and a fourth-order Runge–Kutta integrator was used in our simulations. The initial conditions of the variables can be determined from the variational solutions of the EQPES.

Here we first analyze the EQPES defined above in order to investigate static quantum isotope effects on the proton-transfer reactions. At first we fix the classical variables at the equilibrium geometry on the classical PES, $\mathbf{q}_{0,eq} = \left(x_{0,eq}, y_{0,eq}, z_{0,eq}\right)$, and optimize the cumulant variables on the partially frozen EQPES (fixed geometry search), $\tilde{V}_{\mathrm{eff},2}\left(\mathbf{q}_{0,eq}, \lambda_{2,0}\right)$, and then proceed to fully relaxed geometry search both for the classical and cumulant variables on the EQPES, $\tilde{V}_{\mathrm{eff},2}\left(\mathbf{q}, \lambda_{2,0}\right)$, where $\lambda_{2,0} = (\xi, \eta, \zeta)$. There exist both global and metastable structures in GC pairs. The energy gap between the two states is 13, 17, and 50 kJ/mol for proton, deuteron, and classical cases, respectively. This gap will disappear when the mass is as light as a muon. We found explicit isotope effects on the energy gap between stable and metastable structures. From these EQPES analyses we conclude here that the double proton-transferred structure of the GC pair might be stable both

for protonated and deuterated cases. Nevertheless, the energy gap between global and metastable structures is small enough that thermal activation may drive the proton-transfer reactions from the metastable to global minimum.

Next we perform QCD simulations for both protonated and deuterated isotopomers in order to consider dynamic effects on the stability of the system. In Fig. 7 we have depicted phase space $(x/p_x, y/p_y, z/p_z)$ structures of a trajectory obtained by the QCD simulations for proton (a) and (c) and deuteron cases (b) and (d). For cases (a) and (b), the dynamical features of the closed orbits are the same except for its amplitudes. The phase space of the x/p_x is compact, on the other hand, the phase space of z/p_z is loose in comparison with that ofy/p_y. The explicit isotope effects on the phase space structure are found in the cases of (c) and (d). In Fig. 7(c), the nuclei initially located at the metastable structure (double

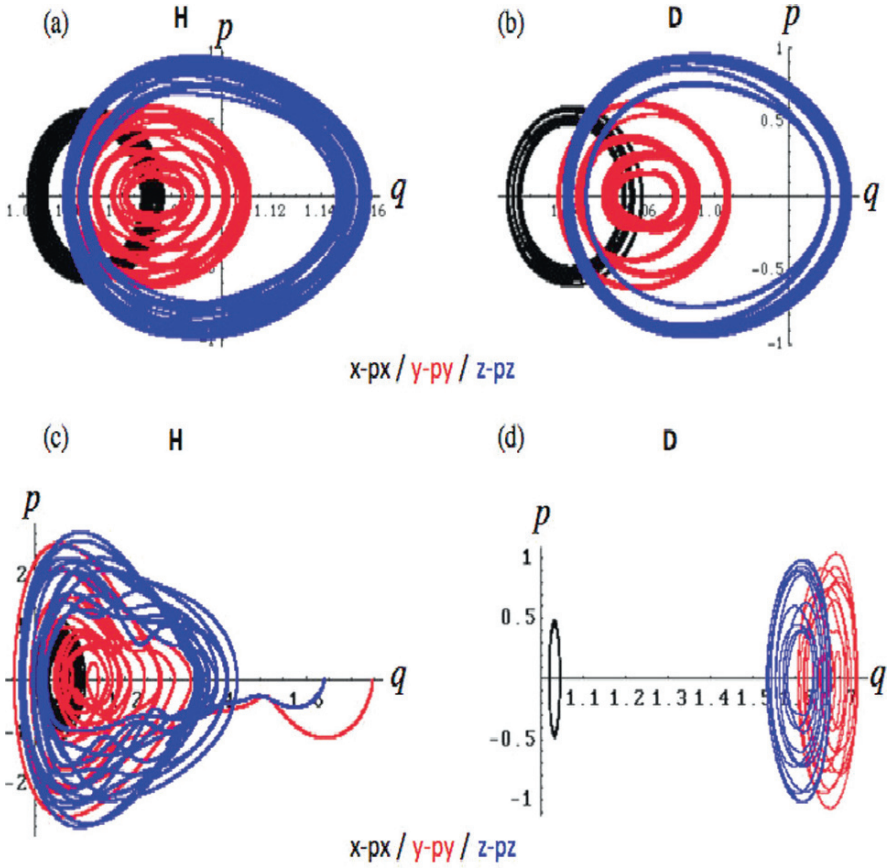

Fig. 7 QCD phase space structures of the GC pair, where $q = x$, y, or z and $p = p_x$, p_y, or p_z; (**a**) and (**b**) are initially located around the global minimum for the protonated and deuterated cases, respectively; (**c**) and (**d**) are initially located around the metastable structure for the protonated and deuterated cases, respectively

proton-transferred structure along y and z hydrogen atoms) go out from the basin and strongly vibrates around the global minimum due to transition from metastable to stable structure. On the other hand, the deuterated isotopomer remains around the metastable structure (see Fig. 7(d)). It is concluded that the metastable structure of the protonated isotopomer is quantum mechanically unstable, though it is classically stable based on the PES analysis. Therefore, it is important to take the quantum effects into isotope effects on the metastable structure with a small energy gap.

4 Summary

We have formulated a quantal cumulant dynamics (QCD) method. The key point is the use of a position shift operator acting on a potential operator and introducing the cumulant variables to evaluate it, so that one need not truncate the potential, and it does not require separating into quantum and classical parts, as is done in the QHD method suggested by Prezhdo and co-workers. In particular, we have derived the coupled equation of motion (EOM) for the position, momentum, and second-order cumulants of the product of the momentum and position fluctuation operators. The EOM consists of variables and a quantal potential and its derivatives, where the quantal potential is expressed as an exponential function of the differential operator acting on the given potential. The advantages of the QCD approach over the QHD method are (i) a systematic construction of the higher-order equations of motion is possible, (ii) there are no errors in the energy and its gradient due to the truncation of the potential, and (iii) there is no tedious derivation with respect to the decomposition scheme in the QHD method.

To evaluate the quantal potential and its derivatives, we have proposed three possible schemes: (i) a truncation; (ii) a series summation of the analytic derivatives; and (iii) convolution schemes. If we truncate the potential at the fourth order, then the EOM is identical to the QHD2 approach with a quartic potential, as we proposed for problems involving molecular vibrations. We have derived the quantal potentials of the Morse potential using the second and third schemes and have provided illustrations of them, and differences between quantal and effective quantal potentials were shown. The third scheme is convenient, because the differential operator is transformed into the convolution integral, and it is applicable to other potentials.

We defined density and joint density evaluated from the cumulant expansion scheme. The joint density obtained here fulfills (i) normalization condition, (ii) marginal condition, and (iii) positive definiteness. The last condition enables one to evaluate the Shannon's entropy, where the Wigner distribution cannot.

The exactly soluble modes such as (a) free particle and (b) harmonic oscillator were shown. The variational energy minima agree well with those obtained by the quantum mechanics. In particular, the energy minimum of the harmonic oscillator is exactly the same as the zero-point energy, $E_0 = \hbar\omega/2$. In both cases, the EOMs of the classical variables decouple with those of the cumulant variables, and the solutions of the classical variables are the same as those obtained by the classical mechanics.

We extended the QCD for the one-dimensional system to treat the multi-dimensional systems. We derived the EOMs with the $15N$ dimensional phase space. The energy conservation law and the other conservation law with respect to the cumulant variables were shown. We also proved the total momentum and total angular momentum conservation laws within the second-order QCD.

As numerical examples, we performed four applications to simple systems. The first is one-dimensional Morse oscillator to test truncation scheme, since the quantal potential of the Morse potential can be evaluated exactly. The first and second schemes were implemented and we carried out QCD simulations on the one-particle Morse potential. We have shown numerically the difference between the truncation, which is equivalent to QHD2, and the analytic schemes in terms of the phase space structure and the trajectories, although both methods preserved the total energy during 10,000-step calculations. The present scheme conserves the energy and is more robust than the truncation scheme that was initially presented by Prezhdo et al. Moreover, we constructed reliable time-reversible integrator for QCD. The order in the partitioned time evolution operator is quite important for the energy-conserving dynamics.

The second is the application to molecular vibrations. At first we showed that the normal mode analysis is extended to the effective potential appeared in the QCD. We illustrated that the anharmonic contribution is taken into account through mixing between the ordinary and the extended coordinates. The QCD simulations for the ab initio-derived quartic force field (QFF) are performed. The vibrational frequencies obtained from its power spectrum are in good agreement with those obtained by accurate methods such as the second-order vibrational perturbation theory (VPT2).

The third is the magnetic field-induced tunneling in the quantum dot nanostructure. We have numerically shown (1) a transition of the potential confinement into the Landau level confinement, (2) magnetic field-induced tunneling in the model ring system, and (3) magnetic field-induced confinement in a well that is closely related to the first phenomenon in more complicated potential.

The last application is the proton-transfer reactions in model DNA base pairs. We have numerically shown the geometric isotope effects on the stability of the proton-transferred structures of the DNA base pairs as a function of the mass. We have performed QCD simulations in order to investigate dynamical stability of the proton-transferred GC pair. The results showed that the proton-transferred structure of the protonated isotopomer is dynamically unstable and that of deuterated isotopomer remains stable. In former case, dynamically induced transition from the metastable to global minimum occurs. It is relevant to include dynamical effects to treat quantum isotope effects on the proton-transfer reactions.

Acknowledgments The authors thank Prof. Villani for providing parameter sets of potential energy surfaces for GC pair. This research was supported by the Core Research for Evolutional Science and Technology (CREST) Program “High Performance Computing for Multi-scale and Multi-physics Phenomena” of the Japan Science and Technology Agency (JST) and by a Grant-in-Aid for the scientific research on priority area “Molecular Theory for Real Systems”

(No. 20038008), and Grant-in-Aid for Young Scientists (B) (No. 20750004). HM and TM acknowledge the Research Fellowships for Young Scientists from the Japan Society for the Promotion of Science (JSPS).

References

1. L.I. Schiff, *Quantum Mechanics* (McGraw-Hill, New York, USA, 1949)
2. G. Gamov, Nature **122**, 805 (1928)
3. R.P. Feynman, A.R. Hibbs, *Quantum Mechanics and Path Integrals* (McGraw-Hill, New York, USA, 1965)
4. G.A. Voth, Adv. Chem. Phys. **93** 135 (1996)
5. J.C. Tully, Annu. Rev. Phys. Chem. **51**, 153 (2000)
6. W.H. Miller, J. Phys. Chem. A **105**, 2942 (2001)
7. G.A. Fiete, E.J. Heller, Rev. Mod. Phys. **75**, 933 (2003)
8. J.L. Gao, D.G. Truhlar, Annu. Rev. Phys. Chem. **53**, 467 (2002)
9. O.V. Prezhdo, Y.V. Pereverzev, J. Chem. Phys. **113**, 6557 (2000)
10. O.V. Prezhdo, Theor. Chem. Acc. **116**, 206 (2006) and references cited therein
11. H. Miyachi, Y. Shigeta, K. Hirao, Chem. Phys. Lett. **432**, 585 (2006)
12. Y. Shigeta, H. Miyachi, K. Hirao, J. Chem. Phys. **125**, 244102 (2006)
13. Y. Shigeta, H. Miyachi, K. Hirao, Chem. Phys. Lett. **443**, 414 (2007)
14. Y. Shigeta, AIP Proceedings **963**, 1317 (2007)
15. Y. Shigeta, Chem. Phys. Lett. **461**, 310 (2008)
16. Y. Shigeta, J. Chem. Phys. **128**, 161103 (2008)
17. Y. Shigeta, H. Miyachi, T. Matsui, K. Hirao, Bull. Chem. Soc. Jpn. **81**, 1230 (2008)
18. Y.V. Pereverzev, A. Pereverzev, Y. Shigeta, O.V. Prezhdo, J. Chem. Phys. **129**, 164103 (2008)
19. J.E. Mayer, J. Chem. Phys. **5**, 67 (1937)
20. R. Kubo, J. Phys. Soc. Jpn. **17**, 1100 (1962)
21. F. Colmenero, C.P. del Valle, C. Valdemoro, Phys. Rev. A **47**, 971 (1993)
22. F. Colmenero, C.P. del Valle, C. Valdemoro, Phys. Rev. A **47**, 979 (1993)
23. H. Nakatsuji, K. Yasuda, Phys. Rev. Lett. **76**, 1039 (1996)
24. D.A. Mazziotti, Chem. Phys. Lett. **289**, 419 (1998)
25. T. Yanai, G.K.L. Chan, J. Chem. Phys. **124**, 194106 (2006)
26. S.H. Mandal, G. Sanyal, D.A. Mukherjee, Lect. Notes. Phys. **510**, 93 (1998)
27. E. Wigner, Phys. Rev. **40**, 749 (1932)
28. M. Hillery, R.F. O'Connell, M.O. Scully, E.P. Wigner, Phys. Rep. **106**, 121 (1984)
29. K. Takahashi, Prog. Theor. Phys. Suppl. **98**, 109 (1989)
30. H.W. Lee, Phys. Rep. **259**, 147 (1995)
31. K. Husimi, Proc. Phys. Math. Soc. Jpn. **22**, 264 (1940)
32. H. Yoshida, Phys. Lett. A **150**, 262 (1990)
33. H. Yoshida, Celest. Mech. A **56**, 27 (1993)
34. M. Suzuki, Phys. Lett. A **146**, 319 (1990)
35. K. Yagi, K. Hirao, T. Taketsugu, M.W. Schmidt, M.S. Gordon, J. Chem. Phys. **121**, 1383 (2004)
36. C. Möller, M.S. Plesset, Phys. Rev. **46**, 618 (1934)
37. R.A. Lendall, T.H. Dunning Jr., R.J. Harrison, J. Chem. Phys. **96**, 6796 (1992)
38. M.W. Schmidt et al., J. Comput. Chem. **14**, 1347 (1993)
39. M.J. Frisch et al., Gaussian 03 (Revision C.02). (Gaussian Inc., Wallingford, CT, USA, 2004)
40. V.R. Khalilov, *Electrons in Strong Electromagnetic Fields, Advanced Classical and Quantum Treatment* (Gordon and Breach, Amsterdam, 1998)
41. M. Tewordt, R.J.F. Hughes, L. Martin-Moreno et al., Phys. Rev. B**49**, 8071 (1994)
42. N. Kim, G. Ihm, H.S. Sim, T.W. Kang, Phys. Rev. B **63**, 235317 (2001)

43. J.A.K. Freire, N. Studart, F.M. Peeters, G.A. Farias, V.N. Freire, Physica E **12**, 946 (2002)
44. A. De Martino, L. Dell'Anna, R. Egger, Phys. Rev. Lett. **98**, 066802 (2007)
45. T. Ihn, A. Fuhrer, L. Meier, M. Sigrist, K. Ensslin, Europhys. News **2005**, 78 (2005)
46. J. Florián, V. Hrouda, P. Hobza, J. Am. Chem. Soc. **116**, 1457 (1994)
47. J. Florián, J. Leszczyski, J. Am. Chem. Soc. **118**, 3010 (1996)
48. G. Villani, Chem. Phys. **316**, 1 (2005)
49. G. Villani, Chem. Phys. **324**, 438 (2006)
50. T. Matsui,Y. Shigeta, K. Hirao, Chem. Phys. Lett. **423**, 331 (2006)
51. T. Matsui, Y. Shigeta, K. Hirao, J. Chem. Phys. B **111**, 1176 (2007)

Nonclassical Phase Space Jumps and Optimal Spawning

Sandy Yang and Todd J. Martinez

Abstract Significant attempts have been made toward the intuitive understanding of nonclassical Franck–Condon factors that govern many important molecular processes from radiationless transitions to electronic spectroscopy. In the classical picture, i.e., Condon approximation, nuclear motion is assumed frozen throughout the duration of electronic transitions. However, as is demonstrated in this chapter, position and momentum jumps can compete in determining the Franck–Condon factor such that the conventional propensity rule can be misleading. We present a new method in this chapter where both position and momenta are simultaneously altered to achieve an improved description of nonadiabatic events. This optimal spawning procedure reduces to simpler approaches such as the strict momentum jump in appropriate limits, but is sufficiently flexible to describe cases where both position and momentum adjustments are important.

Keywords: Full multiple spawning · Franck-Condon · Optimal spawning · Nonadiabatic coupling

1 Introduction

Franck–Condon factors provide propensity rules that govern molecular processes from electronic spectroscopy to radiationless transitions. When two electronic potential energy surfaces (PES) cross in a classically allowed region, nonadiabatic transitions may be thought of as vertical, i.e., the electronic state change occurs while the nuclear framework is effectively frozen. However, violation of this common intuition is probable for population transfer that occurs in nonclassical regions, such

T.J. Martinez (✉)
Stanford University, Stanford, CA and SLAC National Accelerator Laboratory, Menlo Park, CA, e-mail: Todd.Martinez@stanford.edu

S. Yang (✉)
Stanford University, Stanford, CA and SLAC National Accelerator Laboratory, Menlo Park, CA, e-mail: yang1976@stanford.edu

P. Piecuch et al. (eds.), *Advances in the Theory of Atomic and Molecular Systems*, Progress in Theoretical Chemistry and Physics 20, DOI 10.1007/978-90-481-2985-0_2,

as when the lowest lying conical intersection lies above the Franck–Condon point. In the analogous spectroscopic context, this case would correspond to the wings of absorption bands, where simultaneous adjustment of position and momentum, i.e., a "phase space jump," may be required. Heller and coworkers [1] have discussed how one may relate such a phase space jumping picture to the Franck–Condon factors which govern absorption spectroscopy. Small but nonvanishing Franck–Condon factors in the nonclassical wings result from an incomplete oscillatory cancellation or overlapping region of the tails of the vibrational wavefunctions on the two electronic states. If the tail region contributes to the Franck–Condon overlap between donor and acceptor states, a position jump is required. On the other hand, if the donor wavefunction is narrow, there would be no contribution to the Franck–Condon factors from the tail of the donor wavefunction. Nonvanishing Franck–Condon factors then arise from incomplete *oscillatory* cancellation of the acceptor wavefunction. This leads to a momentum jump in the donor state. Heller pointed out that, in principle, position jumps and momentum jumps can compete to contribute to the Franck–Condon overlap integral in the nonclassical region. Such discussion remains valid for radiationless transitions which are critical to the study of many important photochemical processes [2–9].

The surface hopping algorithm introduced by Tully and Preston [10–12] has been a widely used approach to approximate population transfer between different Born–Oppenheimer states. The simple and intuitive surface hopping technique has its deep roots in and goes beyond the primitive Landau–Zener theory [13, 14] that gives an analytic solution to the equations of motion governing the transition dynamics of a two-level quantum mechanical system. As contained in the Landau–Zener–Stuckelberg model, surface hopping between different electronic PESs is localized in the region with large coupling between the surfaces and can be considered as a pure momentum jump. However, just as in the spectroscopic case, hybrid phase space jumps may also be important. In this chapter, we focus on the discussion of nonclassical Franck–Condon transitions, in relation to the newly developed optimal spawning technique used to describe nonadiabatic transitions in ab initio molecular dynamics.

2 Surface Hopping, Jumping, and Spawning

To describe nonadiabatic transitions effectively and accurately, the ab initio multiple spawning (AIMS) method has been developed in which both the electrons and the nuclei are treated quantum mechanically and on a consistent basis. Significant effort has been put into designing AIMS to alleviate the conflict between the locality of quantum chemistry and the global character of the nuclear Schrödinger equation, which has been a challenge to including quantum mechanical effects of the nuclei in ab initio molecular dynamics (AIMD) methods. The full multiple spawning (FMS) method, which is the dynamical core of AIMS, introduces locality in the nuclear dynamics by employing an adaptive, time-dependent basis set of frozen Gaussians [7]. Unlike the original frozen Gaussian approximation (FGA), FMS accounts fully for the nonorthogonal nature of the Gaussian basis.

In terms of electronic wavefunctions $\phi_I(\mathbf{r};\mathbf{R})$ and nuclear wavefunctions $\chi_I(\mathbf{R};t)$, the multiconfigurational total wavefunction used in AIMS can be written in the form $\psi = \sum_I \chi_I(\mathbf{R};t)\phi_I(\mathbf{r};\mathbf{R})$, where the subscript I indexes the electronic state, and vectors $\mathbf{r}$ and $\mathbf{R}$ denote the electronic and nuclear coordinates, respectively. The nuclear wavefunction on each electronic state I is given by

$$\chi_I(\mathbf{R};t) = \sum_{m=1}^{N_I(t)} c_m^I(t)\,\chi_m^I\left(\mathbf{R};\overline{\mathbf{R}}_m,\overline{\mathbf{P}}_m\right), \tag{1}$$

where χ_m^I denotes the standard multidimensional frozen Gaussian with time-independent fixed width and $N_I(t)$ is the time-dependent number of nuclear basis functions on electronic state I at time t. $\bar{\mathbf{R}}_m$ and $\bar{\mathbf{P}}_m$ refer to the centers of frozen Gaussians χ_m^I. Classical Newtonian equations of motion are used to propagate the position and momentum centers of each Gaussian basis function on each individual PES. Hence, these basis functions are often referred to as "trajectory basis functions" or TBFs. Furthermore, the entire set of TBFs in a simulation is referred to as a "bundle." A time-dependent complex amplitude c_m^I associated with each individual nuclear basis χ_m^I is calculated at each time step by solving the nuclear Schrödinger equation within the finite basis set:

$$\frac{d\mathbf{C}^I}{dt} = -i\left(\mathbf{S}^{II}\right)^{-1}\left\{\left(\mathbf{H}^{II} - i\,\dot{\vec{S}}^{II}\right)\mathbf{C}^I + \sum_{J\neq I}\mathbf{H}^{IJ}\mathbf{C}^J\right\}. \tag{2}$$

In Eq. (2), $\mathbf{S}$ is the overlap matrix defined by $\mathbf{S}_{kl}^{IJ} \equiv \left\langle \chi_k^I(\mathbf{R})\,\phi_I(\mathbf{r};\mathbf{R}) \,|\, \chi_l^J(\mathbf{R})\,\phi_J(\mathbf{r};\mathbf{R})\right\rangle$, $\mathbf{H}^{\mathrm{IJ}}$ is the Hamiltonian projected onto electronic PES I and J, and $\dot{\vec{S}}^{II}$ is the time derivative of overlap matrix. Further details can be found in the literature [15].

The spawning procedure is the key to the accuracy and efficiency of FMS. Trajectory basis functions (TBFs) are allowed to spawn new TBFs on another electronic state only when they enter a region of nonadiabatic coupling (defined by a numerical "spawning threshold" chosen before the simulation). The nonadiabatic coupling vector $\mathbf{d}^{IJ}$ is used to help determine when spawning might be needed and along which direction the momentum vector should be adjusted for new TBFs:

$$\mathbf{d}^{IJ} \equiv \left\langle \phi_I(\mathbf{r};\mathbf{R}) \left| \frac{\partial}{\partial \mathbf{R}} \right| \phi_J(\mathbf{r};\mathbf{R}) \right\rangle_{\mathbf{r}}. \tag{3}$$

Once a TBF (denoted as the *parent*) enters a spawning region, it is *forward propagated* (in time) until the effective nonadiabatic coupling falls below the spawning threshold. The newly spawned basis function (referred to as the *child*) is created on the other coupled electronic PES at time t_f and is then *backward propagated* together with the parent until the initial time t_i when the parent entered the coupling region. These forward- and backward-propagation steps involve only the parent and child TBFs, since there is no need to solve Eq. (2) during these steps. After forward and

backward propagation, the child TBF has been spawned and it is treated the same as all other TBFs in the simulation, i.e., subsequent propagation involves coupling with all other TBFs.

The connection with classical mechanics suggests that one places the child trajectory on the classical energy shell of its parent. This might appear to conflict with the first-order perturbation theory which predicts the spawned "child" basis function to be proportional to the product of the parent basis function and the nonadiabatic coupling. In general, the child basis function predicted by first-order perturbation theory will not be a Gaussian and the best Gaussian approximation need not have the same classical energy as the parent. However, conservation of classical energy in the long-time limit is clearly desirable [16], as is also evidenced by the state-to-state form of Fermi's golden rule, which only allows energy-conserving nonadiabatic transitions. Thus, we demand that the classical energies of the parent and child basis functions are identical. This constraint is applied together with maximization of the off-diagonal Hamiltonian matrix element indicating the importance of the new basis function:

$$\frac{\partial}{\partial \bar{\mathbf{P}}^J_{m\rho}} \left|\langle \chi^I_m \left| H^{IJ} \right| \chi^J_n \rangle\right| = 0 \quad , \quad \frac{\partial}{\partial \bar{\mathbf{R}}^J_{m\rho}} \left|\langle \chi^I_m \left| H^{IJ} \right| \chi^J_n \rangle\right| = 0. \tag{4}$$

The subscript ρ in $\bar{\mathbf{P}}^J_{m\rho}$ and $\bar{\mathbf{R}}^J_{m\rho}$ refers to the component along ρth degree of freedom of the multidimensional vectors $\bar{\mathbf{P}}^J_m$ and $\bar{\mathbf{R}}^J_m$. In general, the resulting set of equations does not have a unique solution. Various spawning techniques are thus possible to adaptively increase the size of the basis in order to capture nonadiabatic effects.

It is instructive to study the simplest case first. The optimization condition of Eq. (4) is approximately proportional to maximizing the overlap integral $|\langle \chi^I_m(\mathbf{R}; \overline{\mathbf{R}}^I_m, \overline{\mathbf{P}}^I_m, \gamma^I_m) | \chi^J_n(\mathbf{R}; \overline{\mathbf{R}}^J_n, \overline{\mathbf{P}}^J_n, \gamma^J_n) \rangle_{\mathbf{R}}|$. Two approximate solutions can be proposed as *position-preserving* and *momentum-preserving* spawns. In the two limits, either position or momentum is fixed while the conjugate variable is adjusted to equalize classical energy between parent and child trajectories. Here we consider the position-preserving type of spawn paired with a pure momentum jump.

For a one-dimensional system, momentum jumps are clearly defined and position-preserving spawns lead to the same adjustment used in surface hopping [11, 12]. This procedure has been justified semiclassically by Herman [17]. In practice, the momentum of a new trajectory is calculated as

$$\mathbf{P}^I_{\text{new}} = \mathbf{P}^J_{\text{old}} - D\hat{\mathbf{d}}^{IJ}, \tag{5}$$

where $\mathbf{P}^I_{\text{new}}$ is the momentum vector of Gaussian centers of the newly spawned child trajectory, $\mathbf{P}^J_{\text{old}}$ is that of the parent, and $\hat{\mathbf{d}}^{IJ}$ is a unit vector directed along the nonadiabatic coupling vector (3). D is a scalar value chosen such that the total classical energy of the parent is identical to that of the child.

Sometimes it could happen that the potential energy surface to which a spawn should occur is classically inaccessible, i.e., no real value of D in Eq. (5) achieves

energy conservation. In surface hopping, such failures are known as frustrated hops. Many have tried to tease out the full implications of frustrated hops [18–23]. Recently, frustrated hops were identified as essential to proper equilibrium [18, 19]. In FMS, however, the details of the treatment of the analogous frustrated spawns is not expected to be as critical. The spawning procedure is important in that it allows nonadiabatic transitions in the first place, but spawning itself does not dictate the statistical balance of population among the various electronic surfaces. Population transfer is achieved through the solution of the Schrodinger equation in the expanded basis set and if a spawned basis function is not needed, the equations of motion will not populate it. It is also worth noting that, even using the simplest pure momentum jump, FMS differs from standard surface hopping in its backward propagation of parent–child pairs. In FMS, a to-be-spawned trajectory at time t_f is not discarded immediately upon the case of frustrated spawning. Instead, a backward propagation is then performed by negating the time step in integrating the nuclear equations of motion. The backward propagation is integrated back to time t_i at the beginning of nonadiabatic coupling region where another momentum adjustment is performed. Since nonadiabatic coupling vector differs at time t_i from t_f, occasionally momentum adjustment at t_i might be sufficient and therefore a frustrated spawning at time t_f would be allowed at t_i. Such a delay in checking energy conservation between parent and child TBFs takes into account the global effect of PES on the temporal nuclear dynamics, and thus introduces a small probability of the system "tunneling" through the potential barrier.

To improve upon the position-preserving technique, one can introduce additional quenching to the energy shell in phase space along the nonadiabatic coupling vector. Alternatively, one can choose the descent direction along the negative of the gradient (steepest descent). For one-dimensional problems, the two approaches are identical. In general, however, their relative accuracies might vary with time and system, and the better choice is unclear. If the nonadiabatic coupling vector $\hat{\mathbf{d}}^{IJ}$ is chosen, then the momentum jump is followed by a position shift that minimizes the function

$$\left| E\left(\mathbf{R}^I_{\text{old}} + \gamma \cdot \hat{\mathbf{d}}^{IJ}\right) - E\left(\mathbf{R}^I_{\text{old}}\right) \right|, \tag{6}$$

where $\mathbf{R}_{\text{old}}$ refers to the position vector of the parent trajectory, and γ is computed to minimize (6). The combination of momentum jump and steepest descent generally leads to spawned trajectories that may not preserve position or momentum of the parent TBFs. This introduces a bias against fully populating newly spawned TBFs in cases where the steepest descent is required, because the maximum overlap between parent and child may be poor. This diminished population transfer might be important in ensuring detailed balance, and we will explore this issue in a future paper.

The key to spawning optimally lies in pinpointing the ideal blend of position and momentum displacements of child TBFs. Heller and coworkers [1, 24] noted the importance of hybrid jumps, but this has not been exploited in any general numerical method as far as we are aware. In FMS, however, the proper mix can be realized by minimizing the function

$$\lambda \left| E\left(\chi^I_{\text{parent}}\right) - E\left(\chi^J_{\text{child}}\right)\right|^2 - \left|\left\langle \chi^I_{\text{parent}} \left| V^{IJ}(\mathbf{R}) \right| \chi^J_{\text{child}} \right\rangle_{\mathbf{R}}\right|. \tag{7}$$

Minimizing Eq. (7) is equivalent to jointly minimizing the energy difference and maximizing the coupling between parent and child basis functions. For a fixed value of the parameter λ (which should properly be viewed as a Lagrange multiplier to be optimized), minimization pushes the energy gap toward zero while maximizing the coupling as a function of $\mathbf{R}^J_{\text{child}}$ and $\mathbf{P}^J_{\text{child}}$. Sequentially increasing λ steadily raises the penalty for energy non-conservation while tracking changes in the coupling maximum as smoothly as possible. Each minimization cycle is performed with standard conjugate gradient techniques. Spawning optimally not only improves numerical efficiency by requiring fewer basis functions for branching ratio convergence, but also provides insight into the physical character of nonadiabatic transitions.

3 Results and Discussion

In the simulations in this chapter, the initial (target) wavefunction is chosen to be a single multidimensional Gaussian. Propagation is performed on diabatic PESs. To maximize overlap between the initial FMS wavepacket and the desired initial wavefunction, the complex amplitude of each trajectory basis function in the bundle is initialized by projection:

$$c^I_k(0) = \sum_{n=1}^{N_I(0)} \left(S^{-1}\right)^{II}_{mn} \left\langle \chi^I_n(t=0) \,\middle|\, \Psi^{\text{target}}_{t=0} \right\rangle. \tag{8}$$

The phase space centers of the initial TBFs are sampled from the Wigner distribution of the target initial wavefunction. We further constrain the initial basis functions such that the classical energy of each basis function is within 10% of the quantum mechanical energy of the target initial wavefunction.

We examine the performance of the various spawning procedures with a two-dimensional, two-state conical intersection model [25] introduced by Persico and coworkers. This model has been used to describe collinear reaction of triatomic *ABA* and provides a useful testing bed for study and comparison of nonadiabatic simulation schemes. We have previously provided details of the simulation [26] and showed good agreement between results obtained with FMS dynamics and the numerically exact fast Fourier transform (FFT) method [27, 28].

In this chapter, we develop and discuss the detailed relationship between optimal spawning and surface hopping/jumping. Convergence of branching ratio using various spawning algorithms has been tested and published in a recent paper [26]. We focus here on the detailed comparison of phase space jumps and quenching of energy shells using standard and optimal spawning algorithms. Results are compared using three different spawning methods. Strict p-jump refers to spawning with pure momentum adjustment along the nonadiabatic coupling vector, similar to the

surface hopping algorithm. Standard spawning is of the form most often implemented in previous FMS and AIMS simulations, where a steepest descent quench to the energy shell obviates frustrated spawns. The third method is optimal spawning, as developed recently and outlined above. In all of the simulations, each TBF is allowed to spawn in the nonadiabatic coupling region. The phase space location of the Gaussian center of each parent TBF is labeled by $\overline{\mathbf{R}}^I_{\text{parent}}, \overline{\mathbf{P}}^I_{\text{parent}}$ and that of the child TBF by $\overline{\mathbf{R}}^J_{\text{child}}, \overline{\mathbf{P}}^J_{\text{child}}$. The difference between the various spawning methods lies in the assignment of initial conditions of child basis functions. Ultimately, the efficiency and robustness of assigning phase space locations to newly spawned basis functions should be reflected in the accuracy of the population transfer between the different electronic states (as compared to numerically exact quantum mechanical simulations).

We plot the phase space location of each pair of parent and child trajectories in Fig. 1. The Gaussian centers of parent trajectories at different spawning times are marked with solid circles, while those of spawned child trajectories are marked with red (using pure momentum jump) and green (using optimal spawning) crosses, respectively. Since the total phase space dimensionality is four for the Persico model, phase space locations of all the Gaussian centers are shown in two subfigures, one showing (X,P_x) and the other showing (Y,P_y). The pure momentum-jump method does not allow any jump in coordinate space, such that the spawned child trajectories are not located in the optimal phase space points (which are only possible using optimal spawning method as shown in the figure) to maximize the coupling between the parent and child basis functions. Note that the difference between the two spawning techniques is most significant in (Y,P_y) subspace. The optimal child trajectories should be placed in the region with larger values of Y, since the coupling potential matrix element (between diabatic states) in the Persico model increases with Y, i.e., $V_{12}(X, Y) = \gamma Y e^{-\alpha(X-X_3)^2-\beta Y^2}$. Therefore, the optimal spawning positions can only be achieved by appropriate hybrid surface jump in both coordinate and momentum.

In Fig. 2, we show the coordinates of parent and child trajectories relative to the contour plots of coupling potential V^{pc}, the coupling between parent and child trajectories. The blue contour fills in the figure mark the magnitude of V^{pc}: the deeper the blue, the larger the coupling. The phase space location of the parent trajectory centroid is marked by a red square. The tuning parameter λ in Eq. (7) is increased sequentially to drive the optimization of the child centroid, and a typical optimization path is indicated with the red curve. The region of coordinate space where no choice of the momentum can lead to energy conservation is shaded gray. Any spawn from the parent to a point in this gray area would be frustrated. Optimal spawning places the child trajectory at a phase space point (marked with red circle) with larger V^{pc} than that using conventional spawning techniques (indicated with blue circle). By allowing both momentum and position to vary simultaneously, optimal spawning finds the optimal place for the child trajectory where energy is conserved and parent–child coupling is maximal. In certain cases, a large hybrid phase space jump is needed for the spawned child to have same energy as its parent.

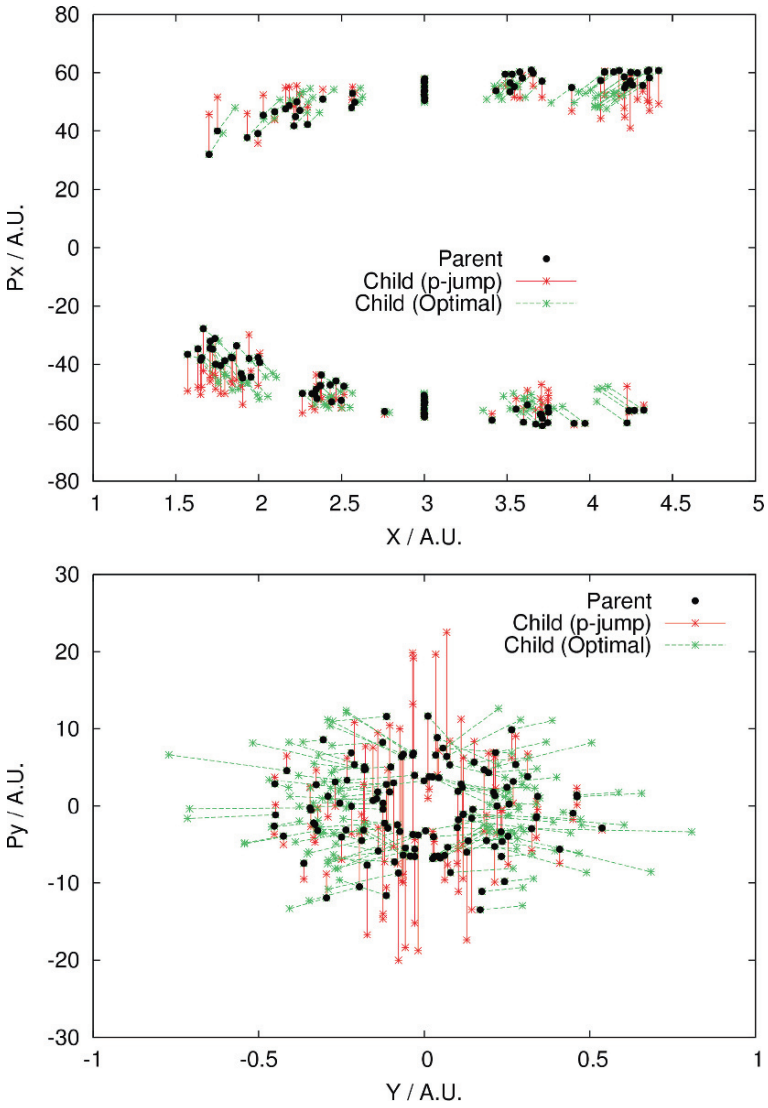

Fig. 1 Gaussian centers of trajectories in (X, P_x) and (Y, P_y) coordinate space. Parent trajectories are marked with *solid circles*, and child trajectories are marked with *red* (pure p-jump) and *green* (optimal spawning) *crosses*

As shown in Fig. 3, such a large hybrid jump is not probable using standard spawning (and of course not possible with pure momentum-jump spawning either). With sequential increase of λ in the penalty function (7), optimal spawning successfully generates a new child basis function with both energy conserved and parent–child coupling maximized.

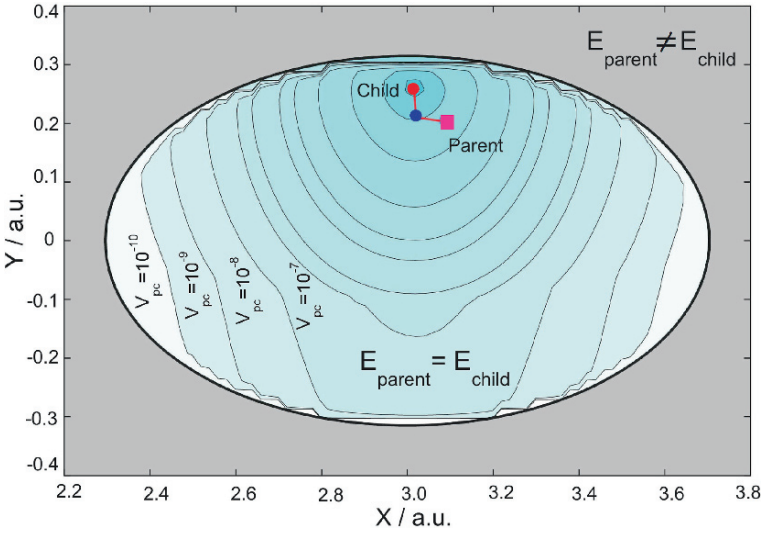

Fig. 2 Gaussian center of parent trajectory is marked with *red square*, and those of child basis generated with standard and optimal spawning methods are marked with *blue* and *red circles*, respectively. Optimal spawning places child in the phase space location with larger coupling V^{pc} between parent and child than that with standard spawning

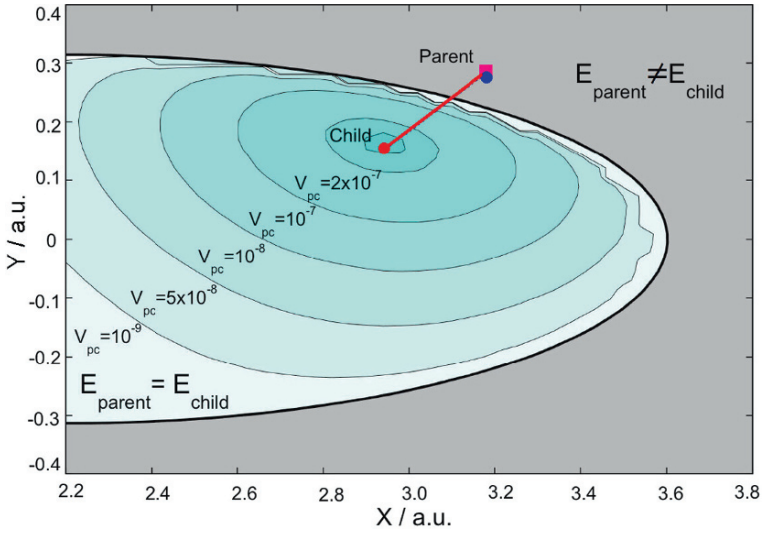

Fig. 3 Standard spawning generate child (marked by *blue circle*) in the energetically forbidden area, which corresponds to frustrated spawning. Optimal spawning is able to place the child (*red circle*) in the area with energy conserved and as well as with coupling V^{pc} maximized

4 Conclusions

In the classical understanding of Franck–Condon factors, nuclear motion is assumed frozen in the duration of electronic transitions as is dictated by the Born–Oppenheimer approximation. However, position jump and momentum jump can compete with each other in adjusting the Franck–Condon factor, especially in the nonclassical regime.

AIMS is an ab initio method developed to efficiently and accurately describe the nonadiabatic radiationless transitions for multidimensional systems. The spawning procedure is the key to the whole method in dealing with nuclear dynamics and allows new basis trajectories to be created on the other coupled PES when the nonadiabatic coupling term is large enough. The optimal spawning method introduced here provides an improved procedure for assigning phase space initial conditions to spawned trajectory basis functions that search for the most important basis function that should be added to the simulation, subject only to the constraint of energy conservation. Optimal spawning improves upon previous implementations in its more flexible addition of new basis functions and this can be expected to lead to faster convergence of the description of nonadiabatic events.

References

1. E.J. Heller, D. Beck, Chem. Phys. Lett. **202**, 350 (1993)
2. T.J. Martínez, Acc. Chem. Res. **39**, 119 (2006)
3. D.R. Yarkony, J. Chem. Phys. **114,** 2601 (2001)
4. M. Ben-Nun, F. Molnar, K. Schulten, T.J. Martínez, Proc. Natl. Acad. Sci. **99**, 1769 (2002)
5. D.R. Yarkony, Acc. Chem. Res. **31**, 511 (1998)
6. M.A. Robb, F. Bernardi, M. Olivucci, Pure Appl. Chem. **67**, 783 (1995)
7. B.G. Levine, T.J. Martínez, Annu. Rev. Phys. Chem. **58**, 613 (2007)
8. J. Michl, Top. Curr. Chem. **46**, 1 (1974)
9. L. Salem, J. Am. Chem. Soc. **97**, 479 (1975)
10. J.C. Tully, R.K. Preston, J. Chem. Phys. **55**, 562 (1971)
11. R.K. Preston, J.C. Tully, J. Chem. Phys. **54**, 4297 (1971)
12. J.C. Tully, J. Chem. Phys. **93**, 1061 (1990)
13. C. Wittig, J. Phys. Chem. B **109**, 8428 (2005)
14. E.E. Nikitin, *Theory of Elementary Atomic and Molecular Processes in Gases* (Clarendon, Oxford, 1974)
15. M. Ben-Nun, T.J. Martínez, Adv. Chem. Phys. **121**, 439 (2002)
16. G.C. Schatz, M.A. Ratner, *Quantum Mechanics in Chemistry* (Prentice Hall, Englewood Cliffs, 1993)
17. M.F. Herman, J. Chem. Phys. **81**, 754 (1984)
18. P.V. Parandekar, J.C. Tully, J. Chem. Theory Comput. **2,** 229 (2006)
19. P.V. Parandekar, J.C. Tully, J. Chem. Phys. **122**, 094102 (2005)
20. A.W. Jasper, D.G. Truhlar, Chem. Phys. Lett. **369**, 60 (2003)
21. A.W. Jasper, S.N. Stechmann, D.G. Truhlar, J. Chem. Phys. **116**, 5424 (2002)
22. J. Fang, S. Hammes-Schiffer, J. Phys. Chem. A **103**, 9399 (1999)
23. U. Muller, G. Stock, J. Chem. Phys. **107**, 6230 (1997)

24. E.J. Heller, B. Segev, A.V. Sergeev, J. Phys. Chem. B **106**, 8471 (2002)
25. A. Ferretti, G. Granucci, M. Persico, G. Villani, J. Chem. Phys. **104**, 5517 (1996)
26. An "optimal" spawning algorithm for adaptive basis set expansion in nonadiabatic dynamics, S. Yang, J.D. Coe, B. Kaduk, T.J. Martínez, J. Chem. Phys. **130**, 134113 (2009)
27. D. Kosloff, R. Kosloff, J. Comput. Phys. **52**, 35 (1983)
28. R. Kosloff, Annu. Rev. Phys. Chem. **45**, 145 (1994)

On the Differential Cross Sections in Complex-Forming Atom–Diatom Reactive Collisions

Pedro Bargueño and Tomás González-Lezana

Abstract The shape of the differential cross section has been studied for years as a helpful indicator for the dynamics of atom–diatom reactive collisions. In particular, a symmetrical profile of the angular distribution about the sideways scattering direction ($\theta \approx 90^\circ$) with prominent peaks for the forward ($\theta \approx 0^\circ$) and backward peaks ($\theta \approx 180^\circ$) is commonly associated with reactions which proceed via the formation of an intermediate complex. In this work we make an overview of the theoretical foundations on this assumption, originally proposed within the framework of nuclear physics and subsequently adopted in the study of molecular reactions. Examples of recent investigations on different atom–diatom processes are shown.

Keywords: Reactive collisions · Statistical models · Atom-diatom reactions · Differential cross sections · Insertion reactions

1 Introduction

One of the goals in the study of molecular collisions is to determine the precise reaction mechanism which leads from reactants to products. Recent developments in the most commonly employed experimental techniques have enabled to obtain a precious information about a large number of bimolecular processes. In addition to the step-by-step picture of the entire chemical transformation gained with the advances at the femtosecond level [1], the refinements introduced in the field of the crossed molecular beam (CMB) reactive scattering (see Ref. [2] and references therein for a complete review on the subject) have made possible to measure

T. González-Lezana (✉)
Instituto de Física Fundamental, Consejo Superior de Investigaciones Científicas, Serrano 123, 28006 Madrid, Spain, e-mail: tglezana@imaff.cfmac.csic.es

P. Bargueño
Instituto de Física Fundamental, Consejo Superior de Investigaciones Científicas, Serrano 123, 28006 Madrid, Spain, and Departamento de Química Física, Universidad de Salamanca, 37008 Salamanca, Spain, e-mail: pbdr@imaff.cfmac.csic.es

P. Piecuch et al. (eds.), *Advances in the Theory of Atomic and Molecular Systems*, Progress in Theoretical Chemistry and Physics 20, DOI 10.1007/978-90-481-2985-0_3,

state-to-state differential cross sections (DCSs) for some simple reactions. Furthermore, from the theoretical side, reactive collisions have been studied by means of exact quantum mechanical (EQM) methods both in the time-independent and time-dependent frameworks. The DCS of an extensive list of atom–diatom reactions can be nowadays calculated with various well-established numerical techniques [3–6]. The relevance of all this progress is enormous, since the centre of mass (CM) angular distribution of the products formed in a reactive collision contains crucial information regarding the specific course followed by the reaction. Thus, for example, the DCSs expected from the two possible limiting cases of atom–diatom reactions (direct or abstraction reactions and complex-forming or insertion reactions) are in general completely different. Whereas the abstraction collisions yield angular distributions of variable shapes, which often reveal the favoured geometry in the reactive process, complex-forming mechanisms are characterised by symmetric DCSs about $\theta \approx 90^{\circ}$, the sideways scattering direction.

This apparent constant dynamical feature observed for the insertion reactions is also connected with the possible statistical nature of these type of processes. The reaction mechanism in these cases consists of a two-step sequence initiated with the formation of the intermediate species after the collision of the reacting atom and diatom. The products of the reaction are formed after the decay of such collision complex, and in principle, independently of the specific initial state of the reactants. Furthermore, the process is usually accompanied with the randomisation of the internal energy among the different degrees of freedom of the intermediate species. Under these conditions, the application of statistical approaches to investigate the overall dynamics of the reaction seems to be justified.

These considerations about the dynamics of molecular processes which proceed via the formation of an intermediate complex have their origin in the context of nuclear physics. In particular, the compound nucleus theory and the statistical approaches developed to explain some of the nuclear reactions occurring after the collision of a neutron with a target nucleus constitute a clear influence for the subsequent theoretical studies on molecular insertion processes. In this work we review the development of such theories decades ago and the efforts to search experimentally for this type of mechanism in nuclear reactions. Then we focus on how such techniques were adopted for molecular atom–diatom reactions. Our study also includes an inspection on some of the mathematical details of the expressions obtained in the past for the DCSs in molecular collisions. Finally, a series of examples in which the investigation of the angular distributions can be used to trace the dynamical mechanism responsible for the reaction are shown.

2 Nuclear Physics

The compound nucleus model [7, 8] was introduced as a possible response to some of the features observed in experimental studies on neutron–nucleus collisions. In such experiments the capture cross sections were of the same order of magnitude of

the cross sections for the full neutron–nucleus scattering. Analogously, the tendency for a neutron to get attached to a heavy nucleus to form another isotope was found to be surprisingly large. The analysis of the γ-ray spectra also reveals that the lifetime of the excited nucleus so formed is longer than expected. Therefore, the duration for the encounter between the neutron and the nucleus must be necessarily longer than the time employed by the neutron to pass through the nucleus. It seemed then plausible to suggest that certain collisions between neutrons and nuclei could lead to the formation of a compound system with some noticeable probability [7]. In fact, virtual states of such complex could be in resonance with states for the separate nucleus+neutron system. This feature would explain, on the other hand, the narrow closely spaced peaks in the experimental cross sections in the bombardment of various target nuclei [8, 9].

The compound nucleus model divides the nuclear reaction into two separate events, with the formation and subsequent disintegration of the intermediate nucleus as independent processes. Within the context of this model, it is assumed that the compound nucleus $A + a$ is formed in a highly excited state after the collision of an incident particle a on a heavy nucleus A. The excitation energy is $E = E_a + \varepsilon$, where ε is the energy of a and E_a is its binding energy to the compound system. This E_a is defined as the energy to supply to the lowest state of the so-formed excited nucleus $A + a$ to dissociate it into A and a [10, 11]. The possible energy excess of the colliding units is assumed to be redistributed among all the nuclear particles forming the compound nucleus. Therefore, after this randomisation of the energy content, the ejection of particles from the nucleus is expected to occur as a result of internal mechanisms with no connection with the first stage of the neutron–nucleus encounter [7]. In fact, the expulsion from a compound nucleus with a large density of levels was statistically treated invoking thermodynamical analogies with the evaporation of a particle from a body at low temperature [10, 11]. The statistical method developed by Weisskopf leads to a Maxwellian expression for the energy distribution of the scattered neutrons from highly excited heavy nuclei [10]. The predictions of such a statistical approach were tested with a series of experimental studies. Theoretical cross sections and estimations of the temperature of the residual nucleus abandoned by the emitted neutron were found to be in good agreement with the measured values in various nuclear processes [12–16]. The existing discrepancies [17], such as much higher nuclear temperatures than those estimated from experimental densities, were attributed to either a possible incomplete total redistribution of the collision energy [15, 18, 19] or to the existence of a larger level spacing of the low lying energy levels of the nucleus in comparison with the energy carried by the incident neutron [13]. The issue of the degree of sharing and exchange of the incident energy [20] establishes the difference between the compound model and some other theoretical approaches, such as, for example, the optical method [21]. In this latter model, the entire energy is focused on a single neutron, which can be in principle distinguished from the other nuclear particles. One then studies the elastic or inelastic (absorption) scattering of this neutron in passing through the nucleus. This process would constitute indeed the necessary first step in the formation of the compound nucleus. An early loss of the energy before its possible randomisation along the nuclear constituents however can prevent the proper scenario for a

statistical description [20]. The limits for the validity of either the compound nucleus or the optical model seem to be found in the energy introduced by the colliding neutron. Thus the nucleus appears as partially transparent to a high-energy bombarding particle ($E \sim 100$ MeV), with scattering mean free paths of the same order as the nucleus size itself [21, 22]. Hence the possibility of forming a compound nucleus after the impact of the incident neutron seems to be restricted to a low-energy regime.

The application of statistical schemes on the basis of the compound nucleus model constitutes a substantial simplification of the required theoretical framework for nuclear reactions. The treatment based on dispersion theory can be avoided, as shown by Weisskopf's formula [10, 11], in the region of overlapping levels since the cross section no longer depends in those situations on the individual energy levels. It is possible to express the reaction cross section for the overall process as the product of a term containing the cross section for the capture of the incident particle by the nucleus to form the compound nucleus and a width describing the decay of this nucleus by particle emission [23–25]. One of the most interesting consequences of this separation between formation and decay is that the interference terms between different values of the total angular momentum (J), orbital angular momentum of the neutron (l) and parity in both the ingoing and outgoing waves cancel out when averaging over many compound states. Thus, the expression of the angular distribution for the transition between the initial states a and α for the incident particle and the target nucleus, respectively, and the final states b and β via the formation and decay of the compound nucleus can be written, for zero spins, as [24]

$$\sigma(a\alpha, b\beta; \theta) \sim \sum_{l=0}^{\infty} \frac{(2l+1)^2}{F(l)} P_{al} P_{bl} \mid P_l^0(\theta) \mid^2, \tag{1}$$

where $P_l^0(\theta)$ are associated Legendre polynomials, P_{al} stands for the penetration factor or "sticking probability" for the incident neutron to form the compound nucleus with the target [23], P_{bl} for the corresponding fragmentation probabilities and $F(l)$ is a sum of formation and decay probabilities over all possible initial and final states. As a result of the above-mentioned considerations, the expression (1) for the DCS exhibits a characteristic symmetry about the outgoing $\theta \approx 90^\circ$ scattering direction [24, 25]. The ratio between the scattering through the forward ($\theta \approx 0^\circ$)–backward ($\theta \approx 180^\circ$) and sideways directions depends on the value of (i) the largest contributing l wave, $l_{\max}$ and (ii) the l wave giving the largest contribution to the cross section. Those $l_{\max}$ values will depend on the ability of the incident and outgoing particles to overcome the angular momentum barrier. In fact, in those cases in which the compound nucleus is formed at large values of the angular momentum and small values of its projection along the direction of the separating fragments, the DCS is predicted to follow a $1/\sin\theta$ curve, with extremely prominent peaks at the forward and backward directions [26–29]. Further connections between the anisotropy of the angular distribution and internal properties of the fissioning nucleus, as the effective moment of inertia, nuclear temperature and the projection of the total angular momentum on the nuclear symmetry axis, can be inferred.

This distinctive character was employed as a crucial test to elucidate whether or not a large series of experimentally investigated nuclear reactions proceed via the formation of an intermediate compound nucleus. The measured angular distributions were compared with the corresponding statistical predictions, and the exhibited forward–backward symmetry was interpreted as a result of the above-mentioned reaction mechanism [30–35]. Observed deviations from the expected result of a statistical treatment led to suggest the occurrence of a reaction mechanism involving a direct process with no formation of the compound nucleus [18, 19, 36–39]. In fact, as Weisskopf discussed in a detailed review of the early theoretical developments on nuclear physics [40], the two-stage description of the nuclear reactions inherent to the compound nucleus model requires some further refinements. The rapid and complete distribution of the energy carried by a nucleon which enters the nucleus from outside seemed to be questionable. As an alternative, the author suggested the possibility of describing the nuclear processes according to three successive stages: (i) the independent particle stage; (ii) the compound system stage and (iii) the final stage in which the reaction products separate from each other. In the first step the incident nucleon interacts with the target nucleus, which mainly represents a potential well for the incoming particle without losing its distinct individuality. As a result of such an interaction, the particle is refracted and partially reflected at the surface due to the change in the potential. The description at this stage regards what happens at the entrance channel, how the particle is partially absorbed, disappearing from the entrance channel and loosing its independence with respect to the target nucleus. The compound system stage describes the more intimate interaction between the particle and the nucleus which cannot be described any longer by means of the potential at the entrance channel. This step can be the result of a direct interaction with the collision of the particle with the target nucleus or of more collective motions as surface vibrations or nuclear rotations. The concept of the compound system would then differ from the compound nucleus in the sense that although some energy exchange between target and particle may take place, some other forms of interactions in which the particle is removed from the entrance channel are also allowed.

Many nuclear processes seem to correspond to the intermediate situation between the two extreme reaction mechanisms: (i) the direct collision between the incident particle with a single nucleon, leading to the ejection of one of the partners outside the nucleus without any further interaction and (ii) the already discussed formation of the compound nucleus with the division of the energy among a large number of the existing nucleons. Weisskopf concludes his study suggesting that despite this variety of possible nuclear processes the probability of formation of a compound nucleus for low incident energies (up to 25 MeV) is quite high. Alternatively, the possibility of finding situations for which the compound nucleus model may remain valid whereas the specific statistical assumptions are not satisfied was investigated in some detail [8, 31, 41, 42]. In this sense, it was pointed out that a strict verification of the statistical postulate would lead to essentially the same probabilities for all energetically possible reaction products in clear contradiction with some experimental findings [8]. Attempts to investigate if the deviation from symmetry could

be due to a violation of the statistical assumptions were made by measuring angular distributions at closely spaced bombarding energies [41]. Although the results did not allow to draw any definitive conclusions with this respect, authors of Ref. [41] suggested possible failures to fulfil the statistical requirements. On the other hand, it is interesting to remind that the symmetry properties of the DCS shown in Eq. (1) are not strictly a consequence of the compound nucleus assumption but a result of the existence of sufficiently large and dense energy levels for such intermediate species for a statistical treatment [31, 42].

3 Molecular Physics

Pioneering CMB performed in the early 1960s constituted an estimable tool to probe the dynamics of chemical reactions. In those works the relationship between the velocity vectors in the asymptotic initial and final states of the collision imposed by the conservation laws for energy and momentum was used to obtain recoil velocity and angular distributions [43]. The goal of such measurements was to see if there were preferred directions relating the reactant and product relative velocity vectors and to understand the mechanism followed in the partition of the reaction energy (and total angular momentum) among the internal degrees of freedom of the product molecules and their relative translational motion [44]. Interestingly, since the early works by Herschbach and collaborators [43–46] and according to the precedent established in the case of nuclear reactions [43, 45], the arguments employed to analyse the measured angular distributions were also based on the observation of signatures of symmetry about 90° to conclude or not the formation of long-living complex during the course of the reaction [47–52].

First efforts to interpret the DCSs obtained in the CMB experiments consisted of the adoption of the same ideas comprised in the compound nucleus theory used for nuclear fission [45]. The shape of the angular distributions for reactions proceeding via the formation of a long-living complex was found to be determined by the total angular momentum disposal in both reactants and products. In fact, the calculation of the distribution is done under purely geometrical considerations regarding the relationships between the total (**J**), initial (**j**) and final (**j**′) angular momenta, the corresponding orbital momenta (**L** and **L'**) and the relative velocities (**v** and **v**′). Expressions for the leading form factors of the distributions were obtained for those cases in which $\mathbf{j} = \mathbf{j}' = 0, \mathbf{j} \neq 0, \mathbf{j}' = 0$ or $\mathbf{j} \neq 0, \mathbf{j}' \neq 0$. On those situations, the projections Ω and Ω' of **J** on **v** and **v**′, respectively, are $\Omega = \Omega' = 0$, $\Omega = 0, \Omega' \neq 0$ and $\Omega, \Omega' \neq 0$. The quantum expressions, reported in Ref. [45] and shown here in Table 1, depend on Legendre polynomials ($P_J(\cos\theta)$), associated Legendre polynomials ($P_J^{\Omega'}(\cos\theta)$) and Wigner rotation matrices ($d^J_{\Omega\Omega'}(\cos\theta)$). The classical expressions, on the other hand, obtained as the asymptotic case for large angular momenta [45, 53] also exhibit dependence on $\alpha = \arccos(\Omega'/J)$ and $\alpha' = \arcsin(\Omega/J)$, the angles of the uniform precession of **v**′ about **J** and of **J** about **v**, required to obtain the probability distribution for the angle θ [45].

Table 1 Quantum and classical form factors of the DCS as reported from Ref. [45] in terms of the projections Ω and Ω' of the total angular momentum on the initial and final relative velocities respectively. See text for details

Ω	Ω'	Quantum	Classical
0	0	$\mid P_J(\cos\theta) \mid^2$	$(\sin\theta)^{-1}$
0	$\neq 0$	$\mid P_J^{\Omega'}(\cos\theta) \mid^2$	$(\sin^2\theta - \cos^2\alpha')^{-1/2}$
$\neq 0$	$\neq 0$	$\mid d^J_{\Omega\Omega'}(\cos\theta) \mid^2$	$(\sin^2\theta - \cos^2\alpha - \cos^2\alpha' + 2\cos\alpha\cos\alpha'\cos\theta)^{1/2}$

These factors are then averaged over the corresponding values for the J, Ω and Ω' numbers to obtain the DCSs. Another interesting consequence of this approach is the fact that the degree of anisotropy can be related to the geometry of the dissociating complex. In particular, the relationship has its origin in the assumption of Ω' as a constant of motion, based on the fact that an uniform radiation of the products about the **J** vector is expected from the decay of a long-lived intermediate complex.

These angular correlation theory considerations were then extended to treat any stereodynamical property depending on the rotational orientation of the reactant or product molecule [54–56]. In particular, one of the directional properties investigated was the product angular distribution in the CM system, which correlates the directions of the initial and final relative velocity vectors, **k** and **k**′, respectively. The DCS can be expanded classically in terms of Legendre polynomials depending on θ, the angle between these two velocity vectors, as [54]

$$I(\theta) = \sum_n (2n+1)\langle P_n(\mathbf{k}, \mathbf{k}')\rangle P_n(\cos\theta). \tag{2}$$

If we choose, as shown in Fig. 1, an arbitrary coordinate system in which the total angular momentum **J** follows the direction of the z-axis, the average in the above equation, according to the addition theorem for Legendre polynomials, is

$$P_n(\mathbf{k}\cdot\mathbf{k}') = P_n(\mathbf{k}\cdot\mathbf{J})P_n(\mathbf{J}\cdot\mathbf{k}') + 2\sum_{m=1}^{n} \frac{(n-m)!}{(n+m)!} P_n^m(\mathbf{k}\cdot\mathbf{J})P_n^m(\mathbf{J}\cdot\mathbf{k}')\cos m(\phi_k - \phi_{k'}). \tag{3}$$

Within the context of a statistical model, the fragmentation of the complex is assumed to be independent of its formation, so the dihedral angle $\phi_k - \phi_{k'}$ between the (**k**, **J**) and (**J**, **k**′) planes (see Fig. 1) will be randomly distributed. The average of such an angle will vanish and therefore we obtain

$$\langle P_n(\mathbf{k}, \mathbf{k}')\rangle = \langle P_n(\mathbf{k}\cdot\mathbf{J})P_n(\mathbf{J}\cdot\mathbf{k}')\rangle. \tag{4}$$

In the specific case of no rotation in either the reactant or product molecules, $\mathbf{j} = 0$ and $\mathbf{j}' = 0$, the total angular momentum **J** is disposed completely as orbital angular

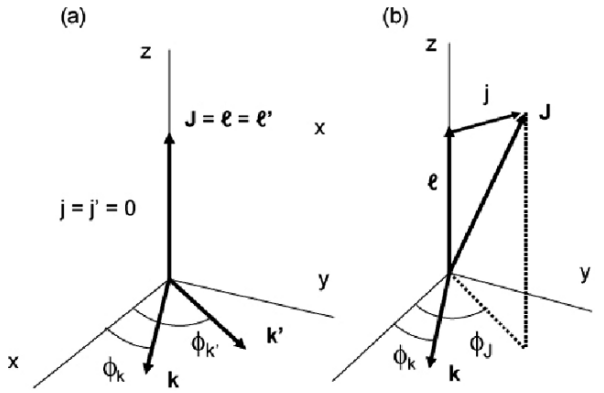

Fig. 1 Scheme of the angular momentum and relative velocity vectors for a reaction with no rotation in either reactants (**j**) or products (**j'**) (in (**a**)). In that case, initial **l** and final **l'** orbital angular momenta are identical to the total angular momentum **J** vector. In (**b**) the situation corresponds to the reactant channel when there exists rotation for the reactanting molecules, $\mathbf{j} \neq 0$

momentum for both the initial and final arrangements (see Fig. 1(a)). As a result, both relative velocity vectors are perpendicular to **J** and thus $\mathbf{k} \cdot \mathbf{J} = \mathbf{J} \cdot \mathbf{k'} = 0$ and

$$\langle P_n(\mathbf{k}, \mathbf{k'}) \rangle = [P_n(0)]^2 \,. \tag{5}$$

The substitution of this result in Eq. (2) yields

$$I(\theta) = \sum_{n=0}^{N} (2n+1) \, [P_n(0)]^2 \, P_n(\cos\theta). \tag{6}$$

The obtained angular distribution is symmetric about $\theta = 90^\circ$ since the terms with n odd vanish. Figure 2 shows the different contribution of the terms involved in the expansion given in Eq. (6), for the upper limits $N = 10$, 20, 30, 50 and 80. The figure shows that the sum tends to the classical limit given by $1/\sin\theta$, which has been also included in Fig. 2.

A similar expression for a more general case with rotation contained in both the reactant and product molecules ($\mathbf{j} \neq 0, \mathbf{j'} \neq 0$) can also be derived [54]. Figure 1(b) shows the relationships between the corresponding vectors for the entrance channel. Now, the z-axis is along the **l** vector and the angle ϕ_J goes up to the projection of the total angular momentum onto the plane perpendicular to the initial orbital angular momentum which contains the initial relative velocity vector **k**. The application of the addition theorem for both the entrance and product channels yields expressions for $P_n(\mathbf{k} \cdot \mathbf{J})$ and $P_n(\mathbf{J} \cdot \mathbf{k'})$, respectively, in a similar fashion as Eq. (3). The random orientation of the **j** vector guarantees the random distribution of the dihedral angle $\phi_k - \phi_J$ between the $(\mathbf{k}, \mathbf{l})$ and $(\mathbf{l}, \mathbf{J})$ planes. Analogous considerations can

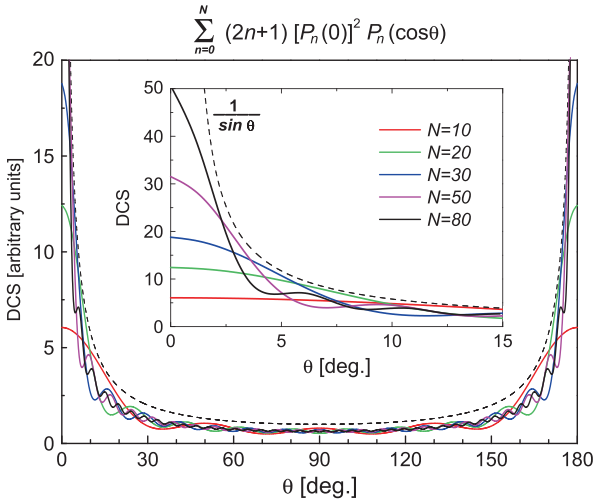

Fig. 2 Contributing terms from the expansion for the DCS given in Eq. (6) considering different values of the upper limit N. In dashed line the classical limit $1/\sin\theta$ has been included. In the inset figure an amplified view of the $0^\circ \leq \theta \leq 15^\circ$ angular region is shown

be addressed, in the product channel, for the $\phi_J - \phi_{k'}$ angle. Therefore, all terms containing these two angles cancel out with the average $\langle P_n(\mathbf{k}\cdot\mathbf{J})P_n(\mathbf{J}\cdot\mathbf{k'})\rangle$, which can be finally written as [54]

$$\langle P_n(\mathbf{k}\cdot\mathbf{k'})\rangle = [P_n(0)]^2\,\langle P_n(\mathbf{l}\cdot\mathbf{J})P_n(\mathbf{J}\cdot\mathbf{l'})\rangle, \tag{7}$$

where the orthogonality conditions $\mathbf{k}\cdot\mathbf{l} = \mathbf{k'}\cdot\mathbf{l'} = 0$ have been used. The corresponding substitution in Eq. (2) finally leads to

$$I(\theta) = \sum_n a_n\,[P_n(0)]^2\,\langle P_n(\mathbf{l}\cdot\mathbf{J})P_n(\mathbf{J}\cdot\mathbf{l'})\rangle\,P_n(\cos\theta). \tag{8}$$

Further derivations of expressions for the DCS within the framework of statistical theories followed soon to the above-discussed approach by Herschbach and collaborators. Thus, Light and coworkers extended the phase space theory (PST), developed some years before [58–62], to the case of angular distributions of the products [57]. In the quantum statistical model by Miller [63], for example, the expression of the DCS, after invoking a random phase approximation, is

$$\sigma_{j'\leftarrow j}(\theta) = \left[4k^2(2j+1)\right]^{-1} \sum_J (2J+1)^2 \sum_{\Omega\Omega'} |\, S^J_{j'\Omega',j\Omega}\,|^2 |\, d^J_{\Omega'\Omega}(\theta)\,|^2\,. \tag{9}$$

An additional statistical consideration on Eq. (9) yields to substitute the square modulus term of the scattering matrix as follows:

$$\mid S^J_{j'\Omega',j\Omega} \mid^2 = p^J_{j'\Omega'} p^J_{j\Omega}/N(J), \tag{10}$$

where $p^J_{j\Omega}$ is the probability for the complex to be formed from the initial channel with a quantum number j for the diatom angular momentum and its component along the z-axis Ω, and $N(J)$ is the quantity obtained as the sum of the capture probabilities, accessible at the corresponding values of the energy and the total angular momentum. This expression has its origin in the assumption of a two-step procedure, describing the total probability of the reaction as the product between the probability of formation of the intermediate complex from the initial state and the fraction of complexes dissociating to the final state. Introducing Eqs. (10) into (9), the expression for the angular distribution results:

$$\sigma_{j'\leftarrow j}(\theta) = \left[4k^2(2j+1)\right]^{-1} \sum_J \frac{(2J+1)^2}{N(J)} \sum_{\Omega\Omega'} p^J_{j'\Omega'} p^J_{j\Omega} \mid d^J_{\Omega'\Omega}(\theta) \mid^2 . \tag{11}$$

The dependence on the reduced rotation matrix elements $d^J_{\Omega'\Omega}(\theta)$, as in the case discussed in Table 1, determines the symmetry of the DCS about the 90° scattering direction. The equivalence between the quantum description by Miller and the classical formalism by Case and Herschbach described above has been outlined in Ref. [54]. It was shown there that the angular factor $(2J+1) \mid d^J_{\Omega'\Omega}(\theta) \mid^2$ can be expanded in a Legendre series whose coefficients, once one considers the classical limits of the Clebsch–Gordan coefficients and Wigner matrices [53] and an average over the J, Ω and Ω' numbers, are identical to those used in the corresponding expansion considered in Eq. (6). This feature is exemplified in Fig. 3, where the values for the corresponding square modulus for two specific values of the total angular momentum, $J = 5$ and 15, are shown.

The results presented in the figure clarify the origin of the symmetry about 90° with a marked propensity for the peaks at the forward and backward scattering directions for the angular distribution obtained within statistical considerations as in Eq. (11). It is worth noting that such a symmetry is guaranteed by the presence of the square modulus term, a result of the random phase approximation. Otherwise, the cross terms connecting different values of J would lead to a completely different profile.

All cases exhibit the above-mentioned symmetry about the sideways scattering direction, but the forward–backward peaking seems to be mainly due to the contribution of those reduced rotation matrix elements with $\Omega' = 0$. The much less prominent peaks produced by those terms with $\Omega' \neq 0$ on the contrary seem to shift closer to the $\theta \sim 0°$ direction. The comparison between the $J = 5$ and $J = 15$ cases shown in Fig. 3 also reveals that the polarised behaviour around 0° and 180° gets more pronounced as the total angular momentum increases. Considering that the

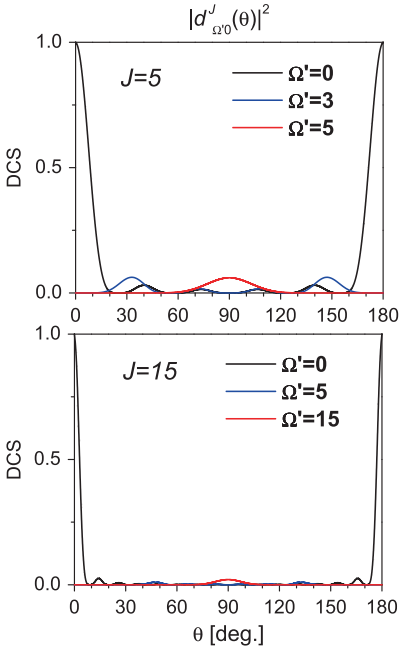

Fig. 3 Values of the reduced rotation matrix $| d_{\Omega' 0}(\theta) |^2$ terms contributing to the expression of the angular distributions of Eq. (11) for the $J = 5$ and 15 values of the total angular momentum at the top and bottom panels, respectively. Different values of Ω' have been considered in each case

larger the value of J is the larger the contribution of the corresponding partial wave to the DCS results, the feature revealed in the above figure is certainly relevant.

4 Selected Examples of Atom–Diatom Reactions

On this last section we will treat a series of examples taken from molecular reactive atom–diatom collisions. Special emphasis will be made on the comparison between the DCSs obtained by means of EQM methods and the predictions of a statistical quantum method (SQM). The technical details of this statistical approach have been explained in detail before [64–66] and are omitted here. The model is directly connected with some of the theoretical basis contained in the methods developed by Light [58] and Miller [63]. Reaction probabilities and angular distributions are also calculated according to Eqs. (10) and (11), respectively. The corresponding capture probabilities $p^J_{j\Omega}$ are obtained, however, via a completely quantum mechanical (QM) calculation in which full ab initio potential energy surfaces (PESs) are employed. Although in the original proposal of the method, a time-independent framework with the propagation of the corresponding wave function was considered [64, 65], versions of the SQM with propagation of wave packets have been recently suggested [67, 68].

The SQM has been applied in the past to study the dynamics of an extensive list of atom–diatom reactions. The comparison with both EQM and experimental

results has enabled to test the possible occurrence of complex-forming mechanisms in the overall dynamics of the reactive collision. Thus, vibrational and rotational cross sections, integral cross sections and a wide variety of distributions (time-of-flight, laboratory angle, product translational energy, etc.) have been studied in detail for reactions such as $N(^2D)+H_2$ [65, 69, 70], $C(^1D)+H_2$ [65, 71], $O(^1D)+H_2$ [65], $S(^1D)+H_2$ [65], $Si+O_2$ [72], $H+O_2$ [73, 74], $H^+ + H_2$ [75–77] and their corresponding isotopic variants when, for those collisions with molecular hydrogen, at least one of the H atoms is changed by deuterium. All these processes share in common the fact that the corresponding overall dynamics seems to be affected at some extent by the occurrence of complex-forming mechanisms. We will focus in this section on the profile found for the DCSs for some of the above-mentioned reactive collisions.

4.1 Collisions with Molecular Hydrogen

The first type of atom–diatom reactions analysed here is the process in which an atom X collides with molecular hydrogen H_2. When the X atom corresponds to an electronically excited atom of C, N, O or S, the reaction seems to occur via the formation of an intermediate complex (see Ref. [66] for an exhaustive review). For a wide range of energies, the dominant dynamics corresponds to the insertion of the X atom between the H–H bond yielding an intermediate species formed by the three atoms with a finite lifetime, typically longer than the corresponding rotational period. The existence of relatively deep potential wells in the region which separates the reactant and product valleys supports, on the other hand, the possibility of the formation of such a reaction complex. As a result, the prototype angular distributions found for these collisions exhibit a typical forward–backward symmetry. The comparison of statistical calculations with the angular distributions obtained by means of EQM approaches reveals an impressive agreement. Examples are shown in Figs. 4 and 5 for the cases of the $C(^1D)+H_2(v = 0, j = 0) \rightarrow CH+H$ reaction at a collision energy of $E_c = 80$ meV and for $S(^1D)+H_2 \rightarrow SH+H$ at $E_c = 97$ meV, respectively. In both cases, the statistical angular distribution seems to reproduce the preference for the forward and backward scattering directions exhibited by the EQM DCS. The sideways scattering is also well described by the SQM result. Such a good agreement, in combination with a similar success of the statistical predictions to reproduce exact rotational and vibrational distributions [66], is interpreted as indicative of the occurrence of a complex-forming mechanism for these two collisions.

For the $S(^1D)+H_2$ reaction, the theoretical angular distributions are also found to describe fairly well the measured DCSs [80], as shown in Fig. 5. The profile of the experimental distribution leads authors of Ref. [80] to suggest that the dynamics of this prototype insertion reaction could be understood by statistical arguments. In order to establish the theory versus experiment comparison of Fig. 5, the measured distribution was scaled to match the theoretical DCSs, whereas cross sections for the $S(^1D)+H_2(v = 0, j = 0)$ and $S(^1D)+H_2(v = 0, j = 1)$ reactions were properly

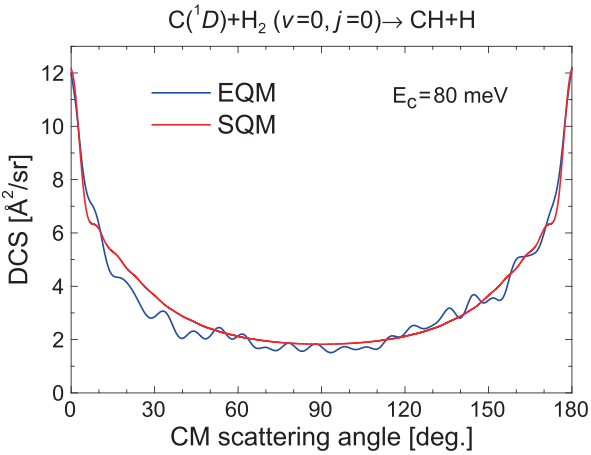

Fig. 4 DCS for the $C(^1D)+H_2(v = 0, j = 0) \rightarrow CH+H$ reaction at $E_c = 80$ meV. EQM results, with *blue* line, are taken from Ref. [78] and the SQM angular distribution is shown with *red* line. Adapted from Fig. 5 of Ref. [66]

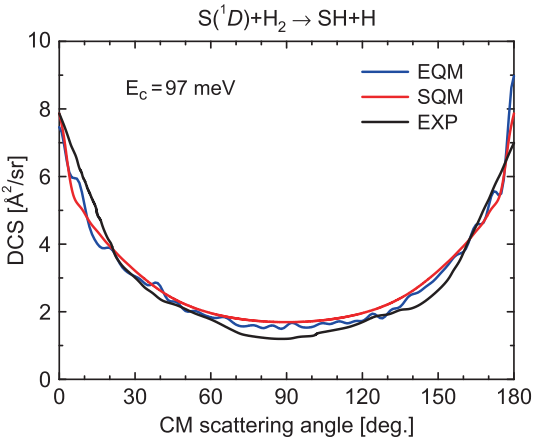

Fig. 5 Same as Fig. 4 for $S(^1D)+H_2 \rightarrow SH+H$ at $E_c = 97$ meV. Theoretical results include the average of the contributions from the $H_2(v = 0, j = 0, 1)$ cases for comparison with the experimental result (in *black* line) [80]. Exact results are from Ref. [79]. Figure adapted from Fig. 25 of Ref. [66]

averaged to obtain the EQM and SQM results. Both the values at the sideways scattering direction and the forward–backward symmetry are correctly accounted for by the statistical calculation.

It is generally well accepted that the mainly complex-forming character of these $X+H_2$ reactions is associated with the fact that the process occurs on the ground PES. However, the contribution from excited surfaces may introduce dynamical features corresponding to abstraction reaction pathways in which the process is the result of a direct atom–diatom collision with no intermediate complex formed. An illustrative example of this competition was found for the $O(^1D)+H_2$ reaction [81]. A slightly different situation is found for the $C(^1D)+H_2$ collision. The excited $^1A''$ PES has a deep potential well ($\sim$ 3.5 eV) but the existence of large barriers (with

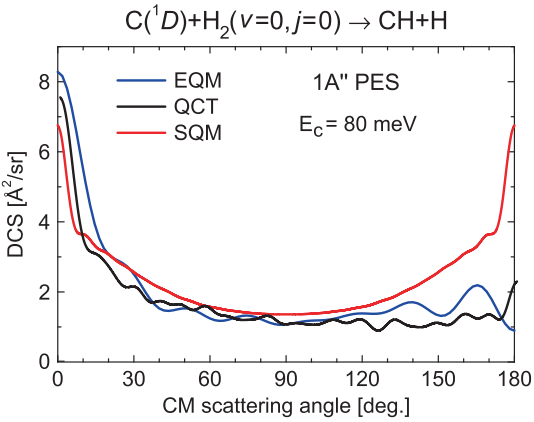

Fig. 6 $C(^1D)+H_2(v = 0, j = 0) \rightarrow CH+H$ at $E_c = 80$ meV on the $^1A''$-excited PES. EQM (in *blue* line) and QCT results (in *black* line) have been taken from Ref. [83]. Figure adapted from Fig. 8 of Ref. [66]

the only exception of geometries about 60°) precludes a pure insertion mechanism [82]. Thus, the "sideways insertion" dynamics of the reaction leads to non-statistical product distributions. In fact, a quasi-classical trajectory (QCT) estimation of the collision times concluded that most of the trajectories were shorter lived (20–200 fs) than those corresponding to the ground electronic state (about 4 ps) [83]. In particular, the DCSs obtained in the study by Honvault et al. exhibit a pronounced asymmetry between the scattering through the forward and backward directions, as shown in Fig. 6, where the EQM and QCT results from Ref. [83] are compared with the SQM predictions. The exact result [83] displays a preference for the forward scattering direction, with a prominent peak at $\theta \sim 0^\circ$ which contrasts with the almost equal propensity over the rest of possible directions. Whereas the QCT calculation manages to reproduce such a behaviour for the DCS, the statistical prediction, with the expected forward–backward symmetry, fails to give account for the correct scattering along the backward direction.

This brief overview of the $X+H_2$ reactions is completed with an example of ion–diatom process in which the X atom corresponds to the H^+ ion. In Fig. 7, we show the comparison between the EQM and SQM DCSs for $H^+ + D_2 \rightarrow DH + D^+$ at $E_c = 100$ meV. The figure corresponds to the case in which the reaction is initiated from the ground rovibrational state $D_2(v = 0, j = 0)$ to produce HD fragments in its vibrationless ground state $v' = 0$. Previous investigations have predicted a transition from a complex-formation dynamics for the reaction at relatively low collision energy to a direct mechanism at a higher energy regime for the $H^+ + H_2$ collisions and its corresponding isotopic variants. For a detailed review of studies which suggest this combined dynamical picture for the reaction we refer the reader to the introduction of Ref. [83]. Results shown in Fig. 7 constitute a nice example of the capabilities of statistical approaches to describe the overall dynamics of the $H^+ + D_2$ reaction at low energy, thus suggesting its insertion character. Despite the slight asymmetry of the exact angular distribution, the agreement between both theoretical methods is certainly impressive.

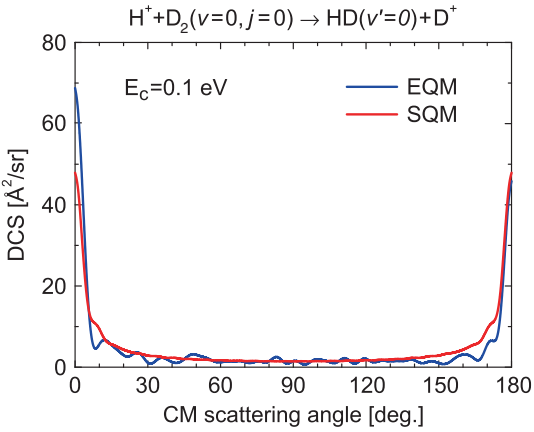

Fig. 7 Comparison between the EQM and SQM DCSs for $H^+ + D_2(v = 0, j = 0) \rightarrow HD + D^+$ at $E_c = 100$ meV. Figure adapted from Ref. [77]

The possible existence of differences in the description of the behaviour exhibited by the angular distributions at the forward and backward scattering directions for this type of reactions yielded by QCT and QM methods has been the subject of fruitful discussions. In particular, given its dynamical interpretation in connection with insertion-like mechanisms, the apparent inability of QCT methods to describe pronounced peaks at those directions constituted an intriguing issue [76, 84]. One of the suggested explanations for such a behaviour was the occurrence of tunnelling effects through centrifugal barriers [65, 85]. However, attempts to complete the classical approach with tunnelling contributions introduced by means of semiclassical approximations in PST calculations did not manage to account for the extreme forward–backward dynamics manifested in some $X+H_2$ reactions [86]. A more conclusive argument was given by Bonnet et al. [87, 88], who attributed the feature to the violation of the parity conservation inherent to QCT methods. DCSs obtained classically under these parity-restoring assumptions were found to exhibit the degree of polarisation of the QM counterparts. These findings encouraged the ulterior development of a version of the SQM of Refs. [64, 65] within the classical theory framework, with the propagation of QCT instead of wave functions. This statistical QCT model has been recently employed to treat different $X+H_2$ reactions [89–91], and the obtained DCSs display the correct behaviour at the forward and backward directions.

4.2 Collisions with Molecular Oxygen

Collisions between an atom of H or Si and molecular oxygen are the last type of molecular reactions treated in this work. These processes constitute examples of coexistence between different reaction mechanisms. The presence of deep potential wells ($\sim$ 2.5 eV for the HO_2 and $\sim$ 7.11 eV for the deepest well of the SiO_2) and the large number of bound and quasibound states make fully converged EQM

calculations extremely demanding in terms of computational time. Thus, whereas it has been only recently that EQM DCSs for the H+O_2 reaction have been reported [95], for Si+O_2 no QM calculation is found in the literature up to date.

For the H+O_2 reaction, for example, statistical predictions have been found to reproduce on average the exact reaction probabilities for low values of the total angular momenta $J \leq 5$, specially at the low-energy range [73]. When the energy is increased, however, beyond the onset of the OH formation channel in its first excited vibrational state $v' = 1$, at $\sim$ 1.2 eV total energy, probabilities obtained by means of either the SQM or PST approaches deviate noticeably from the EQM results [74]. As a consequence, the corresponding ICSs are far from being reproduced by statistical means. Furthermore, the precise shape of the reaction probabilities does depend on the specific PES employed in the calculations [74, 92, 93], questioning thus the apparent success mentioned above of the statistical approaches. In fact, recent reports of EQM calculations just above the threshold energy for reaction concluded significant non-statistical features for this process [94]. The DCSs, however, were found to confirm the dominance of a complex-forming mechanism. In fact, Fig. 8 shows that predictions from the SQM do not compare extremely bad with the exact result reported in Ref. [94] for the reaction initiated from $O_2(v = 3, j = 1)$. Despite the slight degree of asymmetry between the forward and backward peaks, both the sideways scattering direction and the exact cross section for $\theta \approx 180^\circ$ are reasonably well described by the SQM DCS.

State-to-state DCSs obtained at a higher energy, 1.036 eV collision energy, do not exhibit a larger degree of asymmetry about $\theta \sim 90^\circ$ than the situation shown in Fig. 8. Despite this, the feature and the deviations of the exact rotational cross sections from the PST results led authors of Ref. [95] to conclude that the dynamics of the reaction is non-statistical. Interestingly, the differences with the statistical limit mentioned in that work refer exclusively to the intensity of the rotational distributions but not to the profile which resembles to the expected outcome of a complex-forming process suitable to be described on statistical grounds.

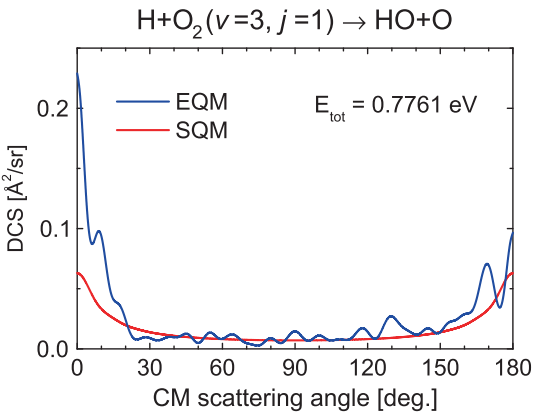

Fig. 8 Angular cross section for H+$O_2(v = 3, j = 1) \rightarrow$ HO+O at $E_{tot} = 0.7761$ eV. EQM result is from Ref. [94]. Figure adapted from [74]

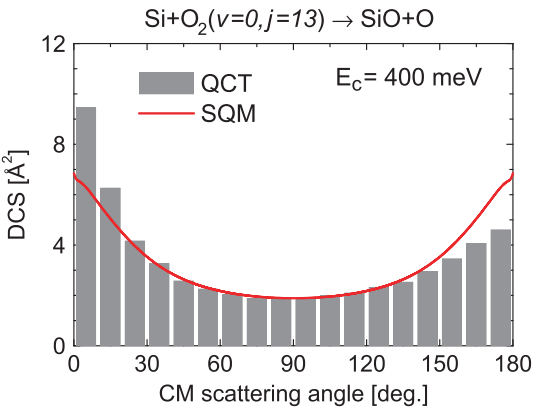

Fig. 9 SQM (*red* line) and QCT (*grey* boxes) DCSs for the Si+O_2($v = 0$, $j = 13$) → SiO+O at $E_c = 400$ meV. Figure adapted from Ref. [72]

The existing PES for the SiO_2 system possesses three different minimum wells associated with the linear OSiO, linear SiOO and triangular OSiO configurations [96]. QCT calculations found that the dynamical mechanism for the Si+O_2 reaction depends on the potential well explored by the trajectories [97]. Rotational, vibrational and angular cross sections were investigated up to $E_c = 0.6$ eV and the overall dynamics of the Si+O_2($v = 0$, $j = 1$) → SiO+O collision was concluded to evolve from a direct reaction mechanism at low-collision energies to a typical insertion process at a higher energy regime. The comparison with statistical approaches such as prior distributions, PST and the above-mentioned SQM seems to confirm such a transition to a complex-forming reaction as the energy increases. Furthermore, a similar trend was observed when, for a specific energy, the rotational excitation j of the $O_2(v = 0, j)$ reactant was augmented [72]. Figure 9 shows the comparison between the QCT angular distribution and the statistically predicted DCS for the extreme case of a relatively large energy, $E_c = 400$ meV, and the O_2 fragment is highly excited to the rotational ($v = 0$, $j = 13$) state. The agreement found for that case contrasts significantly with the comparisons established either at a lower energy or for a lower j state [72] and constitutes an additional evidence for the previously observed complex-forming dynamics for the Si+O_2 reaction.

5 Conclusions

In this work we have tackled the issue of the differential cross sections for atom–diatom reactions which proceed via the formation of an intermediate complex. Since decades ago, the distributions in terms of the centre of mass angle for this type of reactive processes have been found to display a prototype shape consisting of pronounced peaks at the $\theta \sim 0^\circ$ and $\theta \sim 180^\circ$ directions and an almost constant value around the sideways scattering direction. A historical review of the origin of the close connection among (i) this particular dynamics; (ii) the symmetric forward–backward profile of the differential cross section and (iii) the application

of statistical methods for both nuclear and molecular reactions has been presented. We have briefly discussed the theoretical basis for the mathematical expressions employed to describe the angular distributions. The analysis of cross sections by means of a statistical quantum method allows to understand the dynamical mechanisms which govern the atom–diatom reaction. Examples of such a procedure for a series of different molecular collisions have been provided to complete this study.

Acknowledgments This work has been funded by the Spanish MEC under projects FIS2007-62006 and CTQ2005-09185-C02-02 and Grant BES-2006-11976.

References

1. A.H. Zewail, J. Phys. Chem. A **104**, 5660–5694 (2000)
2. K. Liu, J. Chem. Phys. **125**, 132307-1–132307-12 (2006)
3. D. Skouteris, J.F. Castillo, D.E. Manolopoulos, Comput. Phys. Commun. **133**, 128–135 (2000)
4. P. Honvault, J.-M. Launay, in *Theory of Chemical Reaction Dynamics* ed. by A. Lagana, G. Lendvay, Series II: Mathematics, Physics and Chemistry **145** (Kluwer, Dordrecht, 2004) p. 187
5. S.C. Althorpe, Int. Rev. Phys. Chem. **23**, 219–251 (2004)
6. M. Hankel, S.C. Smith, R.J. Allan, S.K. Gray, G.G. Balint-Kurti, J. Chem. Phys. **125**, 164303-1–16403–12 (2006)
7. N. Bohr, Nature **137**, 344–348 (1936)
8. E.P. Wigner, Am. J. Phys. **23**, 371–380 (1955)
9. G. Breit, E.P. Wigner, Phys. Rev. **49**, 519–531 (1936)
10. V. Weisskopf, Phys. Rev. **52**, 295–303 (1937)
11. V. Weisskopf, D.H. Ewing, Phys. Rev. **57**, 472–485 (1940)
12. H.L. Bradt, D.J. Tendam, Phys. Rev. **72**, 1117–1118 (1947)
13. B.T. Feld, Phys. Rev. **75**, 1115–1123 (1949)
14. P.H. Stelson, C. Goodman, Phys. Rev. **82**, 69–71 (1951)
15. E.R. Graves, L. Rosen, Phys. Rev. **89**, 343–348 (1953)
16. B.L. Cohen, Phys. Rev. **81**, 184–188 (1951)
17. B.L. Cohen, Phys. Rev. **92**, 1245–1248 (1953)
18. R.M. Eisberg, G. Igo, Phys. Rev. **93**, 1039–1051 (1954)
19. R.M. Eisberg, Phys. Rev. **94**, 739–740 (1954)
20. D.C. Peaslee, Phys. Rev. **86**, 269–271 (1952)
21. S. Fernbach, R. Serber, T.B. Taylor, Phys. Rev. **75**, 1352–1355 (1949)
22. R. Serber, Phys. Rev. **72**, 1114–1115 (1947)
23. H.A. Bethe, Phys. Rev. **57**, 1125–1144 (1940)
24. L. Wolfenstein, Phys. Rev. **82**, 690–696 (1951)
25. W. Hauser, H. Fesbach, Phys. Rev. **87**, 366–373 (1952)
26. J.J. Griffin, Phys. Rev. **116**, 107–118 (1959)
27. G.E. Gordon, A.E. Larsh, T. Sikkeland, Phys. Rev. **118**, 1610–1611 (1960)
28. G.E. Gordon, A.E. Larsh, T. Sikkeland, G.T. Seaborg, Phys. Rev. **120**, 1341–1348 (1960)
29. V.E. Viola, Jr., T. Darrah Thomas, G.T. Seaborg, Phys. Rev. **129**, 2710–2717 (1963)
30. B.L. Cohen, W.H. Jones, G.H. McCormick, B.L. Ferrell, Phys. Rev. **94**, 625–629 (1954)
31. S.H. Ahn, J.H. Roberts, Phys. Rev. **108**, 110–113 (1957)
32. M.L. Halbert, F.E. Durham, C.D. Moak, A. Zucker, Phys. Rev. **162**, 919–933 (1967)
33. J.B. Marion, G. Weber, Phys. Rev. **103**, 1408–1413 (1956)

34. R.L. Becker, Phys. Rev. **119**, 1076–1079 (1960)
35. W.W. Pratt, Phys. Rev. **94**, 1086–1087 (1954)
36. E.A. Wolicky, H.D. Holmgren, R.L. Johnston, E. Geer Illsley, Phys. Rev. **116**, 1585–1591 (1959)
37. J.J. Leigh, J.M. Blair, Phys. Rev. **121**, 246–252 (1961)
38. G.C. Morrison, Phys. Rev. **121**, 182–183 (1961)
39. B.L. Cohen, Phys. Rev. **98**, 49–55 (1955)
40. V.F. Weisskopf, Rev. Mod. Phys. **29**, 174–181 (1957)
41. R.M. Eisberg, N.M. Hintz, Phys. Rev. **103**, 645–646 (1956)
42. R.G. Thomas, Phys. Rev. **97**, 224–237 (1955)
43. D.R. Herschbach, Disc. Faraday Soc. **33**, 149–161 (1962)
44. D.R. Herschbach, Angew. Chem. Int. Ed. Engl. **26**, 1221–1243 (1987)
45. W.B. Miller, S.A. Safron, D.R. Herschbach, Disc. Faraday Soc. **44**, 108–122 (1967)
46. D.R. Herschbach, Faraday Discuss. Chem. Soc. **55**, 233–251 (1973)
47. D.D. Parrish, D.R. Herschbach, J. Am. Chem. Soc. **95**, 6133–6132 (1973)
48. L.D. Doverspike, R.L. Champion, T.L. Bailey, J. Chem. Phys. **45**, 4385–4391 (1966)
49. D.O. Ham, J.L. Kinsey, J. Chem. Phys. **48**, 939–940 (1967)
50. D.O. Ham, J.L. Kinsey, F.S. Klein, Disc. Faraday Disc. **44**, 174–176 (1967)
51. S. Stolte, A.E. Proctor, R.B. Bernstein, J. Chem. Phys. **65**, 4990–5008 (1976)
52. J.C. Whitehead, R. Grice, Faraday Disc. Chem. Soc. **55**, 320–330 (1973)
53. P.J. Bruusaard, H. Tolhoek, Physica **23**, 955–971 (1957)
54. D.A. Case, D.R. Herschbach, J. Chem. Phys. **64**, 4212–4222 (1976)
55. D.A. Case, D.R. Herschbach, Mol. Phys. **100**, 109–125 (2002)
56. S.K. Kim, D.R. Herschbach, Faraday Discuss. Chem. Soc. **84**, 159–169 (1987)
57. R.A. White, J.C. Light, J. Chem. Phys. **55**, 379–387 (1971)
58. J.C. Light, J. Chem. Phys. **40**, 3221–3229 (1964)
59. P. Pechukas, J.C. Light, J. Chem. Phys. **42**, 3281–3291 (1965)
60. J.C. Light, J. Lin, J. Chem. Phys. **43**, 3209–3219 (1965)
61. P. Pechukas, J.C. Light, C. Rankin, J. Chem. Phys. **44**, 794–805 (1966)
62. J.C. Light, Discuss. Faraday Soc. **44**, 14–29 (1967)
63. W.H. Miller, J. Chem. Phys. **52**, 543–551 (1970)
64. E.J. Rackham, F. Huarte-Larrañaga, D.E. Manolopoulos, Chem. Phys. Lett. **343**, 356–364 (2001)
65. E.J. Rackham, T. González-Lezana, D.E. Manolopoulos, J. Chem. Phys. **119**, 12895–12907 (2003)
66. T. González-Lezana, Int. Rev. Phys. Chem. **26**, 29–91 (2007)
67. S.Y. Lin, H. Guo, J. Chem. Phys. **120**, 9907–9910 (2004)
68. S.Y. Lin, H. Guo, J. Phys. Chem. A **108**, 10066–10071 (2004)
69. N. Balucani, P. Casavecchia, L. Bañares, F.J. Aoiz, T. González-Lezana, P. Honvault, J.-M. Launay, J. Phys. Chem. A **110**, 817–829 (2006)
70. L. Bañares, F.J. Aoiz, T. González-Lezana, V.J. Herrero, I. Tanarro, J. Chem. Phys. **123**, 224301 (2005)
71. N. Balucani, G. Capozza, E. Segoloni, A. Russo, R. Bobbenkamp, P. Casavecchia, T. González-Lezana, E.J. Rackham, L. Bañares, F.J. Aoiz, J. Chem. Phys. **122**, 234309 (2005)
72. F. Dayou, P. Larrégaray, L. Bonnet, J.C. Rayez, P.N. Arenas, T. González-Lezana, J. Chem. Phys. **128**, 174307 (2008)
73. P. Bargueño, T. González-Lezana, P. Larrégaray, L. Bonnet, J.C. Rayez, Phys. Chem. Chem. Phys. **9**, 1127–1137 (2007)
74. P. Bargueño, T. González-Lezana, P. Larrégaray, L. Bonnet, J.C. Rayez, M. Hankel, S.C. Smith, A.J.H.M. Meijer, J. Chem. Phys. **128**, 244308 (2008)
75. T. González-Lezana, A. Aguado, M. Paniagua, O. Roncero, J. Chem. Phys. **123**, 194309 (2005)

76. T. González-Lezana, O. Roncero, P. Honvault, J.-M. Launay, N. Bulut, F.J. Aoiz, L. Bañares, J. Chem. Phys. **125**, 94314 (2006)
77. E. Carmona-Novillo, T. González-Lezana, O. Roncero, P. Honvault, J.-M. Launay, N. Bulut, F.J. Aoiz, L. Bañares, A. Trottier, E. Wrede, J. Chem. Phys. **128**, 014304 (2008)
78. L. Bañares, F.J. Aoiz, B. Bussery-Honvault, P. Honvault, J.-M. Launay, J. Chem. Phys. **118**, 565–568 (2003)
79. P. Honvault, J.-M. Launay, Chem. Phys. Lett. **370**, 371–375 (2003)
80. S.-H. Lee, K. Liu, Appl. Phys. B **71**, 627–633 (2000)
81. K. Liu, Annu. Rev. Phys. Chem. **52**, 139–164 (2001)
82. B. Bussery-Honvault, J. Julien, P. Honvault, J.-M. Launay, Phys. Chem. Chem. Phys. **7**, 1476–1481 (2005)
83. P. Honvault, B. Bussery-Honvault, J.-M. Launay, F.J. Aoiz, L. Bañares, J. Chem. Phys. **124**, 154314 (2006)
84. L. Bañares, F.J. Aoiz, P. Honvault, B. Bussery-Honvault, J.-M. Launay, J. Chem. Phys. **118**, 565–568 (2003)
85. N. Balucani, L. Cartechini, G. Capozza, E. Segoloni, P. Casavecchia, G.G. Volpi, F.J. Aoiz, L. Bañares, P. Honvault, J.-M. Launay, Phys. Rev. Lett. **89**, 013201 (2002)
86. P. Larrégaray, L. Bonnet, J.-C. Rayez, J. Phys. Chem. A **110**, 1552–1560 (2006)
87. L. Bonnet, P. Larrégaray, J.-C. Rayez, T. González-Lezana, Phys. Chem. Chem. Phys. **8**, 3951–3954 (2006)
88. L. Bonnet, P. Larrégaray, J.-C. Rayez, Phys. Chem. Chem. Phys. **9**, 3228–3240 (2007)
89. F.J. Aoiz, V. Sáez-Rábanos, T. González-Lezana, D.E. Manolopoulos, J. Chem. Phys. **126**, 161101 (2007)
90. F.J. Aoiz, V. Sáez-Rábanos, T. González-Lezana, J. Chem. Phys. **127**, 174109 (2007)
91. F.J. Aoiz, V. Sáez-Rábanos, T. González-Lezana, J. Chem. Phys. **129**, 094305 (2008)
92. S.Y. Lin, H. Guo, P. Honvault, D. Xie, J. Phys. Chem. B **110**, 23641–23643 (2006)
93. M. Hankel, S.C. Smith, A.J.H.M. Meijer, J. Chem. Phys. **127**, 064316 (2007)
94. P. Honvault, S.Y. Lin, D. Xie, H. Guo, J. Phys. Chem. A **111**, 5349–5352 (2007)
95. Z. Sun, D. Zhang, C. Xu, S. Zhou, D. Xie, G. Lendvay, S.-Y. Lee, S.Y. Lin, H. Guo, J. Am. Chem. Soc. **130**, 14962–14963 (2008)
96. F. Dayou, A. Spielfiedel, J. Chem. Phys. **119**, 4237–4250 (2003)
97. F. Dayou, W.-Ü.L. Tchang-Brillet, M. Monnerville, J. Chem. Phys. **123**, 084306 (2005)

Shared Memory Parallelization of the Multiconfiguration Time-Dependent Hartree Method and Application to the Dynamics and Spectroscopy of the Protonated Water Dimer

Michael Brill, Oriol Vendrell, and Hans-Dieter Meyer

Abstract The Heidelberg multiconfiguration time-dependent Hartree (MCTDH) code for propagation of wavepackets is parallelized using *shared memory* techniques. A parallelization scheme based on a scheduler–worker approach is introduced. The performance of the parallel code is evaluated by benchmark tests. Using the parallelized version of the MCTDH code, the infrared absorption spectrum of the protonated water dimer ($H_5O_2^+$) is simulated in full dimensionality (15D) in the spectral range 0–4,000 cm^{-1}. The middle spectral region, between 800 and 2,000 wavenumbers, is discussed and the couplings that shape this region of the spectrum are identified and explained, and the corresponding spectral lines are assigned.

Keywords: Quantum Dynamics · MCTDH · IR-Spectroscopy · Parallelization

1 Introduction

Molecular quantum dynamics, i.e., the full quantum study of vibrations and rotations of polyatomic molecules, is fundamental for the understanding of physical and chemical processes on a molecular scale. It is, however, numerically very demanding. The multiconfiguration time-dependent Hartree (MCTDH) method – under active development during the last 15 years – is a very efficient method for propagating wavepackets. The method has proven its capability to treat large systems ($\gtrsim$9 degrees of freedom) fully quantum mechanically and with high accuracy. To be able to tackle larger problems that include more degrees of freedom, the Heidelberg implementation of the MCTDH algorithm has been parallelized using shared memory techniques. The first part of this work has been presented in [1]. In this work we discuss the current developments concerning the Heidelberg MCTDH code. In passing we note that parallelization of MCTDH has also been carried out – using different strategies though – by U. Manthe [2] and A. Scrinzi [3].

M. Brill, O. Vendrell, H.-D. Meyer (✉)
Theoretische Chemie, Physikalisch-Chemisches Institut, Universität Heidelberg, INF 229, D-69120 Heidelberg, Germany, e-mail: Hans-Dieter.Meyer@pci.uni-heidelberg.de

P. Piecuch et al. (eds.), *Advances in the Theory of Atomic and Molecular Systems*, Progress in Theoretical Chemistry and Physics 20, DOI 10.1007/978-90-481-2985-0_4,

We also account for recent results obtained in our investigations on the Zundel cation ($H_5O_2^+$), which we treat in its full dimensionality (15D) on an accurate potential energy surface (PES). These simulations are made possible by the development of the parallel version of MCTDH. This system is a small prototype for the proton-transfer process in water systems. Other important systems can now be fully quantum dynamically simulated thanks to the parallelization of the MCTDH code.

The report is structured as follows. The MCTDH method [4–6] is briefly recalled in Sect. 2. The current progress of the parallelization of the Heidelberg MCTDH code and algorithm is covered in Sect. 4. Section 7 reports on the results on the dynamics and IR spectrum of the $H_5O_2^+$ cation, with particular emphasis on the complicated spectral region between 800 and 2,000 cm^{-1}, and some conclusions and future perspectives are given in Sect. 8.

2 Equations of Motion and Runtime Distribution

In previous publications [1, 4–7] the MCTDH ansatz of the wavefunction and the derivation of the coupled equations of motion of the MCTDH algorithm have been introduced:

$$\Psi(Q_1, \ldots, Q_f, t) = \sum_{j_1=1}^{n_1} \cdots \sum_{j_f=1}^{n_f} A_{j_1 \ldots j_f}(t) \prod_{\kappa=1}^{f} \varphi_{j_\kappa}^{(\kappa)}(Q_\kappa, t), \tag{1}$$

$$i\dot{\mathbf{A}} = \mathcal{K}\mathbf{A}, \tag{2}$$

$$i\dot{\varphi}^{(\kappa)} = \left(1 - P^{(\kappa)}\right)\left(\rho^{(\kappa)}\right)^{-1} \mathcal{H}^{(\kappa)}\varphi^{(\kappa)}. \tag{3}$$

Using the Constant-Mean-Field-approach, that has been introduced in [8] and in Chap. 5.2 of Ref. [6], these equations can be decoupled and solved in three separate steps:

- Calculation of the Hamiltonian matrix and the mean fields.
- Propagation of the MCTDH expansion coefficients.
- Propagation of the single particle functions (SPFs).

The sum of the computation time for the three tasks is the major part of the wall time of an MCTDH run (usually $\geq$99%). The sharing of the work load between these parts depends strongly on the physical system that is treated. Three main distribution schemes for the computation time can be found:

- The computation time is distributed equally to the three tasks. The contribution of each part varies typically between 20 and 50% depending on the investigated system. Such calculations are called “balanced.”
- The propagation of the SPFs contributes only a little to the computation time ($\leq$5%). The other two parts contribute almost equally in a range of 40–60%. These calculations are called “A-vector dominated.”

- The propagation of the SPFs takes more than 60% of the computation time. Such an "SPF-dominated" situation often occurs for small systems where parallelization is not needed. It happens also for over-combined calculations, i.e., calculations in which too many DOFs are combined to build an MCTDH particle. Over combinations are inefficient and should be avoided.

Hence all three parts of MCTDH must be parallelized to receive an adequate speedup. In most cases over 60% of the computation time is taken by the mean-field calculation and the propagation of the expansion coefficients. The parallelization of these two tasks can be done efficiently and, in fact, is similar for both cases. The propagation of the SPFs is more difficult to parallelize and this parallelization is less efficient compared to the other two cases and will be described in the following.

3 Shared Memory Parallelization of the A-Vector Propagation and the Mean-Field Computation

In a previous publication [1] the parallelization of the A-vector propagation and the mean-field computation has already been presented. The main ideas will be summed up in the following.

For the A-vector propagation the time-determining step is the evaluation of the right-hand side of the equations of motion:

$$i\dot{A}_J(t) = \sum_L \langle \Phi_J | H | \Phi_L \rangle A_L(t). \tag{4}$$

For an efficient evaluation of the sum, MCTDH takes advantage of the product structure of the Hamiltonian. The multidimensional integrals $\langle \Phi_J | H | \Phi_L \rangle$ become a product of one-dimensional integrals. These can be computed separately for each Hamiltonian term. These computations are distributed over the available processors: Different processors compute the integrals for different Hamiltonian terms.

For the mean-field computation the following objects must be calculated: the mean field tensor,

$$\mathcal{H}^{(\kappa)}_{rjl} = c_r \sum_J {}^{\kappa} A^*_{J^\kappa_j} \prod_{\lambda=1,\lambda\neq\kappa}^{p} \sum_{l_\lambda} \left\langle \varphi^{(\lambda)}_{j_\lambda} \middle| \hat{h}^{(\lambda)}_r \middle| \varphi^{(\lambda)}_{l_\lambda} \right\rangle A_{L^\kappa_l}, \tag{5}$$

and the action of the mean fields on the potential terms,

$$\mathcal{M}^{(\kappa)}_{kl\alpha} = \sum_r^s \mathcal{H}^{(\kappa)}_{rkl} \left\langle \chi^{(\kappa)}_\alpha \middle| \hat{h}^{(\kappa)}_r \middle| \chi^{(\kappa)}_\alpha \right\rangle. \tag{6}$$

In both cases the parallelization can be done as for the A-vector propagation: The computations for different Hamiltonian terms, labeled by index r, can be distributed to the available processors.

This parallelization approach has proven its efficiency in different cases (H_2+H_2-scattering, $H_5O_2^+$ molecular dynamics), especially for problems with a large number of Hamiltonian terms.

4 Shared Memory Parallelization of the SPF Propagation

For the propagation of the SPFs the evaluation of the right-hand side of the equations of motion (3) is the time-determining step. By splitting the Hamiltonian in uncorrelated and correlated terms,

$$H = \sum_{\kappa=1}^{p} \hat{h}^{(\kappa)} + \sum_{r=1}^{s} c_r \prod_{\kappa=1}^{p} \hat{h}_r^{(\kappa)}, \tag{7}$$

the equations of motion for the SPFs can be rewritten:

$$i\dot{\varphi}_j^{(\kappa)} = \left(1 - P^{(\kappa)}\right) \left(\hat{h}^{(\kappa)} \varphi_j^{(\kappa)}(t) + \sum_{k,l=1}^{n_p} \left(\rho^{(\kappa)^{-1}}\right)_{jk} \sum_{r=1}^{s} \mathcal{H}_{rkl}^{(\kappa)} \hat{h}_r^{(\kappa)} \varphi_l^{(\kappa)}(t) \right). \tag{8}$$

The computation of the right-hand side of this equation is done in several steps. First the sum over the Hamiltonian terms is evaluated. Afterwards the inverse density matrix is applied. Then the action of the uncorrelated Hamiltonian terms on the SPFs is added. Finally the projection is carried out.

The parallelization has to be done for each of these steps separately. The summation over the Hamiltonian terms is parallelized as in the cases of the A-vector propagation and the mean-field computation, see [1]. The loop runs over the kinetic Hamiltonian terms which represent a part of the Hamiltonian that is much smaller than the potential part. The different parts of this summation are distributed over the available processors.

Each of the other steps mainly consists of a loop over the SPFs for the particle considered. Thus the loops over the SPFs are parallelized. For small calculations this parallelization scheme is disadvantageous because the number of processors (e.g., 8) can be larger than the SPF basis for a certain particle. Hence this scheme is better suited for larger calculations with large numbers of SPFs.

5 Implementation Details

5.1 Parallelization Scheme

The parallelization of the different parts of MCTDH is included in a scheduler–worker scheme. The main program has the role of a scheduler that does all

calculations that are not time consuming and controls the other threads. These threads are the worker threads performing the time-consuming computations on different processors. There are – usually – as many threads as processors available. Figure 1 shows the scheme in detail. Each time the main program comes to a point where a computation can be made in parallel the semaphore 1 is increased. The main program halts at the following semaphore 2. When semaphore 1 is increased the threads can do the work. As soon as the computations are finished the semaphore 2 is increased and the threads again wait at the semaphore 1. By increasing semaphore 2 the main program takes control again and proceeds with further calculations.

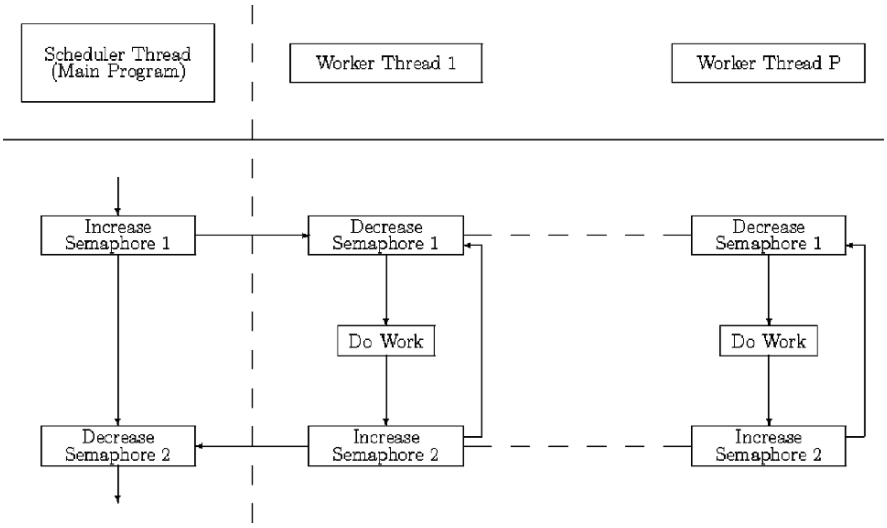

Fig. 1 Organization of the threads in the scheduler–worker scheme

5.2 Load Balancing and Memory Requirements

Two further aspects must be considered regarding the parallelization of MCTDH, the memory requirements and the load balancing. For an efficient parallelization it must be guaranteed that all available processors are used for the computations made. This means the code must take care that the work is distributed equally to the processors. In the current version of MCTDH this is ensured using a global counter variable combined with a mutual exclusion. As already mentioned the parallelization is used to distribute the work of certain loops to the processors. The counter variable of the loops is seen by each thread: If a thread has finished its work in one step of the loop the mutual exclusion is locked, then the counter variable is increased, afterwards the mutual exclusion is unlocked again and the thread starts working in the step determined by the counter variable. The mutual exclusion

secures that no other thread can get the same value for the counter variable, ensuring that the work is done only once. All threads have the same work to do; only at the end of the loop it can happen that some threads stay idle till the loop is finished.

The second problem that must be considered is the memory requirements. MCTDH needs memory to store different objects that are used during a propagation, e.g., the wavefunction (A-vector, SPFs). Further memory is used for the computations itself, the so-called *work arrays*, where intermediate results are stored. Considering several threads working on different parts of the same problem (e.g., mean-field tensor computation), they all need their own *work array* to store data, sum results, build matrices, and so on. Because these threads are calculating different parts of the problem they need the same amount of work memory exclusively. Hence for each thread, extra memory must be allocated. The memory requirements for an MCTDH run with P processors are

$$M(P) = M_{\text{objects}} + P \times M_{\text{work}}, \tag{9}$$

where M_{objects} denotes the memory needed for the storage of all objects (e.g., the wavefunction) and M_{work} is the memory needed for the *work arrays*. Thus the required memory moderately increases with the number of processors.

6 Results

6.1 Benchmark Systems

For the test of the parallelization of the MCTDH code four different benchmark systems were used. These systems are

- The H_2+H_2 inelastic scattering [9, 10].
- The quantum molecular non-adiabatic dynamics of C_2H_4 [11].
- The quantum molecular dynamics of $H_5O_2^+$ using two different mode combinations [12, 13] ($H_5O_2^+$-a and $H_5O_2^+$-b).

The sizes of these systems differ strongly. This is essential to give an overview of the efficiency of the parallelization. The H_2+H_2 scattering and the molecular dynamics of C_2H_4 are the smaller systems; a parallel code is not needed to perform the calculations. These two examples are only given as a reference. The dynamics of $H_5O_2^+$ is a problem that cannot be solved with a serial code at reasonable wall times.

6.2 Results

For the four benchmark systems MCTDH runs have been performed with an increasing number of processors (1, 2, 4, and 8) on the XC2 system in Karlsruhe. The resulting speedups are fitted to Amdahl's law to determine the parallel part of the code.

In Fig. 2 the results for the quantum molecular dynamics of C_2H_4 and $H_5O_2^+$-a are displayed. The dotted and dashed lines are the fits based on Amdahl's law to the data (circles and squares); the solid line shows the ideal linear speedup. The corresponding parallel parts are $p_{C_2H_4} = 0.82$ and $p_{H_5O_2^+-a} = 0.83$. In these cases the parallel algorithm performs quite poorly. For C_2H_4 this is caused by the small size of the problem. The number of Hamiltonian terms is rather small. This downgrades the parallelization of the A-vector propagation and of the mean-field computation. Additionally the particles are small thus the parallelization of the SPF propagation is not very efficient. This is because the algorithm has to synchronize the scheduler and worker threads many times for only a small amount of work. In the $H_5O_2^+$-a case a particle with a very large grid is present causing a less efficient mean-field computation.

In Fig. 3 the corresponding results are displayed for the H_2+H_2 scattering and the molecular dynamics of $H_5O_2^+$-b (The $H_5O_2^+$-a and $H_5O_2^+$-b calculations differ in the way in which the degrees of freedom are combined to particles). Again the circles and squares show the measured data and the dotted and dashed lines are the fits. The fitted values for the parallel part are $p_{H_2+H_2} = 0.97$ and $p_{H_5O_2^+-b} = 0.95$. These are the above-mentioned cases where the computation time of the SPF propagation is negligible. For these examples, MCTDH is very well parallelized. This is because the propagation of the A-vector and the computation of the mean fields generate

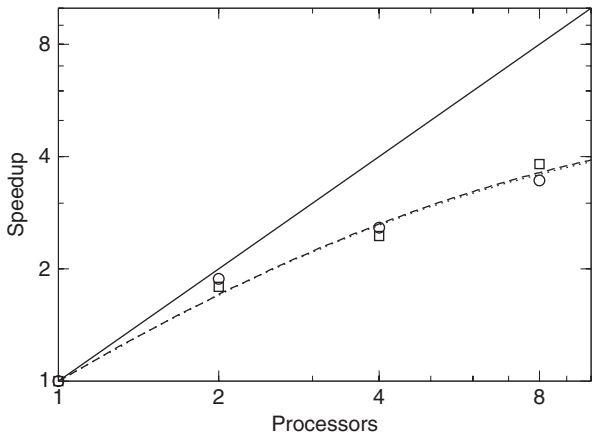

Fig. 2 Speedup behavior of the C_2H_4 (*circles*, *dotted line*, $p = 0.82$) and the $H_5O_2^+$-a (*squares*, *dashed line*, $p = 0.83$) calculations. The *circles* and *squares* are the measured values, the *dotted* and *dashed lines* are the fits to Amdahl's law and the *solid line* is the ideal (linear) speedup

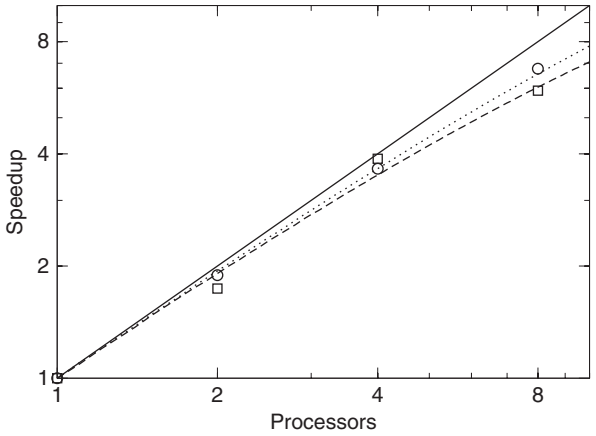

Fig. 3 Speedup behavior of the H_2+H_2 (*circles, dotted line*, $p = 0.97$) and the $H_5O_2^+$-b (*squares, dashed line*, $p = 0.95$) calculations. The *circles* and *squares* are the measured values, the *dotted* and *dashed lines* are the fits to Amdahl's law and the *solid line* is the ideal (linear) speedup

the major part of the computation time. The large number of Hamiltonian terms ensures an efficient parallelization. Here the SPF propagation takes only a small fraction of the total effort thus it is of less importance that this part parallelizes less efficiently.

7 Dynamics and Infrared Spectrum of the Zundel Cation

The infrared (IR) spectroscopy of the Zundel cation $H_5O_2^+$ has been the subject of much research effort during the last years, both from the experimental [14–18] and theoretical [1, 19, 17, 20–22, 12, 13] perspectives. A series of gas-phase measurements based on the messenger-atom technique were able to provide well-defined, clear spectra on the range between 800 and 4,000 cm^{-1}. The most intriguing feature of such spectra, a doublet feature at 1,000 cm^{-1}, could only be reproduced, assigned, and understood by full-dimensional (15D) quantum-dynamical calculations using the MCTDH method [1, 22, 12, 13] In these calculations a set of polyspherical coordinates had to be introduced in order to correctly account for the floppy, anharmonic motions of the cation, and the potential operator was constructed as a cut high-dimensional model representation (cut-HDMR), also known as n-mode representation, which was modified to take advantage of mode combination (for details on the operator set up see Ref. [12]). Careful analysis of such cumbersome simulations yielded, however, a physically appealing and intuitive picture of the nature of the doublet, which could be traced back to a Fermi resonance between the fundamental proton-transfer mode and a vibrational state related to the pyramidalization modes of the water molecules. In this vibrational mode one water molecule has H_3O^+ character (pyramidal), while the other one presents H_2O character (planar).

In this follow-up work on the Zundel cation we analyze the complicated middle spectral region between 800 and 2,000 cm^{-1}. All states in this spectral region are strongly coupled to the central proton motion along the oxygen–oxygen axis. We discuss the analysis strategy that has been applied to assign the nature of the spectral signatures and that can also be applied to label eigenstates of the system computed by *improved relaxation*. All reported calculations were performed in the Rechenzentrum-Karlsruhe using the Heidelberg MCTDH package [23] with the shared memory parallelization described in the previous sections.

7.1 Understanding the Nature of Vibrational Eigenstates and Spectral Lines

The MCTDH spectrum is obtained in the time-dependent picture by Fourier transformation of the autocorrelation of the dipole-operated initial state [24]:

$$I(E) = \frac{E}{6\,c\,\varepsilon_0\,\hbar^2} \int_{-\infty}^{\infty} \exp(i\,(E + E_0)\,t/\hbar) \langle \Psi_{\mu,0}| \exp(-i\,\hat{H}\,t/\hbar)|\Psi_{\mu,0}\rangle \;\; dt,$$

where E_0 is the ground-state energy and $|\Psi_{\mu,0}\rangle \equiv \hat{\mu}\,|\Psi_0\rangle$. It is here assumed that all spectral lines arise from transitions between the ground vibrational state $|\Psi_0\rangle$ and excited vibrational eigenstates of the adequate symmetry $|\Psi_n\rangle$. It is thus necessary to have some means of understanding the important features of the different vibrational states in terms of couplings, quanta of excitation in the harmonic limit, etc. This is the basic information needed to understand the IR spectrum computed with Eq. 10 and subsequently the internal dynamics of the system.

Wavefunctions of excited states converged by *improved relaxation* [25] contain all the possible information of that specific state. The intensity of a given excited state $|\Psi_n\rangle$ is readily obtained by computing the dipole moment $|\langle\Psi_n|\hat{\mu}|\Psi_0\rangle|^2$. But even if an excited state of interest $|\Psi_n\rangle$ has been obtained, it is difficult to directly inspect these mathematical objects due to their high dimensionality. Moreover, for the higher excited states we do not have $|\Psi_n\rangle$ at our disposal but only an autocorrelation function providing spectral lines. In both cases we characterize the eigenstates by their overlaps with carefully chosen test states, i.e., by the numbers $|\langle\Phi_{test}|\Psi_n\rangle|^2$. The following procedures are used:

1. Test states $|\Phi_{\text{test}}\rangle$ are generated

   a) By applying some operator $\hat{O}$ to a previously converged eigenfunction,

$$|\Phi_{\text{test}}\rangle = N\,\hat{O}|\Psi_n\rangle, \tag{10}$$

   where N is a normalization constant, e.g., $N\hat{z}|\Psi_0\rangle$ generates a test state which in essence differs from the ground state $|\Psi_0\rangle$ by a one quantum excitation in the proton-transfer coordinate z.

b) By forming Hartree products, where the SPFs are obtained through diagonalization of mode Hamiltonians $\hat{h}_j$. The $\hat{h}_j$ are low-dimensional Hamiltonians and each $\hat{h}_j$ operates on the space of a group of coordinates (see Paper I for details on coordinates grouping into particles). Rather than using single Hartree products one may use linear combinations of products in order to satisfy a symmetry constraint.

2. The overlaps $|\langle \Phi_{\text{test}}|\Psi_n\rangle|^2$ are then computed

a) By direct evaluation of the scalar product if $|\Psi_n\rangle$ is available.
b) By Fourier transform of the autocorrelation function $a(t) = \langle \Phi_{\text{test}}| \exp(-i\ H\ t)|\Phi_{\text{test}}\rangle$. The overlap is obtained via the formula [25]:

$$|\langle \Phi_{\text{test}}|\Psi_n\rangle|^2 = \frac{\pi}{2T} Re \int_0^T e^{i E_n t} a(t) \cos(\frac{\pi t}{2T}) dt. \tag{11}$$

Excitations related to test states will be denoted $(n_1\, q_1, n_2\, q_2 \ldots)$, where n_1 represents the quanta of excitation on coordinate q_1 (in a separable limit). A test state will be denoted by $|\Phi_{n_1\, q_1, n_2\, q_2 \ldots}\rangle$ where the terms with $n_j = 0$ are omitted. In case a test state has been generated such that it cannot be represented by this simple notation, it will be defined more explicitly.

7.2 Analysis of the Middle Spectral Region

The simulated spectrum in the range between 0 and 4,000 cm^{-1} is depicted in Fig. 4. The region below 700 cm^{-1} has not yet been accessed experimentally. We will center our analysis in the region between 800 and 2,000 cm^{-1} that contains lines related to global, highly coupled motions of the whole cation. The region between the proton-transfer doublet and the doublet centered at 1,800 cm^{-1} features couplings related to the [O-H-$O_{\|}$] and [O-$O_{\|}$] motions. The MCTDH spectrum reported in Fig. 4 presents three main absorptions in this range, located at 1,411, 1,741, and 1,898 cm^{-1}. We call the eigenstates producing these peaks $|\Psi_{m1}\rangle$, $|\Psi_{m2}\rangle$, and $|\Psi_{m3}\rangle$, respectively, where the *m* stands for middle spectral range.

Propagation of test states followed by Fourier analysis of their autocorrelation functions as described above was used to assign these peaks. The following test states were generated using eigenfunctions of low-dimensional Hamiltonians: $|\Phi_{1z,1R}\rangle$, $|\Phi_{1z,2R}\rangle$, $|\Phi_{bu}\rangle$. The test state $|\Phi_{bu}\rangle$ consists of the water bending with *ungerade* symmetry, i.e., it is characterized by $(|01\rangle - |10\rangle)/\sqrt{2}$ where the two entries indicate the quanta of bending motion of monomer A and B.

The overlaps $|\langle \Phi|\Psi\rangle|^2$, where $|\Phi\rangle$ is a test state and $|\Psi\rangle$ is an eigenstate, are given in Table 1. The analysis contemplates also the states of the doublet at 1,000 cm^{-1}, since these states are coupled to some extent to the ones in the middle spectral

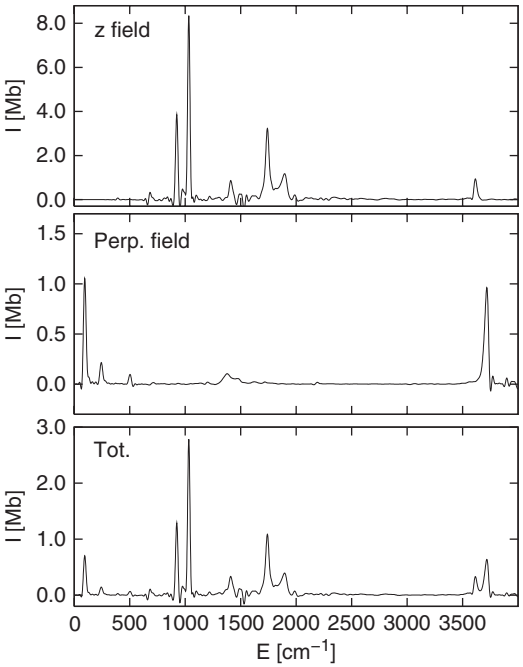

Fig. 4 Simulated MCTDH spectrum in the range between 0 and 4,000 cm^{-1}. Absorption is given in absolute scale in mega-barns (Mb)

region, e.g., the eigenstate $|\Psi_d^h\rangle$ has a squared overlap of 0.10 with the test state $|\Phi_{bu}\rangle$. All states in Table 1 are of B_2^+ symmetry.

State $|\Psi_{m1}\rangle$, absorbing at 1,411 cm^{-1} in the MCTDH spectrum, has a largest contribution from the $|\Phi_{1z,1R}\rangle$ test state. The experimental $H_5O_2^+ \cdot$Ne spectrum shows a weak absorption in this region, at about 1,470 cm^{-1}. We propose that this peak is the same peak observed at a similar frequency in the MCTDH spectrum, namely the state with the largest character of the combined excitation $(1z, 1R)$. A band appearing at 1,600 cm^{-1} in the MM/VCI spectrum [17] was assigned to the $(1z, 1R)$ transition. However, the experimental spectrum of $H_5O_2^+ \cdot$Ne shows no absorption at 1,600 cm^{-1} [17].

Table 1 Overlaps $|\langle\Phi|\Psi\rangle|^2$, where $|\Phi\rangle$ are test states and $|\Psi\rangle$ are eigenstates

Energy [cm^{-1}]	$\|\Psi_d^l\rangle$ 918	$\|\Psi_d^h\rangle$ 1033	$\|\Psi_{m1}\rangle$ 1411	$\|\Psi_{m2}\rangle$ 1741	$\|\Psi_{m3}\rangle$ 1898
$\langle\Phi_{1R,w_3}\|$	0.83	0.09	0.00	0.00	0.00
$\langle\Phi_{1z}\|$	0.10	0.46	0.04	0.10	0.04
$\langle\Phi_{1z,1R}\|$	0.00	0.00	0.44	0.06	0.01
$\langle\Phi_{bu}\|$	0.07	0.12	0.10	0.38	0.02
$\langle\Phi_{1z,2R}\|$	0.00	0.00	0.00	0.10	0.38

State $|\Psi_{m2}\rangle$, which is responsible for the absorption at 1,741 cm^{-1} in the MCTDH spectrum, has the largest contribution from the $|\Phi_{bu}\rangle$ test state. This peak is then mainly related to the *ungerade* water bending and has been already assigned in Ref. [17] and in a number of works. This peak can be assigned already from a standard normal modes analysis, since its main contribution is from an internal motion of the water monomers and less from the relative motions between them. However, it must not come as a surprise that the eigenstate $|\Psi_{m2}\rangle$ has a total squared overlap of 0.26 with the test states containing one quanta of excitation in the proton-transfer coordinate, namely $|\Phi_{1z}\rangle$, $|\Phi_{1z,1R}\rangle$, and $|\Phi_{1z,2R}\rangle$. In a fashion similar to the coupling to the w_3 wagging motion, as the proton approaches one water molecule, the equilibrium value of the H–O–H angle shifts to a larger value because this water molecule acquires more H_3O^+ character. Conversely, the water molecule at a larger distance of the central proton acquires H_2O character and the angle H–O–H shifts to lower values. The coupling between the proton-transfer and bending motions is rather strong. This coupling shifts the proton transfer line down and the bending line up by at least 120 cm^{-1}. This estimate was obtained by suppressing the correlation between proton transfer and bending by setting the number of SPFs to 1, for alternatively the proton transfer mode and the water modes. The frequency of the *ungerade* bending when decoupled from the proton-transfer motion resembles that of the bare-water bending mode. Thus the shift to a higher frequency is almost entirely due to coupling with the proton-transfer mode. In a similar fashion, the proton-transfer absorption appears at a lower frequency than would be expected from low-dimensional models which neglect the coupling to the water molecules [26]. This emphasizes again the need of a full-dimensional treatment.

State $|\Psi_{m3}\rangle$ is responsible for the absorption at 1,898 cm^{-1} in the MCTDH spectrum, which is the low-intensity feature of the broad double peak centered at about 1,800 cm^{-1}. This state has the largest overlap with the $|\Phi_{1z,2R}\rangle$ test state. Comparison in position and intensity of this peak to the corresponding one in the experimental $H_5O_2^+ \cdot Ne$ spectrum suggests that the latter is mainly related to the $(1z, 2R)$ excitation.

Analysis of the values in Table 1 shows that the eigenstates in the region 1,400–1,900 cm^{-1} are characterized by the asymmetric bending and combinations of the proton-transfer fundamental and water–water-stretch fundamental and first overtone, with important couplings between them. Such a coupling was already noted by Bowman and collaborators by analyzing the CI coefficients of their MM/VCI expansion [17]. However, the exact nature of each band could not be disentangled, and it was concluded that this "is indicative of large couplings among various zero-order states in this region." We show that, despite such couplings exist and play an important role in shaping the spectrum, the different eigenstates involved retain each its particular character (note that the largest numbers in Table 1 appear at the diagonal) and can be assigned to well-defined transitions.

8 Conclusions

The existing serial Heidelberg MCTDH code has been further extended to make use of parallel shared memory hardware. In this work a scheduler–worker parallelization scheme was developed and applied. Now the three main tasks of the MCTDH propagation algorithm, the propagation of the A-vector, the propagation of the SPFs, and the computation of the mean fields, are parallel. The resulting code was tested on benchmarks systems to determine the efficiency of the parallelization. It turned out that for special cases where the propagation of the SPF is negligible, the code is well parallelized. In the general case the problem arises that the parallelized routines for the SPF propagation contain – usually short – loops over the SPFs which makes the parallelization less efficient. In both cases – loops over SPFs and over Hamiltonian terms – the parallelization works better if the larger is the size of the loops. The degree of parallelization lies between $p = 0.82$ (worst case tested) and $p = 0.97$ (best case tested) leading to speedups between 3 and 7 when running on 8 processors. Hence the parallelization of the wavepacket propagation of MCTDH can be seen as a success.

The described development improved the MCTDH code essentially. However, the present implementation is restricted to shared memory hardware. The number of processors combined in parallel shared memory machines is still growing but at a lower rate than the number of processors in the distributed memory computing clusters. Hence it is an important task to use the experience of the shared memory parallelization of MCTDH to develop a parallel code for distributed memory machines. This, however, requires a severe re-structuring of the existing code.

Simulations of the IR spectrum of the Zundel cation in full dimensionality (15D) were reported. These simulations represent an update with respect to the simulations reported in [1]. In particular we dealt with the spectral region between 800 and 2,000 cm^{-1}, which is dominated by strong couplings of various large amplitude motions to the proton-transfer fundamental. A strategy to analyze the nature of the eigenstates of the system was discussed and applied. The recent advances in the parallelization of the MCTDH code played a fundamental role in the success of the simulations. Future directions of this work include the simulation of the isotopically substituted forms of the Zundel cation for which recently their IR spectra were measured.

Acknowledgments The authors thank Prof. J. Bowman for providing the potential energy routine, F. Gatti for deriving the kinetic energy operator, D. Lauvergnat for performing the TNUM calculations, and the Scientific Supercomputing Center Karlsruhe for generously providing computer time. M.B. thanks the International Graduiertenkolleg IGK 710 “Complex Processes: Modelling, Simulation and Optimization” for a fellowship. M.B. and H.D.M. thank Prof. P. Bastian for helpful discussions on the parallelization of the code. O.V. is grateful to European Commission for financial support through the Marie Curie (FP6) program.

References

1. M. Brill, O. Vendrell, F. Gatti, H.-D. Meyer, in *High Performance Computing in Science and Engineering 07*, eds. by W.E. Nagel, D.B. Kröner, M. Resch (Springer, Heidelberg, 2008), pp. 141–156
2. C. Meier, U. Manthe, J. Chem. Phys. **115**, 5477 (2001)
3. J. Caillat, J. Zanghellini, A. Scrinzi, AURORA Technical Reports **19**, 1 (2004)
4. H.-D. Meyer, U. Manthe, L.S. Cederbaum, Chem. Phys. Lett. **165**, 73 (1990)
5. U. Manthe, H.-D. Meyer, L.S. Cederbaum, J. Chem. Phys. **97**, 3199 (1992)
6. M.H. Beck, A. Jäckle, G.A. Worth, H.-D. Meyer, Phys. Rep **324**, 1 (2000)
7. H.-D. Meyer, G.A. Worth, Theor. Chem. Acc. **109**, 251 (2003)
8. M.H. Beck, H.-D. Meyer, Z. Phys. D **42**, 113 (1997)
9. F. Otto, F. Gatti, H.-D. Meyer, J. Chem. Phys. **128**, 064305 (2008)
10. A.N. Panda, F. Otto, F. Gatti, H.-D. Meyer, J. Chem. Phys. **127**, 114310 (2007)
11. M.R. Brill, F. Gatti, D. Lauvergnat, H.-D. Meyer, Chem. Phys. **338**, 186 (2007)
12. O. Vendrell, F. Gatti, D. Lauvergnat, H.-D. Meyer, J. Chem. Phys. **127**, 184302 (2007)
13. O. Vendrell, F. Gatti, H.-D. Meyer, J. Chem. Phys. **127**, 184303 (2007)
14. K.R. Asmis et al., Science **299**, 1375 (2003)
15. T.D. Fridgen et al., J. Phys. Chem. A **108**, 9008 (2004)
16. J.M. Headrick et al., Science **308**, 1765 (2005)
17. N.I. Hammer et al., J. Chem. Phys. **122**, 244301 (2005)
18. L. McCunn, J. Roscioli, M. Johnson, A. McCoy, J. Phys. Chem. B **112**, 321 (2008)
19. J. Dai et al., J. Chem. Phys. **119**, 6571 (2003)
20. X. Huang, B.J. Braams, J.M. Bowman, J. Chem. Phys. **122**, 044308 (2005)
21. A.B. McCoy et al., J. Chem. Phys. **122**, 061101 (2005)
22. O. Vendrell, F. Gatti, H.-D. Meyer, Angew. Chem. Int. Ed. **46**, 6918 (2007)
23. G.A. Worth, M.H. Beck, A. Jäckle, H.-D. Meyer, The MCTDH Package, Version 8.2 (2000) H.-D. Meyer, Version 8.3 (2002), Version 8.4 (2007); see http://mctdh.uni-hd.de/
24. G.G. Balint-Kurti, R.N. Dixon, C.C. Marston, J. Chem. Soc., Faraday Trans. **86**, 1741 (1990)
25. H.-D. Meyer, F. Le Quéré, C. Léonard, F. Gatti, Chem. Phys. **329**, 179 (2006)
26. M.V. Vener, O. Kühn, J. Sauer, J. Chem. Phys. **114**, 240 (2001)

Structural Properties and Torsional Dynamics of Peroxides and Persulfides

Glauciete S. Maciel, Ana Carla P. Bitencourt, Mirco Ragni, Gaia Grossi, and Vincenzo Aquilanti

Abstract For the study of molecules containing O—O and S—S bonds, an analysis on the effect of level of theory and basis sets on electronic properties and geometrical parameters for H_2O_2 and H_2S_2 was done. Substitutions of one or both hydrogens in these molecules either by halogen atoms or alkyl groups were investigated for properties like geometries, dipole moments, *cis* and *trans* barriers. Attention has also been dedicated to the study of energy levels in the very anharmonic torsional potentials, obtaining their distributions as a function of temperature and partition functions for the torsional motion, of relevance for the isomerization rate leading to exchange between chiral enantiomers. Estimated rates both for underbarrier tunnelling and overbarrier transitions are consistently smaller for the S—S cases with respect to the corresponding O—O ones, due to the generally higher barriers. Regarding intermolecular interactions, of specific importance for collisional chirality exchange, an exploration was done for both H_2O_2– and H_2S_2–rare gases systems, extending the joint experimental and theoretical approach already tackled in this laboratory for interactions of H_2O and H_2S with the rare gases.

V. Aquilanti (✉)
Dipartimento di Chimica, Università degli Studi di Perugia, Perugia 06123, Italy,
e-mail: aquila@dyn.unipg.it

G.S. Maciel
Dipartimento di Chimica, Università degli Studi di Perugia, Perugia 06123, Italy,
e-mail: ciete@dyn.unipg.it

A.C.P. Bitencourt
Dipartimento di Chimica, Università degli Studi di Perugia, Perugia 06123, Italy,
e-mail: carla@dyn.unipg.it

M. Ragni
Dipartimento di Chimica, Università degli Studi di Perugia, Perugia 06123, Italy,
e-mail: mirko@dyn.unipg.it

G. Grossi
Dipartimento di Chimica, Università degli Studi di Perugia, Perugia 06123, Italy,
e-mail: gaia@dyn.unipg.it

P. Piecuch et al. (eds.), *Advances in the Theory of Atomic and Molecular Systems*,
Progress in Theoretical Chemistry and Physics 20, DOI 10.1007/978-90-481-2985-0_5,

Keywords: Geometries · Energy profiles · Barriers heights · Peroxides · Persulfides · Torsional energy levels · Temperature distributions · Chirality exchange rates · Intermolecular interactions

1 Introduction

For the series of molecules considered here, theoretical approaches to their structure and to their dynamics (both intramolecular and intermolecular) are usually motivated both by their interesting floppy nature and also by reference to applications. Indeed several investigations have been dedicated in the recent years towards the understanding and control of the reactions involved in phenomena of strong environmental impact such as acid deposition and decrease of the ozone shell [1, 2]. In both processes the participation of peroxides and of the corresponding radicals has been observed [3]. The relevant experimental and theoretical information on these compounds are accordingly very large. In this laboratory, starting from Ref. [4], a systematic and detailed analysis on the effect of the choice of both theory level and basis set has been carried out for hydrogen peroxide with respect to the determination of equilibrium geometry, dipole moment, *cis* and *trans* barriers and has been continued studying the effect of substituents for the hydrogen atoms.

Persulfides also have been investigated with increasing interest, due to their importance in biochemistry and in atmospheric processes [5–8]. The biological activity of several molecules, like proteins, enzymes and antibiotics, is characterized by the presence of the persulfide linkage. A number of experimental [9–13] and theoretical studies [14–27] of the structural and energetic aspects of some persulfide molecules have been performed and provide useful information on the electronic mechanism involved in the S—S bond cleavage.

This work is an account of our recent work on the title systems. It started by focusing on the properties of the simplest example of a chiral molecule, H_2O_2 [4]. Structural and energetic properties were studied by quantum mechanical methods for this molecule, with the purpose of elucidating the features of the internal modes, and in particular the torsion around the O—O bond which leads to the chirality changing isomerizations. The pictures in terms of stretching, bending and torsion modes based both on the usual valence type description of the molecule and on orthogonal local vectors have been compared and the greater accuracy of the latter has been demonstrated [4].

The next section gives an account also of subsequent research where the structural effects of the substitution of hydrogen peroxides by halogens have been considered. We have performed [28] a systematic study by quantum mechanical methods of a series of XOOX' molecules, corresponding to substitutions of one or both hydrogens by halogen atoms (X) in HOOH'. The *cis* and *trans* barriers appear to vary remarkably upon substitution. They have been compared with experimental and theoretical information, when available. In addition, we have analyzed and similarly compared also the effects of alkyl substitutions (ROOR') [29]. The following

presentation reports also corresponding work carried out regarding the analogous compounds containing the S—S bond and includes some remarks related to dipole moments.

Section 3 outlines, for this class of systems, the energy profiles along the dihedral angles, of relevance for the torsional mode around —OO— and —SS— bonds. In view of the interest for statistical approaches to equilibrium properties and to rates of processes where torsional anharmonicity is relevant, as required for recent atmospheric modelling studies and also for prototypical chiral separation experiments, and in view of a possible dynamic mechanism for chirality exchange by molecular collisions [29, 30], in subsequent work we have calculated level distributions and partition functions for the torsional mode around the O—O and S—S bonds for a series of derivatives of hydrogen peroxide [30] and hydrogen persulfide [31], respectively, for which we had previously determined potential energy profiles along the dihedral angles [4, 28–31]. These topics are covered in Sect. 4. Specifically for the hydrogen peroxide system, we have used two procedures for the reduction of the kinetic energy operator and the calculated partition functions were compared with previous work. Partition functions for the torsional mode are evaluated both by direct quantum levels state sum and by a hierarchy of semi-classical and classical approximations. It has been shown that among the tested semi-classical approaches which applied to the torsional mode greatly improve the classical approximations [30, 31], remarkable improvement is obtained by the explicit introduction of the dependence of the moment of inertia from the torsional angle. These results permit one to discuss the characteristic time for chirality changes for the investigated molecules, either by quantum mechanical tunnelling (dominating at low temperature) or by transition state theory (expected to provide an estimate of racemization rates in the high energy limit) [30, 31].

Further considerations follow regarding also information on intermolecular interactions [32–34], having specific implications for theoretical and possibly experimental studies of molecular dynamics of collisional-induced chirality changing processes [35, 36].

Being focused on our own recent work, the present account makes no full justice of the vast literature existing on the subject. The reported results are put into the context of current and prospective research in the final section.

2 Structural and Energetic Aspects of Peroxides and Persulfides

2.1 XOOX' and ROOR' Molecules

An extensive systematic study, described in a previous paper [4], has been performed on the choice of method and basis set for hydrogen peroxide. It was found that the results obtained by the B3LYP density functional method using 6-311++G (3df, 3pd) basis set and by the CCSD(T)//aug-cc-pVTZ method gave both consistent geometric parameters and concordance with experimental data. Also the important

available experimental features for stereomutation, such as the height of the *trans* barrier, were accurately reproduced, justifying the use of this method and basis set (B3LYP//6-31G++3df, 3pd) for the systematic investigation of alkyl substitution. All calculations have been executed by the Gaussian package [37].

We have collected DFT results for the equilibrium geometrical parameters and dipole moments for a series of substituents of the hydrogen and also extensions to the persulfides, to be accounted for below. Our calculated coupled cluster results were also reported in the cited references, together with other data from the literature, and shown to permit comparison and assessment. The most relevant geometrical parameter of interest for us for peroxides is the dihedral angle in the equilibrium configuration. Its determination has suffered a long and controversial history: explicitly, discrepancies have regarded both experimental data and theoretical values, as documented for hydrogen peroxide [4] and dimethyl peroxide [38], consequently leading to uncertainties also in a property such as the dipole moment.

Let us focus now on alkyl substitution [29]. In detail, regarding bond angles, OOH shows larger sensitivity to variations of conformal configurations than to the changes in the alkyl substituent. For all compounds this angle is close to 100° in the equilibrium structure, similarly to hydrogen peroxide, and variations are negligible in the *trans* forms. An increase by 5° or 6° is observed when hydrogen peroxide and its alkyl monosubstituted compounds are in the *cis* configurations. This increase roughly doubles for double substitution. The dihedral angle for H_2O_2 had been discussed previously [4] and assessed at around 112°, also in general agreement with a large body of experimental and theoretical evidence. The OH bond length is practically invariant (between 0.965 and 0.968 Å) both as the alkyl substituent varies and as a function of torsion angle. For the OC bond the largest fluctuation was observed (0.05 Å) for the dimethyl peroxide and the *tert*-butyl hydroperoxide. It is necessary to note that in the comparison between CCSD [29] and B3LYP data, the first set presents consistently larger lengths for the peroxidic bond by 0.01–0.03 Å.

The behaviour of bond lengths with halogen substitution and with configuration can be presumed by inspection of data in Ref. [28]. The constancy of the OH bond length, 0.97 Å, for almost all systems is remarkable. For CN substitution, it is 0.04 Å larger. However, the O—O length shortens to 1.42, 1.41 and 1.36 Å for monosubstitution by NO, Cl and F, respectively, at the equilibrium configuration, for which still greater is the shrink for double substitution (1.36 Å for ClOOCl, 1.34 Å for FOONO, 1.28 Å for FOOCl and 1.22 Å for FOOF: the latter value is similar to that of in O_2). There appears to be a qualitative correlation between the energy profile and the lengths of the O—O bond and those of the OX bond, where X is Cl or F, as a function of the dihedral angle. The case of ClOOF exhibits an example of the shortening at equilibrium of the O—O bond, accompanied by lengthening of the O—F and O—Cl bonds [15, 28]. As far as bond angles are concerned, in the case of alkyl substitution, the effect on the OOH angle of hydrogen peroxide has been found to be negligible, and for halogens, CN and NO substitution is also small, fluctuations being of the order of 3° for monosubstitution, the OOR angles increase with respect to the OOH in hydrogen peroxide by 5–6° in most cases, similar to what is observed in the alkyl cases [29]. This increase is somewhat smaller for substitution of one of

the hydrogens by F. The OON angles show values around 104° both in HOONO and in FOONO. Regarding the angle OOF, that in the FOONO case is practically the same as in HOOF and increases by 2° and 3° in the equilibrium configurations obtained for substitution of H by Cl and F, respectively. Likewise, the OOCl angle increases slightly (1° or 2°) by insertion of a second electronegative atom.

Our results for *cis* and *trans* barrier heights confirm deficiencies of previous analysis of available experimental data and will form part of our discussion in a later section.

2.2 RSSR' and XSSX' Molecules

The persulfide compounds are characterized by a *gauche* conformation around the S—S bond, which means that the dihedral HSSH angle is approximately 90° [8, 31, 33]. The formed bond properties are mainly accounted by the *p*-character of the nonbonding electrons, which occupy mutually perpendicular *p* orbitals over each sulphur atom. The extension of these orbitals leads to superposition in the molecular orbitals. A lone pair–lone pair repulsion, inherently caused by the formation of and molecular orbitals, results in the destabilization and consequently in stretching of the S—S bond, which is maximal on *cis* and *trans* geometries, 0° and 180°, respectively, and so the destabilization is minimal on 90° and 270° because of the orthogonality of the two 3*p* orbitals. For all theoretical levels and basis sets, the HSS bond angle is 98°. These values are in good agreement with the experimental ones reported in Refs. [8, 40–43], and in contrast with that of Winnewisser et al. that underestimated the HSS angles at around 91° [43]. Generally these data are assessed on the basis that the microwave-derived geometries rely on the uncertainty of the value of the HSS angle, which serves as reference. In fact, the localization of hydrogen atoms in the presence of heavy atoms is often problematic by diffraction techniques. Since the bond lengths derived from rotational constants are interrelated with the bond angles, an erroneous determination of the latter will affect other parameters. The torsional angles are weakly correlated with other geometrical parameters and appear internally consistent [8, 44].

Preliminary studies have shown us that the inclusion of polarization functions is crucial for the accurate determination of geometrical parameters [8]. For example, the use of Pople basis sets of the type 6-311++G overestimates the —SS— bond length by 0.2 Å, and the dihedral angle by 3°, with accompanying variation of dipole moment. Larger basis sets such as 6-311++G (2df, 2pd) yield comparable results both with the experimental values and with those by Dunning-type basis sets.

Regarding specific features of molecular orbitals for H_2S_2 in the equilibrium geometry, a maximal stabilization arises because of the overlap which occurs between each pair of free electrons with the adjacent molecular orbital of σ* type of HS. Two electronically degenerate conformations are possible and they are antipodal with respect to the S—S bond. The rotational barriers around the SS bonds depend on the dihedral angle according to similar consideration regarding

the molecular orbitals. Although there are variations in the measured and calculated barriers with different methodologies [8], the *cis* barriers are consistently larger than the *trans* ones.

The geometrical parameters of the transitional *cis* and *trans* structures indicate a distortion of the equilibrium geometry. For MP2(FU)/aug-cc-pVTZ results [33], the calculated values of the S—S bond lengths appear larger by 0.043–0.052 Å when compared with the equilibrium length (2.059 Å), and the angles HSS appear smaller by 1.6° and 5.3°, for *trans* and *cis* geometries, respectively. For all methods, the HS bond length appears not to vary appreciably with the geometry, ranging from 1.33 to 1.37 Å, around an average of 1.35 Å. Regarding the SS bond length, there is a stretching, moving from the equilibrium to the *cis* and *trans* geometries by 0.05 Å on the average. The HSS angles are reduced by 2° and 6°, for *trans* and *cis* geometries, in comparison with the equilibrium structure. The effect of the basis sets is to reduce bond lengths and dipole moment when we used triple and quadruple zetas. The inclusion of diffuse functions has little effect on the geometrical parameters but is important to determine the dipole moments.

The geometrical parameters of the persulfides are substantially influenced by the presence of electronegative atoms [31]. In both theoretical and experimental data, we found that for the molecules with single and double halogen substitutions (HSSF, HSSCl, FSSF and ClSSCl), the S—S bond lengths decrease for increasing electronegativity of the substituent, whereas the S—F and S—Cl bond lengths increase. An exception is observed for ClSSF, in which the S—S bond length is 0.01 Å larger than in the HSSH molecule. The decreases in the SS bond lengths correspond to increases in RS bond lengths, the effects being much larger for SS than for RS. In general, for the F—S bond, the increase is 0.30 Å, whereas for S—Cl, it is 0.71 Å. For all persulfide compounds, the dihedral angles are 2–4° lower than HSSH, and SSR bond angles increase by 3–7° for monohalopersulfides and by 8–10° for dihalopersulfides. In the alkyl persulfides, a variation of the SSR angle is very small as the substituent group size increases (∼0.6°) and similarly is small for the passage from single to double substitution.

The relative stabilities as well as isomerizations between ASSA' and A2S = S (A = H, F, Cl and alkyl) have received some interest but still need further investigation (see Ref. [8] and references therein). Here, we have limited our study to ASSA' structures.

2.3 Cis *and* Trans *Barriers*

The sensitivity to substitution of the values for barrier heights can be seen from data in Table 1 and Figs. 1, 2 and 3, where comparison is also made with the analogous cases for substitutions in peroxides [28, 29] and persulfides [31, 33]. The first observation that emerges from the Table is the difference between the values of the barrier heights for the two series of compounds. Regarding persulfides, *cis* and *trans* barriers are practically symmetrical for all compounds, while for peroxides it

Table 1 *Cis* and *trans* barriers (cm^{-1}) for a series of peroxides and persulfides at the B3LYP/6-311++G (3*df*, 3*pd*) level[a]

Peroxides	*Cis*	*Trans*	Persulfides	*Cis*	*Trans*
HOOH	2575.5	386.3	HSSH	2764.4	2009.9
HOOF	3338.7	3542.2	HSSF	5562.3	5131.2
HOOCl	2317.8	1617.8	HSSCl	4481.5	3929.5
ClOOCl	3523.7	2166.8	ClSSCl	7969.3	6218.3
ClOOF	6037.5	4718.4	ClSSF	9617.5	8252.5
FOOF	9728.5	8304.0	FSSF	12144.5	10923.0
$HOOCH_3$	2080.0	151.9	$HSSCH_3$	2881.4	2107.5
$HOOC_2H_5$	2270.6	236.5	$HSSC_2H_5$	3030.0	2248.7
CH_3OOCH_3[b]	3904.4	0.0	CH_3SSCH_3	4008.2	2094.0
C_2H_5 OO C_2H_5[b]	4365.7	0.0	$C_2H_5SSC_2H_5$[c]	–	2451.8

[a] For details, see text and references therein, where other methods and basis sets are also compared.
[b] These two systems have a minimum (equilibrium geometry) at 180° dihedral angles (*trans* configuration).
[c] *Cis* barrier not computed.

is possible to see that the heights of *cis* and *trans* barriers vary appreciably with the nature of the substituent: they generally increase with the electronegativity of the substituent group.

This increase in the barriers in the *trans* geometry for persulfides has to be ascribed to the higher lone pair–lone pair repulsion in the 3*p* diffuse orbitals of sulfur with respect to the oxygen case [8]. For H_2S_2, we also note a smaller dipole–dipole and atom–atom interactions, and a decrease in SH bond polarity with respect to OH. This difference between *trans* barriers had also been interpreted in terms of hyperconjugation [50, 51]. The 90° dihedral angle of H_2S_2 reflects the pure

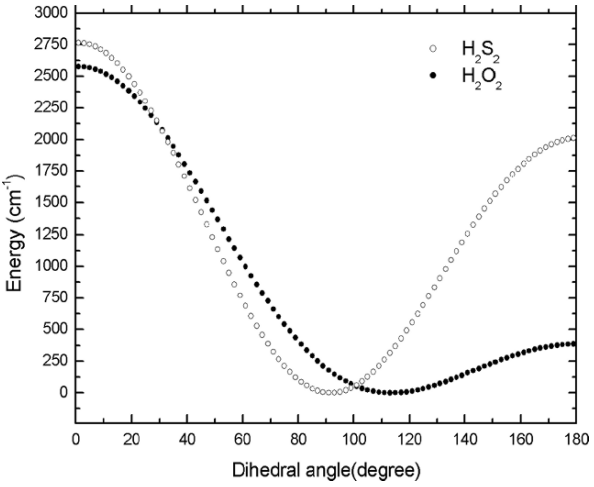

Fig. 1 Energy profiles as functions of dihedral angle for H_2O_2 and H_2S_2 molecules, calculated by the MP2(FU)//aug-cc-pVTZ method. Based in part and adapted from Refs. [4, 33]

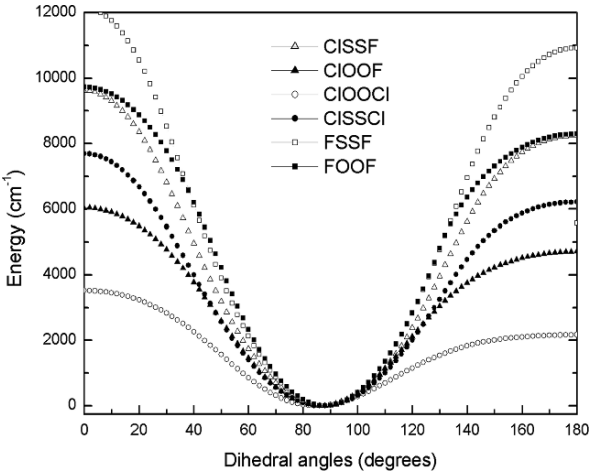

Fig. 2 Energy profiles as functions of dihedral angle for XOOX' and XSSX' molecules, calculated by the B3LYP//6-31++G (3*df*, 3*pd*) method. Based in part and adapted from Refs. [28, 31]

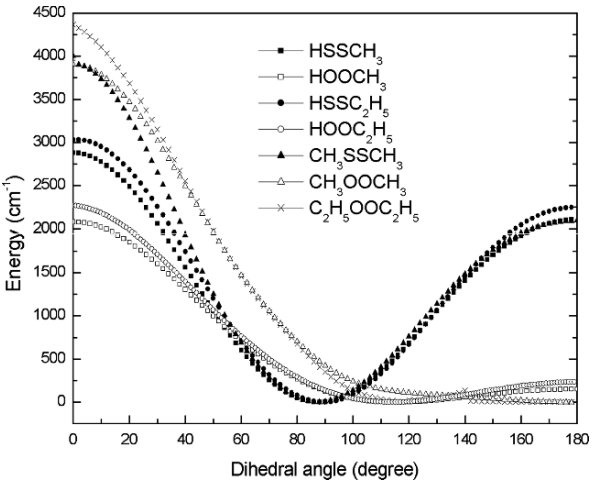

Fig. 3 Energy profiles as function of dihedral angle for ROOR' and RSSR' molecules, calculated by the B3LYP//6-31++G (3*df*, 3*pd*) method. Based in part and adapted from Refs. [29, 31]

character of *p* orbitals of sulfur, as well as the low electronegativity difference between H and S, which allows for partial S—S double bonding at the expense of some H—S bonding. This has to be contrasted with H_2O_2. Another possibility is the participation of 3*d* orbitals [8].

Regarding the employed basis sets, for H_2S_2, the use of the smallest of the series of correlation consistent basis sets developed by Dunning, the cc-pVDZ, produced unsatisfactory results for the *trans* barriers independently of the utilized level of theory [33]. A maximum deviation of 230 cm^{-1} for this molecule was observed

with this basis set with the coupled cluster method. The expansion of the series up to triple and quadruple zetas leads to an increase of both the *cis* and *trans* barrier heights, but is not sufficient to improve the quality of results [33].

The comparison among several theory levels shows that, for H_2S_2, the B3LYP and CCSD(T) methods underestimate barrier heights and mutually agree, independently of the Dunning basis sets used. The B3PW91 method produced, with all basis sets, *cis* barrier heights in agreement with experiment, while only the aug-cc-pVTZ basis set leads to acceptable results for *trans* barriers. The better set of results was observed for MP2, including all electrons [33]. For all aug-cc-pVXZ basis sets, good agreement was found for both *cis* and *trans* barriers, while only the cc-pVTZ basis set reproduces satisfactorily the *trans* barriers. In this case, particularly appropriate was the use of a triple zeta function. So, the aug-cc-pVTZ basis set was chosen for the study of interactions with rare gases [33], to be accounted for in a later section. It has to be noted that by the B3LYP/6-311++G (3df, 3pd) methodology the *cis* and *trans* barrier heights are 2764 and 2009 cm^{-1}, respectively, which in this case are better than when we used Dunning basis sets. On the effects of Pople and Dunning basis sets, see Ref. [44]. Note that what appears as the "best" results do not always come from what are objectively our best calculations, presumably because of some fortuitous cancellation of errors. This procedure is of course based on the assumption, to be checked in each case, that experimental data are sufficiently reliable.

Table 1 and Fig. 2 show that the presence of a single halogen atom practically doubles the *cis* barrier height with respect to that of HSSH. Further substitution by another halogen has a similar effect. As can be seen that the mono- and disubstituted chloro compounds present lower barriers than do their fluoro analogues, both for peroxides and for persulfides. Those of the latter are consistently several times higher than those of the former. In all cases except HOOF [28], *trans* barriers are lower than *cis* ones so that racemization is expected to proceed essentially via a route involving the *trans* barrier. Existing experimental information for peroxides is discussed in Refs. [4] and [28–30] and is not available for several persulfides.

The increase in the calculated barriers for FSSF, accompanied by the shortening of the S—S bond [31], has been attributed to the two hyperconjugated interactions between the lone pair of $3p$ free electrons for each sulfur atom.

2.4 Interlude on Dipole Moments

A large discrepancy was observed between the experimental and calculated dipole moments for H_2O_2 [4]. So, it was considered interesting to examine the correlation between the dihedral angle and the dipole moment. For this quantity there are conflicting experimental values in the literature, obtained with different methodologies, the more recent one being 1.573 ± 0.016 D [45, 46]. To explain the large discrepancy which is observed between the experimental and calculated dipole moments, it is interesting to consider the correlation between the dihedral angle and the dipole

moment. We performed calculations for structures corresponding to the variation of the dihedral angle range of interest for the characterization of equilibrium configuration. The results obtained show a decrease in the dipole moment by 0.02 D as the dihedral angle increases by 1° [4]. So a decrease by 8° of the computed dihedral angle with respect to the experimental one would correspond to a difference by 0.16 D between experimental and computed structures.

In detail, the relationship between dihedral angle and dipole moments suggests how to explain the discrepancies. In the calculations the molecule is considered as frozen in the vacuum while in the measurements in the gaseous state an ensemble of torsional levels and the corresponding distribution of dihedral angles must be considered. For a related discussion, see [47, 48]. This would lead to averaged distributions more probably towards the *trans* rather than the *cis* configuration, so that dynamically one observes an effective larger dihedral angle and thus a lower dipole moment, lower than that corresponding to the calculated equilibrium structure. Using the fact that, as discussed in the next section, we have computed the wavefunctions for the torsional states populated up to room temperature, it becomes possible to compute the dipole moment of hydrogen peroxide as a function of temperature by averaging the calculated dipole moment-dependent torsional angle over the square of wavefunction and over the torsional level distribution [29], reconciling theory and experiment data from the literature.

A similar discussion can be carried out for hydrogen persulfide. The origin of experimental information for this and related molecules is summarized in Ref. [8]. Also in this case it has to be considered the fact that in the calculations, the molecule is considered to be frozen in the vacuum, while in the measurements, it is in the gaseous state in an ensemble of torsional levels, and the corresponding distribution of dihedral angles must be taken into account. This would lead to averaged distributions more probably towards the *trans* rather than the *cis* configuration. It is also reported below how the torsional modes of the S—S bond are affected by substituent groups of the hydrogens in H_2S_2. This is of relevance for stereomutation issues [31].

Regarding intermolecular interactions, of specific importance for collisional chirality exchange, a study has been completed on the H_2O_2–rare gas systems, for which information should also come from molecular beam experiments in our laboratory. This will extend to these systems the joint experimental and theoretical approach already tackled for interactions of H_2O and H_2S with the rare gases. Attention has also been dedicated in this work to a study of energy levels in the very anharmonic torsional potentials, obtaining their distributions as a function of temperature. This has been shown to be of relevance for the comparison of calculated and experimental quantities other than dipole moments but can be straightforwardly extended to prospective estimates of torsional partition functions configuration, so that dynamically one may observe an effective larger dihedral angle and thus a dipole moment, lower than that corresponding to the calculated equilibrium structure. Using the fact that we can compute the wavefunctions for the torsional states populated as a function of temperature, it is possible to compute also the effective dipole moment by averaging the calculated dipole moment dependence from the

torsional angle over the square of the wavefunction and over the torsional level distribution. In the case of H_2O_2, we have just documented (see above) that this led to reconciling theoretical and experimental results.

The results on torsional levels [30] and the temperature dependence of their distribution for FOOF served for the calculation of the effective dipole moment as a function of temperature following the same steps outlined previously for hydrogen peroxide [29]. Such a dependence is weak in this case and does not improve the agreement with experiment: in fact, our DFT value for the room temperature dipole moments, accounting for the relative population of the torsional levels, is 1.32 D, to be compared with the accepted experimental value of 1.44 D [49]. Note, however, that probably the most accurate CCSD(T) values are consistently higher. Similar results for the other cases are available, but for them, there appear to be no experimental data for comparison. We reported in the cited references the variation of dipole moments as a function of the dihedral angle for both H_2O_2 [4] and H_2S_2 [33], and it is possible to see that the smaller is the dihedral angle the larger is the dipole moment for both systems. However, in H_2O_2 for the *cis* geometry, the dipole moment is almost double than that of H_2S_2. As explained earlier, the electronegativity difference between oxygen and sulfur justifies this behaviour. Dependence on the basis set in general decreases with the increase of the basis. The behaviour is similar for different theory levels, leading for both MP2(FU) and CCSD(T) to an overestimate with respect to experimental information while DFT produces better agreement. Possibly an analysis in terms of torsional wavefunction displacements, similar to the one discussed in the hydrogen peroxide case, may lead to a more accurate description in this case also.

3 Torsional Modes

3.1 Energy Profiles

Figure 1 shows the energetic profile for torsion around —OO— and —SS— bonds for the simplest molecules for each series, H_2O_2 and H_2S_2, for peroxides and persulfides, respectively. The most important observation regards the much higher value for the *trans* barrier in the H_2S_2 case, while the height of the *cis* barriers is comparable in both cases.

Figure 2 shows energy profiles along the dihedral angles for substitution of one or two of the hydrogens in HOOH and HSSH by halogen atoms [28, 31]. Taking the case of hydrogen peroxide as a reference for comparison, the *trans* barriers for Cl and F substitution are progressively higher in this order. For all monosubstituted systems, except HOOF, the *cis* barriers are lower than hydrogen peroxide. For halogen substitution, the *cis* and *trans* barriers are of similar height, so that the energy profile looks reasonably symmetric. Regarding peroxides with double substitutions by halogens, both *cis* and *trans* barriers appear to increase consistently, the effect of

F being larger than that of Cl, as just observed in the case of single substitution. The *cis* and *trans* barriers turn out to be of similar magnitudes in these cases. Equilibrium dihedral angles are only slightly less than 90° [28]. For ClOOCl, the literature is also ample, and Quack and Willeke [52] report a state-of-the-art computational study with detailed reference to both previous theory and experimental data. With respect to geometries of equilibrium and *cis* and *trans* configurations, our results agree with theirs. They also discuss torsional dynamics, with particular reference to parity violation in tunnelling switching stereomutation.

Regarding the NO substitution on peroxidic bonds, see Ref. [28] and [53–58]. Our interest is in the behaviour with respect to torsion around the O—O bond, and the designations as *cis* or *trans* refer to the HOON dihedral angle, while the OONO dihedral angle is 180° in all our structures (*trans* configurations). Reference [59] gives an extensive account of the*cis* configurations for the OONO dihedral angle. The chosen orientation of the NO group is the one expected to show minimal influence of the O atom on the peroxide bond under focus here. The same choice was made for CN substitution [28].

Comparison of the results obtained for hydrogen persulfide and for its alkyl derivatives suggests that inclusion of the alkyl groups increases in a significant way the *cis* barrier heights only for double substitution, as for CH_3SSCH_3. The other compounds of the series appear not to have large enough "volume" to influence the barrier heights. It is interesting to note that in the corresponding ROOR′ systems [29], even a single methyl or ethyl group substitution leads to the lowering of both barriers with respect to hydrogen peroxide, and double substitution gives rise to an increase of the*cis* barriers and disappearance of the *trans* barriers. In view of the higher S—S distances as compared to the O—O ones in these series of compounds, it is reasonable to expect here a lower role of steric effects. Both in Fig. 3 and in Table 1, it can be noted that monosubstitution of the hydrogen in hydrogen persulfide does not alter significantly the heights for both barriers, but disubstitution increases the *cis* barrier height correspondingly to the "size" of the alkyl group.

The torsional modes around three different bonds, O—O (hydrogen peroxide), S—S (hydrogen persulfide) and O—S (hydrogen thioperoxide), were compared in Ref. [31]. The HOSH molecule is worth to be studied because its radicals are involved in various processes associated with the atmospheric oxidation of sulfides, one of the chemical processes that leads to acid rain and the depletion of ozone. It is possible to see that, although HOOH has an equilibrium dihedral angle of 112°, even a single S atom shifts this angle towards 90°.

Summarizing the discussion of differences between the effect of substitution on peroxides and persulfides, the main one is on the *trans* barrier, which by alkyl substitution is practically unaffected in H_2S_2 but drastically decreases for H_2O_2.

The energy profiles presented in this chapter refer to ground electronic states. In view of relevance for atmospheric chemistry and of the role of the UV photons in the photo-chemical processes in the ozone layer, it would be interesting to extend these studies to the torsional modes of the excited electronic states.

3.2 Torsional Levels and Their Temperature Distribution

We have emphasized in the previous sections our specific interest on the floppy nature of these molecules. This poses the important problem of the dynamics around the very anharmonic mode associated with torsion around the O—O and S—S bonds. In Ref. [4] the observation that the torsional dynamics in H_2O_2 is best described in *local orthogonal coordinates* was crucial leading to the interpretation of the OH groups as rigid rotors executing a torsion motion around a (Jacobi) vector joining their centres of mass. The corresponding dihedral angle is thus the variable, while the other five degrees of freedom are frozen at the equilibrium configuration. Formulas relating geometrical and local vector parameters are given in Ref. [4]. In both cases, one has to consider the Hamiltonian describing the torsional mode as involving three vectors. For the local vector parameterization, in view of their orthogonality, one has very simple expressions, rigorously eliminating couplings in the Hamiltonian.

As discussed in Ref. [29], this approach is not easily extendable in general to the case of substituents. Accordingly, in all cases energy levels were estimated using the torsional potential profile as a function of the dihedral angle. The cited references in Ref. [28] and the supporting information of Ref. [29] list calculated data for these profiles, for a 10° spacing; a finer grid is available on request. The simplified procedure is adopted in the old literature, namely, an expansion of the torsional potential as truncated to only four terms according to a recipe given in Ref. [60], used as input *cis* and *trans* barrier heights, and the equilibrium dihedral angle only. We extended it by a more accurate expansion where moments were obtained by a Newton–Raphson fitting including at least six terms. Basis sets in terms of sine and cosine functions were used, giving rise to secular equations, where the matrix elements are analytical integrals over trigonometric functions. Obtained information also includes composition of zero-point energies from the two approaches, exhibiting the level of accuracy that can be obtained by truncation to only four terms, when only equilibrium and *cis* and *trans* information are available.

Note that in view of the symmetry of the torsional potential by reflection on the two (*cis* and *trans*) planar configurations, the problem block diagonalizes in four symmetry classes, denoted by the quantum label $\tau = 1, 2, 3$ and 4. Levels within each symmetry classes are denoted by the quantum number $n = 0, 1, 2, \ldots$. The energy separation between levels with same n and different τ is associated to tunnelling through *cis* and *trans* barriers. Specifically, splitting between $\tau = 1$ and 2 and between 3 and 4 is for tunnelling through the *cis* barriers, which practically degenerates for lower levels.

The *trans* tunnelling is responsible for the separation between levels with $\tau = 1$ and 3 or with 2 and 4. In Ref. [29], we showed, for the case of hydrogen peroxide, a comparison between the obtained levels with both approaches and those observed experimentally. Wavefunctions were also obtained. Once the energy $E_{n\tau}$ of levels has been obtained, another interesting property of these molecules can be easily calculated, namely, their relative population $(N_{n\tau}/N)$ as a function of temperature

T, using the Boltzmann distribution formula

$$\frac{N_{n\tau}}{N} = \frac{\exp[-E_{n\tau}/k_B T]}{\sum_{n\tau} \exp[-E_{n\tau}/k_B T]}, \tag{1}$$

where k_B is Boltzmann's constant. This interesting piece of information is also exhibited in our paper [29] for the distributions at room temperature for all systems. An extensive recent study of a set of approaches to the level distributions, also for isotopic substitutions in H_2O_2, is to be consulted for the general issue of the statistical thermodynamics of bond torsional modes [61]. We extended to persulfides, for that series of molecules, a systematic quantum chemical investigation has been outlined in the previous section. In these investigations, the emphasis has been on the characterization of the torsional mode, which is responsible for the stereomutation, namely the exchange between chiral enantiomers through the *trans* and *cis* barriers, a motivation being the understanding of the possible role of collisional mechanism for such processes [35, 36]. We also estimated torsional levels and their populations as a function of temperature.

Interest in the specific features of torsional modes has been renewed recently; see, for example, Refs. [62–64] for spectroscopic investigations. The following section will deal with the calculation of partition functions, of relevance both for statistical thermodynamics and for reaction kinetic problems, see Refs. [65–70] and references therein. Partition functions can be computed according to well-established formulas by explicit use of the calculated torsional levels and also by giving a test for simple classical and semi-classical approximations. In the calculation of the classical partition function, we found it important to consider a correction proposed in Refs. [71, 72], which uses features of the linear approximation of the classical path (LCP) approach and the quadratic Feynman–Hibbs (QFH) approximation of the Feynman path integral. Another delicate aspect of the calculation of the classical torsional partition functions is the dependence of the moment of inertia on the geometrical parameters and on the dihedral angle. For discussions and calculations of the effective moment of inertia of molecules with internal rotation, see, for example, Refs. [60] and [73] and references therein. In our work [28], we tested alternative expressions for the moment of inertia, which can be considered as a constant only in a first approximation, and also considered a more general approach based on the kinetic energy operator, which takes into account the dependence from the dihedral angle, verifying that the explicit introduction of such a dependence from the dihedral angle improves the classical approximations.

For both the peroxide and persulfide cases, the obtained results allowed us to characterize the racemization rates, which determine the process of stereomutation between the two enantiomeric forms connected by torsion around the O—O and S—S bonds. As we will see below, computed level splittings provide the characteristic time for quantum mechanical tunnelling, which is the mechanism responsible for the chirality changing process at low temperature, whereas for high temperature,

the time of racemization is estimated by transition state theory using the computed partition functions.

4 Intramolecular and Intermolecular Chirality Changing Processes

4.1 Intermolecular Rates

As an important application of the results of previous sections, we calculated the tunnel splittings and racemization times for some of the investigated systems in the spirit of Quack and co-workers [52]. The tunnelling time is calculated directly from the level splitting of the symmetries $\tau = 1$ and $\tau = 4$ using the two-level equation and the Heisenberg uncertainty principle,

$$\tau_0 \cong \frac{h}{2\Delta E}. \tag{2}$$

This can be interpreted as a racemization time at very low temperatures where only the ground state is populated. In the opposite limit of high temperature, the racemization time is modelled as occurring by passage over the *trans* barrier using transition state theory with no tunnelling correction:

$$\tau_T \cong \frac{h}{2k_B T} Q(T) \exp(E_{trans}/k_B T), \tag{3}$$

where E_{trans} is the *trans* barrier height (lower than the *cis* in the cases considered here, Table 1), k_B the Boltzmann's constant, and $Q(T)$ the partition function for the torsional mode calculated by any of the methods of previous section.

It can be observed in Table 2 that racemization times, for both low (τ_0) and high (τ_T) temperatures, can be quite high, reaching the order of seconds (or more) for some molecules containing the S—S bond. This behaviour is related to the height of the *trans* barriers, which for the persulfides presented in Table 1 is always of the same order of magnitude as the *cis* barriers. The reader will find it interesting to compare the results in Table 2 for persulfides and those reported in the corresponding peroxides molecules, in which the respective rates were generally much smaller.

4.2 Intermolecular Interactions to Study Collisional Dynamics

Motivated by the perspective use in collisional dynamics studies, in a series of papers, we consider atom–molecule interactions related to the systems considered in the previous sections. To this aim, we calculated atomic and molecular

Table 2 Tunnelling splittings and racemization times for some peroxides and persulfides. Based on data and adapted from Refs. [30, 31]

			τ_T			
System	$\Delta E(\text{cm}^{-1})$	τ_0(sec)	$T = 200$ K	$T = 300$ K	$T = 600$ K	$T = 2{,}400$ K
HOOH	1×10^{1}	3×10^{-12}	1×10^{-12}	6×10^{-13}	2×10^{-13}	1×10^{-13}
HSSH	4×10^{-6}	5×10^{-6}	1×10^{-7}	1×10^{-9}	1×10^{-11}	3×10^{-13}
HOOF	4×10^{-7}	4×10^{-5}	4×10^{-3}	1×10^{-6}	3×10^{-10}	6×10^{-13}
HSSF	–	–	5×10^{2}	3×10^{-3}	2×10^{-8}	2×10^{-12}
ClOOCl	$< 10^{-12}$	>7	1×10^{-6}	5×10^{-9}	3×10^{-11}	8×10^{-13}
ClSSCl	–	–	5×10^{6}	2×10^{0}	7×10^{-7}	1×10^{-11}
HOOCN	6×10^{0}	1×10^{-12}	8×10^{-13}	5×10^{-13}	3×10^{-13}	1×10^{-13}
HOONO	4×10^{-2}	6×10^{-10}	2×10^{-11}	4×10^{-12}	8×10^{-13}	2×10^{-13}
FOONO	$< 10^{-11}$	>2	4×10^{2}	6×10^{-4}	1×10^{-8}	3×10^{-12}
HSSCl	–	–	1×10^{-1}	1×10^{-5}	1×10^{-9}	1×10^{-12}
FSSF	–	–	1×10^{21}	7×10^{9}	3×10^{-2}	1×10^{-10}
ClSSF	–	–	8×10^{12}	2×10^{4}	7×10^{-5}	3×10^{-11}
$HSSCH_3$	2×10^{-10}	8×10^{-2}	3×10^{-7}	2×10^{-9}	2×10^{-11}	4×10^{-13}
$HSSC_2H_5$	1×10^{-10}	2×10^{-2}	1×10^{-6}	5×10^{-9}	2×10^{-11}	5×10^{-13}

polarizabilities for the H_2O—Rg, H_2S—Rg, hydrogen peroxide–Rg and hydrogen persulfide–Rg systems in order also to compare with correlation formulas developed to predict strength and range of the intermolecular interactions [34]. It was seen that this requires also inclusion of induction effects, for which we will use the calculated dipole moments (see a previous section). Relevant comparison can be made with available experimental data (H_2O, H_2S), while for H_2O_2 and H_2S_2 reference data come from intermolecular potential energy surfaces based on ab initio calculations obtained in the previous work [32, 33]. It can be observed that the investigated atom–molecule interactions extended previous experimental and theoretical studies of those of H_2O and H_2S with rare gases [74, 75].

The extension of phenomenology of atom–atom interaction to molecules, where additional features emerge in the picture of van der Waals interactions, requires that account is taken of anisotropy and covalent-type contributions that manifest at medium and short distances and which are expected to play a role. Systems under focus here are the gas-phase complexes of molecules H_2X, containing an atom with a high electron affinity (in our case X = O,S), interacting with rare gas atoms [34]. They exhibit intermediate and short-range contributions that can be probed by molecular beam experiments and can also be modelled by reliable ab initio calculations. Total cross sections measured in these experiments at different collision energies give direct information on the isotropic interaction.

Combining theoretical and experimental data, in a strict interplay between theory and experiments, the relative importance of the various contributions to the interaction can be evaluated. A paradigmatic example is the water molecule, for which an integrated experimental and theoretical investigation [74, 76] demonstrated the incipient hydrogen bond formation for complexes with the heavier rare gas atoms Ar, Kr and Xe. Previously obtained results from analogous experiments on O_2–rare

gases (prototypical van der Waals interactions [77–79]) suggested that both the long- and medium-range features can be compared with those of the water systems in view of the similarity of oxygen and water in terms of molecular polarizability, which is the basic property for scaling van der Waals forces in the full distance range [80–82]. For the lighter gases, He and Ne, similar cross sections in collisions with water or oxygen confirm that a van der Waals interaction is the main component also in the water case.

Indeed, the involved components (repulsion, dispersion, induction) can be modelled on the basis of the polarizabilities of the partners [80–82]. For the heavier members of the series, the orientationally averaged components of the water cross sections still are comparable with those of the oxygen systems and continue to be in accord with polarizability-based models for van der Waals' long range attraction [80, 82]. This has been found not to be the case for the "glory" features [74], which are very sensitive to the depth and position of the potential wells showing, on going towards Xe, an increasing binding strength, larger than expected for pure van der Waals forces.

Phenomenological evaluation [80, 82] using atomic and molecular polarizabilities and the permanent dipole moment of water suggests that under the condition of the experiment, which involved water at high rotational temperature, the long range attraction is accounted for more than 90% by dispersion forces, and induction contributions play a minor role. This indicates that the increase in well depths is the manifestation of a short-range reinforcing attractive component to the bond. Its role amplifies as distance decreases (as typical of a covalent or charge-transfer contribution): moving towards Xe along the series of rare gases, ionization potentials decrease, proton affinities increase and there is circumstantial evidence for sharing of external electrons between the partners in the complexes.

This is confirmed by quantum calculations [74], which are reliable in this case to determine the most stable geometries of the complexes, and have shown that as the atom approaches to the molecule, an alignment along the O—H bond direction becomes progressively more pronounced for the heavier rare gases. The alignment is a signature of the hydrogen bond [83], to be contrasted with the sideways approach predicted on the basis of a pure van der Waals interaction, and shown to contribute by about 30% for Xe at the distance of the minimum in the well R_m. Similar experimental studies have been done for H_2S–rare gases [13, 14]. Complementary quantum calculations [75, 84] have shown that the pathways in different directions are nearly isoenergetic for the atoms, and there is evidence that even an embryonic hydrogen bond contribution is negligible. Experimental data [75] have been used to characterize the relative role of the basic components of the interaction, by comparison with the potential parameters predicted accounting for dispersion and induction terms, with the conclusion that the van der Waals nature is dominant. Again, the interesting picture emerged from recently measured experimental cross sections for the H_2S—Xe system: comparison with the ones calculated assuming a pure van der Waals interaction indicates an additional attractive component [84], that although small, could however be estimated to be of the order of 5-10% at R_m.

In order to study H_2O_2–Rg and H_2S_2–Rg interactions, the role of theory is prominent due to the lack of experimental information for such systems [85]. These molecules play a crucial role not only in atmospheric science, but also in other ample fields of chemistry, such as combustion and biochemical processes. Again, note that additional interest is deserved by these systems because they are the simplest examples of chiral molecules [4]. The theme of the previous section was the internal torsion mode [4, 30–33], which is a floppy one, so that the cut of the molecular potential energy surfaces (Figs. 1, 2 and 3) along its direction shows a double well profile which connects the two possible enantiomers [35, 36].

For atom–molecule systems, well depths are comparable with the typical strength of the atom–molecule interactions and a realistic representation of the potential surfaces (of use also for molecular dynamics simulations) must include the torsional degree of freedom. As outlined in previous sections, quantum calculations are possible, for such semi-rigid models, at a quite accurate level and work has been done for both H_2O_2 and H_2S_2 to determine the potential profile of torsion and torsional levels and dipole moments [4, 29, 32, 33].

As customary for dimers of diatomic molecules [86–88], the potential energy surface is represented as a finite sum of spherical harmonics, whose momenta are radial coefficients accounting for the isotropic part of the interaction potential (electrostatic, dispersion, repulsion due to overlap, induction, spin–spin coupling). The profile described by these coefficients, as a function of the radial distance, is directly comparable to experimental data, while the leading spherical zeroth order term can be correlated with the van der Waals-type interaction. The calculated potential energy surfaces for the systems Rg–hydrogen peroxide and persulfide [32, 33] have been obtained keeping fixed bond distances and angles of the molecule. The ab initio data have been fit as a sum of real hyperspherical harmonics involving explicitly the internal dihedral angle of the molecule.

Three characteristic molecular configurations, corresponding to *cis*, equilibrium and *trans* geometries, are of particular interest. As the dihedral angle varies, polarizabilities and dipole moments [29] for these geometries so do, so that the total atom–molecule interaction energy can be partitioned as a sum of three terms each for one of the geometries. The expansion basis functions were built up from symmetry considerations, and the zeroth order term of the expansion obtained as a spherical average represents the isotropic part of the interaction. When we specify the torsional angle dependence, we can discuss the interactions for various molecular geometries, in particular for the *cis*, equilibrium and *trans* cases.

5 Remarks and Conclusion

The developments described in the previous section emphasizes the interplay with experiments and in general the relevance of the results with reference to intra- and intermolecular dynamics. The reader will find more information on how they can be inserted in a proper context by reference to accounts and reviews we have presented elsewhere.

Specifically, Refs. [35] and [36] deal with the relevance for chirality change processes, [85] with the interest for the chemistry of the atmosphere, while [77] provides the background for the characterization of interatomic interaction.

On this last aspect, we have made references in the preceding section in particular to correlation formulas which have been tested with respect to their capabilities to estimate the potential parameters for the intermolecular interactions of various molecule–Rg systems. For H_2S—Rg, H_2O—He and H_2O—Ne systems, as well as for H_2S_2—Rg and H_2O_2—He and Ne [83] systems, the predicted well depths and well positions reproduce the available experimental and theoretical data. The intermolecular interaction of heavier gas atoms (Ar, Kr and Xe) with water and hydrogen peroxide appears to involve additional significant contributions of possible "chemical" nature, such as charge transfer [89] or embryonic hydrogen bond [74]. For these systems the isotropic contribution is only a part of the interaction and the use of the correlation formulas leads to consistently underestimated results for the interaction strength. A full interpretation of this behaviour will have to be obtained by improving the ab initio potential energy surfaces beyond the semi-rigid model, especially for H_2O_2. The inclusion of the internal torsional angle has to be considered as a starting point in order to account for the effects that even small changes in geometry can induce at the level of local short-range contributions to the atom–molecule interaction. These effects, as yet quantified only for water, are expected to involve specifically the stretching of OH and SH bonds of the molecules.

Acknowledgments We thank the Agenzia Spaziale Italiana (ASI) for support and the Italian Ministero per l'Istruzione,l'Università e la Ricerca (MIUR) for PRIN and FIRB grants. ACPB acknowledges a CAPES Brazilian fellowship. We thank Patricia Barreto, Andrea Lombardi, Frederico Prudente and Federico Palazzetti for their collaborations to these investigations.

References

1. F. Cacace, G. de Petris, A. Troiani, Rapid Commun. Mass Spectrom. **13**, 1903 (1999); M. Lee, B.G. Heikes, D.W. O'Sullivan, Atmos. Environ. **34**, 3475 (2000); S. Françoise, I. Sowka, A. Monod, B. Temime Roussel, J.M. Laugier, H. Wortham, Atmos. Res. **74**, 525 (2005); V. Vaida, Int. J. Photoenergy **7**, 61 (2005). B. Volgel, W. Feng, M. Streibel, R. Müller, Atmos. Chem. Phys. **6,** 3099 (2006)
2. M. Streibel, M. Rex, P. Von der Gathen, R. Lehmann, N.R.P. Harris, G.O. Braathen, E. Reimer, H. Deckelmann, M. Chipperfield, G. Millard, M. Allaart, S. B. Andersen, H. Claude, J. Davies, H. De Backer, H. Dier, V. Dorokov, H. Fast, M. Gerding, E. Kyró, Z. Litynska, D. Moore, E. Moran, T. Nagai, H. Nakane, C. Parrondo, P. Skrivankova, R. Stubi, G. Vaughan, P. Viatte, V. Yushkov, Atmos. Chem. Phys. **6**, 83 (2006)
3. B. Messer, D.E. Stielstra, C.D. Cappa, K.W. Scholtens, M. Elrod, J. Int. J. Mass. Spectrom. **197,** 219 (2000)
4. G.S. Maciel, A.C.P. Bitencourt, M. Ragni, V. Aquilanti, Chem. Phys. Lett. **432**, 383 (2006)
5. G.I. Cardenas-Jirón, A. Toro-Labbé, J. Mol. Struct. (THEOCHEM) **390**, 79 (1997)
6. J. Bergès, G.A. Rickards, A. Rauk, C. Houée-Levin, Chem. Phys. Lett. **421**, 63 (2006)
7. G.A. Rickard., J. Bergès, C. Houée-Levin, A. Rauk, J. Phys. Chem. B **112**, 5774 (2008)
8. E. Zysman-Colman, D.N. Harp, J. Sulfur Chem. **24**, 291 (2004)

9. J.J. Grabowski, L. Zhang, J. Am. Chem. Soc. **111**, 1193 (1989)
10. C.J. Marsden, H. Oberhammer, O. Lösking, H. Willner, J. Mol. Struct. (THEOCHEM) **193**, 233 (1989)
11. G.N. Dolenko, E.N. Deryagina, L.P. Turchaninova, V.P. Elin, E.I. Basina, T.O. Pavlova, V.K. Voronov, J. Heteroat. Chem. **6**, 623 (1995)
12. B.-M. Cheng, W.-C. Hung, J. Phys. Chem. **100**, 10210 (1996)
13. X. Cao, C. Qiao, D. Wang, Chem. Phys. Lett. **290**, 405 (1998)
14. C.J. Marsden, B.J. Smith, J. Phys. Chem. **92**, 347 (1988)
15. F.M. Bickelhaupt, M. Solà, P.v.R. Schleyer, J. Comp. Chem. **16**, 465 (1995)
16. G.I. Cardenas-Jirón, J. Lahsen, A. Toro-Labbé, J. Phys. Chem. **99**, 5325 (1995)
17. J. Koput, Chem. Phys. Lett. **259**, 146 (1996)
18. J. Altmann, N.C. Handy, V.E. Ingamells, Int. J. Quantum Chem. **57**, 533 (1996)
19. B.R. Jursic, J. Comput. Chem. **17**, 835 (1996)
20. R. Steudel, Y. Drozdova K. Miaskiewicz, R.H. Hertwig, W. Koch, J. Am. Chem. Soc. **119**, 1990 (1997)
21. D. Das, S.L. Whittenburg, J. Phys. Chem. A **103**, 2134 (1999)
22. B. Braida, P.C. Hiberty, J. Phys. Chem. A **107**, 4741 (2003)
23. D.W. Ball, J. Mol. Struct. (THEOCHEM) **676**, 15 (2004)
24. B.P. Prascher, A.K. Wilson, J. Mol. Struct. (THEOCHEM) **814**, 1 (2007)
25. F.R. Ornellas, Chem. Phys. Lett. **448**, 24 (2007)
26. Y. Zeng, X. Li, X. Zhang, S. Zheng, L. Meng, J. Mol. Struct. (THEOCHEM) **851**, 115 (2008)
27. E. Dumont, P.-F. Loos, X. Assfeld, Chem. Phys. Lett. **458**, 276 (2008)
28. G.S. Maciel, A.C.P. Bitencourt, M. Ragni, V. Aquilanti J. Phys. Chem. A **111**, 12604 (2007)
29. G.S. Maciel, A.C.P. Bitencourt, M. Ragni, V. Aquilanti, Int. J. Quant. Chem. **107**, 2697 (2007)
30. A.C.P. Bitencourt, M. Ragni, G.S. Maciel, V. Aquilanti, F.V. Prudente, J. Chem. Phys. **129**, 154316 (2008)
31. V. Aquilanti, M. Ragni, A.C.P. Bitencourt, G.S. Maciel, F.V. Prudente, J. Phys. Chem. A, **113**, 3804 (2009)
32. P.R.P Barreto, A.F.A. Vilela, A. Lombardi, G.S. Maciel, F. Palazzetti, V. Aquilanti, J. Phys. Chem. A **111**, 154 (2007)
33. G.S. Maciel, P.R.P. Barreto, F. Palazzetti, A. Lombardi, V. Aquilanti J. Chem. Phys. **129**, 164302 (2008)
34. P.R.P. Barreto, F. Palazzetti, G. Grossi, A. Lombardi, G.S. Maciel, A.F.A. Vilela, Int. J. Quantum Chem. in press (2009)
35. V. Aquilanti, G.S. Maciel, Orig. Life Evol. Biosph. **36**, 435(2006)
36. V. Aquilanti, G. Grossi, A. Lombardi, G.S. Maciel, F. Palazzetti, Phys. Scr. **78**, 058119 (2008)
37. M.J. Frisch et al. Gaussian 03, Revision C.02 (Gaussian, Inc. Wallingford, CT, 2004)
38. H. Oberhammer, J. Comput. Chem. **2**, 123 (1998); S. Tonmunphean, V. Parasuk, A. Karpfen, J. Phys. Chem. A, **106**, 438 (2002); S.C. Homitsky, S.M. Dragulin, L.M. Haynes, S. Hsieh, J. Phys. Chem A **108**, 9492 (2004)
39. J. Matthews, A. Sinha, J.S. Francisco, J. Chem. Phys. **122**, 221101 (2005); J.D. Watts, J.S. Francisco, J. Chem. Phys. **125,**104301 (2006)
40. C.J. Marsden, B.J. Smith, J. Phys. Chem. **92**, 347 (1988)
41. D. Harmony, V.W. Laurie, R.L. Kuczkowski, R.H. Schwendeman, D.A. Ramsay, F.J. Lovas, W.J. Lafferty, A.G. Maki, J. Phys. Chem. **8**, 619 (1979)
42. J. Koput, Chem. Phys. Lett. **259**, 146 (1996)
43. G. Winnewisser, M. Winnewisser, W. Gordy, J. Chem. Phys. **49**, 3465 (1968)
44. K.B. Wiberg, J. Comput. Chem. **25**, 1342 (2004)
45. R.R.M. Moreno, A.M. Grana, R.A. Mosquera, Struct. Chem. **11**, 9 (2000)
46. D.R. Lide, *Handbook of Chemistry and Physics*, 80th ed. (CRC Press, Cambridge, MA, 2000)
47. J. Koput, Chem. Phys. Lett. **257**, 36 (1996)
48. A. Perrin, J.-M. Flaud, C. Camy-Peyret, R. Schermaul, M. Winnewisser, J.-Y. Mandin, V. Dana, M. Badaoui, J. Koput, J. Mol. Spectrosc. **176**, 287 (1996)
49. A.G. Steng, Chem. Rev.**63**, 607 (1967)

50. G.N. Dolenko, E.N. Deryagina, L.P. Turchaninova, V.P. Elin, E.I. Basina, T.O. Pavlova, V.K. Voronov, J. Heteroat. Chem. **6**, 623 (1995)
51. B.P. Winnewisser, M. Winnewisser, I.R. Medvedev, M. Behnke, F.C. De Lucia, S.C. Ross, J. Koput, Phys. Rev. Lett. **95**, 243002 (2005)
52. M. Quack, M. Willeke, J. Phys. Chem A **110**, 3338 (2006)
53. T.S. Dibbe, J.S. Francisco, J. Am. Chem. Soc. **119**, 2894 (1997)
54. Y. Li, J.S. Francisco, J. Chem. Phys. **113**, 7976 (2000)
55. S.A. Nizkorodov, P.O. Wennberg, J. Phys. Chem. A **106**, 855 (2002)
56. D.A. Dixon, D. Feller, C.-G. Zhan, J.S. Francisco, J. Phys. Chem. A **106**, 3191 (2002)
57. B.D. Bean, A.K. Mollner, S.A. Nizkorodov, G. Nair, M. Okumura, S.P. Sander, K.A. Petersos, J.S. Francisco, J. Phys. Chem. A **107**, 6474 (2003)
58. J. Matthews, A. Sinha, J. Chem. Phys. **122**, 1043313 (2005)
59. M.P. McGrath, F.S. Rowland, J. Chem. Phys. **122**, 134312 (2005)
60. R.H. Hunt, R.A. Leacock, C.W. Peters, K.T. Hecht, J. Chem. Phys. **42**, 1931 (1965)
61. B.A. Elligson, V.A. Lynch, S.L. Mielke, D.G. Truhlar, J. Chem. Phys. **125**, 084305 (2006)
62. G. Pelz, K.M.T. Yamada, G. Winnewisser, J. Mol. Spectrosc. **159**, 507 (1993); K.M.T. Yamada, G. Winnewisser, P. Jensen, J. Mol. Struct. **695**, 323 (2004); A. Bakasov, R. Berger, T.-K. Ha, M. Quack, Int. J. Quantum Chem. **99**, 393407 (2004)
63. G. Winnewisser, P. Jensen, J. Mol. Struct. **695**, 323 (2004); P. Winnewisser, M. Winnewisser, I.R. Medvedev, M. Behnke, M. Winnewisser, B.P. Winnewisser, I.R. Medvedev, F.C. De Lucia, S.C. Ross, L.M. Bates, J. Mol. Struct. **798**, 1 (2006)
64. S.C. Ross, K.M.T. Yamada, Phys. Chem. Chem. Phys. **9**, 5809 (2007)
65. Y.-Y. Chuang, D.G. Truhlar, J. Chem. Phys. **112**, 1221 (2000); **121**, 7036(E) (2004), **124**, 179903(E) (2006)
66. V.A. Lynch, S.L. Mielke, D.G. Truhlar, J. Chem. Phys, **121**, 5148 (2004)
67. V.A. Lynch, S.L. Mielke, D.G. Truhlar, J. Phys. Chem. A **109**, 10092 (2005); **110**, 5965 (2006)
68. B.A. Ellingson, V.A. Lynch, S.L. Mielke, D.G. Truhlar, J. Chem. Phys. **125**, 084305 (2006)
69. Y.K. Sturdy, D.C. Clary, Phys. Chem. Chem. Phys. **9**, 2065 (2007)
70. Y.K. Sturdy, D.C. Clary, Phys. Chem. Chem. Phys. **9**, 2397 (2007)
71. F.V. Prudente, A. Riganelli, A.J.C. Varandas, J. Phys. Chem. A **105**, 52 (2001)
72. F.V. Prudente, A.J.C. Varandas, J. Phys. Chem. A **106**, 6193 (2002)
73. K.S. Pitzer, W.D. Gwinn, J. Chem. Phys. **10**, 428 (1942)
74. V. Aquilanti, E. Cornicchi, M.M. Teixidor, N. Saendig, F. Pirani, D. Cappelletti, Angew. Chem. Int. Edition **44**, 2356 (2005)
75. D. Cappelletti, A.F.A. Vilela, P.R.P. Barreto, R. Gargano, F. Pirani, V. Aquilanti, J. Chem. Phys. **125**, 133111 (2006)
76. D. Cappelletti, V. Aquilanti, E. Cornicchi, M.M. Teixidor, F. Pirani, J. Chem. Phys. **123**, 024302 (2005)
77. F. Pirani, G.S. Maciel, D. Cappelletti, V. Aquilanti Int. Rev. Phys. Chem. **25**, 165 (2006)
78. V. Aquilanti, D. Ascenzi, D. Cappelletti, S. Franceschini, F. Pirani, Phys. Rev. Lett. **74**, 2929 (1995)
79. V. Aquilanti, D. Ascenzi, D. Cappelletti, M. de Castro, F. Pirani, J. Chem. Phys. **109**, 3898 (1998)
80. V. Aquilanti, D. Cappelletti, F. Pirani, Chem. Phys. **209**, 299 (1996)
81. R. Cambi, D. Cappelletti, G. Liuti, F. Pirani, J. Chem. Phys. **95**, 1852 (1991)
82. F. Pirani, D. Cappelletti, G. Liuti, Chem. Phys. Lett. **350**, 286 (2001)
83. A.E. Reed, L.A. Curtiss, F. Weinhold, Chem. Rev. **88**, 899 (1998)
84. V. Aquilanti, D. Cappelletti, F. Pirani, L.F. Roncaratti, Int. J. Mass Spectrom. **280**, 72 (2009)
85. G.S. Maciel, D. Cappelletti, G. Grossi, F. Pirani, Adv. Quantum Chem. **55**, 311 (2008)
86. V. Aquilanti, D. Ascenzi, M. Bartolomei, D. Cappelletti, S. Cavalli, M. De Castro Vitores, F. Pirani, J. Am. Chem. Soc. **121**, 10794 (1999)
87. M.C. van Hemert, P.E.S. Wormer, A. van der Avoird, Phys. Rev. Lett. **51**, 1167 (1993)
88. S. Green, J. Chem. Phys. **62**, 21 (1975)
89. V. Aquilanti, D. Cappelletti, F. Pirani, Chem. Phys. Lett. **271**, 216 (1997)

Theoretical Spectroscopy of Inner-Shell Electronic Processes and Photochemistry of Fluorescent Molecules

Masahiro Ehara and Hiroshi Nakatsuji

Abstract The SAC-CI method has been applied to the theoretical spectroscopy of the inner-shell electronic processes and the photochemistry of the organic light-emitting diodes (OLED) and biological chemosensors. Wide varieties of the core-electronic processes such as core-electron ionizations, shake-up satellites, vibrational excitations, valence–Rydberg coupling, and its thermal effect have been investigated by the SAC-CI calculations. The method has also been applied to the electronic spectra and the excited-state dynamics of the polymer materials of OLED such as poly *para*-phenylene vinylene and fluorene-thiophene. The photochemistry of the biological chemosensor has been elucidated in particular for the photo-induced electron transfer mechanism of the acridine-type fluorescent probe.

Keywords: SAC-IC · Theoretical spectroscopy · Inner-cell electronic processes · Organic-light emitting diodes · Priological chemosensors

1 Introduction

Recently, investigations of the core-electronic processes invoked renewal of interest, because significant developments in both high-resolution soft X-ray spectroscopy and accurate state-of-the-art theoretical methods have made us possible to obtain precise knowledge of the core-electronic processes. One can observe vibrational structures in the core-level photoelectron spectrum and thereby discuss the excited-state dynamics. This situation has motivated intensive cooperative researches on the core-electron processes from the experimental and theoretical sides.

Masahiro Ehara (✉)
Institute for Molecular Science, 38 Nishigo-Naka, Myodaiji, Okazaki 444-8585, Japan; JST, CREST, Sanboncho-5, Chiyoda-ku, Tokyo 102-0075, Japan, e-mail: ehara@ims.ac.jp

Hiroshi Nakatsuji
Quantum Chemistry Research Institute, Kyodai Katsura Venture Plaza 106, Kyoto 615-8245, Japan; JST, CREST, Sanboncho-5, Chiyoda-ku, Tokyo 102-0075, Japan,
e-mail: h.nakatsuji@qcri.or.jp

P. Piecuch et al. (eds.), *Advances in the Theory of Atomic and Molecular Systems*, Progress in Theoretical Chemistry and Physics 20, DOI 10.1007/978-90-481-2985-0_6,

The photochemistry of fluorescent molecules like organic light-emitting diodes (OLED) and biological chemosensors is an attractive and important subject. The OLED is recognized as one of the promising candidates for the next generation electro-optical devices. Theoretical interpretation and prediction of the photophysical properties of the OLED molecules are relevant for developing the new materials. The fluorescent probe which works as biological chemosensor has also been focused and extensively investigated, since it enables the direct and real-time measurements of the enzyme activities. The fluorescence change by the interaction with the enzyme is essential and the elucidation of the electronic mechanism of the fluorescence and the color-tuning are important for developing new fluorescent probes.

In the series of our recent works, we have investigated the theoretical spectroscopy of the inner-shell electronic processes and the photochemistry of organic light-emitting diodes and biological chemosensors with the SAC-CI method. The SAC-CI method [1–3] has been successfully applied to the wide varieties of chemistry in particular for the molecular excited states. The method has been established as an accurate molecular excited-state theory applicable to the various kinds of electronic processes in the wide energy region [3–5]. In this chapter, we review our recent SAC-CI studies on the inner-shell electronic processes [6–18] and the organic light-emitting diodes [19, 20] and biological chemosensors.

2 Theoretical Spectroscopy of Inner-Shell Electronic Processes

Core-electron ionization spectra contain the information not only about inner-core electrons but also valence electrons and chemical bonds. Extensive experimental studies have measured the core-electron binding energies of numerous molecules [21, 22] and the recent development of X-ray photoelectron spectroscopy (XPS) has enabled the detailed analysis of the satellites accompanied by the inner-shell ionization [8, 11–13]. The high-resolution XPS has also been applied to observe the vibrational structure to investigate the geometry change and the dynamics in the inner-shell electronic processes [6, 9–17].

The SAC-CI method is useful to study both the main and satellite peaks in the core-electronic spectra as well as valence spectra. In the series of studies [6–18], the SAC-CI method have been successfully applied to the various kinds of core-electron processes; the core-electron binding energies [7]; the inner-shell ionization satellite spectra of CH_4, NH_3 [7], H_2O [11], formaldehyde [8]; and the vibrational spectra of the core-hole state of H_2O [6], CO [10], N_2 [12], CO_2 [14], and N_2O [16]. The g–u splitting of homonucleus molecules like N_2, C_2H_2, C_2H_4, and C_2H_6 has been well predicted [7, 12]. The overlapping vibrational spectra of the low-lying shake-up satellite states of CO [9, 13] and N_2 [12] were also successfully interpreted by the present method; the potential energy curves of the inner-shell shake-up states were accurately calculated. The method has also been applied to the core-electronic excited states [15, 17, 18]. The irregular Rydberg behavior observed for the O1*s*

excited states of N_2O [15] and its drastic change due to the ground-state vibrational excitations were clarified [17].

In this section, we briefly review the SAC-CI methodologies for the inner-shell electronic processes and the recent applications to the core-electronic processes like core-electron binding energy, inner-shell shake-up satellite spectrum, vibrational spectrum of main line and satellites, and core-electronic excitation spectrum.

2.1 SAC-CI Methodologies for Inner-Shell Electronic Processes

The SAC-CI method can be applied to the electronic processes in a wide energy region. There are two approaches in SAC-CI for studying the inner-shell electronic processes. One is based on the general-R method [23–25] in which the neutral ground-state Hartree–Fock is adopted for the reference function. The wave function for core ionization, for example, is given by

$$\Psi^{\text{SAC-CI}}_{\text{general}-R} = \left(\sum_i R_i + \sum_{ija} R^a_{ij} + \sum_{ijkab} R^{ab}_{ijk} + \sum_{ijklabc} R^{abc}_{ijkl} + \cdots \right) \exp\left(\sum_I S_I \right) \Phi_{HF}, \tag{1}$$

where R and S represent the operators in the SAC-CI expansion and Φ_{HF} is the closed-shell ground-state Hartree–Fock. In this method, the higher-order R-operators such as triples and quadruples are necessary for describing both orbital relaxation and electron correlations of the core-electronic processes. Although the SD-R method is accurate for the one-electron processes of the valence excitations and ionizations, higher-order operators are indispensable for the core-electronic processes. For example, for calculating the core-electron binding energy, R-operators up to triples are necessary and for the shake-up satellite states, the SDTQ-R calculations are required. One-rank higher operator is necessary for describing large orbital relaxation in the calculation of the core-electronic processes. Thus, this method is simple and accurate, but, its computational cost is relatively high since it usually includes higher operators for the accurate calculations. Nonetheless, this method is useful since it can be applied to the general core-electronic processes like the g–u splitting in the molecules with equivalent atoms.

The other approach is the open-shell reference (OR) SAC-CI method [26], in which the core-ionized ROHF is used for the reference:

$$\Psi^{\text{OR-SAC-CI}}_{\text{SD}-R} = \left(\sum_i R_i + \sum_{ija} R^a_{ij} \right) \Psi^{\text{OR-SAC}}, \tag{2}$$

$$\Psi^{\text{OR-SAC}} = \exp\left(\sum_I S_I \right) \exp\left(\sum_J S'_J \right) O_K \Phi_{HF}, \tag{3}$$

where $O_K \Phi_{HF}$ represents the core-hole ROHF. The S and S' operators are the excitation and de-excitation operators, respectively. Since the OR-SAC-CI method starts from the core-hole state, the method is efficient and accurate; the SD-R method is sufficient for describing the core-hole state. However, it introduces the complex expansion of the wave function due to the de-excitation operators. For applying the g–u splitting of the molecules with equivalent atoms, the accurate calculations including higher-order product terms are necessary since it starts from the different reference functions for g and u states.

In the present applications, the former type of the method, the SAC-CI general-R method, has been adopted and applied to the various kinds of the core-electronic processes.

2.2 Core-Electron Binding Energies

For the theoretical study on the core-electron binding energy, the pioneering works have been performed by the ΔSCF and DFT methods [27–29], however, the accurate prediction is still difficult. The SAC-CI method has been systematically applied to the core-electron binding energies of the C, N, O, and F ionizations of 22 molecules [7]. For calculating the core-electron binding energy based on the method starting from the neutral ground-state reference function, the R-operators up to triples are necessary for describing orbital relaxations as well as electron correlations. In Fig. 1, we show a comparison between the theoretical and experimental values for

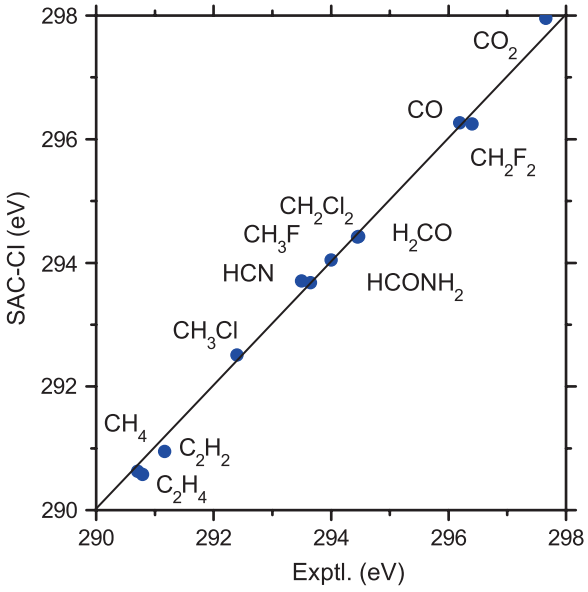

Fig. 1 C1*s* core-electron binding energy [7]

the C1*s* ionizations of 12 molecules. The SAC-CI SDT-*R* method calculated the core-electron binding energies of these molecules quite accurately. In general, the core-electron binding energy shifts into higher energy, when the adjacent atom is electron withdrawing. The SAC-CI method reproduced this chemical shift accurately and the averaged absolute deviation from the experimental values was 0.13 eV for these molecules.

2.3 Vibrational Spectra of Core-Hole States

In the core-electron processes, the reorganization of the electron distribution affects the valence electrons and the characteristic geometry change usually occurs. This geometry change can be observed in the vibrational spectrum. Vibrationally resolved C1*s* and O1*s* photoelectron spectra of carbon monoxide have been measured by the high-resolution X-ray photoelectron spectroscopy. To understand the physics in the vibrational spectra, the potential energy curves of the ground and C1*s* and O1*s* core-ionized states were calculated and the vibrational analysis was performed with the grid method [10]. These vibrational spectra were also studied by the Green's function method [30]. The experimental and theoretical vibrational spectra for the C1*s* and O1*s* ionizations are compared in Fig. 2. The geometry changes and the Franck Condon factors (FCF) are summarized in Tables 1 and 2, respectively. In the C1*s* ionized state, the CO bond shrinks by $\Delta R = -0.051$ Å, while the CO bond length in the O1*s* ionized state was predicted to become longer by $\Delta R = +0.028$ Å. The bond shrink in the C1*s* ionization can be explained by the enhancement of the charge distribution $C^{\delta+}$–$O^{\delta-}$. On the other hand, the O1*s* ionization causes the Coulomb repulsion described by $C^{\delta+}$–$O^{\delta+}$ and results in the CO bond elongation. Although the FCF is the sensitive quantity, the calculated FCF satisfactorily agrees with those extracted from the experimental spectra in the sudden limit as shown in Table 2.

2.4 Inner-Shell Shake-Up Satellite Spectra

Shake-up satellites that appear in the photoelectron spectra are challenging spectroscopic subject from both theoretical and experimental viewpoints. Theoretically, a precise description of the satellite states is possible only with advanced theoretical methods because the spectra reflect very complex electron-correlation and orbital-reorganization effects. Experimentally, the weak intensities of photoelectron satellites make high-resolution photoelectron spectroscopy difficult. In this section, we show the cooperative study by the SAC-CI and XPS on the inner-shell satellite spectra of CO [13]. In these spectra, the valence and Rydberg excitations accompanying the inner-shell ionizations make the satellite spectra complex. Therefore, the

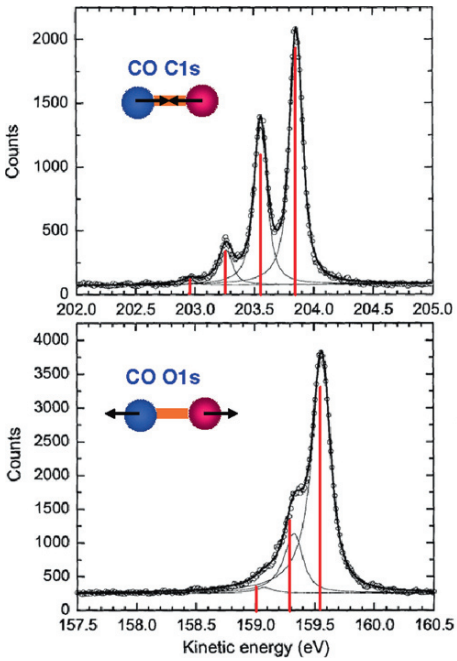

Fig. 2 Vibrational spectra of C1*s* and O1*s* ionizations of CO. The SAC-CI spectra are shown with the *vertical lines* [10]

Table 1 Geometry and harmonic frequency of the C1*s* and O1*s* ionized states of CO [10]

	C1*s*		O1*s*	
	Exptl.	SAC-CI	Exptl.	SAC-CI
R_e (Å)	1.077	1.075	1.165	1.156
ΔR_e (Å)	−0.051	−0.051	+0.037	+0.028
ω_e (cm^{-1})	2479	2444	1864	1928

Table 2 Franck–Condon factors of the C1*s* ionizations of CO [10]

Transition	Exptl.	SAC-CI
0–0	1.000	1.000
0–1	0.637	0.628
0–2	0.154	0.134
0–3	0.019	0.012

accurate theoretical study of these spectra in a wide energy region is challenging [31, 32].

Figure 3 shows the observed XPS and the SAC-CI general-*R* spectra of the C1*s* satellites of CO. The SAC-CI method satisfactorily reproduces the shape of the

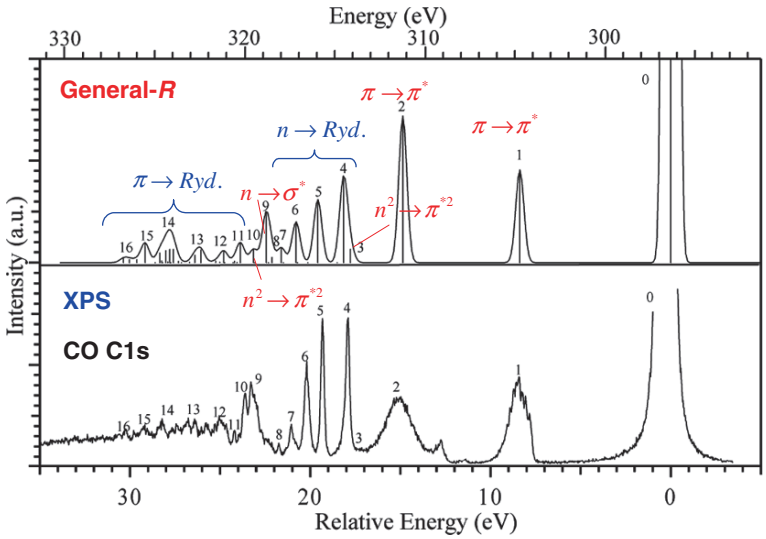

Fig. 3 C1*s* shake-up satellite spectrum of CO [13]

experimental satellite spectrum, although the intensity of the XPS does not necessarily agree with the theoretical monopole intensity. For reproducing the inner-shell satellite spectrum, it is necessary to include *R*-operators up to quadruples, that is the SDTQ-*R* calculations: the conventional SAC-CI SD-*R* method gives errors beyond 10 eV for these satellites and even qualitative assignment is impossible. The SAC-CI SDTQ-*R* spectrum enabled the reliable assignments for the 16 satellite bands. The satellite band 1 was assigned to the $\pi\pi^*$ shake-up state, while the strongest band 2 was the $\pi\pi^*$ shake-up state strongly interacting with the three-electron processes like $C1s^{-1}\pi^{-2}\pi^{*^2}$. Weak satellite peak 3 is also assigned to the double excitation, $n^{-2}\pi^{*^2}$ transition. The continuous sharp peaks above peak 4 in the higher energy region are dominantly assigned to the numerous Rydberg transitions.

In contrast to the C1*s* satellite spectrum, theoretical analysis of the O1*s* satellite spectrum has been very limited. Like formaldehyde, the O1*s* satellite spectrum has different characteristics from the C1*s* spectrum. The different features of these spectra can be interpreted in terms of charge reorganization. The comparison with the experimental and theoretical spectra was made in Fig. 4. The accurate theoretical prediction of the O1*s* satellite spectrum is difficult since most of the satellite states are contributed by the three-electron processes. Peaks 1 and 2 are assigned to the $\pi\pi^*$ state and have the significant contribution of three-electron process $\pi^{-2}\pi^{*^2}$ compared to the C1*s* ionization. Peaks 3–9 are characterized as $5\sigma\sigma^*$ or $5\sigma n\sigma$ transitions interacting with the three-electron process of $n^{-2}\pi^{*^2}$ and $\pi^{-2}\pi^{*^2}$

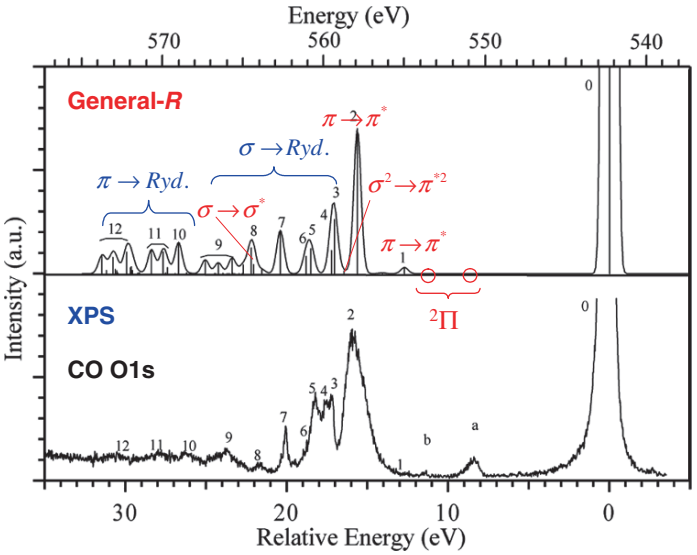

Fig. 4 O1*s* shake-up satellite spectrum of CO [13]

configurations. The broad continuous bands in the higher energy region are dominantly assigned to the transitions to the Rydberg orbitals.

2.5 *Geometry Changes and Vibrational Spectra of Inner-Shell Shake-Up Satellites*

For the C1*s* shake-up satellite peak at 8−9 eV above the mainline of CO, the angle-resolved ion-yield (ARIY) spectroscopy was applied to observe the vibrational structure. By measuring at the two different angles 0° and 90° relative to the polarization vector, space symmetry of the electronic states can be resolved; the measurement at 0° mainly observes the direct shake-up in Σ symmetry, while the measurement at 90° observes the conjugate shake-up in Π symmetry. However, since the Σ and Π states interfere with each other at the polarization angle of 0°, the separation of the symmetry is not complete in the spectrum at the measurement of 0°. Therefore, we decomposed the overlapping spectra using the SAC-CI calculations [9, 13].

We calculated the potential energy curves of the shake-up satellites in this energy region. Figure 5 shows the SAC-CI SDTQ-*R* potential energy curves of these satellites. One Σ^+ state and two Π states were found to exist in this energy region and the Δ and Σ^- states were also located in the higher region. The geometry change in the Σ^+ state is large since this state is characterized as the π–π^* excitation accompanied by the C1*s* ionization. On the other hand, two Π states are n–π^* transition and therefore, the structure relaxation of these two states is small. The Δ and Σ^-

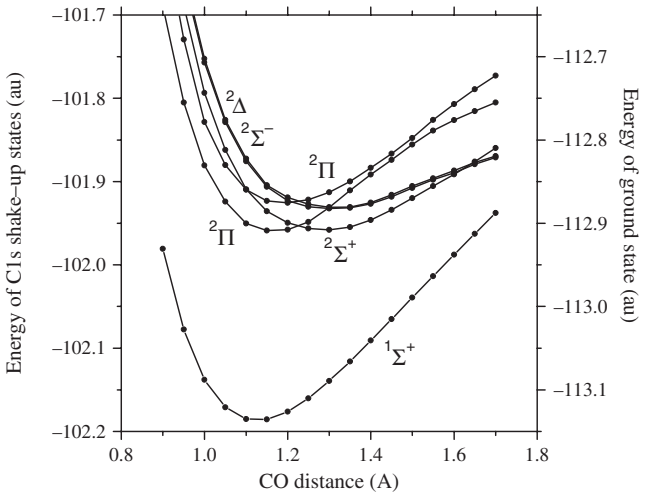

Fig. 5 Potential energy curves of the ground and C1*s* shake-up satellite states of CO calculated by the SAC/SAC-CI method [9]

states have the same character as the Σ^+ state and the potential curves of these states are very similar to that of the Σ^+ state.

Vibrational analysis was performed with the potential energy curves in Fig. 5. Figure 6 shows the theoretically decomposed vibrational spectra; the experimental spectra were successfully decomposed into one Σ^+ state and two Π states. Calculating the accurate vibrational spectra of the Σ and Π states theoretically, the experimental Σ spectrum was obtained as $I(0)$–$c \times I(90)$, where $I(0)$ and $I(90)$ are the spectral distributions of the 0° and 90° measurement, respectively, and c=0.4 was selected with the help of the SAC-CI calculations. The satellite Σ^+ state shows the excitation to the high vibrational levels reflecting the large geometry change, while the vibrational excitations are not prominent in the two Π states. The vibronic coupling is sometimes relevant for the core-ionized states. In the present case, two Π states are relatively separated in the FC region and the independent vibrational analysis for each state is reasonable. The Δ and Σ^- states may contribute to the higher energy region of the band, but they are not prominent.

2.6 Strong Valence–Rydberg Coupling in Inner-Shell Excited States

ARIY spectra were also measured in the O K edge of N_2O [15]. The first ARIY spectra of N_2O were investigated in 1995 with the help of *ab initio* calculations [33]. Figure 7 shows the ARIY spectra measured at the angles of 0° and 90° compared

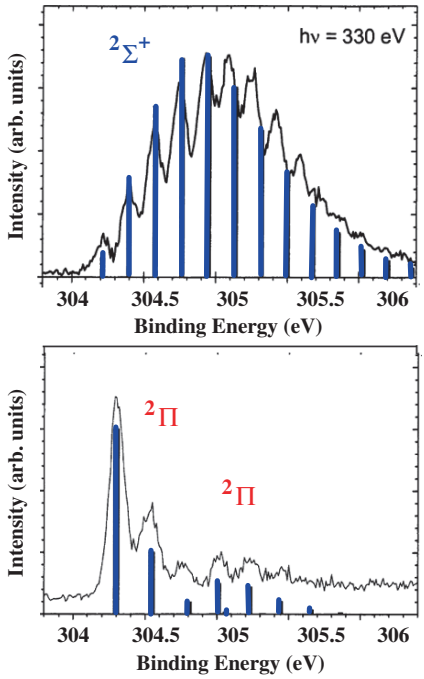

Fig. 6 Vibrational spectra of the C1*s* shake-up satellite states of CO decomposed by the SAC-CI method [9]. The SAC-CI spectrum was shown with the *vertical lines*

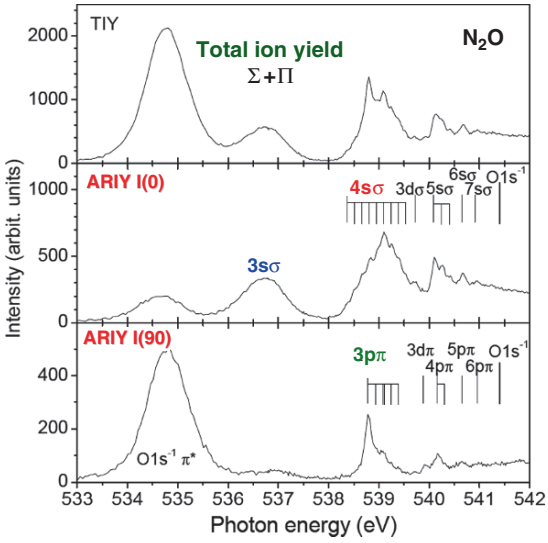

Fig. 7 Angle-resolved ion-yield (ARIY) spectra of O1*s* excitations of N_2O measured at 0° and 90° compared with the total ion-yield (TIY) spectrum [15]

with the total ion-yield measurement. The measurement at 0° mainly observes the Σ states, while the measurement at 90° observes Π states. As shown in Fig. 7, in the Rydberg $4s\sigma$ state, irregular excitation to the higher vibrational levels was observed [15].

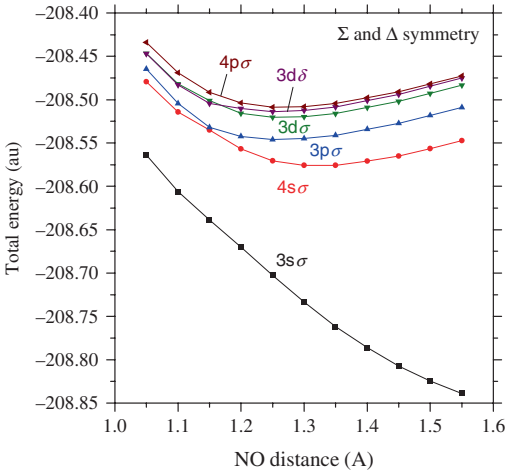

Fig. 8 Potential energy curves of the O1s excited states of N_2O with the cut of $R_{NN} = 1.1$ Å [15]

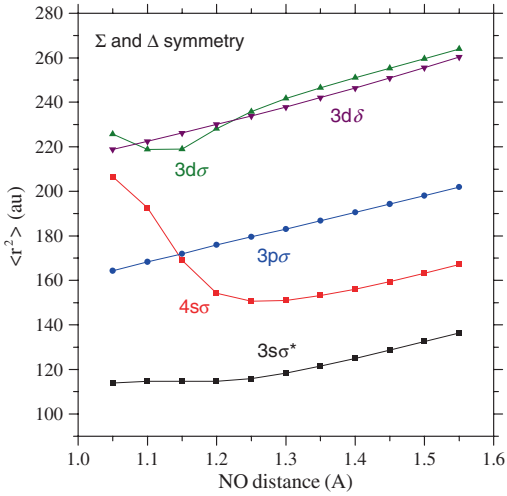

Fig. 9 Electronic part of the second moments $< r^2 >$ of the O1s excited states of N_2O with the cut of $R_{NN} = 1.1$ Å [15]

For clarifying this irregular vibrational progression, the potential energy surfaces of the O1s core-excited states were examined [15]. In the SAC-CI calculations, the equivalent-core approximation was adopted and the direct SAC-CI algorithm [34] was used. Figures 8 and 9 show the potential energy curves and the electronic part of the second moments $<r^2>$, respectively, for the O1s excited states in Σ and Δ symmetry along the R_{NO} distance. The second moment $<r^2>$ of the $4s\sigma$ state drastically decreases in the large R_{NO} distance and this shows that the strong valence–Rydberg coupling occurs in the $4s\sigma$ state having σ^* component. Due to this strong valence–Rydberg coupling, the $4s\sigma$ state has the potential minimum at large

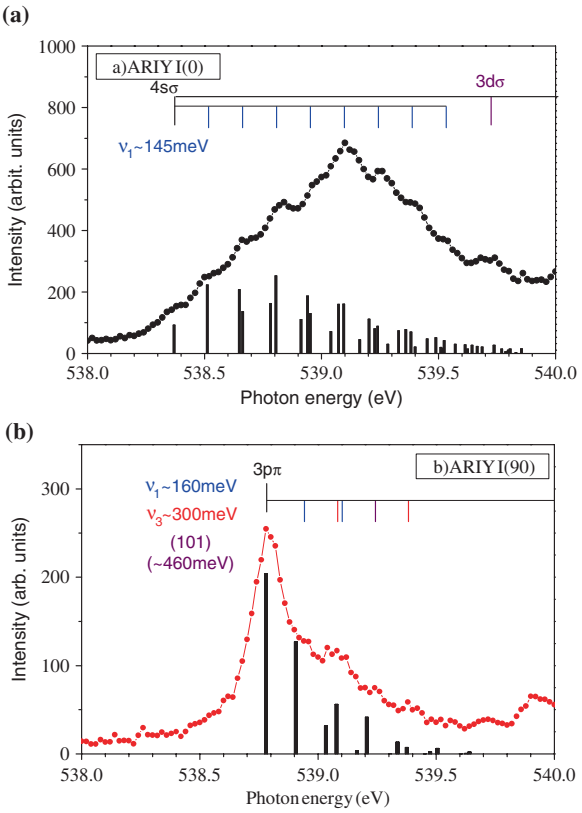

Fig. 10 Vibrational spectra of (a) O1s–4$s\sigma$ and (b) O1s–3$p\pi$ excited states of N_2O. The SAC-CI spectra are shown by the *vertical solid lines* [15]

R_{NO} distance. Thus, we conclude that the irregular Rydberg behavior in the 4$s\sigma$ state is caused by the strong valence–Rydberg coupling.

Based on the SAC-CI two-dimensional potential energy surfaces, Franck–Condon analysis was performed for the 4$s\sigma$ and 3$p\pi$ states. Theory reproduced the observed vibrational excitations satisfactorily as shown in Fig. 10. The higher vibrational levels are excited in the 4$s\sigma$ state, while the vibrational spectrum of the 3$p\pi$ state shows the standard Rydberg-type vibrational progression. For the deviation of the 4$s\sigma$ state, the 3$p\sigma$ state may contribute to the higher energy region and the vibronic coupling among these states is important.

2.7 Thermal Effect in Inner-Shell Excitation Spectra

Absorption spectra of the vibrationally excited "hot" molecules were observed for the O1s excitations of N_2O. The absorption spectra were measured at 300/700 K and

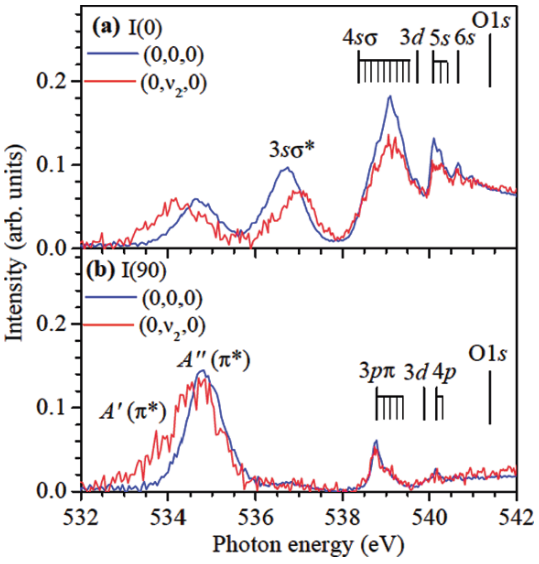

Fig. 11 ARIY spectra in the N_2O O1*s* excitation region: *blue* and *red lines* show the spectra from vibrationally ground and excited states, respectively [17]

the vibrationally excited absorption spectrum was extracted assuming the Boltzmann distribution (Fig. 11) [17]. Comparing the spectra of (0,0,0) and (0,v_2,0), the intensity of the $ns\sigma$ Rydberg series is significantly suppressed, while that of the $A'(\pi)$ state is enhanced in the excitation from the vibrationally excited states (0,v_2,0). These observations suggest that the decrease in the bond angle causes a decrease in the mixing of the valence character that enhances the transition probability to the Rydberg states. Energy shift was also observed in the spectra from the vibrationally excited states.

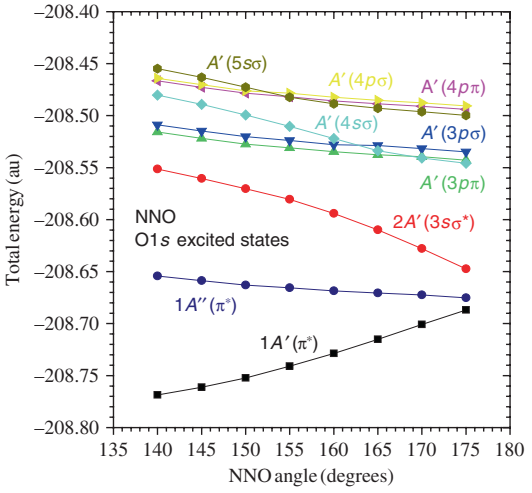

Fig. 12 Potential energy curves of the low-lying O1*s* excited states of N_2O along the bending coordinate [17]

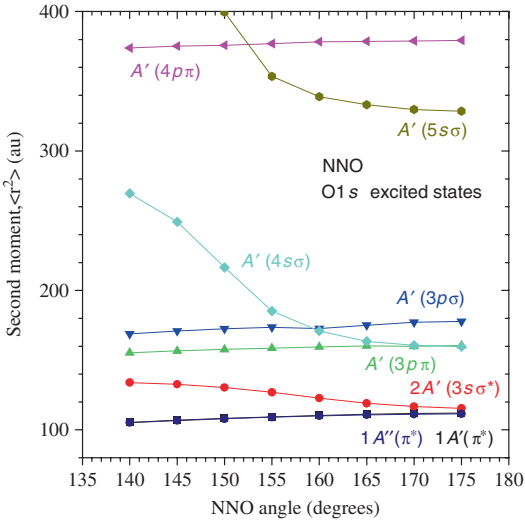

Fig. 13 Electronic part of the second moments $<r^2>$ of the low-lying O1s excited states of N_2O along the bending coordinate [17]

In order to understand these phenomena, we executed the SAC-CI calculations of the energies and the second moment $<r^2>$ of the O1s excited states varying the bond angle [17]. Figure 12 shows the cuts of the calculated potential energy surfaces of the O1s excited states of A' symmetry. The $1A'$ state correlates with the π^* state and stabilizes along the bending coordinate. All other states are stable in the linear structure. A characteristic curve crossing occurs between the σ and π Rydberg states along the bending coordinate. These potential curves explain the red shift of the π^* state and the blue shift of $3s\sigma$ and $4s\sigma$ states. In order to analyze the mixing of the valence character in the Rydberg states, we examined the second moment $<r^2>$, which is anticorrelated with the amount of valence character (Fig. 13). The second moments of the $3s\sigma$, $4s\sigma$, and $5s\sigma$ states become large as the molecule becomes bent. This indicates that the mixing of the valence character in these states becomes less as the bond angle decreases. Consequently, the absorption oscillator strength to the $ns\sigma$ Rydberg states becomes small. These results confirm the interpretation of the intensity changes observed for excitation from vibrationally excited molecules.

As seen in Fig. 12, the $A'(\pi^*)$ state stabilizes along the bending coordinate, whereas the $3sA'$ state destabilizes more than the $A''(\pi^*)$ state. This anticorrelation indicates that the $A'(\pi^*)$ and $3sA'$ states are strongly coupled. This coupling opens a flow of the valence character from the $3sA'$, $4sA'$, and $5sA'$ Rydberg states to the $A'(\pi^*)$ state. Analyzing the MOs which contribute to the excitations, we concluded that the counterpart of the decrease in the mixing of the valence character in the $3s$, $4s$, and $5s$ states is an increase in the $s\sigma$-type character of the $a'(\pi^*)$ orbital.

Based on the SAC-CI calculations of the electronic part of the second moment $<r^2>$, the suppression is interpreted as being due to a decrease in the mixing of the valence character in the $ns\sigma$ Rydberg states with decreasing bond angle.

3 Photochemistry of Organic Light-Emitting Diodes and Biological Chemosensor

Organic light-emitting diodes are one of the promising candidates for the next generation electro-optical devices such as panel display. Theoretical prediction of the photo-physical properties of the OLED is relevant for the molecular design. The excited-state chemistry of the OLED contains the interesting issue like localization/delocalization of the excitation and the effect of the flexible conformation. We have studied the absorption and emission spectra and the excited-state dynamics of some OLED molecules like poly *para*-phenylene vinylene [19] and fluorene-thiophene [20].

The biological chemosensor has also been focused and extensively investigated since they enable the direct detection of the physiologically active substances in cell and real-time monitoring of enzyme activities without influencing the proteins so much. The photochemistry of some fluorescent probes is interesting since they are controlled by the photo-induced electron transfer. We have investigated the photochemistry of the biological chemosensor which probes the anion species.

3.1 Electronic Spectra and Excited-State Geometries of Poly Para-Phenylene Vinylene

The optical properties of poly *para*-phenylene vinylene (PPV) that is well known as an efficient light emitter have been extensively investigated [35–40], however, the accurate theoretical prediction of the transition energies is still challenging. The electronic spectra and excited-state geometries of the PPV oligomer (Fig. 14) were investigated by the SAC-CI SD-*R* method. The calculated absorption and emission energies of the lowest singlet excited state of PPV*n* ($n = 1$–4) are compared with the experimental values [36] and other theoretical values [37, 38] in Fig. 15. The SAC-CI method predicted the experimental values in high accuracy; the mean deviations are 0.09 eV for absorption and 0.03 eV for emission. The method reproduced the chain length dependence of the excitation energy better than the TDDFT/B3LYP calculations. The conventional TDDFT should be carefully used for the transition energies of the molecules with long π-conjugated chains.

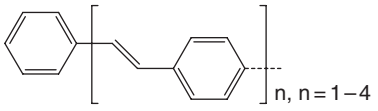

Poly-*para*-phenylene vinylene (PPVn)

Fig. 14 Molecular structure of PPV*n* oligomer

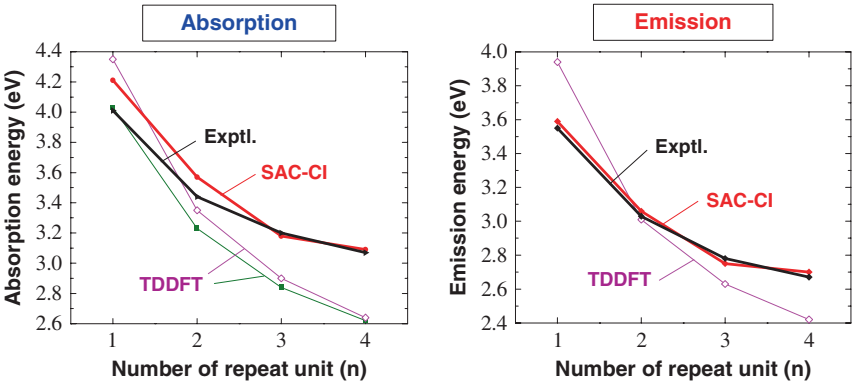

Fig. 15 Excitation (*left*) and emission (*right*) energies of the S_1 state of PPV*n* (n=1–4) plotted to the repeat unit n [19]

The ground-state and lowest singlet (S_1) and triplet (T_1) excited-state structures of PPV*n* were calculated to be planar by the SAC-CI method. The calculated ground-state geometry agrees very well with the experimental values; the deviations are within 0.005 Å and 0.07° for the bond length and bond angle, respectively, for PPV1. The changes in bond length (Δr) along the CC conjugation due to singlet and triplet excitations of PPV1 are shown in Fig. 16. In the S_1 and T_1 states, the central vinylene C═C bond length increases, whereas the vinylene C–C bond length

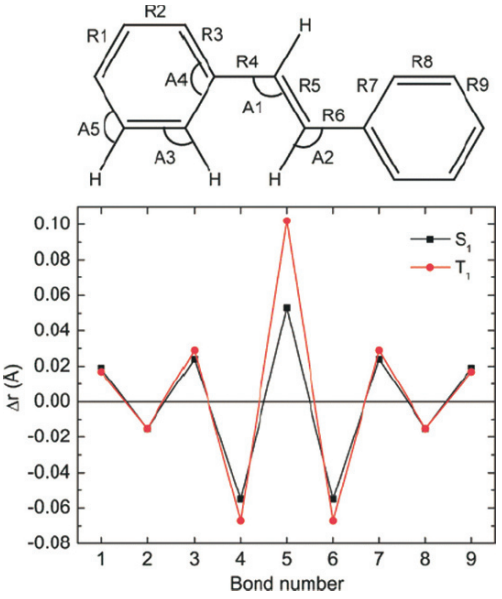

Fig. 16 CC bond length changes in the S_1 and T_1 states of PPV1 [19]

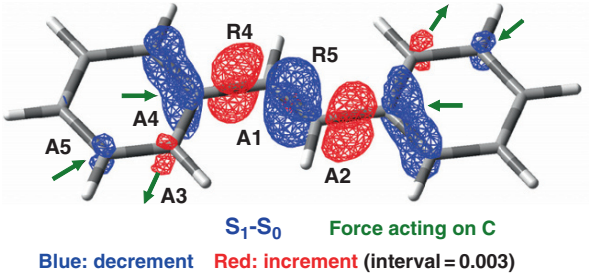

Fig. 17 Electron density difference between the S_0 and S_1 states calculated by the SAC/SAC-CI method [19]

decreases. These changes are localized in the central part of the PPV*n* oligomers. The bond length alternation changes significantly in the excited states from that of the ground state. Larger bond length changes were obtained for the T_1 state than for the S_1 state.

These changes in the geometry due to excitation can be explained using the electrostatic force (ESF) theory [41, 42]. In ESF theory, the geometric relaxation in the excited state can be explained by the force acting on nuclei caused by changes in the electron distribution. Molecular shape in the ground and excited states is determined by the balance of the atomic dipole (AD), exchange (EC), and gross charge (GC) forces. The SAC/SAC-CI electron density difference between the ground and S_1 states due to excitation of PPV1 is shown in Fig. 17. The electron density in the central vinylene C=C bond region decreases and that in the vinylene C–C bond region increases. More precisely, the electron density in the σ-bond region increases and that in the π-bond region decreases; this is a general trend in these PPV*n* molecules. The EC force along the central vinylene C=C bond decreases because of the decrement of electron density in the C=C bond region, whereas the EC force is enhanced along the vinylene C–C bond. Consequently, the central vinylene C=C bond length increases and the vinylene C–C bond length decreases. The accumulations (depletions) of electron density in the vicinity of C nuclei also explain the bond angle change in the excited states. For example, in PPV1, angle A3 (Fig. 17) is enlarged in the singlet excited state (119.4°) from that in the ground state (118.3°) as a result of an accumulation of electron density in the region of the associated C nucleus.

3.2 Conformational Effect of Fluorene-Thiophene and Its Derivative on Electronic Spectra

The fluorene co-polymers constitute rigorous candidates for the flexible and tunable light-emitting diodes [43–45]. By introducing the suitable substituents, the optical properties can be controlled because of its flexible structure. In particular, fluorene-thiophene co-polymers have been focused since they are the candidates for the

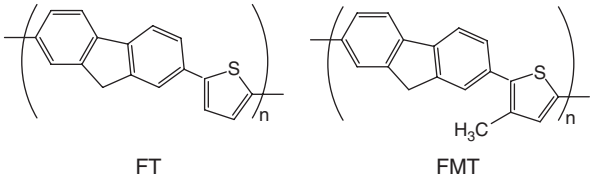

Fig. 18 Molecular structures of the FT and FMT oligomers

blue-light emitter. The unit of these co-polymers, fluorene-thiophene (FT), and fluorene-methyl-thiophene (FMT) (Fig. 18) show the characteristic electronic spectra [43]. The energy region of the absorption spectrum is almost the same; however, the shape of the electronic spectra of these molecules is different. To interpret the difference of the spectra, the ground and excited states of these molecules and the conformational effect on the electronic spectra were investigated by the SAC-CI method [20]. The FT and FMT monomers were examined for elucidating the essence of the spectrum shape, and the electronic spectra up to trimers were calculated.

The ground-state potential energy curves of the FT and FMT monomers along the torsion angle are shown in Fig. 19. The dihedral angles of the most stable conformation of FT and FMT are $\theta = 27^\circ$ and 43°, respectively. These molecules have very flexible structure with regard to the torsion. The potential energy curves are very flat for the torsion; the relative energy of the conformers for $\theta = 0^\circ$–60° is within about 1.0 kcal/mol. This low rotational energy barrier indicates that it allows a wide range of nonplanar conformation of these molecules at room temperature.

The optical properties of the low-lying excited states of these molecules are dependent on the torsion angle. The excitation energy and oscillator strength as the function of the torsion angle are displayed in Fig. 20. The first to third excited states interact with each other along the torsion. The avoided crossing occurs between the first and third excited states in the region of $\theta = 30$–60°; this interaction is clearly seen in the oscillator strength.

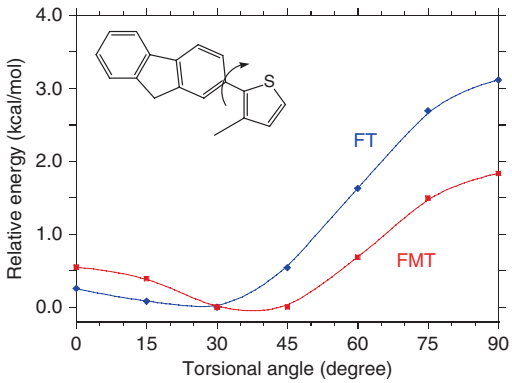

Fig. 19 The ground-state potential energy curves of the FT and FMT monomers [20]

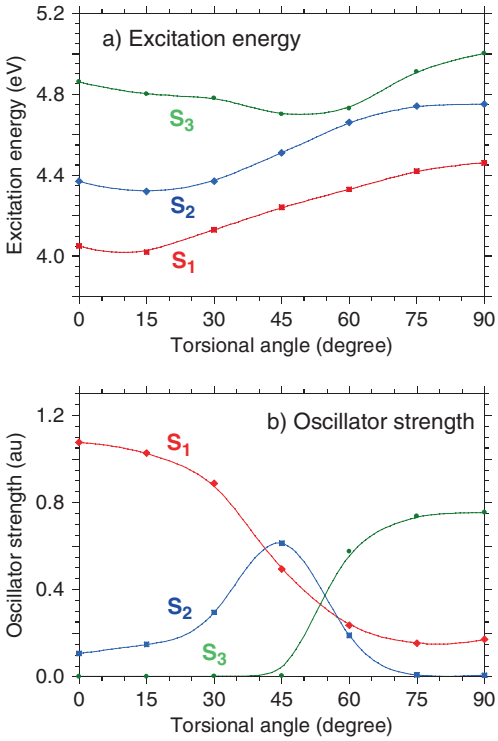

Fig. 20 SAC-CI (**a**) excitation energy and (**b**) oscillator strength of the lowest three excited states of FT versus torsion angle [20]

Since the ground-state potential energy surfaces are flat for the torsion and the excitation spectra are dependent on this coordinate, thermal average of the conformers should be considered in order to simulate the absorption spectra. The simulated absorption spectra of FT and FMT, in which thermal distribution at 298 K is taken into account, are compared with the experimental spectra in Fig. 21. The simulated spectra with thermal average showed excellent agreement with the experimental spectra. For FT, the contribution of the conformer whose torsion angle is up to $\theta = \sim 30^\circ$ is dominant and the asymmetric spectrum is obtained. In the case of FMT, the strong shoulder was measured in the higher energy side of the peak. This shoulder is attributed to the second excited state of the conformer of θ=30–45°.

The SAC-CI calculations show that the thermal average of the conformers is important to interpret the electronic spectra of the fluorene-thiophene co-polymer.

3.3 Photochemistry of Biological Chemosensor

The fluorescent artificial chemosensor has been focused since they can directly detect the physiological active substances in cell and enables real-time monitoring of enzyme activities. In this field, probes of anions are the most relevant and

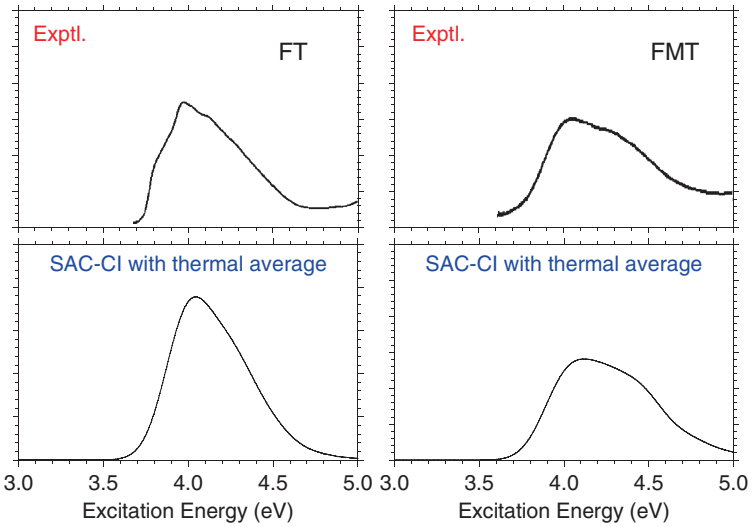

Fig. 21 Experimental and SAC-CI absorption spectra of FT and FMT [20]

difficult issue. Recently, novel molecular fluorescent probes which can selectively recognize the phosphodiesters have been developed [46, 47]. One of these fluorescent probes, acridine-based probe, shows drastic fluorescence change in the presence of Zn^{2+} ion. The photochemistry of this acridine-based fluorescent probe has been investigated by the SAC-CI method, in particular for the electronic mechanism of the photo-induced electron transfer and the origin of the energy shift in the fluorescence. First, the stable structures of the mono-nuclear and bi-nuclear Zn(II) complexes were determined with the density functional theory. The fivefold structure was most stable for the mono-nuclear complex and threefold+threefold structure was stable for the bi-nuclear complex. The fluorescence of this probe molecule is controlled by the photo-induced electron transfer. For the photo-induced electron transfer, relative energy of the charge transfer state and $\pi\pi^*$ excited state is very important. The solvation effect and the geometry relaxation were found to be relevant for these states. These two factors control the photo-induced electron transfer of this fluorescent probe. Characteristic energy shift of the fluorescence was found to be determined by the location of the Zn(II) ion in the fluorescent acridine unit.

4 Summary

The SAC-CI method has been applied to the theoretical spectroscopy of the inner-shell electronic processes and the photochemistry of the organic light-emitting diodes and biological chemosensor.

Various kinds of the core-electronic processes such as core-electron ionizations, shake-up satellites, vibrational excitations, and valence–Rydberg coupling have been investigated by the SAC-CI general-R method. The general-R method calculated the core-electron binding energies and the shake-up satellite spectra very accurately. The method also predicted the geometry changes of the core-hole states and the shake-up satellites and reproduced the vibrational spectra of these states. The irregular vibrational progressions observed in the O1s–4$s\sigma$ excited state of N_2O and the thermal effect of the O1s absorption spectra were elucidated in terms of the valence–Rydberg coupling.

The SAC-CI method has also predicted the absorption and emission spectra of the organic light-emitting diodes in high accuracy. The geometry changes in the excited states of PPV were interpreted with the ESF theory. For FT and FMT, the thermal average was shown to be important to simulate the electronic spectra. The method clarified the electronic mechanism of the photo-induced electron transfer of the acridine-type fluorescent probe. The solvation effect and geometry relaxation in the charge transfer state and the $\pi\pi^*$ excited state were found to be essential.

Acknowledgments The authors are grateful to Prof. K. Ueda for the works on the inner-shell electronic processes, to Drs. B. Saha, P. Poolmee, and S. Hannongbua for the works of OLED, and to Prof. I. Hamachi and Dr. A. Ojida for the work on biological chemosensor. This study was supported by JST, CREST, and a Grant-in-Aid for Scientific Research in Priority Areas "Molecular Theory for Real Systems" from the Ministry of Education, Culture, Sports, Science and Technology of Japan.

References

1. H. Nakatsuji, Chem. Phys. Lett. **59**, 362 (1978)
2. H. Nakatsuji, Chem. Phys. Lett. **67**, 329 (1979)
3. H. Nakatsuji, *SAC-CI method: Theoretical Aspects and Some Recent Topics*, in *Computational Chemistry, Review of Current Trends*, ed. by J. Leszczyński (World Scientific, Singapore, 1997), Vol. 2, p. 62
4. M. Ehara, J. Hasegawa, H. Nakatsuji, *SAC-CI Method Applied to Molecular Spectroscopy*, in *Theory and Applications of Computational Chemistry: The First 40 Years*, eds. by C.E. Dykstra, G. Frenking, K.S. Kim, G. E. Scuseria (Elsevier, Oxford, 2005), p. 1099
5. M. J. Frisch et al., *GAUSSIAN03* (Gaussian Inc., Pittsburgh, PA, 2003)
6. R. Sankari, M. Ehara, H. Nakatsuji, Y. Senba, K. Hosokawa, H. Yoshida, A.D. Fanis, Y. Tamenori, S. Aksela, K. Ueda, Chem. Phys. Lett. **380**, 647 (2003)
7. K. Kuramoto, M. Ehara, H. Nakatsuji, J. Chem. Phys. **122**, 014304 (2005)
8. K. Kuramoto, M. Ehara, H. Nakatsuji, M. Kitajima, H. Tanaka, A.D. Fanis, Y. Tamenori, K. Ueda, J. Electron Spectrosc. Relat. Pheonom. **142**, 253 (2005)
9. K. Ueda, M. Hoshino, T. Tanaka, M. Kitajima, H. Tanaka, A.D. Fanis, Y. Tamenori, M. Ehara, F. Oyagi, K. Kuramoto, H. Nakatsuji, Phys. Rev. Lett. **94**, 243004 (2005)
10. M. Matsumoto, K. Ueda, E. Kukk, H. Yoshida, T. Tanaka, M. Kitajima, H. Tanaka, Y. Tamenori, K. Kuramoto, M. Ehara, H. Nakatsuji, Chem. Phys. Lett. **417**, 89 (2006)
11. R. Sankari, M. Ehara, H. Nakatsuji, A.D. Fanis, S. Aksela, S.L. Sorensen, M.N. Piancastelli, K. Ueda, Chem. Phys. Lett. **422**, 51 (2006)

12. M. Ehara, H. Nakatsuji, M. Matsumoto, T. Hatamoto, X.-J. Liu, T. Lischke, G. Prümper, T. Tanaka, C. Makochekanwa, M. Hoshino, H. Tanaka, J.R. Harries, Y. Tamenori, K. Ueda, J. Chem. Phys. **124**, 124311 (2006)
13. M. Ehara, K. Kuramoto, H. Nakatsuji, M. Hoshino, T. Tanaka, M. Kitajima, H. Tanaka, Y. Tamenori, A.D. Fanis, K. Ueda, J. Chem. Phys. **125**, 114304 (2006)
14. T. Hatamoto, M. Matsumoto, X.-J. Liu, K. Ueda, M. Hoshino, K. Nakagawa, T. Tanaka, H. Tanaka, M. Ehara, R. Tamaki, H. Nakatsuji, J. Electron Spectrosc. Relat. Phenom. **155**, 54 (2007)
15. T. Tanaka, R. Feifel, H. Tanaka, M. Hoshino, M. Kitajima, L. Karlsson, K. Ueda, M. Ehara, R. Fukuda, R. Tamaki, H. Nakatsuji, Chem. Phys. Lett. **435**, 182 (2007)
16. M. Ehara, R. Tamaki, H. Nakatsuji, R. R. Lucchese, J. Soderstrom, T. Tanaka, M. Hoshino, M. Kitajima, H. Tanaka, A. D. Fanis, K. Ueda, Chem. Phys. Lett. **438**, 14 (2007)
17. T. Tanaka, M. Hoshino, H. Kato, M. Ehara, N. Yamada, R. Fukuda, H. Nakatsuji, Y. Tamenori, J. R. Harries, G. Prümper, H. Tanaka, K. Ueda, Phys. Rev. A **77**, 012709 (2008)
18. M. Ehara, H. Nakatsuji, Coll. Czech. Chem. Commun **73**, 771 (2008)
19. B. Saha, M. Ehara, H. Nakatsuji, J. Phys. Chem. A **111**, 5473 (2007)
20. P. Poolmee, M. Ehara, S. Hannongbua, H. Nakatsuji, Polymer **46**, 6474 (2005)
21. K. Siegbahn, C. Nordling, G. Johansson, J. Hedman, P.-F. Heden, K. Hamrin, U. Gelius, T. Bergmark, L. O. Werme, R. Manne, Y. Baer, *ESCA Applied to Free Molecules* (North-Holland, Amsterdam, 1969)
22. A.A. Bakke, A.W. Chen, W.L. Jolly, J. Electron Spectrosc. Relat. Phenom. **20**, 333 (1980)
23. H. Nakatsuji, Chem. Phys. Lett. **177**, 331 (1991)
24. M. Ehara, H. Nakatsuji, Chem. Phys. Lett. **282**, 247 (1998)
25. M. Ehara, M. Ishida, K. Toyota, H. Nakatsuji, *SAC-CI General-R method: Theory and Applications to the Multi-Electron Processes*, in *Reviews in Modern Quantum Chemistry*, ed. by K.D. Sen (World Scientific, Singapore, 2002)
26. Y. Ohtsuka, H. Nakatsuji, J. Chem. Phys. **124**, 054110 (2006)
27. P.S. Bagus, H. F. Schaefer III, J. Chem. Phys. **55**, 1474 (1971)
28. J.C. Slater, Adv. Quantum Chem. **6**, 1 (1972)
29. D.P. Chong, J. Chem. Phys. **103**, 1842 (1995)
30. A. Thiel, J. Schirmer, H. Köppel, J. Chem. Phys. **119**, 2088 (2003)
31. G. Angonoa, I. Walter, J. Schirmer, J. Chem. Phys. **87**, 6789 (1987)
32. G. Fronzoni, G.D. Alti, P. Devleva, J. Phys. B **32**, 5357 (1999)
33. J. Adachi, N. Kosugi, E. Shigemasa, A. Yagishita, J. Chem. Phys. **102**, 7369 (1995)
34. R. Fukuda, H. Nakatsuji, J. Chem. Phys. **128**, 094105 (2008)
35. J.H. Burroughes, D.D.C. Bradley, A.R. Brown, R.N. Kckay, R.H. Friend, P.L. Burn, A.B. Holmes, Nature **347**, 539 (1990)
36. J. Gierschner, H.-G. Mack, L. Luer, D. Oelkrug, J. Chem. Phys. **116**, 8596 (2002)
37. A. Pogantsch, G. Heimel, E. Zojer, J. Chem. Phys. **117**, 5921 (2002)
38. Y. Han, S.U. Lee, J. Chem. Phys. **121**, 609 (2004)
39. A. Shukla, H. Ghosh, S. Mazumdar, Phys. Rev. B **67**, 245203 (2003)
40. S. Karabunarliev, M. Baumgarten, K. Mullen, J. Phys. Chem. A **104**, 8236 (2000)
41. H. Nakatsuji, J. Am. Chem. Soc. **95**, 345 (1973)
42. H. Nakatsuji, T. Koga, *The Force Concept in Chemistry* (Van Nostrand Reinhold, New York, 1981)
43. M. Belletete, S. Beaupre, J. Bouchard, P. Blandin, M. Leclerc, G. Durocher, J. Phys. Chem. B **104**, 9118 (2000)
44. M. Belletete, M. Bedard, M. Leclerc, G. Durocher, J. Mol. Struct.: THEOCHEM **679**, 9 (2004)
45. V. Lukes, D. Wegh, P. Hrdlovic, M. Stefko, K. Matsuzna, V. Laurinc, Syn. Met. **148**, 179 (2005)
46. A. Ojida, I. Hamachi, Bull. Chem. Soc. Jpn. **79**, 35 (2006)
47. A. Ojida, Y. Miyahara, J. Wongkongkatep, S. Tamaru, K. Sada, I. Hamachi, Chem. Asian J. **1**, 555 (2006)

Electron-β-Nuclear Spectroscopy of Atoms and Molecules and Chemical Bond Effect on the β-Decay Parameters

Alexander V. Glushkov, Olga Yu. Khetselius, and Ludmila Lovett

Abstract We discuss the cooperative electron β-nuclear processes in atoms and molecules, including the excitation, ionization, electronic rearrangement, induced by the nuclear reactions and β-decay. The relativistic many-body perturbation theory (PT) with the optimized Dirac–Kohn–Sham (DKS) zeroth approximation is used to calculate the β-decay parameters for a number of allowed (superallowed) transitions (^{33}P–^{33}S, ^{241}Pu–^{241}Am, etc.) and study a chemical bond effect on β-decay parameters. A few factors are taken into account: changing the integration limits in the Fermi function integral, energy corrections for different chemical substances and the possibility of the bound β-decay or other decay channels. We studied the electronic rearrangement induced by nuclear transmutation in the β-decay ${}^{6}_{2}\mathrm{He}_4 \rightarrow ({}^{6}_{3}\mathrm{Li}^{+}_{3})^{*} + e^{-} + \bar{\nu}_{e}$. The half-life period $T_{1/2}$ for β-decay of tritium atom (ion) has been estimated while taking into account the bound β-decay channel and some other accompanying effects. The estimated values of $T_{1/2}$ for the tritium β-decay and free triton decay are $(T_{1/2})_a = 12.26$ years (correction due to the electron-atomic effects $(\Delta T_{1/2}/T_{1/2})_a = 0.82\%$) for the tritium atom and $(T_{1/2})_t = 12.36$ years for the triton decay. These data are in physically reasonable agreement with experimental data. We first present the value $T_{1/2}$ in a case of the β-decay in the halogen-containing molecular tritium (^{3}HCl): $(T_{1/2})_m$=12.28 years (^{3}HCl) and the correction due to the chemical bond effect is $(\Delta T_{1/2})_{am}$=0.024 (i.e. 0.20%).

Keywords: Atomic and molecular systems · Electron-β-nuclear spectroscopy · Beta decay parameters · Chemical bond effect

A.V. Glushkov (✉)
Odessa University, Odessa-9, 65009, Ukraine; Russian Academy of Sciences, Troitsk, 142090, Russia, e-mail: glushkov@paco.net

O.Yu. Khetselius
Odessa University, Odessa-9, 65009, Ukraine; Russian Academy of Sciences, Troitsk, 142090, Russia

L. Lovett
UK National Academy of Sciences and Bookdata Co., London SW1Y 5AG, UK

P. Piecuch et al. (eds.), *Advances in the Theory of Atomic and Molecular Systems*, Progress in Theoretical Chemistry and Physics 20, DOI 10.1007/978-90-481-2985-0_7,

1 Introduction

Methods for influencing the radioactive decay rate have been sought from the first year of formation of nuclear physics. β-decay strengths influence nuclear transmutations, the pathways of stellar nucleosynthesis in stars and the resulting abundance of atomic nuclei. Nuclear transmutation (i.e. change in the nuclear charge) induced by nuclear reactions of radioactivity is often accompanied by a redistribution of the electrons around the final transmuted nucleus. Electrons originally in the ground state of the target atom (molecule) can be excited either in the bound spectrum or to the continuum of energy. Calculations of the population distribution of the atomic states of the daughter atom require a complete description of both the bound spectrum and the continuum of energy. Calculation of the β-decay parameters while taking into account the cooperative electronic processes (an interaction between beta particle, generated by an atomic nucleus, and the electron shells, which surround a beta active nucleus in the atomic or molecular system) and the chemical environment contribution is now of a great theoretical and experimental interest (see, for details, Refs. [1–148]). Discrepancies in the experimental data for parameters of the β-decay in the heavy radioactive nuclei can be partly explained by contributions of the cooperative electron-nuclear processes and chemical bond effect. Naturally, the problem of detecting a neutrino mass is of a great importance. The possible source of the corresponding data about it is the β-decay spectrum shape. As it is well known, neutrinos were postulated by Pauli (1930) to properly explain the β-decay of the free neutron $n \rightarrow p + e^{-} + \bar{\nu}_{e}$ without violating energy-momentum conservation. In recent years new experimental feasibilities have allowed for improvements in the measurement of the β-decay parameters resulting in a more accurate definition of the neutrino mass [1–16]. These data are especially important for standardization of the β-decay parameters for a whole number of the heavy radioactive nuclei [1–16, 24, 29–31]. It is interesting to note that discrepancies in data on the half-life period for ^{241}Pu are not explained hitherto, though quite a reasonable comment is connected with taking into account the bound β-decay channel, etc. (see Refs. [3–13, 15, 31, 41]). The population distribution of the atomic states of the daughter atom requires a complete and correct description of the cooperative electron-nuclear processes and chemical environment effect on the β-decay parameters [1–19, 24, 29–31]. One has to consider the following effects: (i) Changing the electron wave functions because of the changing atomic electric field; changing the valence shell occupation numbers in different chemical substances. (ii) The integration limits (calculating the Fermi integral function) are also changed in a case of the different chemical substances; as a rule, β-particle and neutrino take away the difference between the initial and transmuted final nuclei, provided by the nuclear and electronic rearrangement. One must also mention the additional channel, when β-electron occupies a free state in the bound atomic spectrum. Approaches implemented up to now can be characterized as force ones using, first of all, the change in energy balance of radioactive decay: creation of isomeric states, variation of energy of the chemical bond in molecules with radioactive atoms and β-decay to bound states in the ionized atoms [1–37, 29–31, 42–76].

The last channel was discovered for the first time in experiments on the synchrotron and SIS/ESR (GSI, Germany), when the bound β-decay $^{163}Dy^{66+} \rightarrow {}^{163}Ho^{66+}$ was studied by using the technology of the highly or fully ionized atomic beams (multicharged ions) [5, 6, 42]. In fact, the β-transition $Dy^{66+} \rightarrow Ho^{66+}$ was observed, which is accompanied by a capture of the β-particle on the K and L shell levels in the bound spectrum of the daughter atom. In fact, the complete ionization of ^{163}Dy in the storage ring of a heavy ion accelerator makes its β-decay to the K-shell of ^{163}Ho possible, with a half-life of 47 days, while in the neutral atom this decay is energetically forbidden [6]. The similar effect was obtained for ^{187}Re [7]. The authors of Ref. [7] observed the bound-state β-decay of fully ionized ^{187}Re nuclei circulating in a storage ring. Let us remember also that such an effect may be responsible for creation of elements in the space and astrophysical plasma (see details in Refs. [10–16, 124, 143, 144]). The authors of Ref. [8] reported the first measurement of a ratio $\lambda_{\beta b}/\lambda_{\beta c}$ of bound-state ($\lambda_{\beta b}$) and continuum-state ($\lambda_{\beta c}$) β-decay rates for the case of bare $^{207}Tl^{81+}$ ions. These ions were produced at the GSI fragment separator FRS by projectile fragmentation of a ^{208}Pb beam. In Ref. [4] the half-lives of isomeric states of fully ionized ^{144}Tb, ^{149}Dy and ^{151}Er were measured. These nuclides were produced via fragmentation of about 900 MeV/u ^{209}Bi projectiles, separated in flight with the fragment separator (FRS) and stored in the cooler ring (ESR). The authors of Ref. [4] observed for the first time drastic increases of the half-lives of bare isomers by factors of up to 30 compared to their neutral counterparts. This phenomenon is due to the exclusion of the strong internal conversion and electron-capture channels in the radioactive decay of these bare nuclei. The authors of Ref. [7] reported on the study of the dominating breakup channels involving $n\alpha^6$He or $3n2\alpha$ in the final state, with special emphasis dedicated in this contribution to the three-particle channel.

One could also mention the known change of the decay rate for ^{7}Be, which was measured most thoroughly. The change in the K-capture rate by $\sim 10^{-2}$ due to the influence of the energy of chemical bond and the atomic configuration of the environment (including measurements with ^{7}Be placed inside the fullerene C_{60}) was registered (see Refs. [10–12, 50–59, 62–68]). It has been experimentally and theoretically found that the chemical environment (chemical bond, pressure, etc.) effect resulted in changing ($\sim$ 0.1–1.0%) the corresponding decay constant. The helium isotope mass-spectroscopy method for measuring the triton decay constant for various cases of the electron environment was used to determine the tritium half-life without allowance for decay to beta-electron bound states and to calculate the respective reduced half-life in Ref. [9]. More intriguing effects are considered in a case of α-decay (see Refs. [13, 145–147]). Results on variation of the decay rate of Mössbauer isomers due to interference of electromagnetic waves in the system of the emitter and a screen from the same atom in the ground state situated at a distance of $\sim$2 mm seem quite impressive [146]. The values of the measured relative variation of the decay rate for ^{119m}Sn and ^{125m}Te reach $\sim$10%.

The elementary cooperative electron-β and γ-nuclear processes in atoms and molecules were considered in the pioneering papers by Migdal (1941), Levinger (1953), Schwartz (1953), Gol'dansky–Letokhov–Ivanov (1971–1976),

Kaplan–Markin–Yudin (1973–1975), reviews by Batkin–Smirnov (1980), papers by Freedman (1974), Carlson et al. (1968), Intemann (1983), Isozumi et al. (1977), Law–Campbell (1975), Martin–Cohen (1975), Mukouama et al. (1978), Law–Suzuki (1982) and Wauters–Vaeck (1997) et al. [1–5, 14, 43–60, 60–82, 120, 124]. The elementary cooperative electron-α-nuclear processes were considered in the papers by Levinger (1953), Hansen (1974), Watson (1975), Anholt–Amundsen (1982), Law (1977) and Mukoyama–Ito et al. (1988) (see Refs. [14, 43–60, 60–82, 120]). In this context, the known Mössbauer, Szilard–Chalmers and other cooperative effects should be mentioned [14, 60]. The consistent quantum electrodynamics (QED) theory of cooperative electron-γ-nuclear processes in atoms and molecules is developed in Refs. [25–28, 39, 40, 71–76]. In fact, it is possibly a reverse bridging between nuclear structure theory and quantum chemistry (atomic and molecular physics). Data on β-decay parameters can be used for studying the chemical bond nature, treating the spatial structure of molecular orbitals, identifying the electron states in some tritium-containing systems and diagnostics of the compounds by means of exchange of the hydrogen atoms by tritium ("tritium probe") [56, 57, 62–72].

In this chapter we discuss the cooperative electron-β-nuclear processes in atomic systems (e-β-nuclear spectroscopy), including the processes of excitation, ionization and electronic rearrangement, induced by nuclear reactions and β-decay. The relativistic many-body PT with the optimized DKS zeroth approximation and taking into account the nuclear, radiation, exchange-correlation corrections is used to calculate the β-decay parameters for a number of allowed (super allowed) transitions (^{33}P–^{33}S, ^{241}Pu–^{241}Am, etc.) and study the chemical bond effect on β-decay parameters. There are a few factors that have to be taken into account: changing the integration limits in the Fermi function integral, energy corrections for different chemical substances, and the possibility of the bound β-decay or other decay channels. We studied the electronic rearrangement induced by nuclear transmutation in the β-decay $^{4}_{2}\mathrm{He}_4 \rightarrow (^{6}_{3}\mathrm{Li}^{+}_{3})^{*} + e^{-} + \bar{\nu}_{\mathrm{e}}$. The half-life periods for β-transition in the tritium atom (molecule) are estimated by taking into account the bound β-decay channel correction and some other accompanying effects.

2 Calculation Method in a Theory of the β-decay and Cooperative Electron- β-Nuclear Processes

2.1 Introduction: General Formalism

As it is well known, the fundamental process behind β-decay is weak interaction of the down (up) quarks (for example, $\mathrm{d} \rightarrow \mathrm{u} + e^{-} + \bar{\nu}_{\mathrm{e}}$, etc.) via the exchange of virtual bosons [81.8 ($W^{\pm}$) and 91.2 (Z^{0}) GeV/c^2], opened in CERN (1983). The first theory of β-decay was proposed by Fermi (1934), who introduced the local (contact) 4-fermion interaction of the nucleons and leptons. Hamiltonian of the Fermi nucleon–lepton interaction is as follows:

$$H_\beta = G_\beta(\bar{\Psi}_p\gamma_\mu\Psi_n)(\bar{\Psi}_e\gamma^\mu\Psi_\nu). \quad (1)$$

Here G_β is the Fermi constant, $\Psi$are the four-component wave functions of the particles (solutions of the Dirac equation), $\bar{\Psi}_e = \Psi^+\gamma_0$, $\gamma^\mu$are the Dirac matrices, $\mu = 0,1,2,3,4$; $\gamma^0 = \gamma_0$; $\gamma^i = -\gamma_i$ $(i = 1,2,3)$. The nucleon–lepton interaction had purely vector form in the Fermi theory. The modern "V–A" theory usually uses an effective β-decay Hamiltonian which was introduced by Feynman and Gell-Mann:

$$H_\beta = \frac{G_\beta}{\sqrt{2}} J^\mu(x)L_\mu(x) + \text{c.c.}, \quad (2)$$

where J^μ is the nucleonic current, L_μ is the leptonic current and x is a spatial–temporal coordinate. Despite a great progress in development of the comprehensive theory for the nuclear β-decay (electroweak interactions), hitherto many practical questions are far from a satisfactory treatment. The further consistent calculations of the β-decay parameters that take into account accompanying cooperative effects are needed. The wide-spread quantum mechanical methods (such as the Hartree–Fock (HF) method, the random-phase approximation, the Coulomb approximation (CA), the Hartree–Fock–Slater (HFS) and Dirac–Fock (DF) methods, DFT etc.) are usually used in the atomic calculations and calculations of the β-allowed (superallowed) transitions parameters [1, 2, 11–16, 29–31, 80–133]. The difficulties of the corresponding calculations are well known (insufficiently correct account for exchange and correlation in the wave functions of β-particle, problem of gauge invariance, generation of the non-optimized bases of the wave functions for a discrete spectrum and continuum, etc.). The nuclear, relativistic, radiative corrections should be accurately taken into account too. As a rule, to estimate the β-spectrum shape and decay parameters, the special tables [15, 29–31] of the Fermi functions are usually used (the CA data). In some papers (see Refs. [13–16, 29–31]), the HFS approach that takes into account the nuclear finite size effect was used. In Ref. [15], the finite size correction was taken into account as correction to the CA calculation result and the screening effect was calculated within the atomic model potential scheme. In some papers (see Refs. [29–31] and references therein), the DF method is used. A gauge-invariant QED PT formalism for the calculation of the spectra and wave functions for heavy atoms while taking into account the relativistic, correlation, nuclear and QED effects has been developed in Refs. [24–28, 37–41, 76–82, 120, 122–124]. This formalism provides two optimized gauge-invariant (GI) calculation schemes with the DF (GIDF) and DKS (GIDKS) zeroth approximation. Below, the DKS scheme is used in our calculation.

As it is well known, a probability of the transition from the initial state $|\xi>$ with the energy E_ξ to some final state $<f|$ with the energy E_f per unit of time is defined as follows [15, 124]:

$$dW_{\xi,f} = (2\pi/\hbar)|<f|H|\xi>|^2(dN/dE)|_{E=E_0}, E_0 = E_f - E_\xi, \quad (3)$$

where the value (*dN/dE*) defines a density of the final states of a system per unit of energy and the corresponding matrix element is

$$< f|H|\xi >= \int \psi_f H_\beta \psi_\xi d^3 r_1 \ldots d^3 r_A, \tag{4}$$

where H_β is the interaction Hamiltonian and ψ_ξ, ψ_f are the wave functions of the initial and final states correspondingly. The expression for a number of the β-, $\tilde{\nu}$-particles with energy in the interval from E till $E+dE$ is as follows:

$$dW_{\xi f} = \frac{1}{2\pi^3 \hbar^7 c^5} \left| < f|H_\beta|\xi > \right|^2 \sqrt{E_e^2 - m^2 c^4} E_e (E_0 - E_e)^2 \, dE_e, \tag{5}$$

$$dW_{\xi f} = \frac{1}{2\pi^3 \hbar^7 c^5} \left| < f|H_\beta|\xi > \right|^2 \sqrt{(E_0 - E_{\tilde{\nu}})^2 - m^2 c^4} (E_0 - E_{\tilde{\nu}}) E_{\tilde{\nu}}^2 dE_{\tilde{\nu}}. \tag{6}$$

Further we will study the allowed and super allowed β-transitions. The contribution of these transitions is most significant to the resulting spectrum of the β-decay. At the same time, the forbidden transitions contribution is usually about a few per cent of the total intensity. Distribution of β-particles on energy in a case of the allowed transitions is as follows:

$$dW_\beta(E)/dE = \frac{1}{2\pi^3} G^2 \cdot F(E, Z) \cdot E \cdot p \cdot (E_0 - E)^2 \cdot |M|^2. \tag{7}$$

Here E and p=$(E^2–1)^{1/2}$ are the total energy and pulse of β-particle, respectively; E_0=1+$(E_b/m_e c^2)$, E_b is the boundary energy of β-spectrum; $|M|$ is a matrix element, which is not dependent on an energy in a case of the allowed β-transitions. The Fermi and integral Fermi functions are defined as follows [13, 29, 124]:

$$F(E, Z) = \frac{1}{2p^2}(g_{-1}^2 + f_{+1}^2), \tag{8}$$

$$f(E_0, Z) = \int_1^{E_0} F(E, Z) \cdot E \cdot p \cdot (E_0 - E)^2 dE. \tag{9}$$

Here f_{+1} and g_{-1} are the relativistic electron radial functions; the indexes $\pm 1 = \chi$, where $\chi = (l - j)/(2j + 1)$. The half-life period can be defined as follows:

$$T_{1/2} = 2\pi^3 ln2/[G_\beta^2 |M|^2 f(E_0, Z)]. \tag{10}$$

Here two calculation schemes are usually used: (i) The relativistic electron radial wave functions are calculated on the boundary of the spherical nucleus with radius R (see [13, 14]). (ii) The values of these functions in zero are used [24, 29–31].

2.2 The DKS Basis of the Relativistic Wave Functions

As usual, a multielectron atom is described by the Dirac relativistic Hamiltonian (the atomic units are used):

$$H = \sum_i h(r_i) + \sum_{i>j} V\left(r_i r_j\right). \tag{11}$$

Here, $h(r)$ is one-particle Dirac Hamiltonian for electron in a field of the finite size nucleus and V is potential of the inter-electron interaction. In order to take into account the retarding effect and magnetic interaction in the lowest order on parameter α^2 (the fine structure constant), one could write [77, 86]

$$V\left(r_i r_j\right) = exp\left(i\omega_{ij} r_{ij}\right) \cdot \frac{\left(1 - \alpha_i \alpha_j\right)}{r_{ij}}, \tag{12}$$

where ω_{ij} is the transition frequency; α_i, α_j are the Dirac matrices. The Dirac equation potential includes the electric and polarization potentials of a nucleus and exchange-correlation potentials. The standard KS exchange potential is [91]

$$V_X^{\mathrm{KS}}(r) = -(1/\pi)[3\pi^2 \rho(r)]^{1/3}. \tag{13}$$

In the local density approximation the relativistic potential is [92]

$$V_X[\rho(r), r] = \frac{\delta E_X[\rho(r)]}{\delta \rho(r)}, \tag{14}$$

where $E_X[\rho(r)]$ is the exchange energy of the multielectron system corresponding to the homogeneous density $\rho(r)$, which is obtained from a Hamiltonian having a transverse vector potential describing the photons. In this theory the exchange potential is [98]

$$V_X[\rho(r), r] = V_X^{\mathrm{KS}}(r) \cdot \left\{ \frac{3}{2} \ln \frac{[\beta + (\beta^2 + 1)^{1/2}]}{\beta(\beta^2 + 1)^{1/2}} - \frac{1}{2} \right\}, \tag{15}$$

where $\beta = [3\pi^2 \rho(r)]^{1/3}/c$. The corresponding correlation functional is [91, 92]

$$V_C[\rho(r), r] = -0.0333 \cdot b \cdot \ln[1 + 18.3768 \cdot \rho(r)^{1/3}], \tag{16}$$

where b is the optimization parameter (for details see Refs. [80, 124–126]). Earlier it was shown [80, 124–126] that an adequate description of the atomic characteristics requires using the optimized basis of wave functions. In Ref. [80], a new ab initio optimization procedure for construction of the optimized basis is proposed. It is reduced to minimization of the gauge-dependent multielectron contribution $Im\delta E_{\mathrm{ninv}}$ of the lowest QED PT corrections to the radiation widths of atomic levels.

In the fourth order of QED PT (the second order of the atomic PT), there appear the diagrams, whose contribution to the $Im\delta E_{\text{ninv}}$ accounts for the correlation (polarization) effects. This contribution describes the collective effects and it is dependent upon the electromagnetic potentials gauge (the gauge non-invariant contribution). All the gauge non-invariant terms are multielectron by their nature (the particular case of the gauge non-invariance manifestation is a non-coincidence of the oscillator strengths values, obtained in the approximate calculations with the "length" and "velocity" transition operator forms). The above-cited contribution to imaginary part of the electron energy can be defined after quite complicated calculation as follows [80]:

$$Im\delta E_{\text{ninv}}(\alpha - s|b) = -C\frac{e^2}{4\pi}\iiint dr_1 dr_2 dr_3 dr_4 \sum_{n>f,m\le f}\left(\frac{1}{\omega_{mn}+\omega_{\alpha s}}+\frac{1}{\omega_{mn}-\omega_{\alpha s}}\right)$$
$$\times\Psi_\alpha^+(r_1)\Psi_m^+(r_2)\Psi_s^+(r_4)\Psi_n^+(r_3)\cdot[(1-\alpha_1\alpha_2)/r_{12}]\cdot\{[\alpha_3\alpha_4-(\alpha_3 n_{34})(\alpha_4 n_{34})]/r_{34}$$
$$\times\sin[\omega_{\alpha n}(r_{12}+r_{34})]+[1+(\alpha_3 n_{34})(\alpha_4 n_{34})]\omega_{\alpha n}\cos[\omega_{\alpha n}(r_{12}+r_{34})]\}$$
$$\times\Psi_m(r_3)\Psi_\alpha(r_4)\Psi_n(r_2)\Psi_s(r_1). \tag{17}$$

Here, C is the gauge constant, f is the boundary of the closed shells; $n \ge f$ indicating the unoccupied bound and the upper continuum electron states; $m \le f$ indicates the finite number of states in the atomic core and the states of a negative continuum (accounting for the electron vacuum polarization). The minimization of the functional $Im\delta E_{\text{ninv}}$ leads to the DKS-like equations for the electron density which are numerically solved. As a result one can get the optimal PT at one-electron basis. In concrete calculations it is sufficient to use a more simplified procedure, which is reduced to the functional minimization using the variation of the correlation potential parameter b in Eq. (16) [124–126].

The differential equations for the radial functions $F$and G (components of the Dirac spinor) are

$$\frac{\partial F}{\partial r}+(1+\chi)\frac{F}{r}-(\varepsilon+m-V)G=0,$$
$$\frac{\partial G}{\partial r}+(1-\chi)\frac{G}{r}+(\varepsilon-m-V)F=0, \tag{18}$$

where F and G are the large and small components, respectively; χ is the quantum number. At large χ, the functions F and$G$ vary rapidly at the origin; we have $F(r), G(r) \approx r^{\gamma-1}$, $\gamma=\sqrt{\chi^2-\alpha^2 z^2}$. This creates difficulties in numerical integration of the equations in the region $r \to 0$. To prevent the integration step from becoming too small it is usually convenient to turn to new functions isolating the main power dependence: $f = Fr^{1-|\chi|}$, $g = Gr^{1-|\chi|}$. The Dirac equations for F and G components are transformed as follows:

$$f' = -(\chi + |\chi|)f/r - \alpha ZVg - (\alpha ZE_{n\chi} + 2/\alpha Z)g,$$
$$g' = (\chi - |\chi|)g/r - \alpha ZVf + \alpha ZE_{n\chi} f. \tag{19}$$

Here $E_{n\chi}$ is one-electron energy without the rest energy. The boundary values are defined by the first terms of the Taylor expansion:

$$g = \left(V(0) - E_{n\chi}\right) r\alpha Z \big/ (2\chi + 1); \quad f = 1 \text{ at } \chi < 0,$$
$$f = \left(V(0) - E_{n\chi} - 2\left/\alpha^2 Z^2\right.\right)\alpha Z; \quad g = 1 \text{ at } \chi > 0. \tag{20}$$

The condition $f, g \to 0$ at $r \to \infty$ determines the quantified energies of the state $E_{n\chi}$. The system of equations (19) is numerically solved by the Runge–Kutta method ("Superatom" package is used [76–86, 124–126]). The self-consistence condition of the continuum-state functions means that the normalized functions differ by less than 10^{-6} in relation to their values at the maximum point on two neighbour iterations. The normalization of the electron radial functions f and g provides the behaviour for large values r as follows:

$$g_\chi(r) \to r^{-1}[(E+1)/E]^{1/2} \sin(pr + \delta_\chi),$$
$$f_\chi(r) \to r^{-1}(\chi \left/|\chi|\right.)[(E-1)/E]^{1/2} \cos(pr + \delta_\chi). \tag{21}$$

2.3 Nuclear Finite Size and Radiation Effects

In order to account for the nuclear finite size effect we described the charge distribution in the nucleus $\rho(r)$ by the following Gaussian function:

$$\rho(r|R) = \left(4\gamma^{3/2} \left/\sqrt{\pi}\right.\right) \exp\left(-\gamma r^2\right),$$
$$\int_0^\infty dr r^2 \rho(r|R) = 1; \quad \int_0^\infty dr r^3 \rho(r|R) = R, \tag{22}$$

where $\gamma = 4 \left/ \pi R^2\right.$ and R is the effective nuclear radius. The following simple dependence of R on Z is assumed: $R = 1.606 \times 10^{-13} Z^{1/3}$ (cm). Such a definition of R is rather conventional. We assume it as some zeroth approximation. The Coulomb potential for the spherically symmetric density $\rho(r|R)$ is

$$V_{\text{nucl}}(r|R) = -((1/r)\int_0^r dr' r'^2 \rho\left(r'\middle|R\right) + \int_r^\infty dr' r' \rho\left(r'\middle|R\right). \tag{23}$$

It is determined by the following system of differential equations:

$$V'_{\rm nucl}(r,R)=\left(1\,/r^2\right)\int\limits_0^r dr'r'^2\rho\left(r',R\right)\equiv\left(1\,/r^2\right)y\left(r,R\right),$$

$$y'(r,R)=r^2\rho(r,R),$$

$$\rho'(r,R)=-8\gamma^{5/2}r\,/\sqrt{\pi}\,\exp\left(-\gamma r^2\right)=-2\gamma r\rho(r,R)=-\frac{8r}{\pi r^2}\rho(r,R), \quad (24)$$

with the boundary conditions

$$V_{\rm nucl}(0,R)=-4\,/(\pi r)\,,\ \ y(0,R)=0,$$
$$\rho(0,R)=4\gamma^{3/2}\,/\sqrt{\pi}\,=32\,/R^3\,. \quad (25)$$

The presented nuclear model was used earlier in many calculations of the atomic and nuclear systems [91–142]. It can be improved where necessary. Moreover, any relativistic mean field model, nuclear DFT, the HF theory with density dependent forces, etc., may be used [91, 92, 98, 120–126].

The procedure for taking into account the QED corrections is given in Refs. [124–126]. Different approaches to estimating the QED corrections are developed and discussed, for example, in Refs. [93–132]. Regarding the vacuum polarization effect let us note that this effect is usually taken into account by means of the Uehling potential in the first PT order. This potential is usually written as

$$U(r)=-\frac{2\alpha}{3\pi r}\int\limits_1^\infty dt\exp\left(-2rt\,/\alpha Z\right)\left(1+1\,/2t^2\right)\frac{\sqrt{t^2-1}}{t^2}\equiv-\frac{2\alpha}{3\pi r}C(g), \quad (26)$$

where $g=r/\alpha Z$. The more exact approach is proposed in Refs. [77, 124–126]. The Uehling potential may be approximated by the analytical Ivanov–Ivanova function [77]. The use of the new approximation for the Uehling potential allows one to decrease the calculation error for this term down to 0.5–1% [79, 126]. Besides using a quite simple analytical functional form for approximating the potential, Eq. (26) allows its easy inclusion into the general system of differential equations. At least, this procedure was earlier approbated in the precise atomic calculations [79, 124–126]. The function $C(g)$ in two limited cases has the known asymptotics as follows:

$$C(g)\to\tilde{C}_1(g)=\ln\left(g\,/2\right)+1.410548-1.037845g,\quad g\to 0,$$
$$C(g)\to\tilde{C}_2(g)=-1.8800\exp(-g)\,/g^{3/2}\,,\quad g\to\infty. \quad (27)$$

An account of the two limiting expressions for $C(g)$ is realized as follows:

$$\tilde{C}(g) = \tilde{C}_1(g)\,\tilde{C}_2(g) / \left(\tilde{C}_1(g) + \tilde{C}_2(g)\right). \tag{28}$$

The final expressions are as follows:

$$\tilde{\tilde{C}}(g) = \tilde{C}_1(g)\,\tilde{\tilde{C}}_2(g) / \left(\tilde{C}_1(g) + \tilde{\tilde{C}}_2(g)\right),$$
$$\tilde{\tilde{C}}_2(g) = \tilde{C}_2(g)\,f(g),$$
$$f(g) = \left(\left(1.1022 / g - 1.3362\right) / g + 0.8028\right).$$

Other details can be found in Refs. [77, 124–126, 148].

2.4 Test Calculation of the He Spectrum

Below we present the test calculation results for the excited state spectrum of He to check the quality of the wave function basis without and with an account of the optimization. The energies ΔE of the transitions to the He low lying excited states and dipole electric transition oscillator strengths are presented in Table 1. The experimental data and theoretical multiconfiguration HF approximation, Wauters–Vaeck B-spline method, data are listed too (cf. [51, 87, 90, 120, 124]). In a whole, there is an acceptable agreement between all theoretical and experimental data. Using the optimization scheme leads to the improvement of the corresponding oscillator strengths values in a comparison with other theoretical results.

Table 1 Energies ΔE of the transitions to the He-excited states and the oscillator strengths

State	ΔE Exp.	ΔE MCDF	ΔE B-spline	ΔE GIDKS	f MCDF	f DKS	f GIDKS	f Exp.
$2s\ ^3S_1$	19.820	20.00	20.83	20.83				
$2s\ ^1S_0$	20.616	20.88	20.64	20.63				
$2pP_{0,1,2}$	20.965	21.24	20.97	20.97				
$2p\ ^1P_1$	21.218	21.51	21.24	21.23	0.264	0.286	0.276	0.276
$3s\ ^3S_1$	22.719	22.91	22.75	22.73				
$3s\ ^1S_0$	22.921	23.14	22.94	22.94				
$3pP_{0,1,2}$	23.007	23.22	23.02	23.02	0.072	0.076	0.073	0.0734
$3p\ ^1P_1$	23.088	23.32	23.11	23.10				

3 Study of the Electronic Rearrangement Induced by Nuclear Transmutation: the β-Decay of ^{6}He

Here we consider the electronic rearrangement effect induced by the β-decay of ^{6}He. The main purpose is to treat the polyelectronic system:

$$^{6}_{2}\mathrm{He}_4 \rightarrow (^{6}_{3}\mathrm{Li}^{+}_{3})^{*} + e^{-} + \bar{\nu}_{\mathrm{e}}. \tag{29}$$

As in Ref. [51], we have calculated within the framework of the sudden approximation (since the velocity of most β-electrons is quasirelativistic) the population of the bound and continuum states of Li^+. If we neglect the effect of recoil of the daughter nucleus, the corresponding transition probability to a final atomic state is given by

$$|T^{0}_{fi}|^2 = < \Psi_f | \Psi_i >^2, \tag{30}$$

where Ψ_i corresponds to the wave function of the initial state with nuclear charge Z and Ψ_f to the wave function of the transmuted ion with nuclear charge $Z'(Z' = Z+1$ for β-decay). The sum over all the transitions involving the same initial state is 1. In Tables 2 and 3 we present the DKS calculation results of the energy eigenvalues (in at. units) and the excitation energies (in cm^{-1}) for $1snl\ ^1S$ states in the He-like ion of Li^+. The total energies of the lowest members of $Li^{+1}S$ Rydberg states obtained using the B-spline basis set by Wauters–Vaeck and the Hylleraas basis sets (within the complex coordinate approach) are listed in Tables 2 and 3 too [25, 26, 51]. The agreement between our results, the B-spline results and the complex coordinate values using Hylleraas basis sets is satisfactory. In Table 4 we present the values of calculated transition probabilities (in %; >0.05) to Li^+ states induced by β-decay of ^{6}He. Our results are compared in Table 4 with data of the pioneering work by Winther and B-spline data by Wauters–Vaeck (see Refs. [48–52, 120, 124]).

Table 2 Eigenvalues of energy (in atomic units) for the $1snl\ ^1S$ states in Li^+

State	Hylleraas	B-spline	DKS
$1s^2\ ^1S$	−7.2799135	−7.2793492	−7.2795438
$1s2s\ ^1S$	−5.0408767	−5.0408201	−5.0408413
$1s3s\ ^1S$	−4.7337556	−4.7337397	−4.7337488
$1s4s\ ^1S$	−4.6297832	−4.6297767	−4.6297798
$1s5s\ ^1S$	−4.5824274	−4.5824240	−4.5824256
$1s6s\ ^1S$		−4.5569496	−4.5569529
$1s7s\ ^1S$		−4.5416882	−4.5416916
$1s8s\ ^1S$		−4.5318274	−4.5318322
$2s^2\ ^1S$	−1.905845	−1.904924	−1.9052764
$2p^2\ ^1S$	−1.630439	−1.628787	−1.6293165

Table 3 Excitation energies (in cm^{-1}) for the $1snl\ ^1S$ states in Li^+

State	Experiment	B-spline	GIDKS
$1s^2\ ^1S$	0	0	0
$1s2s\ ^1S$	4,91,335	4,91,262	4,91,298
$1s3s\ ^1S$	5,58,778	5,58,653	5,58,704
$1s4s\ ^1S$	5,81,597	5,81,464	5,81,502
$1s5s\ ^1S$	5,91,989	5,91,860	5,91,917
$1s6s\ ^1S$	5,97,581	5,97,451	5,97,513
$1s7s\ ^1S$	6,00,930	6,00,800	6,00,875
$1s8s\ ^1S$	–	6,02,964	6,03,032

Table 4 Transition probabilities (in %) to the Li^+ states induced by the β-decay of ^6He

State	Winther	Wauters–Vaeck, B-spline	GIDKS
$1s^2\,^1S$	67.0	70.85	68.13
$1s2s\,^1S$	16.6	14.94	14.37
$1s3s\,^1S$	2.7	1.86	1.81
$1s4s\,^1S$	0.8	0.62	0.63
$1s5s\,^1S$		0.29	0.26
$1s6s\,^1S$		0.16	0.14
$1s7s\,^1S$		0.10	0.10
$2s^2\,^1S$		1.56	1.24
$2p^2\,^1S$		0.18	0.16
$2s3s\,^1S$		0.23	0.21
$2s4s\,^1S$		–	0.05

Table 5 Total transition probabilities (in %) for the population of different electronic states induced by the β-decay of ^6He

Final $^6Li^+$ state	Experiment	Wauters–Vaeck B-spline	Present work
Bound states		89.09	87.4
Autoionizing states		2.97	2.56
Ionization of one electron	10.4.±0.2	7.47	9.85
Ionization of two electrons	0.042.±0.007	0.32	0.09

Contrary to the wave functions used in the B-spline of Wauters–Vaeck and in our scheme, the Li^+ wave functions used by Winther are not orthogonal. It implies that the sum over the transition probabilities to all the Li^+ states is not 1.

In Table 5 we present the results of calculating the total transition probabilities for the population of different electronic states induced by the β-decay of ^6He. It is interesting to calculate not only the transition probabilities to discrete states but also the ionization probability of one or two electrons. Using a radioactive recoil spectrometry experiment, Carlson et al. have measured that the single ionization probability is (10.4±0.2)% and the B-spline and DKS values agree very well with this result [24, 48–52]. In the same experiment the double ionization probability was found to be (0.042±0.007)%. Our value is well correlated with this result. Further we consider the quantity P_K, the probability per nuclear disintegration, which an atomic K vacancy (a hole in the $1s^2$ shell) is created. The analysis of different calculation schemes is presented in Ref. [51]. In the sudden approximation this quantity is simply defined as follows [51]:

$$P_K = 1 - [\,< \Psi_f(1s^2\,^1S)|\Psi_i(1s^2\,^1S) >]^2. \tag{31}$$

If electronic correlation effects are not taken into account, this formula simply reduces to $1-(1s_f|1s_i)^4$, with the $1s$ radial distributions being optimized in, for example, HF approximation. This approach has been used by Carlson et al., who predicted a P_K value of 26.9% for the β-decay of ^6He.

The introduction of electronic correlation significantly increases the probability to P_K=27.61% (Law–Campbell result), P_K=32.91% (Izozumi et al.), P_K=29.15% (Wauters–Vaeck) and P_K=31.87% (our result). In any case one can conclude that the optimized DKS method is quite an adequate approach to the calculation of parameters for excitation, ionization and electronic rearrangement in atoms, ions and molecules induced by the β-decay. It is obvious also that the method as applied here is not restricted to using the sudden approximation. Moreover the main corrections (kinematics, recoil, etc.) to this approximation, for example, in a case of nuclear reactions may be further considered [51, 71, 72, 124, 149, 150].

4 Theory of the Chemical Environment Effect on the β-Decay Parameters

4.1 Introduction

Here we consider the contributions of the chemical bond and electronic rearrangement effects on the numerical values of β-decay parameters. We have estimated the energy corrections due to the electronic rearrangement induced by the β-decay. The allowed (superallowed) β-transitions, ^{3}H–^{3}He, ^{6}He–^{6}Li, ^{33}P–^{33}S, ^{35}S–^{35}Cl, ^{63}Ni–^{63}Cu, ^{241}Pu–^{241}Am, are studied. The parameters of some allowed and superallowed β-transitions are listed in Table 6 [79, 80]. Indeed, such a choice is defined by the following circumstance. The expressions (12)–(15) are exact for these transitions and the corresponding nuclear matrix elements are simplified in comparison with forbidden transitions. For example, the value $\int 1$ can be defined exactly for superallowed $\beta^{\pm}$-transitions: $\int 1 = [(T \mp T_3)(T \pm T_3 + 1)]^{1/2}$. Here T_3 is the isospin projection, which is defined as $T_3 = (Z - N)/2$. An account of the meson exchange currents (this contribution is about a few percent) for β-transition between purely isospin states does not change the result, connected with the isospin conservation. The value $\int \sigma = 0$ for the superallowed $0^+ \to 0^+$transition between the neighbour members of an isomultiplet and for $T = 1 : \int 1 = \sqrt{2}$. Let us remember that the known theoretical parameter ξ for a majority of the β-transitions is [15] $\xi = \alpha Z/2R \gg 1$.

Table 6 Parameters of the allowed (superallowed) β-transitions

Decay	Z_{mat}–Z_{daught}	$I_i^{\pi_i} \to I_f^{\pi_f}$	Type	E_0, keV	$T_{1/2}$	*lg ft*
^{3}H–^{3}He	1 → 2	$1/2^+ \to 1/2^+$	super.	18.65	12.296 years	3.05
^{6}He–^{6}Li	2 → 3	$0^+ \to 1^+$	super.	3,500	0.813 s	2.9
^{33}P–^{33}S	15→16	$1/2^+ \to 3/2^+$	allow.	249	25.3 days	5.0
^{35}S–^{35}Cl	16→17	$3/2^+ \to 3/2^+$	≪≫	167.4	87.4 days	5.0
^{42}Sc–^{42}Ca	21→20	$0^+ \to 0^+$	super.	5,409	0.683 s	3.5
^{45}Ca–^{45}Sc	20→21	$7/2^- \to 7/2^-$	≪≫	257	165 days	6.0
^{63}Ni–^{63}Cu	28→29	$1/2^- \to 3/2^-$	≪≫	65.8	100 years	6.6
^{241}Pu–^{241}Am	94→95	$5/2^+ \to 3/2^-$	1 forb.	20.8	14.4 years	5.8

The β-decay ^{241}Pu–^{241} Am is non-unique of the first forbiddance (ξ=18, i.e. $\xi \gg 1$). As a result, the expressions are correct for this transition too. The chemical bond effect on the β-decay parameters is studied in a number of publications (see Refs. [1–15, 24–27, 29–31, 124–126]). An account (or non-account) of the chemical environment contribution leads to the known discrepancies in the data for half-life periods. A part of these discrepancies is due to the β-decay channel contribution (the β-particle occupies the external non-occupied atomic level). One could also take into account a few additional factors, provided by the chemical bond effect: (i) Changing the electron wave functions because of the changing atomic electric field and shell occupation numbers in different chemical substances; (ii) The integration limits (Fermi integral function) are also changed in a case of the different chemical substances; as a rule, the β-particle and neutrino take away the difference between the initial and final nuclei, provided by the nuclear and electronic rearrangement. We already mentioned the bound β-decay channel. The confirmation of this decay channel was found in the synchrotron and SIS/ESR experiments (GSI, Darmstadt, Germany) [3–8, 42]. The mass-spectrometric St. Petersburg experiment (Russia) should also be mentioned [9]. It was the first to measure a change in the lifetime of a tritium nucleus due to changes in its electron surroundings. Despite these remarkable experimental results of previous years, accurate data on the corresponding parameters are absent for a majority of the β-decays.

4.2 β-Decay of Tritium

In the experiment of Ref. [9] a change in the tritium nucleus lifetime due to changes in its electron surroundings was discovered. To calculate the absolute values of the difference of the decay constants $\Delta\lambda_{am}$ and half-life periods ($T_{1/2} = ln2/\lambda$) for molecular and atomic tritium $\Delta T_{1/2} = (T_{1/2})_m - (T_{1/2})_a$ we use the value: $(T_{1/2})_m$= (12.296±0.017) years. The experimental values for $\Delta\lambda_{am}$ and $\Delta T_{1/2}$ are as follows [9]:

$$\Delta\lambda_{am} = (4.6 \pm 0.8) \cdot 10^{12}\ \mathrm{s}^{-1}$$
$$(\Delta T_{1/2})_{am} = (0.03152 \pm 0.00553)\ \text{years} = 11.5 \pm 2.0\ \text{days}.$$

In the reaction $H^+ \rightarrow {}^3He^{++} + e^- + 18.6\,\mathrm{keV}$ the β-electrons are generated with wavelengths, which are characteristic for the atomic electron systems. In this case the interaction between the beta-electron and orbital electrons and vacancies is very effective. Further it leads to observable changes in the half-life period. It is well known [1–3, 9, 124] that hitherto the attempts to define nuclear constant values (which characterize the beta processes) on the basis of data for the tritium decay fail. The obtained values for the half-life period and boundary beta spectrum energy in the corresponding experiments are dependent upon the type of the studied chemical compound. As a result, there is no possibility of agreement between the experimental values of $T_{1/2}$ and E_0. It is of great interest to study an effect of the triton

chemical surrounding on $T_{1/2}$. It is especially important in light of the known simplicity of such atomic structures as ^{3}H, $^3H^+$, $^3H^-$. Using the experimental data on the difference between the decay parameter values for atomic and molecular tritium it experimentally found the half-life period value for the atomic tritium [9]: $(T_{1/2})_a$=$(T_{1/2})_m$–$(\Delta T_{1/2})_{am}$=(12.264±0.018) years. Further it is possible to find an absolute value of the free triton half-life period $(T_{1/2})_t$ by using the experimental value $(T_{1/2})_a$ and theoretical data on the β-decay atomic effects in ^{3}H. We have taken into account the following effects: (i) the electron excitation in the bound spectrum while occupying the He level by the β-electron; (ii) excitation to the continuum spectrum due to the exchange of the orbital electron by β-electron; (iii) the charge screening effect by the orbital electron; and (iv) the excited states in $^3He^+$. According to Ref. [9], the corresponding correction to the value $(T_{1/2})_a$is 0.86±0.08%, which results in the value of the free triton half-life period as follows: $(T_{1/2})_t$= (12.369±0.020) years. An account of the chemical surrounding effect in a case of the T-containing compounds is an important problem not only from the point of view of the β-decay theory, but in light of using the tritium electron sensor (probe) to reveal the spatial correlations of coordinates for molecular studying object, definition of the electron density distribution, direction of the chemical bonds, etc. (see Refs. [1, 2, 9, 50–52, 56–59, 62–68]). The tritium electron probe possesses a complex of the known parameters, provided by specific features of the β-decay (namely, by an opposite direction of the β-electrons pulse in relation to a nucleus spin direction because of the non-conserving parity in the β-decay; definite helicity of the corresponding antineutrino; a spin of antineutrino is collinear to a pulse and the definite helicity is taken by an electron too; the exact representation of the β-electrons energy spectrum in the range from zero to the boundary energy 18.6 keV, which is not perturbed by the atomic effects). It is obvious that studying the tritium β-decay in some atomic-molecular systems allows one in principle to define a whole set of parameters for the input electron flux. Further it allows one to treat the electron structure of a system. We have estimated the numerical values of the β-decay parameters in the atom (ion) of tritium while taking into account the atomic factors. Let us note that a channel of forming β-electron in the K-shell is not significant in the case of the tritium ion β-decay [124]. Our estimate for the tritium atom half-life period $(T_{1/2})_a$ =12.26 years; the correction to value $(T_{1/2})_a$due to the electron-atomic effects is 0.0082×12.26 years [i.e. $(\Delta T_{1/2}/T_{1/2})_a$=0.82%]. In result, the half-life period value $(T_{1/2})_t$ is [31, 134] 12.36 years. Obviously, there is a physically reasonable agreement between the calculated and measured values. One could wait for more contradictory picture in the case of the β-decay in more complicated atoms because of the large complexity of taking into account the atomic effects in comparison with quite simple system ^{3}H. In Refs. [31, 134] the first estimate of the T half-life period in the case of β-decay for the halogen-containing molecular T (^{3}HCl) was presented. The calculation was carried out within the non-relativistic KS approach while using the exchange-correlation potentials (13) and (16). The obtained value for $(T_{1/2})$ is $(T_{1/2})_m$ = 12.28 years; the corresponding correction due to the chemical bond effect is $(\Delta T_{1/2})_{am}$ = 0.024, i.e. 0.20%. For comparison let us remember the experimental (molecular tritium) value: $(T_{1/2})_m$ = 12.296 years

and the chemical bond effect correction $(\Delta T_{1/2})_{am} = 0.03152$, i.e. 0.26%. Obviously, here there is physically reasonable agreement too. From the other side, the corrections due to the chemical bond effect for the molecular tritium and halogen-containing tritium compound will be different.

4.3 The Chemical Bond Effect on the β-Decay Parameters

Further we present the DKS calculation results for the β-decay parameters and corrections due to the chemical bond and other atomic effects [14, 24–27, 30, 124–126]. The energy corrections to the boundary energy of β-spectrum due to the electron shells reconstruction are presented in Table 7. The following β-decays $^{33}P^{(0)}\_^{33}S^{(+1)}$, $^{33}P^{(+1)}\_^{33}S^{(+2)}$, $^{35}S^{(0)}\_^{35}Cl^{(+1)}$, $^{35}S^{(+2)}\_^{35}Cl^{(+3)}$, $^{63}Ni^{(0)}\_^{63}Cu^{(+1)}$, $^{63}Ni^{(+2)}\_^{63}Cu^{(+3)}$, $^{241}Pu^{(0)}\_^{241}Am^{(+1)}$, $^{241}Pu^{(+2)}\_^{241}Am^{(+3)}$, $^{241}Pu^{(+2)}\_^{241}Am^{(+3)}$ and $^{241}Pu^{(+4)}\_^{241}Am^{(+5)}$ are studied. Calculation is carried out in the free ion approximation. The value δE corresponds to the correction for the boundary β-spectrum energy due to the electron shell reconstruction. The value $\delta^2 E$ is the difference of the corresponding corrections. Analysis shows that the DKS values are a little larger than the corresponding values that are obtained on the basis of the relativistic HFS and DF methods [14–16, 24, 29–31]. Obviously, the classical DF and HFS methods give a little more error in calculating the energy parameters in comparison with their optimized versions. It is worth comparing the Fermi function values for different calculation models [24, 29–31]. Two alternative definitions of the Fermi function values are usually used: (i) the relativistic electron radial wave functions calculated on the boundary of the spherical nucleus with radius R (see [14, 15]) and (ii) a definition of the Fermi function by means of the squares of expansion amplitudes of the radial wave functions $f^2_{+1}(0) + g^2_{-1}(0)$, $r \to 0$ (see [29–31, 24]). According to Refs. [3, 24, 29–31], the difference in the Fermi function values increases with increasing Z. The same effect is characteristic for the integral

Table 7 The energy corrections to boundary energy of the β-spectrum due to the electron shells reconstruction

		The total shell energy, eV		Differences in energy, eV	
Decay	Configuration	Mat. atom	Daught. atom	δE	$\delta^2 E$
$P^{(0)} \to S^{(+1)}$	$[Ne]3s^2 3p^2_{1/2} 3p_{3/2}$	9,239	10,782	1, 543	
$P^{(+1)} \to S^{(+2)}$	$[Ne]3s^2 3p^2_{1/2}$	9,230	10,759	1, 529	14
$S^{(0)} \to Cl^{(+1)}$	$[Ne]3s^2 3p^2_{1/2} 3p^2_{3/2}$	10,791	12,471	1, 680	
$S^{(+2)} \to Cl^{(+3)}$	$[Ne]3s^2 3p^2_{1/2}$	10,760	12,407	1, 647	33
$Ni^{(0)} \to Cu^{(+1)}$	$[Ar]3d^4_{3/2} 3d^4_{5/2} 4s^2$	41,238	44,871	3, 633	
$Ni^{(+2)} \to Cu^{(+3)}$	$[Ar]3d^4_{3/2} 3d^4_{5/2}$	41,214	44,821	3, 607	26
$Pu^{(0)} \to Am^{(+1)}$	$[Rn]5f^6_{5/2} 7s^2$	8,06,868	8,29,365	22, 497	
$Pu^{(+2)} \to Am^{(+3)}$	$[Rn]5f^6_{5/2}$	8,06,852	8,29,331	22, 480	17
$Pu^{(+2)} \to Am^{(+3)}$	$[Rn]5f^4_{5/2} 7s^2$	8,06,845	8,29,309	22, 464	33
$Pu^{(+4)} \to Am^{(+5)}$	$[Rn]5f^4_{5/2}$	8,06,800	8,29,245	22, 445	52

Fermi function. It is found that the integral Fermi function f is changed for different β-decays [for example, ^{33}P–^{33}S ($E_0 = 249$ keV), ^{35}S–^{35}Cl ($E_0 = 167$ keV) on 2–4%; ^{63}Ni–^{63}Cu ($E_0 = 65.8$ keV) on 5%, ^{241}Pu–^{241}Am ($E_0 = 20.8$ keV) − 32%] in the case of using the Fermi function definition on the basis of the wave functions values on the boundary of a nucleus and values of these functions in zero [29–31, 124].

In Table 8 we present the calculation data regarding the chemical bond effect on the half-life period for the β-decay $^{33}P^{(0)}$–^{33}S. In column A, we present the data obtained on the basis of calculation within the optimized DF approach (GIDF). The GIDKS data are listed in column B and the standard DF calculation data in column C [24, 29–31]. We use the following notations: $\Delta f/f$ is the relative changing decay probability (Fermi integral function), which is equal to the change in the β half-life period with the opposite sign ($-\Delta T_{1/2}/T_{1/2}$). Let us give a short comment regarding the choice of the boundary energy values. The value 2,49,000 eV is accepted for the boundary energy of the $P^{(0)}$ decay. Analogously, the value 2,49,014 eV is used for the decay of $P^{(+2)}$ in the first variant of calculation. The pair of the energy values 2,48,986 and 2,49,000 eV is chosen in the second variant of the calculation correspondingly. All presented results lead to an identical conclusion about the dependence of the change in the half-life period on the ionic degree. All versions of the calculation give very close values of $\Delta f/f$ [29–31]: $\Delta f/f = 0.0079\%$ (GIDF), $\Delta f/f = 0.0082\%$ (GIDKS), $\Delta f/f = 0.0075\%$ (DF). One concludes that the corresponding change $\Delta f/f$ is sufficiently small. The experimental data for β-decay $^{33}P^{(0)}$–^{33}S are absent. But our data are correlated with recent theoretical and experimental data for ^{7}Be, ^{22}Na and ^{40}K isotopes [10, 11]. These data suggest that the effect of chemistry (plus pressure) is quite little and discernible. Calculation for ^{33}P–^{33}S decay shows that the integral Fermi function is less in the case of the ionized phosphor β-decay in comparison with the neutral phosphor. As a result, β-decay of the ionized phosphor runs more slowly. From the other side, the Fermi function value is more for neutral phosphor and its decay runs more quickly. In Table 9 we present the GIDKS data on the chemical bond effect on the half-life period for the β-decay $^{35}S \rightarrow {}^{35}$Cl. The value 1,67,453 eV is accepted for the boundary energy of the $S^{(0)}$ decay.

Analogously, the value 1,67,420 eV is used for decay of $S^{(+2)}$ in the first variant of the calculation. The pair of energy values 1,67,420 and 1,67,390 eV is cho-

Table 8 The chemical bond effect on the half-life period for the decay $^{33}P^{(0)} \rightarrow {}^{33}$S decay

Decay of a neutral atom				Decay of an ionized atom			
Atom	E_0, eV	$f(E_0, Z)$		Ion	E_0, eV	$f(E_0, Z)$	$\Delta f/f$, 10^{-3} %
$P^{(0)}$	2,49,000	4.87541(−2)	A	$P^{(1+)}$	2,48,987	4.87501(−2)	8.2
	2,49,013	4.87617(−2)			2,49,000	4.87580(−2)	
$P^{(0)}$	2,49,000	4.87565(−2)	B	$P^{(1+)}$	2,48,986	4.87524(−2)	8.39
	2,49,014	4.87637(−2)			2,49,000	4.87598(−2)	
$P^{(0)}$	2,49,000	4.87529(−2)	C	$P^{(1+)}$	2,48,988	4.87492(−2)	7.5
	2,49,012	4.87608(−2)			2,49,000	4.87572(−2)	

Table 9 The chemical bond effect on the half-life period for the decay $^{35}S \rightarrow {}^{35}Cl$ (DKS data)

Decay of a neutral atom			Decay of an ionized atom			
Atom	E_0, eV	$f(E_0, Z)$	Ion	E_0 , eV	$f(E_0, Z)$	$\Delta f/f$, %
$S^{(0)}$	1,67,420	1.36835(−2)	$S^{(2+)}$	1,67,387	1.36780(−2)	∼ 0.04
	1,67,453	1.36913(−2)		1,67,420	1.36858(−2)	

sen in the second variant of the calculation correspondingly. The two versions of the calculation give practically the same data for $\Delta f/f$: 0.037% (GIDF), 0.039% (GIDKS), 0.03% (DF). Calculation for the ^{35}S–^{35}Cl transition shows that the integral Fermi function is less in the case of the ionized sulphur β-decay in comparison with the neutral S case. So, the ionized sulphur decay runs more slowly. From the other side, the Fermi function value is more for neutral sulphur in comparison with the ionized S and its decay runs more quickly. However, the corresponding difference in values of the half decay period $T_{1/2}$is sufficiently small. The released energy due to the electron shell rearrangement (∼ 1.7 keV) for the considered decay ^{35}S–^{35}Cl is added to the energy, which is given to the β-particle by a nucleus. In the case of the $S^{(0)}$ decay this correction to the boundary kinetic energy is more than 33 eV when compared to the case of the $S^{(+2)}$decay. The experiment allows one to define only the sum of energies, obtained by leptons from atomic nucleus and electron shells [29–31]. In our case, the experimental value E_0 is 1,67,400±100 eV. There is absolutely the same situation in the case of the decay ^{63}Ni–^{63}Cu. The corresponding data are presented in Table 10. The value 65,800 eV for the boundary energy is accepted in the case of the $Ni^{(0)}$decay. Analogously, the value 65,826 eV is used for decay of $Ni^{(+2)}$ in the first variant of the calculation. The pair of energies 65,774 and 65,800 eV is chosen in the second variant of the calculation. Surely a little more significant changing of the $T_{1/2}$value occurs for ^{63}Ni. The Fermi function value in the case of the double ionization (i.e. $Ni^{(+2)}$) is less on 0.11–0.13% (the HFS, DF, GIDF, GIDKS schemes) than in a case of neutral Ni. So, the neutral ^{63}Ni decay runs more quickly. Our results are correlated with the recent theoretical and experimental data [10, 11].

There is another situation (significant changes in the $T_{1/2}$value) for ^{241}Pu–^{241}Am decay. This transition is of great interest because of the different dependence of the change in $T_{1/2}$on the chemical surrounding and the large discrepancies in the β-decay parameters data. The typical example of the Pu compounds is the pair PuO_2 and PuO. In Table 11 we present the GIDKS calculation results ($\Delta f/f = -\Delta T_{1/2}/T_{1/2}$) regarding the chemical bond effect on the half-life period for the β-decay ^{241}Pu–^{241}Am.

Table 10 The chemical bond effect on the half-life period for the decay ^{63}Ni–^{63}Cu (DKS data)

Decay of a neutral atom			Decay of an ionized atom			
Atom	E_0, eV	$f(E_0, Z)$	Ion	E_0, eV	$f(E_0, Z)$	$\Delta f/f$,%
$Ni^{(0)}$	65,800	1.38439(−3)	$Ni^{(+2)}$	65,774	1.38287(−3)	0.11
	65,826	1.38583(−3)		65,800	1.38430(−3)	

Table 11 The chemical bond effect on the half-life period for the decay ^{241}Pu–^{241}Am

Decay of a neutral atom			Decay of an ionized atom			
Atom	E_0 , eV	$f(E_0, Z)$	Ion	E_0, eV	$f(E_0, Z)$	$\Delta f/f = -\Delta T_{1/2}/T_{1/2}$, %
	20,800	1.72164(−3)		20,783	1.71596(−3)	−0.33
	20,817	1.72522(−3)	$Pu^{(+2)}$	20,800	1.71953(−3)	−0.33
	20,800	1.72164(−3)	$Pu^{(+2)}$	20,767	1.71148(−3)	−0.59
$Pu^{(0)}$	20,833	1.72952(−3)		20,800	1.71931(−3)	−0.59
	20,800	1.72164(−3)	$Pu^{(+4)}$	20,748	1.70615(−3)	−0.90
	20,852	1.73403(−3)		20,800	1.71842(−3)	−0.90

According to the DF, GIDF and GIDKS calculation results [12–14], the Fermi function values in the case of the Pu double ionization are less than ∼0.1–0.9% in comparison with analogous data for the neutral Pu decay. So, the neutral ^{241}Pu decay runs more slowly in comparison with ionized $Pu^{(+2)}$. The Fermi function value change is ∼0.1–0.4% (the HFS data) and ∼0.3–0.8% (GIDF data). An account of the channel of β-decay with occupying the external atomic orbitals gives a reasonable explanation of the Pu half decay period values dependent on the chemical composition [24, 29–31, 15, 124]. Surely, it would be desirable to compare the theoretical data with any experiment. It is known that in a compound the typical (Mulliken, etc.) atomic charge often is about half of the nominal oxidation state. Our results ($\Delta f/f \sim 1\%$) are correlated with other theoretical and experimental data [10, 11]. From the other side, one could wait for a possible giant change in the half-lives of bare isotopes compared to their neutral counterparts [94]. Our preliminary data indicates such an effect. Surely, the FRS–ESR experimental studying is of a great interest in this case.

5 Concluding Remarks and Future Perspectives

We considered the cooperative electron-β-nuclear processes in atomic systems (including processes of the excitation, ionization, electronic rearrangement) and chemical bond effect on the β-parameters. The optimized relativistic DKS calculation method that takes into account the finite size of the nucleus, radiation and exchange-correlation corrections is applied to calculation of the β-decay parameters for a set of the allowed (superallowed) transitions: ^{33}P–^{33}S, ^{35}S–^{35}Cl, ^{63}N–^{63}Cu, ^{241}Pu–^{241}Am, etc. We have also studied the chemical bond effect on parameters of the β-transitions $^{33}P^{(0)}$–$^{33}S^{(+1)}$, $P^{(+1)}$–$S^{(+2)}$, $^{35}S^{(0)}$–$^{35}Cl^{(+1)}$, $S^{(+2)}$–$Cl^{(+3)}$, $^{63}Ni^{(0)}$–$^{63}Cu^{(+1)}$, $Ni^{(+2)}$–$Cu^{(+3)}$, $^{241}Pu^{(0)}$–$^{241}Am^{(+1)}$, $Pu^{(+2)}$–$Am^{(+3)}$, $Pu^{(+2)}$–$Am^{(+3)}$, $Pu^{(+4)}$–$Am^{(+5)}$. The correct treatment of chemical environment effect is shown to modify the β-decay characteristics (integral Fermi function, half-life period, probability). We studied the electronic rearrangement induced by nuclear transmutation (i.e. change in the nuclear charge) in the β-decay $^{6}_{2}He_4 \rightarrow (^{6}_{3}Li^{+}_{3})^* + e^- + \bar{\nu}_e$. We

have calculated the excitation to the final discrete states of $^6Li^+$ (including to the double excited autoionizing states) as well as the total probabilities for single and double ionization. The half-life period for β-decay of the tritium atom (ion) has been estimated, taking into account the bound β-decay channel correction and some other accompanying effects (population of the bound states of ^{3}He, population of the continuum states resulting from exchanging the orbital electron by β-electron, the charge screening effect due to the orbital electron, etc.). The estimated values of the half-life period $T_{1/2}$ for tritium β-decay and free triton β-decay are as follows: $(T_{1/2})_a = 12.26$ years (correction due to the electron-atomic effects $(\Delta T_{1/2}/T_{1/2})_a = 0.82\%$) for the tritium atom and $(T_{1/2})_t = 12.36$ years for the free triton. These data are in physically reasonable agreement with the experimental data: $(T_{1/2})_a$= (12.264±0.018) years, $(\Delta T_{1/2}/T_{1/2})_a = 0.86 \pm 0.08\%$ and $(T_{1/2})_t = (12.369 \pm 0.020)$ years for atomic tritium and $(T_{1/2})_m = (12.296 \pm 0.017)$ years, $(\Delta T_{1/2})_{am} = 0.03152$ (i.e. 0.26%) for the molecular tritium. We presented the values $T_{1/2}$ in a case of β-decay for the halogen-containing molecular tritium (^{3}HCl): $(T_{1/2})_m = 12.28$ years (^{3}HCl) and the correction due to chemical bond effect $(\Delta T_{1/2})_{am}$=0.024 (i.e. 0.20%).

In conclusion let us note that the further development of the electron-β-nuclear spectroscopy of atoms, ions and molecules is of a great theoretical and practical interest. The development of new experimental methods (combination of the FRS and ESR) [3–12, 147]) for the measurement of the β-decay parameters promises the further essential progress in our understanding of radioactive nuclear decays. Obviously, the storage rings are ideal tools for precise measurements of masses and β-decay lifetimes of nuclei of relevance for astrophysics. Such an approach can be useful, providing perspective for the development of new nuclear models, search of the new cooperative effects on the boundary of atomic and nuclear physics, carrying out new methods for treating the spatial structure of molecular orbitals, diagnostics of the hydrogen-containing compounds by means of exchange of the hydrogen atoms by tritium, studying the chemical bond nature and checking different theoretical models in quantum chemistry and solids physics and studying the properties of energy releasing in the tritium (DT, TT) plasmas. Finally, an availability of more exact data on the β-decay lifetimes and other (nuclear) parameters with taking into account the chemical bond and much larger bound β-decay effects is also important in astrophysics and cosmology, studying the substance transformation in the Universe, relationships for n/p, ^{3}H/^{3}He, cosmological constants, etc. [1–16, 120, 124, 140–150]. In any case, the electron-β (more generally, α, γ, μ)-nuclear spectroscopy of atoms and molecules opens absolutely new possibilities in the bridging of nuclear physics and traditional quantum chemistry (atomic and molecular physics) [1–16, 124, 140–150]. Obviously, these possibilities are strengthened by quickly developed nuclear quantum optics (see Refs. [14, 20–28, 40, 41, 56–80, 147–150]). Really, a superintense laser (more exactly, x-raser or graser) field may provide a definite measurement of the change in the dynamics of the nuclear processes, including β- (or γ- and α-) decay, as it has been underlined, for example, in Refs. [20, 56–59, 74, 76, 150].

Acknowledgments The authors are grateful to Professors L.N. Ivanov, E.P. Ivanova, W. Kohn, E. Brandas, S. Malinovskaya, S. Wilson, M. Bonits, I. Kaplan, J. Maruani, C. Roothaan, A. Theophilou, A. Migdal, V. Lisitsa, A. Starostin and Yu. Lozovik for useful comments regarding different topics of the paper. The useful comments of the anonymous referee are very much acknowledged too. The support of the Institute for Spectroscopy ISAN (Russian Academy of Sciences, Troitsk, Russia), Max-Plank Institute for Physics of Complex Systems of Dresden, University of Dresden and Christian-Albrechts-University of Kiel (Germany), Universities of Geneva (DFT grant) and Zurich (Switzerland), the Abdus Salam ICTP Centre (Trieste, Italy) is acknowledged. The authors would like to thank Prof. P. Piecuch and Mr. J. Gour for help in preparing the manuscript.

References

1. R.G.H. Robertson, D.A. Knapp, Ann. Rev. Nucl. Part. Sci. **38**, 185 (1988); R. Tegen, Nucl. Phys. A **706**, 193 (2002)
2. I.G. Kaplan, V.N. Smutny, Adv. Quantum Chem. **19**, 289 (1988); I.G. Kaplan, J. Phys. G: Nucl. Part. Phys. **23**, 683 (1997)
3. M. Madurga, M.J.G. Borge, J.C. Angelique, L. Bao, U. Bergmann, A. But /ca, J. Ceerk, J.M. Daugas, C.A. Diget, L.M. Fraile, H.O.U. Fynbo, H.B. Jeppesen, B. Jonson, E. Lienard, F. Marechal, M. Marques, V. Meot, F. Negoita, T. Nilsson, G. Nyman, F. Perrot, K. Riisager, O. Roig, O. Tengblad, E. Tengborn, M. Turrion, K. Wilhelmsen Rolander, J. Phys.: Conf. Ser. **111**, 012024 (2008)
4. Yu.A. Litvinov, F. Attallah, K. Beckert, F. Boscha, D. Boutina, M. Falch, B. Franzke, H. Geissel, M. Hausmann, Th. Kerscher, O. Klepper, H.-J. Kluge, C. Kozhuharov, K.E. Löbner, G. Münzenberg, F. Nolden, Yu.N. Novikov, Z. Patyk, T. Radona, C. Scheidenberger, J. Stadlmann, M. Stecka, M.B. Trzhaskovskaya, H. Wollnik, Phys. Lett. B **573**, 80 (2003)
5. K. Takahashi, R.N. Boyd, G.I. Mathews, K. Yokoi, Phys. Rev. C **36**, 1522 (1987)
6. M. Jung, F. Bosch, K. Beckert, H. Eickhoff, H. Folger, B. Franzke, A. Gruber, P. Kienle, O. Klepper, W. Koenig, C. Kozhuharov, R. Mann, R. Moshammer, F. Nolden, U. Schaaf, G. Soff, P. Spädtke, M. Steck, T. Stöhlker, K. Sümmerer, Phys. Rev. Lett. **69**, 2164 (1992)
7. F. Bosch, T. Faestermann, J. Friese, F. Heine, P. Kienle, E. Wefers, K. Zeitelhack, K. Beckert, B. Franzke, O. Klepper, C. Kozhuharov, G. Menzel, R. Moshammer, F. Nolden, H. Reich, B. Schlitt, M. Steck, T. Stöhlker, T. Winkler, K. Takahashi, Phys. Rev. Lett. **77**, 5190 (1996)
8. T. Ohtsubo, F. Bosch, H. Geissel, L. Maier, C. Scheidenberger, F. Attallah, K. Beckert, P. Beller, D. Boutin, T. Faestermann, B. Franczak, B. Franzke, M. Hausmann, M. Hellström, E. Kaza, P. Kienle, O. Klepper, H.J. Kluge, C. Kozhuharov, Yu. Litvinov, M. Matos, G. Münzenberg, F. Nolden, Yu. Novikov, M. Portillo, T. Radon, J. Stadlmann, M. Steck, T. Stöhlker, K. Sümmerer, K. Takahashi, H. Weick, M. Winkler, T. Yamagushi, Phys. Rev. Lett. **95**, 052501 (2005)
9. Yu.A. Akulov, B.A. Mamyrin, Phys. Lett. B **600**, 41 (2004); Phys. Atom. Nuclei **67**, 464 (2004); Physics Uspekhi **174,** 1791 (2004); Phys. Lett. B **610**, 45 (2005)
10. G.T. Emery, Ann. Rev. Nucl. Sci. **22**, 165 (1972); T. Ohtsuki, H. Yuki, M. Muto, J. Kasagi, K. Ohno, Phys. Rev. Lett. **93**, 112501 (2004); Y. Nir-El, G. Haquin, Z. Yungreiss, M. Hass, G. Goldring, S.K. Chamoli, B.S. Nara Singh, S. Lakshmi, U. Köster, N. Champault, A. Dorsival, G. Georgiev, V. Fedoseyev, B.A. Marsh, D. Schumann, G. Heidenreich, S. Teichmann, Phys. Rev. C **75**, 012801 (2007)
11. G. Gyürky, J. Farkas, C. Yalçin, G.G. Kiss, Z. Elekes, Zs. Fülöp, E. Somorjai, Europhys. Lett. **83**, 42001 (2008); K.K.M. Lee, G. Steinle-Neumann, Earth Planet. Sci. Lett. **267**, 628 (2008); R. Blackburn, T. Yassine, Int. J. Rad. Appl. C. Rad. Phys. Chem. **40**, 263 (1992); A.M. Nicolás, A. Trifone, S.J. Nassiff, J. Radioanal. Nucl. Chem. **125**, 473 (1988)

12. T. Kurtukian-Nieto, J. Benlliure, K. Schmidt, Nucl. Instr. Methods Phys. Res. A: Acceler., Spectr., Det. Ass. Equip. **589**, 472 (2008); V. Kozlov, N. Severijns, D. Beck, M. Beck, S. Coeck, B. Delauré, A. Lindroth, S. Kopecky, P. Delahaye, F. Wenander, V.V. Golovko, I.S. Kraev, T. Phalet and ISOLDE, NIPNET and TRAPSPEC Collab., Int. J. Mass. Spectr. **251**, 159 (2006)
13. V.L. Mikheev, V.A. Morozov, N.V. Morozova, Phys. Particles Nucl. Lett. **5**, 371 (2008); V.I. Vysotskii, Phys. Rev. C **58**, 337 (1998)
14. A. Dykhne, G. Yudin, *Sudden Perturbations and Quantum Evolution* (UFN, Moscow, 1996)
15. B.S. Gelepov, L.N. Zyryanova, Yu.P. Suslov, *Beta Processes* (Nauka, Leningrad, 1978); V. Rusov, V. Tarasov, D. Litvinov, *Theory of Beta Processes in Georeactor* (URS, Moscow, 2008)
16. *Photonic, Electronic and Atomic Collisions*, eds. by F. Aumar, H. Winter (World Scientific, Singapore, 1997)
17. C. Ching, T. Ho, Phys. Rev. **112**, 1 (1984)
18. I. Kopytin, K. Karelin, A. Nekipelov, Phys. Atom. Nucl. **67**, 1429 (2004); I. Izosimov, A. Kazimov, V. Kalinnikov, Phys. Atom. Nucl. **67**, 1876 (2004)
19. L.I. Urutskov, D.V. Filippov, Physics-Uspekhi **174,** 1355 (2004); F.F. Karpeshin, M.B. Trzhaskovskaya, Yu.P. Gangrskii, JETP **99**, 286 (2004)
20. C. Müller, A. Di Piazza, A. Shahbaz , T.J. Bürvenich, J. Evers, H.Z. Hatsagortsyan, C.H. Keitel, Laser Physics **11**, 175 (2008); T.J. Burnevich, J. Evers, C.H. Keitel, Phys. Rev. C **74**, 044601 (2006); Phys. Rev. Lett. **96**, 142501 (2006); A. Shahbaz, C. Müller, A. Staudt, T.J. Burnevich, C.H. Keitel, Phys. Rev. Lett. **98**, 263901 (2007)
21. M. Romanovsky, Laser Physics **1**, 17 (1998); M.R. Harston, J.J. Caroll, Laser Physics **7**, 1452 (2004); E.V. Tkalya, Phys. Rev. A **75**, 022509 (2007)
22. I. Ahmad, R. Dunfird, H. Esbensen, D.S. Gemmell, E.P. Kanter, U. Run, S.H. Siuthwirth, Phys. Rev. C **61**, 051304 (2000); S. Kishimoto, Y. Yoda, Y. Kobayashi, S. Kitao, R. Haruki, R. Masuda, M. Seto, Phys. Rev. C **74**, 031301 (2006)
23. S. Olariu, T. Sinor, C.B. Collins, Phys. Rev. B **50**, 616 (1994); A.V. Glushkov, L.N. Ivanov, Preprint ISAN RAS, N-2AS (1991); Preprint ISAN RAS, N-3AS (1992)
24. A.V. Glushkov, S.V. Ambrosov, A.V. Loboda, Yu.G. Chernyakova, O.Yu. Khetselius, A.A. Svinarenko, Nucl. Phys. A **734S**, 21 (2004)
25. A. Glushkov, S. Malinvoskaya, O. Khetselius, Eur. Phys. J. ST **160**, 195 (2008)
26. A. Glushkov, S. Malinvoskaya, O. Khetselius, Mol. Phys. **106**, 1257 (2008)
27. A.V. Glushkov, O.Yu. Khetselius, S.V. Malinovskaya, in *Frontiers in Quantum Systems in Chemistry and Physics*, *Progress in Theoretical Chemistry and Physics* , vol. 18, eds. by S. Wilson, P.J. Grout, J. Maruani, G. Delgado-Barrio, P. Piecuch (Springer, Berlin, 2008), p. 523
28. A.V. Glushkov, S. Malinovskaya, L. Vitabetskaya, Y. Dubrovskaya, O.Yu. Khetselius, in *Recent Advances in Theoretical Physics and Chemistry Systems, Progress in Theoretical Chemistry and Physics*, vol. 15, eds. by J.-P. Julien, J. Maruani, D. Mayou, S. Wilson, G. Delgado-Barrio (Springer, Berlin, 2006), p. 301
29. H. Behrens, J. Janske, *Landolt-Berstein: New Series, Group 1*, vol. 4 (Berlin, Springer, 1999)
30. I. Band, M. Listengarten, M.B. Trzhaskovskaya, Izv. AN USSR **51**, 1998 (1986)
31. A. Glushkov, O. Khetselius, T. Florko, Y. Dubrovskaya, Sensor Electr. Microsyst. Techn. **3**, 21 (2006); **4**, 11 (2007); **5**, 41 (2008)
32. N. Nica, J.C. Hardy, V.E. Iacob, W.E. Rockwell, M.B. Trzhaskovskaya, Phys. Rev. C **75**, 024308 (2007)
33. N. Nica, J.C. Hardy, V.E. Iacob, S. Raman, C.W. Nestor M.B. Trzhaskovskaya, Phys. Rev. C **70**, 054305 (2004)
34. S. Raman, M. Ertugrul, C. Nestor, M. Trzhaskovskaya, At. Data Nucl. Data Tabl. **92**, 207 (2006)
35. S. Raman, C. Nestor, A. Ichihara, M. Trzhaskovskaya, Phys. Rev. C **66**, 044312 (2004)
36. L.N. Ivanov, E.P. Ivanova, L. Knight, Phys. Rev. A **48,** 4365 (1993)

37. A.V. Glushkov, L.N. Ivanov, E.P Ivanova, *Autoionization Phenomena in Atoms* (Moscow University Press, Moscow, 1986)
38. A.V. Glushkov, S.V. Malinovskaya, A.V. Loboda, E.P. Gurnitskaya, D.A. Korchevsky, J. Phys.: Conf. Ser. **11**, 188 (2005)
39. A.V. Glushkov, S.V. Ambrosov, A.V. Loboda, E.P. Gurnitskaya, G.P. Prepelitsa, Int. J. Quantum Chem. **104**, 562 (2005)
40. A. Glushkov, S. Malinovskaya, G. Prepelitsa, V. Ignatenko, J. Phys.: Conf. Ser. **11**, 199 (2004)
41. A. Glushkov, *Atom in Electromagnetic Field. Numerical Models* (KNT, Kiev, 2005)
42. P. Kienle, Phys. Scripta **46**, 81 (1993)
43. A.B. Migdal, J. Phys. USSR **4**, 449 (1941)
44. J.S. Levinger, Phys. Rev. **90**, 11 (1953); J. Phys. Radium **16**, 556 (1955)
45. P.A. Amudsen, P.H. Barker, Phys. Rev. C **50**, 2466 (1994)
46. R. Anholt, P.A. Amundsen, Phys. Rev. A **25**, 169 (1982)
47. O. Bohr, B. Motelsson, *Structure of Atomic Nucleus* (Plenum, New York, 1971)
48. Th. Carlson, C.W. Nestor, T.C. Tucker, F.B. Malik, Phys. Rev. **169**, 27 (1968)
49. G. Ciocchetti, A. Molinari, Nuovo Cim. **40**, 69 (1965)
50. T. Mukoyama, Sh. Ito, Phys. Lett. A **131**, 182 (1988); T. Mukoyama, S. Shimizu, J. Phys. G: Nucl. Phys. **4**, 1509 (1978)
51. L. Wauters, N. Vaeck, Phys. Rev. C **53**, 497 (1996)
52. L. Wauters, N. Vaeck, M. Godefroid, H. van der Hart, M. Demeur, J. Phys. B **30**, 4569 (1997)
53. A.V. Glushkov, I.T. Makarov, E. Nikiforova, M.I. Pravdin, I.E. Sleptsov, Astroparticle Phys. **4**, 15 (1995)
54. A.V. Glushkov, L.G. Dedenko, M.I. Pravdin, I.E. Sleptsov, JETP **99**, 123 (2004)
55. P. Piecuch, M. Wloch, J.R. Gour, D.J. Dean, M. Hjorth-Jensen, T. Papenbrock, in *Nuclei and Mesoscopic Physics: Workshop on Nuclei and Mesoscopic Physics WNMP 2004, AIP Conference Proceedings,* vol. 995, ed. by V. Zelevinsky (American Institute of Physics, Melville, NY, 2005), p. 28
56. V.I. Gol'danskii, Sov. Phys.-Uspekhi **19**, 180 (1976); G.G. Baldwin, J.C. Salem, V.I. Gol'dansky, Rev. Mod. Phys. **53,** 687 (1981)
57. V.S. Letokhov, in *Application of Lasers in Atomic, Molecular and Nuclear Physics*, eds. by A.M. Prokhorov, V.S. Letokhov (Nauka, Moscow, 1979), p. 412
58. V.S. Letokhov, V.I. Gol'dansky, JETP **67**, 513 (1974); L.N. Ivanov, V.S. Letokhov, Com. Mod. Phys. D **4**, 169 (1985); A.V. Glushkov, L.N. Ivanov, S.V. Malinovskaya, Preprint ISAN RAS, N-1AS (1991)
59. I.G. Kaplan, A.P. Markin, Reports of the USSR Acad. Sci. **223**, 1172 (1973); **232**, 319 (1977); JETP **64**, 424 (1973); JETP **69**, 9 (1975)
60. R. M Mössbauer, Z. Phys. A: Hadrons Nuclei **151**, 124 (1958); L. Szilard, T. Chalmers, Nature (London) **134**, 462 (1934)
61. D.J. Dean, M. Hjorth-Jensen, K. Kowalski, P. Piecuch, M. Wloch, in *Condensed Matter Theories,* eds. by J.W. Clark, R.M. Panoff, H. Li (Nova Sci. Publishers, 2006)
62. J.S. Hansen, Phys. Rev. A **9**, 40 (1974)
63. J. Law, Nucl. Phys. A **286**, 339 (1977); Can. J. Phys. **58**, 504 (1980)
64. E.G. Drukarev, M.I. Strikman, JETP **64**, 1160 (1986)
65. J. Law, J.L. Campbell, Phys. Rev. C **25**, 514 (1982)
66. R.L. Wolfgang, R. Anderson, R.W. Dodson, J. Chem. Phys. **24**, 16 (1956); R.L. Martin, J.S. Cohen, Phys. Lett. A **110**, 95 (1985)
67. A. Glushkov, S. Malinovskaya, Rus. J. Phys. Chem. **62**, 100 (1988); **65**, 2970 (1988)
68. A. Glushkov, S. Malinovskaya, in *New Projects and New Lines of Research in Nuclear Physics*, eds. by G. Fazio, F. Hanappe (World Scientific, Singapore, 2003), p.242
69. V.Z. Maidikov, in *New Projects and New Lines of Research in Nuclear Physics*, eds. by G. Fazio, F. Hanappe (World Scientific, Singapore, 2003), p. 227
70. A. Glushkov, S. Malinovskaya, A. Loboda, G. Prepelitsa, J. Phys.: Conf. Ser. **35**, 420 (2006)

71. A.V. Glushkov, S.V. Malinovskaya, Yu.G. Chernyakova, A.A. Svinarenko, Int. J. Quantum Chem. **99**, 889 (2004)
72. A.V. Glushkov, S.V. Malinovskaya, Int. J. Quantum Chem. **104**, 496 (2005)
73. L. Bandurina, I. Krivsky, A. Lendel, S. Medvedev, Nucl. Phys. **39**, 296 (1984)
74. V.S. Letokhov, Phys. Lett. A **46**, 257 (1974)
75. V.S. Letokhov, *Laser Specktroskopie* (Akad.-Verlag, Berlin, 1977)
76. L.N. Ivanov, V.S. Letokhov, JETP **68**, 748 (1975); JETP **71**, 19 (1976)
77. E.P. Ivanova, L.N. Ivanov, E.V. Aglitsky, Phys. Rep. **166**, 315 (1988)
78. V.S. Letokhov, V.G. Minogin, JETP **69**, 1568 (1985)
79. E.P. Ivanova, L.N. Ivanov, JETP **83**, 258 (1996)
80. A.V. Glushkov, L.N. Ivanov, Phys. Lett. A **170**, 33 (1992); J. Phys. B: At. Mol. Opt. Phys. **26,** L379 (1993)
81. A.V. Glushkov, JETP Lett. **55**, 97 (1992)
82. A.V. Glushkov, in *Low Energy Antiproton Physics: Eighth International Conference on Low Energy Antiproton Physics (LEAP '05), AIP Conference Proceedings*, vol. 796, eds. by D. Grzonka, R. Czyzykiewicz, W. Oelert, T. Rozek, P. Winter (American Institute of Physics, Melville, NY, 2005), p. 206
83. M. Hehenberger, H. McIntosh, E. Brändas, Phys. Rev. A **10**, 1494 (1974); A.V. Glushkov, S.V. Ambrosov, A.V. Ignatenko, D.A. Korchevsky, Int. J. Quantum Chem. **99**, 936 (2004)
84. A.V. Glushkov, O.Yu. Khetselius, A.V. Loboda, A.A. Svinarenko, in *Frontiers in Quantum Systems in Chemistry and Physics*, *Progress in Theoretical Chemistry and Physics*, vol. 18, eds. by S. Wilson, P.J. Grout., J. Maruani, G. Delgado-Barrio, P. Piecuch (Springer, Berlin, 2008), p. 541
85. A.V. Glushkov, E.P. Ivanova, J. Quant. Spectr. Rad. Transfer. **36**, 127 (1986)
86. E.P. Ivanova, L.N. Ivanov, A.V. Glushkov, A. Kramida, Phys. Scripta **32**, 512 (1985)
87. J.C. Slater, *The Consistent Field Method for Molecules and Solids: Quantum Theory of Molecules and Solids*, vol. 4 (McGraw-Hill, New York, 1974)
88. E.G. Gross, W. Kohn, *Exchange-Correlation Functionals in Density Functional Theory* (Plenum, New York, 2005)
89. S. Wilson, in *Recent Advances in Theoretical Physics and Chemistry Systems, Progress in Theoretical Chemistry and Physics*, vol. 16, eds. by J. Maruani, S. Lahmar, S. Wilson, G. Delgado-Barrio (Springer, Berlin, 2007), p. 11
90. S. Wilson, *Handbook on Molecular Physics and Quantum Chemistry* (Wiley, Chichester, 2003)
91. W. Kohn, L.J. Sham, Phys. Rev. A **140**, 1133 (1964); P. Hohenberg, W. Kohn, Phys. Rev. B **136**, 864 (1964)
92. R.M. Dreizler, Phys. Scripta T **46**, 167 (1993)
93. P. Indelicato, J.P. Desclaux, Phys. Scripta T **46**, 110 (1993)
94. A. Glushkov, O. Khetselius, in *Nuclear Physics in Astrophysics* NPA-III (Dresden, Germany, 2007), p. 95; J. Phys. G., to be published
95. K.N. Koshelev, L.N. Labzowsky, I.I. Tupitsyn, J. Phys. B **37**, 843 (2004)
96. J. Bieron, P. Pyykkö, P. Jonsson, Phys. Rev. A **71**, 012502 (2005); J. Bieron, P. Pyykk, Phys. Rev. A **71**, 032502 (2005)
97. P. Mohr, Atom. Data Nucl. Data Tabl. **24**, 453 (1993); Phys. Scripta T **46**, 44 (1993)
98. M.P. Das, M.V. Ramana, A.K. Rajagopal, Phys. Rev. **22**, 9 (1980)
99. K. Cheng, Y. Kim, J. Desclaux, Atom. Data Nucl. Data Tabl. **24**, 11 (1979)
100. G. Drake, Phys. Scripta T **46**, 116 (1993)
101. H.M. Quiney, I.P. Grant, Phys. Scripta T **46**, 132 (1993)
102. I. Klaft, S. Borneis, T. Engel, B. Fricke, R. Grieser, G. Huber, T. Kuhl, D. Marx, R. Neumann, S. Schroder, P. Seelig, L. Volker, Phys. Rev. Lett. **73**, 2425 (1994)
103. G. Gould, Phys. Scripta T**46**, 61 (1993); S. Blundell, Phys. Scripta T **46**, 144 (1993)
104. V. Dzuba, V. Flambaum, P. Silvestrov, O. Sushkov, Phys. Rev. A **44**, 2828 (1991)
105. H. Persson, I. Lindgren, S. Salomonson, Phys. Rev. Lett. **76**, 204 (1996)

106. W. Johnson, J. Sapirstein, S. Blundell, Phys. Scripta **46**, 184 (1993)
107. S.N. Tiwary, Rivista del Nuovo Cimento **18,** 1 (1995)
108. K.N. Koshelev, L.N. Ivanov, Phys. Rev. A **42,** 5784 (1990)
109. L.N. Ivanov, E.P. Ivanova, JETP **110**, 483 (1996)
110. J. Bieron, C. Froese-Fisher, S. Fritzsche, K. Pachucki, J. Phys. B: At. Mol. Opt. Phys. **37**, L305 (2004)
111. U. Safranova, T. Cowan, M. Safranova, J. Phys. B: At. Mol. Phys. **38**, 2741 (2005)
112. V. Dzuba, V. Flambaum, M.S. Safranova, Phys. Rev. A **73**, 022112 (2006)
113. U.I. Safranova, M.S. Safranova, W.R. Johnson, Phys. Rev. A **71**, 052506 (2005)
114. V. Yerokhin, A.N. Artemyev, V.M. Shabaev, Phys. Rev. A **75**, 062501 (2007)
115. B. Sahoo, G. Gopakumar, R. Chaudhuri, B. Das, H. Merlitz, U. Mahapatra, D. Mukherjee, Phys. Rev. A **68**, 040501 (2003)
116. J. Santos, F. Parenre, S. Boucard, P. Indelicato, J. Desclaux, Phys. Rev. A **71**, 032501 (2005)
117. A. Derevianko, S.G. Porsev, Phys. Rev. A **71**, 032509 (2005)
118. V. Zagrebaev, Yu. Oganessian, M. Itkis, W. Greiner, Phys. Rev. C **73**, 031602 (2006)
119. I. Theophilou, S. Thanos, A. Theophilou, J. Chem. Phys. **127**, 234103 (2007)
120. A.V. Glushkov, *Relativistic and Correlation Effects in Spectra of Atomic Systems* (Nauka, Moscow-Odessa, 2006)
121. I.P. Grant, *Relativistic Quantum Theory of Atoms and Molecules, Theory and Computation, Springer Series on Atomic, Optical, and Plasma Physics*, vol. 40 (Springer, Berlin, 2007), p. 587
122. E.P. Ivanova, I.P. Grant, J. Phys. B **31**, 2871 (1998); E.P. Ivanova, N.A. Zinoviev, Quant. Electronics **29**, 484 (1999); Phys. Lett. A **274**, 239 (2000)
123. K.G. Dyall, K. Faegri, Jr. *Introduction to Relativistic Quantum Theory* (Oxford University Press, Oxford, 2007)
124. A.V. Glushkov, *Relativistic Quantum Theory. Quantum Mechanics of Atomic Systems* (Astroprint, Odessa, 2008)
125. A.V. Glushkov, O.Yu. Khetselius, E.P. Gurnitskaya, A.V. Loboda, T.A. Florko, D.E. Sukharev, L. Lovett, in *Frontiers in Quantum Systems in Chemistry and Physics, Progress in Theoretical Chemistry and Physics*, vol. 18, eds. by S. Wilson, P.J. Grout., J. Maruani, G. Delgado-Barrio, P. Piecuch (Springer, Berlin, 2008), p. 505
126. A.V. Glushkov, S.V. Ambrosov, A.V. Loboda, E.P. Gurnitskaya, O.Yu. Khetselius, in *Recent Advances in Theoretical Physics and Chemistry Systems, Progress in Theoretical Chemistry and Physics*, vol. 15, eds. by J.-P. Julien, J. Maruani, D. Mayou, S. Wilson, G. Delgado-Barrio (Springer, Berlin, 2006), p. 285
127. A.V. Glushkov, S.V. Malinovskaya, G.P. Prepelitsa, A.V. Ignatenko, J. Phys.: Conf. Ser. **11**, 199 (2005)
128. *The Fundamentals of Electron Density, Density Matrix and Density Functional Theory in Atoms, Molecules and the Solid State, Progress in Theoretical Chemistry and Physics*, vol. 14, eds. by N. Gidopoulos, S. Wilson (Springer, Berlin, 2004), p.1
129. I.P. Grant, H.M. Quiney, Int. J. Quantum Chem. **80**, 283 (2000)
130. *Supercomputing, Collision Processes, and Applications, Physics of Atoms and Molecules*, eds. by K. Bell, K.A. Berrington, D.S.F. Crothers, A. Hibbert, K. Taylor (Kluwer, New York, 1999)
131. *Advanced Topics in Theoretical Chemical Physics, Progress in Theoretical Chemistry and Physics*, vol. 12, eds. by J. Maruani, R. Lefebvre, E. Brändas (Springer, Berlin, 2004)
132. S. Wilson, J. Mol. Struct.: Theochem. **547**, 279 (2001)
133. A. Glushkov, S. Malinovskaya, E. Gurnitskaya, O. Khetselius, J. Phys.: Conf. Ser. **35**, 426 (2006)
134. A.V. Glushkov, Rus. J. Struct. Chem. **31**, 9 (1990); **32**, 11 (1992); **34**, 3 (1993)
135. A.V. Glushkov, Rus. J. Phys. Chem. **66**, 589 (1992); **66**, 1259 (1992)
136. A.V. Glushkov, S.V. Malinovskaya, I.M. Shpinareva, V.P. Kozlovskaya, V.I. Gura, Int. J. Quantum Chem. **104**, 512 (2005)

137. A.V. Glushkov, A.V. Loboda, E.P. Gurnitskaya, A.A. Svinarenko, Phys. Scripta T **134**, 137740 (2009)
138. A.V. Glushkov, S.V. Malinovskaya, Yu.V. Dubrovskaya, L.A. Vitavetskaya, in *Recent Advances in Theoretical Physics and Chemistry Systems, Progress in Theoretical Chemistry and Physics*, vol. 15, eds. by J.-P. Julien, J. Maruani, D. Mayou, S. Wilson, G. Delgado-Barrio (Springer, Berlin, 2006), p. 301
139. V.N. Gedasimov, A.G. Zelenkov, V.M. Kulakov, V.A. Pchelin, M.V. Sokolovskaya, A.A. Soldatov, L.V. Chistyakov, JETP **94**, 1169 (1984)
140. K. Kar, S. Sarkar, A. Ray, Phys. Lett. B **261**, 217 (1991)
141. A.V. Glushkov, V.D. Rusov, S.V. Ambrosov, A.V. Loboda, in *New Projects and New Lines of Research in Nuclear Physics*, eds. by G. Fazio, F. Hanappe (World Scientific, Singapore, 2003), p. 126
142. V. Rusov, V. Pavlovich, V. Vaschenko, V. Tarasov, T. Zelentsova, V. Bolshakov, D. Litvinov, S. Kosenko, O. Byegunova, J. Geophys. Res. B **112**, 09203 (2007)
143. Q.-Q. Sun, Z.-G. Huang, H.-G. Piao, Z.-Q. Luo, Chinese Astr. Astrophys. **31**, 229 (2008)
144. J.A. Behr, G. Gwinner, J. Phys. G: Nucl. Part. Phys. **36**, 033101 (2009)
145. K.U. Kettner, H.W. Becker, F. Strieder, C. Rolfs, J. Phys. G: Nucl. Part. Phys. **32**, 489 (2006)
146. S.K. Godovikov, Izv. RAN, Ser. Phys. **65**, 1063 (2001); N. Zinner, Nucl. Phys. A **781**, 81 (2007)
147. C. Bertulani, Nucl. Phys. A **626**, 187 (1997)
148. A.V. Glushkov, O.Yu. Khetselius, A.V. Loboda, E.P. Gurnitskaya, in *Proceedings of the 11th International Conference on Meson-Nucleon Physics and the Structure of the Nucleon*, eds. by S. Krewald, H. Machner (IKP, Juelich, Germany), SLAC eConf C070910 (Menlo Park, CA, USA) **2**, 186 (2007); A.V.Glushkov, *ibid*. **2**, 111 (2007)
149. S. Aseev, B. Mironov, S. Chekalin, V.S. Letokhov, JETP Lett. **87**, 361 (2008)
150. A.V. Glushkov, *Nuclear Quantum Optics* (Astroprint, Odessa, 2009)

Part II
Complexes and Clusters

Quantum Chemical Approach to Interatomic Decay Rates in Clusters

V. Averbukh, P. Kolorenč, K. Gokhberg, and L.S. Cederbaum

Abstract Since their theoretical prediction in 1997, interatomic (intermolecular) Coulombic decay (ICD) and related processes have been in the focus of intensive theoretical and experimental research. The spectacular progress in this direction has been stimulated both by the fundamental importance of the discovered electronic decay phenomena and by the exciting possibility of their practical application, for example, in spectroscopy of interfaces. Interatomic decay phenomena take place in inner-shell-ionized clusters due to electronic correlation between two or more cluster constituents. These processes lead to the decay of inner-shell vacancies by electron emission and often also to the disintegration of the resulting multiple ionized cluster. The primary objective of the theory is, thus, to predict the kinetic energy spectra of the emitted electrons and of the cluster fragments. These spectra are determined by an interplay between the electronic decay process and the nuclear dynamics. Key to the reliable prediction of the observable quantities is the knowledge of the time scale of the interatomic decay. Here we review the recent progress in the development of ab initio quantum chemical methods for the calculation of interatomic decay rates in excited, singly ionized, and doubly ionized systems as well as some of their applications, e.g., to rare gas systems and to endohedral fullerenes.

V. Averbukh (✉)
Max Planck Institute for the Physics of Complex Systems, Nöthnitzer Str. 38, D-01187 Dresden, Germany, e-mail: vitali@mpipks-dresden.mpg.de

P. Kolorenč
Institute of Theoretical Physics, Faculty of Mathematics and Physics, Charles University in Prague, V Holešovičkách 2, 180 00 Prague, Czech Republic, e-mail: kolorenc@mbox.troja.mff.cuni.cz

K. Gokhberg
Theoretische Chemie, Physikalisch-Chemisches Institut, Universität Heidelberg, Im Neuenheimer Feld 229, D-69120 Heidelberg, Germany, e-mail: Kirill.Gokhberg@pci.uni-heidelberg.de

L.S. Cederbaum
Theoretische Chemie, Physikalisch-Chemisches Institut, Universität Heidelberg, Im Neuenheimer Feld 229, D-69120 Heidelberg, Germany, e-mail: Lorenz.Cederbaum@pci.uni-heidelberg.de

P. Piecuch et al. (eds.), *Advances in the Theory of Atomic and Molecular Systems*, Progress in Theoretical Chemistry and Physics 20, DOI 10.1007/978-90-481-2985-0_8,

Keywords: Interatomic Coulombic decay · Ab initio calculations · Inner-shell ionization · Clusters

1 Introduction

The present day knowledge of interatomic (intermolecular) decay mechanisms in clusters encompasses a diversity of distinct physical phenomena, all stemming from interatomic (intermolecular) electronic interaction. In this section we give an overview of the predicted and observed interatomic decay processes.

1.1 Interatomic (Intermolecular) Coulombic Decay: A General Decay Mode of Auger-Inactive Inner-Shell-Ionized States

Core vacancy states of atoms and molecules represent very highly excited states of the corresponding atomic or molecular ions, typically lying above the double or even multiple ionization thresholds. As a result, these states decay by electron emission in a specific type of autoionization process named after its discoverer, Auger [1]. Kinetic energies of the electrons emitted in the course of Auger decay are given by the differences between the bound states of singly and doubly charged species and thus are quantized. This property explains the great spectroscopic value of the Auger electron spectroscopy (AES) [2], as well as its importance for numerous analytical applications, e.g., in surface science (see, for example, Ref. [3]). Auger decay is typically an intraatomic process, only modestly affected by the environment. Usually, such an effect is manifested in the so-called chemical shift of the Auger electron lines (see, for example, Ref. [4]).

In 1997, the authors of the theoretical work [5] took a pioneering approach to the issue of the environment effects on the decay of vacancy states [5]. The question posed by the authors was:

> Can a vacancy decay non-radiatively *only* due to the effect of the environment?

Surprisingly, it turned out that such an environment-mediated decay is not only possible, but also a general phenomenon, typical of relatively low-energy inner-shell vacancies in a wide variety of clusters [5]. In order to get an idea of the new decay process discovered by Cederbaum and co-workers, one can consider the decay of $2s$ vacancy of neon, once in an isolated ion and once in a cluster, e.g., in Ne_n. The $2s^{-1}$ state of the isolated Ne^+ lies below the double ionization threshold of Ne and thus cannot decay by Auger mechanism. As a result, $(2s^{-1})$ Ne^+ decays radiatively on a nanosecond time scale. However, if $(2s^{-1})$ Ne^+ is allowed to interact with an environment, e.g., with other Ne atoms, the situation changes dramatically. Indeed, as shown schematically in Fig. 1 for neon dimer, in a Ne_n cluster, one can consider not only the high-energy $Ne^{2+}Ne_{n-1}$ doubly ionized states, but also the ones of the type $(Ne^+)_2Ne_{n-2}$. The latter states are relatively low in energy due to the separation of the positive charge between two neon atoms. In fact, the charge-separated states

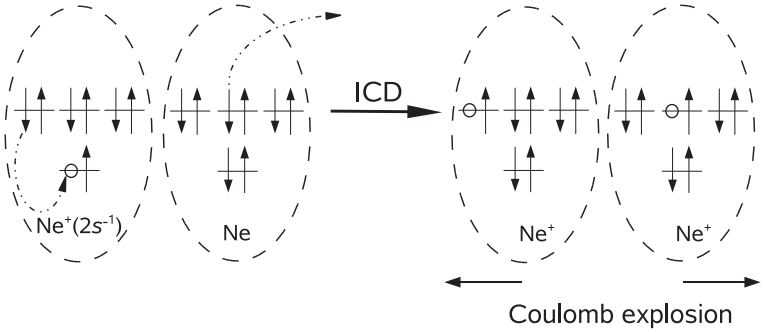

Fig. 1 A schematic representation of the ICD process in Ne dimer. A $2p$ electron of the inner-valence-ionized Ne recombines into the $2s$ vacancy while a $2p$ electron of another Ne is ejected into continuum. The resulting doubly charged cluster decomposes by Coulomb explosion mechanism

lie several electron-volts lower than $(2s^{-1})$ $Ne^{+}Ne_{n-1}$. This leads to a very interesting *interatomic* decay process in which $2p$ electron of the ionized Ne fills the $2s$ vacancy, while $2p$ electron of another Ne atom is ejected into continuum. Since such a process is enabled by the Coulombic interaction between the electrons of the two Ne atoms, it has been called interatomic Coulombic decay (ICD). In a small loosely bound cluster, such as neon dimer, the repulsion between the two charges created by ICD leads to Coulomb explosion of the system [6] (see Ref. [7] for an exception). Under such conditions, the excess energy of the initial vacancy state is partitioned between the outgoing electron and the separating positively charged fragments. Thus, while Auger decay leads to quantized Auger electron energies, ICD in small clusters makes the total of the electron and the cluster fragment energies to be quantized. The kinetic energy of the relative motion of the fragments is often called kinetic energy release (KER).

The last several years have witnessed a series of remarkable advances in the experimental study of ICD. Hergenhahn, Möller, and co-workers have presented the first experimental evidence of ICD by clearly identifying the new process in neon clusters [8]. Dörner, Jahnke, and co-workers have conducted a detailed study of ICD in neon dimer [9] using the cold target recoil ion momentum spectroscopy (COLTRIMS) [10]. They have been able to measure in coincidence both the ICD electrons and the neon ions generated by the Coulomb explosion of $(Ne^{+})_2$. The coincidences detected by Frankfurt group were found to be arranged along the energy conservation line corresponding to the sum of the electron energy and the KER being about 5 eV. Thus, the experiment of Dörner and co-workers constitutes the most detailed direct proof of the ICD. The electron kinetic energy and the KER spectra of Frankfurt group were later confirmed by theoretical calculations [11]. Going back to larger neon clusters, Örwall et al. have estimated the dependence of the ICD lifetime on the neon cluster size by distinguishing between the "bulk" and the "surface" peaks in the ICD electron spectra [12]. These experimental findings were found it to be in a reasonable agreement with earlier theoretical predictions of Santra et al. [13] (see also the more recent theoretical work of Vaval and Cederbaum [14]).

Both theoretical and experimental investigations have established ICD as a highly general and a very efficient decay process. Indeed, ICD is characteristic of vacancy states of van der Waals clusters (see, e.g., Refs. [5, 8]), hydrogen-bonded clusters (see, e.g., Refs. [15, 61]), and even endohedral fullerenes [16]. The ICD lifetimes were found to belong to the range of 1–100 fs [12, 13, 16], many orders of magnitude shorter than those of the competing photon emission process. Thus, ICD is the main decay mode of moderate-energy (Auger-inactive) inner-shell vacancies in clusters. Further studies of ICD are motivated, however, not only by the generality and efficiency of this new physical process, but also by the perspectives of its practical use, for example, in spectroscopy. The very first step in this highly promising direction has been already done by Hergenhahn and co-workers who have shown that the ICD electron spectra can be used in order to identify the Ne/Ar interface [17].

1.2 Beyond ICD of Singly Ionized States

1.2.1 Interatomic Decay in Inner-Shell Excitations

Recently, Barth et al. [18] have addressed the question whether interatomic decay can occur not only in the inner-valence-ionized, but also in the inner-valence-excited states of clusters. They have created Ne $(2s^{-1}3p)$ excitations in Ne_n clusters (n being 70 on average) and detected the electrons emitted due to the (Ne $2s^{-1}3p$)$Ne_{n-1} \rightarrow$ (Ne $2p^{-1}3p$)(Ne^+ $2p^{-1}$)$Ne_{n-2} + e^-$ process. Aoto et al. [19] studied in detail a similar decay phenomenon in neon dimer. This process is related to ICD exactly in the same way in which the resonant Auger effect [20, 21] is related to the regular Auger effect [1, 2]. Consequently, it has been called resonant interatomic Coulombic decay (RICD) [18].

The RICD physics is richer and more involved than the ICD physics due to several reasons. First, the interatomic decay of inner-shell-excited states is accompanied by the intraatomic autoionization, e.g., $(2s^{-1}3p)\text{Ne} \rightarrow (2p^{-1})\text{Ne} + e^-$. Whereas ICD competes only with slow radiative decay, RICD has to compete with a fast non-radiative process. Nevertheless, both experimental [18, 19] and theoretical [22] evidences show that this competition does not lead to a suppression of RICD. Another important difference between ICD and RICD comes from the fact that the inner-valence-excited electron can participate in the RICD process. Exactly as the resonant Auger decay [20, 21], RICD can occur either by *spectator* (sRICD) or by *participator* (pRICD) mechanism. While the sRICD process has been observed experimentally, pRICD has yet to be identified in the RICD electron spectra.

Yet another distinction between ICD and RICD has its origin in the higher energy accumulated in the inner-valence-excited states relative to the one of the inner-valence-ionized states. For example, $(2s^{-1}3p)$Ne lies about 45.5 eV above the Ne ground state, whereas $(2s^{-1})$ Ne^+ lies only about 26.9 eV above the Ne^+ ground state. As a result, decay of inner-valence-ionized states can be accompanied by double ionization of the cluster. This can happen according to a variety of mechanisms which have been discussed qualitatively in Ref. [22]. The predicted double ioniza-

tion interatomic processes still await their detailed quantitative study. The essential question is whether the double ionization processes are fast enough to compete with autoionization and *s*RICD.

1.2.2 Auger–ICD Cascade

It is well known that Auger decay of core vacancies often results in highly excited states of the corresponding doubly ionized species. Sometimes, this brings about another stage (or even several stages) of Auger decay, forming what is usually called a decay cascade. Often, however, the excited doubly ionized states created by Auger process are not energetic enough to decay by an intraatomic mechanism. Under such conditions, formation of decay cascade is impossible in isolated species, but can occur in clusters with the second step of the cascade being of the ICD, rather than of the Auger type. The Auger–ICD cascade has been first predicted by Santra and Cederbaum [23] in neon dimer (see also the more recent theoretical work [24]) and has first been observed by Ueda and co-workers [25] in argon dimers (see also the theoretical work [26]).

The Auger–ICD cascade in neon dimer can be represented as $(1s^{-1})\mathrm{Ne}^{+}\mathrm{Ne} \rightarrow (2s^{-1}2p^{-1})\mathrm{Ne}^{2+}\ \mathrm{Ne} + e^{-} \rightarrow (2p^{-2})\mathrm{Ne}^{2+} + \mathrm{Ne}^{+} + e^{-}$. Interestingly, a similar process starting with $2p$ ionization of argon dimer is energetically forbidden: the $3s^{-1}3p^{-1}$ states of Ar^{2+} are not energetic enough to lead to ICD. Observation of Auger–ICD cascade in Ar_2 [25] has been nevertheless possible due to the fact that Auger decay populates not only the $3s^{-1}3p^{-1}$ main states, but also higher-energy satellites having admixture of $3p^{-3}3d$ configurations. More recently, ICD after Auger decay in neon dimer has been extensively studied [27–29]. Experimental work on the Auger–ICD cascade in NeAr is now in progress [30].

Further exploration of the fascinating subject of the interatomic decay phenomena and development of spectroscopic tools on their basis requires intensive theoretical effort to guide the experimental work. Such an effort is hardly possible without efficient, advanced theoretical tools involving both ab initio description of the electron correlation driving the decay and a treatment of the ensuing dynamics of the ionized cluster fragments. The next section gives the theoretical picture of interatomic decay within the Born–Oppenheimer (BO) approximation. Ab initio theory of the interatomic decay widths is presented in some detail for the case of the ICD process in Sect. 3. Sections 4 and 5 are devoted to ab initio theory and computational algorithms for the interatomic decay widths in doubly ionized and inner-shell-excited systems, respectively. Some considerations on the future of the field are summarized in Sect. 6.

2 Born–Oppenheimer Picture of Interatomic Decay

The main objective of the theory of ICD is to enable efficient and reliable calculation of the measurable spectra, i.e., ICD electron kinetic energy spectrum and (where applicable) KER spectrum. The theoretical description is usually given

within Born–Oppenheimer approximation, in which the electronic states are decoupled from nuclear motion and depend only parametrically on the nuclear coordinates. In this picture, the inner-shell ionization and the subsequent ICD process can be visualized as a series of transitions between potential energy surfaces (PESs) belonging to electronic states of different number of electrons (i.e., accompanied by electron emission). These transitions are represented schematically in Fig. 2. Initially, the system is assumed to be in the ground electronic state of the neutral (N-electron) system. The corresponding PESs of loosely bound clusters are characterized by shallow minima (e.g., in meV range for van der Waals systems) and large equilibrium interatomic distances. Photoionization brings the cluster almost instantaneously into inner-shell-ionized (typically, inner-valence-ionized) [$(N-1)$-electron] state, being the intermediate state of the decay. The PES of the singly ionized system is affected by the charge-induced dipole interaction that increases the binding energy and decreases the equilibrium interatomic distances relative to

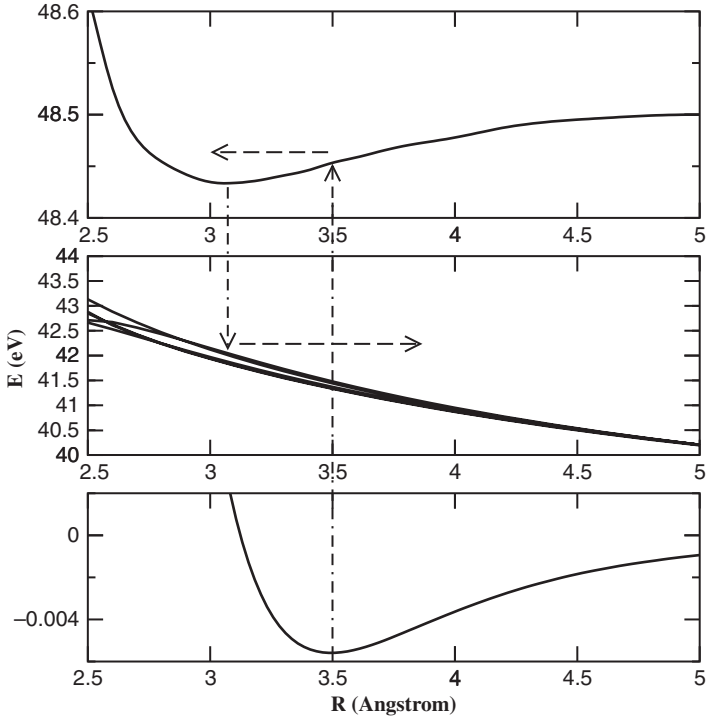

Fig. 2 Schematic representation of ICD process in Born–Oppenheimer picture. PESs of NeAr [33] are used as a representative example. Lower frame: ground-state PES of the neutral diatom (initial state). Upper frame: inner-valence-ionized (intermediate state) PES. Middle frame: doubly ionized (final state) PESs. Transitions between the PESs accompanied by loss of an electron are shown by *dashed–dotted lines*. Directions of motion of nuclear wave packets on intermediate and final state PESs are shown by *dashed lines*

the van der Waals ground state. This means that after landing on the inner-shell-ionized PES, the nuclear wave packet is driven toward shorter internuclear distances. Due to the ICD, the intermediate state has finite lifetime. This means that the nuclear wave packet moving on the intermediate state PES can lose some of its density to the final (doubly ionized) state PESs. The latter are typically dominated by the repulsion between the two positive charges and are often close to the purely Coulombic repulsive shape. The geometry at which the decay occurred determines the partition of energy between the outgoing electron and the repelling fragments.

The above qualitative picture has its full formal analog in the so-called time-dependent formulation of the theory of nuclear dynamics of electronic decay processes. This theory is given in some detail in Ref. [11] and in references therein. Here we will consider only its few principal points. Let us denote the nuclear wave packets for the initial (i), intermediate (d), and final (f) electronic states as Ψ_i, Ψ_d, and Ψ_m^f, respectively, where the index m accounts for the possibility that there are several final electronic states (see Fig. 1). We assume that the electric field used in order to ionize the initial state is weak enough (weak-field approximation) and describes the coupling between the intermediate and the final states of the decay in the so-called local approximation [11]. Under these approximations, the nuclear wave packets obey the following set of coupled differential equations:

$$\begin{aligned}
\hbar\frac{\partial}{\partial t}|\Psi_i(R,t)\rangle &= \hat{H}_i(R)|\Psi_i(R,t)\rangle,\\
\hbar\frac{\partial}{\partial t}|\Psi_d(R,t)\rangle &= \hat{F}(R,t)|\Psi_i(R,t)\rangle + \hat{\mathcal{H}}_d(R)|\Psi_d(R,t)\rangle,\\
\hbar\frac{\partial}{\partial t}|\Psi_m^f(R,\varepsilon,t)\rangle &= \hat{W}_m(R,\varepsilon)|\Psi_d(R,t)\rangle + (\hat{H}_m^f(R)+\varepsilon)|\Psi_m^f(R,\varepsilon,t)\rangle\,,
\end{aligned} \tag{1}$$

where ε is the energy of the electron emitted during ICD.

The Hamilton operators for the nuclear motion in the initial and final electronic states in Eq. (1) are defined as $\hat{H}_i = \hat{T}_N + \hat{V}_i$ and $\hat{H}_m^f = \hat{T}_N + \hat{V}_m^f$, where $\hat{T}_N$ is the nuclear kinetic energy and $\hat{V}_i$ and $\hat{V}_m^f$ are the initial and final state PESs, respectively. The effective Hamilton operator governing the intermediate state dynamics has to account for the fact that the intermediate state is an electronic resonance. Within the local approximation, this is done by lending the intermediate state Hamiltonian a non-Hermitian character:

$$\hat{\mathcal{H}}_d(R) = \hat{T}_N(R) + \hat{V}_d(R) - i\hat{\Gamma}(R)/2\,, \tag{2}$$

where $\hat{V}_d(R)$ is the intermediate state PES and $\hat{\Gamma}(R)$ is the total decay width.

The coupling operators $\hat{F}$ and $\hat{W}_m$ describe the excitation from the initial to the intermediate electronic state and the coupling of the latter to the mth final state, respectively. Since we assume the inner-shell ionization to occur instantaneously, $\hat{F}$ can be taken to be R independent and simply a δ-function in time. The $\hat{W}_m$

operators describe the coupling of the intermediate state to the different final states. Within the local approximation, they are energy independent and are related to the corresponding partial decay widths: $\Gamma_m(R) = 2\pi |\hat{W}_m(R)|^2$.

As shown, e.g., in Ref. [11, 31, 32], all the information concerning the decay spectrum can be derived from the knowledge of the final nuclear wave packets. Indeed, at sufficiently large time (i.e., when the decay is complete and the norm of all the intermediate wave packet is zero), only the final states are populated and thus carry all the spectroscopic information of interest. In particular, the decay spectrum as a function of the emitted electron energy ε is given by [11, 31]

$$\sigma(\varepsilon) = \lim_{t\to\infty} \sum_m \sigma_m(\varepsilon, t) = \lim_{t\to\infty} \sum_m \langle \Psi_m^f(R, \varepsilon, t) | \Psi_m^f(R, \varepsilon, t) \rangle \,. \tag{3}$$

Equations in (1) show clearly that the shape of the spectrum (3) is determined by two competing time scales: that of the nuclear wave packet motion on the intermediate PES and that of the interatomic decay. If the decay is fast relative to the nuclear motion, the ICD occurs around the equilibrium geometry of the neutral (see Ref. [33] for a recent example of this kind). If, on the other hand, decay is slow on the scale of the nuclear wave packet evolution, ICD occurs within a wide range of geometries. In the latter case, various contributions are expected to interfere resulting in a complex pattern of $\sigma(E)$ [see Eq. (3)]. Thus, an accurate computation of the ICD width of the intermediate state is crucial for a reliable prediction of the ICD spectra.

3 ICD Widths by Fano–ADC–Stieltjes Method

Calculation of ICD widths can be achieved within one of the two main theoretical approaches. One of them relies on the introduction of complex absorbing potential (CAP) [34, 35] into the $(N-1)$-electron Hamiltonian [36] (see Refs. [37] on the relation between the CAP method and the method of exterior complex scaling). The decay widths are then given by the imaginary parts of those eigenvalues of the resulting non-Hermitian Hamiltonian [$E = \Re(E) - i\Gamma/2$] that are stationary with respect to the non-physical CAP parameters. The $(N-1)$-electron Hamiltonian can be represented using a variety of ab initio techniques, such as, for example, configuration interaction (CI) or algebraic diagrammatic construction (ADC) [38] within the intermediate state representation (ISR) [39]. The application of the CAP–CI method to calculate ICD widths has been reviewed in detail in Ref. [40]. More recently, CAP–ADC method [40] based on the ADC–ISR representation of the many-electron Hamiltonian has been developed [41–43] and applied to ICD [14]. An alternative ab initio approach to calculate the interatomic decay widths on which we would like to concentrate here [44] relies on Fano theory of resonances [45], ADC–ISR representation of the many-electron wave functions [39], and Stieltjes imaging technique [46].

3.1 ICD Within Fano Theory of Resonances

Fano theory of resonances [45] as well as its generalized version [47, 48] developed for the description of Auger decay widths represents the wave function Ψ_E at some energy E above threshold as a superposition of bound-like (Φ) and continuum-like (χ_ε) components, which can be thought of as the initial and final states of the decay:

$$\Psi_{\alpha,E} = a_\alpha(E)\Phi + \sum_{\beta=1}^{N_c} \int C_{\beta,\alpha}(E,\varepsilon)\,\chi_{\beta,\varepsilon}\,d\varepsilon\,, \tag{4}$$

where the index β runs over the N_c possible decay channels. In the specific case of interatomic (intermolecular) decay in clusters, the bound part of the wave function, Φ, corresponds to the singly ionized state, typically created by the inner-valence ionization of one of the cluster subunits. The state Φ is characterized by the mean energy

$$E_\Phi = \langle \Phi | H | \Phi \rangle\,, \tag{5}$$

H being the full Hamiltonian of the system. The N_c decay channels in Eq. (4) are defined by the doubly ionized states of the cluster characterized by the energies $E_\beta < E$, $\beta = 1, \ldots, N_c$, i.e., by the energetically accessible final states of the interatomic (intermolecular) decay. The continuum functions corresponding to the decay channels are assumed to diagonalize the Hamiltonian to a good approximation:

$$\langle \chi_{\beta',\varepsilon'} | H - E | \chi_{\beta,\varepsilon} \rangle \approx (E_\beta + \varepsilon - E)\,\delta_{\beta',\beta}\,\delta(E_{\beta'} + \varepsilon' - E_\beta - \varepsilon)\,. \tag{6}$$

Using the assumption of uncoupled continuum functions, Fano theory provides an analytic expression for the evaluation of the decay width:

$$\Gamma = \sum_{\beta=1}^{N_c} \Gamma_\beta = 2\pi \sum_{\beta=1}^{N_c} \left| M_\beta(E_r, \varepsilon_\beta) \right|^2\,, \quad M_\beta(E,\varepsilon) = \langle \Phi | H - E | \chi_{\beta,\varepsilon} \rangle\,, \tag{7}$$

where E_r is the real energy of the decaying state, $E_r \approx E_\Phi = \langle \Phi | H | \Phi \rangle$ and ε_β is the asymptotic kinetic energy of the ejected electron for the decay channel β, $E_r = E_\beta + \varepsilon_\beta$.

3.2 Initial and Final States of the ICD by Algebraic Diagrammatic Construction in the Framework of the Intermediate State Representation

For the result (7) to be applicable to the computation of the interatomic decay rates, one has to provide sensible approximations for the multi-electron bound (Φ) and continuum ($\chi_{\beta,\varepsilon}$) wave functions. In our case, these are wave functions of a singly ionized N-electron cluster, i.e., $(N-1)$-electron states. Such states can be conveniently constructed using the single ionization ADC technique. The ADC methodology has been originally developed within the Green's function formalism [38]. Here, however, we would like to briefly review the single ionization ADC from a different standpoint, using the intermediate state representation (ISR) as proposed by Schirmer et al. [39].

Consider the Hartree–Fock (HF) ground state of the N-electron neutral cluster, Φ_0^N. One can form a complete orthonormal set of the $(N-1)$-electron basis functions, $\Phi_J^{(N-1)}$, applying the so-called physical excitation operators, $\{\hat{C}_J\}$, to the HF ground state:

$$\begin{aligned} \Phi_J^{(N-1)} &= \hat{C}_J \Phi_0^N, \\ \{\hat{C}_J\} &\equiv \{c_i;\, c_a^\dagger c_i c_j, i<j;\, c_a^\dagger c_b^\dagger c_i c_j c_k, a<b, i<j<k;\, \ldots\}, \end{aligned} \tag{8}$$

where c_i and $c_a^\dagger$ are annihilation and creation operators, respectively, the subscripts $i, j, k, \ldots$ relate to the occupied spin orbitals, and the subscripts $a, b, c, \ldots$ relate to the unoccupied spin orbitals. The basis set (8) is used in the familiar CI expansion of the wave function. This expansion, once truncated after some specific excitation class $[J]$, possesses such important drawbacks as slow convergence and lack of size consistency. The ADC method overcomes these drawbacks by using a more complicated basis for the expansion of the $(N-1)$-electron wave functions. The idea is to apply the physical excitation operators, $\{\hat{C}_J\}$, to the perturbation theoretically corrected or "correlated" ground state of the neutral system,

$$\begin{aligned} \Psi_J^0 &= \hat{C}_J \Psi_0^N \\ \Psi_0^N &= \Phi_0^N + \Psi_0^{(1)} + \Psi_0^{(2)} + \Psi_0^{(3)} + \cdots, \end{aligned} \tag{9}$$

where $\Psi_0^{(n)}$ is the nth-order correction to the HF ground state obtained by the standard many-body perturbation theory (see, e.g., Ref. [49]). Unfortunately, the resulting correlated excited states (CESs), Ψ_J^0, are not orthonormal. ADC takes care of this problem by orthonormalizing them in two steps to obtain the so-called intermediate states, $\tilde{\Psi}_J$. First, Gram–Schmidt orthogonalization *between the excitation classes* is performed to obtain the "precursor" states

$$\Psi_J^{\#} = \Psi_J^0 - \sum_{[K]}^{K<[J]} \langle \tilde{\Psi}_K | \Psi_J^0 \rangle \tilde{\Psi}_K \,, \tag{10}$$

i.e., the functions belonging to the higher [e.g., two-hole, one-particle (2h1p) or $[J] = 2$] excitation class are made orthogonal to those of all the lower [in this case, only one-hole (1h) or $[K] = 1$] excitation classes. Second, the precursor states are orthonormalized symmetrically *inside each excitation class*:

$$\tilde{\Psi}_J = \sum_{[J']=[J]}^{J'} \left(\underline{\underline{\rho}}^{\#-\frac{1}{2}}\right)_{J',J} \tilde{\Psi}_{J'} \,, \qquad \left(\underline{\underline{\rho}}^{\#}\right)_{J',J} = \langle \Psi_{J'}^{\#} | \Psi_J^{\#} \rangle, \tag{11}$$

where $\left(\underline{\underline{\rho}}^{\#}\right)_{J',J}$ is the overlap matrix of the precursor states belonging to the same excitation class. The above two-step procedure can be applied iteratively, noting that the correlated excited states of the lowest (1h) excitation class are by definition also the precursor states.

Any state of the $(N-1)$-electron system can be represented using the orthonormal basis of the intermediate states:

$$\Psi_q^{(N-1)} = \sum_i \sum_{[J]=i} Y_{q,J} \tilde{\Psi}_J \,. \tag{12}$$

The expansion coefficients, Y_J, are obtained by the diagonalization of the Hamiltonian matrix constructed in the basis of the intermediate states. It is a crucial feature of the ADC approach that the Hamiltonian matrix elements of the type $\langle \tilde{\Psi}_J | H | \tilde{\Psi}_J \rangle$ can be expressed analytically via the orbital energies and the electron repulsion integrals if one performs the orthonormalization procedure of Eqs. (10, 11) approximately and consistently with the order of the many-body perturbation theory which is used for the construction of the correlated ground state [see Eq. (9)]. Moreover, it can be shown [39] that truncation of the expansion (12) after the excitation class $[J] = m$ introduces an error of the order of $2m$, which should be compared to $m + 1$ for the slower-converging CI expansion. The accuracy of the expansion in excitation classes (12) should be, of course, consistent with that of the perturbation-theoretical series for the correlated ground state (9). Thus, the order, n, at which the perturbation-theoretical expansion (9) is truncated is the single parameter defining the level of the ADC approximation. For this reason, ADC schemes of various quality are usually denoted as ADC(n), $n = 2, 3, 4, ...$, in full analogy with the well-known MP2, MP3, MP4, ... perturbation-theoretical techniques for the ground state of the neutral system. The ADC(2) scheme for singly ionized states describes the many-electron wave functions in the basis of 1h and 2h1p intermediate states treating the coupling between the 1h states and between 1h states and 2h1p states in the second and in the first order, respectively. ADC(2) approximation neglects the coupling between the different 2h1p basis functions. The extended ADC(2) scheme [ADC(2)x] takes into account the coupling between the 2h1p states in the

first order (i.e., on CI level). The third-order ADC(3) scheme, while still confined to the basis of 1h and 2h1p intermediate states, treats the coupling between the 1h states and between 1h states and 2h1p states in the third and in the second order, respectively. A detailed description of the single ionization ADC(2) and ADC(3) schemes, including the expressions for the Hamiltonian matrix elements can be found in Ref. [50]. The proof of the size consistency of the ADC(n) schemes has been given in Ref. [39]. The main limitation of the existing ADC(n) schemes is that they are applicable to ionized and/or excited states of closed shell systems only. Here we are interested in applying ADC to the interatomic (intermolecular) decay in ionized van der Waals and hydrogen-bonded clusters, all of which satisfy this requirement.

Our main purpose is to demonstrate that the ADC(n) schemes can be used for the ab initio calculations of the decay rates within Fano formalism. To this end, we need to show that both bound (Φ) and continuum ($\chi_{\beta,\varepsilon}$) components of the $(N-1)$-electron wave function describing the decay process [see Eq. (4)] can be approximated by the expansion in the basis of the intermediate states (12). Suppose, a vacancy residing on the subunit A of a weakly bound cluster can decay by one of the interatomic (intermolecular) mechanisms, but cannot decay non-radiatively if created in the isolated species A. Clearly, the final state of such a decay will be characterized by two vacancies, one or both of them residing on another cluster subunit. Thus, in order to construct the ADC(n) approximation for the bound part, Φ, one can restrict the physical excitation operators of the higher excitation classes to such where all the holes reside on the subunit A only:

$$\Psi_J^0 = \hat{C}_J \Psi_0^N, \tag{13}$$
$$\{\hat{C}_J\} \equiv \{c_i;\, c_a^\dagger c_i c_j, i<j, \varphi_{i,j} \in A; c_a^\dagger c_b^\dagger c_i c_j c_k, a<b, i<j<k, \varphi_{i,j,k} \in A; \ldots\},$$

where $\varphi_i \in A$ is an occupied spin orbital of the neutral cluster localized on the subunit A. In this way, the intraatomic (intramolecular) relaxation and correlation effects inside the subunit A are taken into account, whereas any kind of interatomic decay cannot be described due to the restriction imposed on the holes. Upon the completion of the selection process, one can construct and diagonalize the Hamiltonian in the basis of the restricted set of the intermediate states using the standard methods. The ADC(n) state approximating the Φ component can be identified, for example, as the one possessing the maximal overlap with the cluster orbital representing the initial vacancy. Since no configurations corresponding to the open decay channels were used in the ADC–ISR expansion for the bound-like component, Φ will be one of the lowest energy eigenvectors of the ADC Hamiltonian. Therefore, a highly efficient Davidson diagonalization technique [51] can be used to diagonalize the matrix.

Once the ADC(n) approximation for the bound component of the wave function has been provided, the remaining task is to construct the approximate continuum components, $\chi_{\beta,\varepsilon}$, describing the possible final states of the interatomic (intermolecular) decay. Such states are naturally found among the ADC(n) eigenstates of the

2h1p character:

$$\chi_{\beta,\varepsilon} \sim \Psi_q^{2\mathrm{h1p}} = \sum_i \sum_{[J]=i} Y_{q,J} \tilde{\Psi}_J \,, \quad 1 - \sum_{[J]=2} |Y_{q,J}|^2 \ll 1 \,. \tag{14}$$

The $\Psi_q^{2\mathrm{h1p}}$ functions can be constructed without any restriction of the kind of (13) being imposed on the physical excitation operators. It is, thus, possible that some intermediate states contribute both to Φ and to $\Psi_q^{2\mathrm{h1p}}$ expansions, leading to $\langle \Phi | \Psi_q^{2\mathrm{h1p}} \rangle \neq 0$. This does not lead to complications as the Fano formalism that we are using does not assume the orthogonality of the bound and the continuum components.

Application of the selection scheme described above is not straightforward in the case of symmetric clusters, e.g., those in which the ionized inner-shell orbital is delocalized due to inversion symmetry. As has been shown in Ref. [52], this difficulty can be circumvented by using the appropriate linear combinations of the "standard" configurations.

3.3 Stieltjes Imaging Technique for Calculation of the Interatomic Decay Widths

Despite the ability of ADC(n) to produce 2h1p-like wave functions in the continuum region of the spectrum , there still exists a series of major difficulties in associating these ADC(n) eigenstates with the approximate continuum states of Fano theory. All these difficulties stem from the fact that the ADC(n) calculations, and ab initio quantum chemical calculations in general, are routinely performed using the $\mathcal{L}^2$ bases, usually the Gaussian ones. As a result, the $\mathcal{L}^2$ and not the scattering boundary conditions are imposed and the $\Psi_q^{2\mathrm{h1p}}$ functions are not properly normalized:

$$\langle \Psi_q^{2\mathrm{h1p}} | \Psi_{q'}^{2\mathrm{h1p}} \rangle = \delta_{q,q'} \tag{15}$$

[compare to Eq. (6)]. Moreover, the corresponding eigenenergies, $E_q^{2\mathrm{h1p}}$, are discrete and are not expected to fulfill the energy conservation relation for the non-radiative decay, $E_q^{2\mathrm{h1p}} = E_\Phi$, except by a coincidence. Finally, it is not possible to define rigorously to which decay channel such or another $\Psi_q^{2\mathrm{h1p}}$ state belongs. Indeed, the scattering boundary conditions corresponding to the outgoing electron of the kinetic energy ε_β are not imposed on the $\mathcal{L}^2$ $\Psi_q^{2\mathrm{h1p}}$ function, neither is it derived from an $(N-2)$-electron state of a well-defined energy E_β.

In order to deal with the above complications, one should reconsider the relation (7) for the total decay rate and adapt it to the limitations imposed by the $\mathcal{L}^2$ character of the final state wave functions. To this end, let us rewrite Eq. (7) as following:

$$\Gamma = 2\pi \sum_{\beta=1}^{N_c} \langle \Phi | H - E_r | \chi_{\beta,\varepsilon_\beta} \rangle \langle \chi_{\beta,\varepsilon_\beta} | H - E_r | \Phi \rangle \,. \tag{16}$$

It is easily noticed that the $\chi_{\beta,\varepsilon_\beta}$ functions define an N_c-dimensional space at the resonance energy, in which they act as basis vectors. If the objective is the calculation of the total width only, one can make also any other choice of the basis in this N_c-dimensional space,

$$\sum_{\beta=1}^{N_c} |\chi_{\beta,\varepsilon_\beta}\rangle\langle\chi_{\beta,\varepsilon_\beta}| = \sum_{\beta=1}^{N_c} |\chi'_\beta\rangle\langle\chi'_\beta|, \tag{17}$$

where $\{\chi_{\beta,\varepsilon_\beta}\}$ and $\{\chi'_\beta\}$ basis sets are related by a unitary transformation. This shows that the 2h1p states, Ψ_q^{2h1p}, do not have to correspond directly to the open decay channels in order to be used in the calculation of the total (but not partial!) decay width.

The remaining gap between the $\mathcal{L}^2$ ADC(n) eigenstates and the true continuum functions appearing in Eq. (7) can be bridged in the following way. The expression (7) relates the total decay width to the matrix elements coupling the bound and the continuum components of the wave function, $\langle \Phi | H - E_r | \chi_{\beta,\varepsilon_\beta} \rangle$. The bound wave function component, Φ, is effectively zero outside some region in space which we will call here the "interaction region." The interaction region roughly defines the dimensions of the system in which the decay process occurs and is spanned by $\mathcal{L}^2$ basis used for the construction of Φ. The continuum components, $\chi_{\beta,\varepsilon_\beta}$, are on the other hand non-zero even at the infinite distance from the cluster. It is clear that the Hamiltonian matrix element between the two components has a contribution only from the interaction region. One can, thus, substitute the continuum components in Eq. (7) by the approximate ones, $\tilde{\chi}_{\beta,\varepsilon_\beta}$, which are equal to the true continuum components within the interaction region and go to zero (e.g., as Gaussians) outside the interaction region. Consequently, it is possible to use $\mathcal{L}^2$ approximations in the true continuum components, such as Ψ_q^{2h1p}, in the total widths calculation, provided that the $\mathcal{L}^2$ functions are (i) renormalized, such that they are equal to the continuum wave functions inside the interaction region and (ii) interpolated in energy, such that they satisfy the energy conservation, $E_q^{\mathrm{2h1p}} = E_\Phi$. Both of these goals can be achieved using the procedure known as Stieltjes imaging. This technique has been introduced by Langhoff in the context of calculation of photoionization cross-section using $\mathcal{L}^2$ wave functions and later generalized to the decay rate evaluation by Hazi [46]. Both mathematical foundations and the implementation algorithms of Stieltjes imaging have been repeatedly described in the literature. Here we will only note that the renormalization of the so-called pseudospectrum of the discrete $\mathcal{L}^2$ states possessing energies in the continuum region of the true spectrum can be achieved using the fact that the spectral moments of the quantities of the type of (7) calculated using the pseudospectrum are good approximations to the spectral moments constructed using the true continuum. In our case, this leads to

$$\sum_{\beta} \int E^k \left| \langle \Phi | H - E_r | \chi_{\beta,\varepsilon_\beta} \rangle \right|^2 dE \approx \sum_{q} \left(E_q^{2\mathrm{h1p}} \right)^k \left| \langle \Phi | H - E_r | \Psi_q^{2\mathrm{h1p}} \rangle \right|^2 . \quad (18)$$

The property (18) allows one to use the techniques of moment theory in order to obtain the correct matrix element of the kind of (7) interpolated to the needed value of the continuum state energy. This can be done through a series of consecutive approximations of increasing order, n_S. The more spectral moments one can reliably calculate using the pseudospectrum, the higher is the maximal possible value of n_S and with it, the quality of the final result. A reliable calculation of the spectral moments, in turn, requires a sufficient density of the pseudospectrum states throughout the energy range contributing to the sum (18). This density can be controlled by the choice of the $\mathcal{L}^2$ basis. In the present work, we use the computationally efficient implementation of Stieltjes imaging described in detail by Müller-Plathe and Diercksen [53].

As we have noted above, $\mathcal{L}^2$ methods, such as Stieltjes imaging, do not allow one to formulate a rigorous procedure for the calculation of the *partial* widths. Such a rigorous calculation must involve the true degenerate continuum functions corresponding to the various decay channels. Despite the fact that these functions are not available within the framework of the method used in this work, it is still possible to estimate ICD partial widths using Stieltjes imaging technique [44] by an ad hoc procedure suggested in Ref. [54].

Equation (18) implies that one has to know the *full* discretized spectrum of the Hamiltonian in order to reproduce the spectral moments required in the Stieltjes imaging procedure. It has been realized very early that such a requirement can make the technique inapplicable for large systems in high-quality $\mathcal{L}^2$ basis sets [55]. Very recently, we have proposed a method to overcome the full diagonalization bottleneck of the Stieltjes imaging [56] by using the block Lanczos pseudospectrum [57] much smaller than the Hamiltonian matrix dimension. This technique has been applied successfully to the calculation of the total photoionization cross-section of benzene within the ADC(2) scheme explicitly taking into account single and double electronic excitations [56]. Generalization of the Stieltjes–Lanczos method to the calculation of decay widths is currently being developed by the authors.

3.4 Selected Applications of the Fano–ADC–Stieltjes Method to Interatomic Decay Widths in Clusters

Interatomic decay widths as functions of cluster geometry are not only an essential input for simulations of ICD electron spectra [11, 33], but are also very interesting physical quantities in their own right. The magnitude and the functional form of $\Gamma(R)$ can tell us a lot about physics of interatomic decay. For instance, at large distances, the ICD width can be shown to follow an inverse power law, in most cases $\Gamma_{\mathrm{ICD}}(R) \propto R^{-6}$ [13, 58, 61]. This asymptotic behavior of the decay width can be

explained by a physically appealing virtual photon transfer model which represents the decay process as an emission of a virtual photon by the inner-shell-ionized atom followed by its absorption by a neighboring neutral. The virtual photon transfer model neglects the overlap between the atomic orbitals of the atoms participating in the interatomic process and thus its validity around the equilibrium geometry of the neutral cluster was a subject of debate (see, e.g. Ref. [59]). Using the Fano–ADC–Stieltjes ab initio approach of Sects. 3.1,3.2, 3.3, we have been able to show that the orbital overlap effect leads to a dramatic enhancement of ICD widths in rare gas–alkaline earth diatoms [44, 61] (see Fig. 3).

The discovery of the overlap effect on the ICD rates led us to ask the question of what kind of chemical environment leads to highest possible ICD rates retaining the clear-cut interatomic nature of the process. It has been realized quite early [13] that higher ICD rates are favored by environments with the highest possible number of nearest neighbors. In large neon clusters, for example, a "bulk" $2s$ vacancy would decay faster than the "surface" one [12]. It turns out, though, that even the "bulk" neon ICD rates can be outmatched by interatomic decay in a very interesting group of chemical compounds called endohedral fullerene complexes, e.g., in $Ne@C_{60}$ [16]. Indeed, in $(2s^{-1})$ $Ne^{+}@C_{60}$, the inner-valence-ionized Ne has as many as 60 nearest neighbors to interact with (see Fig. 4), which leads to as many as several hundreds of ICD channels. As a result, the lifetime of $(2s^{-1})$ $Ne^{+}@C_{60}$ is only about 2 fs, in fact shorter than Auger lifetime of isolated core-ionized neon atom [16]. The ultrafast character of ICD is not the only unique feature of interatomic decay

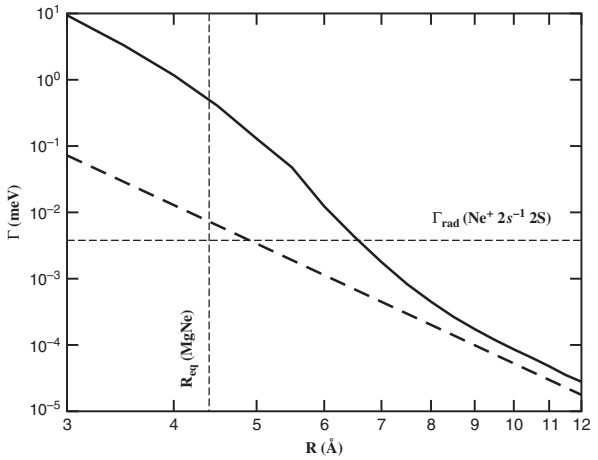

Fig. 3 Doubly logarithmic plot of the total non-radiative decay width of Ne $2s$ vacancy in MgNe cluster as a function of internuclear separation. *Full line*–ADC(2e) result; *dashed line* – virtual photon transfer prediction ([61]) for ICD width. Radiative width of the $2s$ vacancy in free neon atom [60] and the equilibrium distance of MgNe in the ground state are shown by *horizontal* and *vertical dashed lines*, respectively

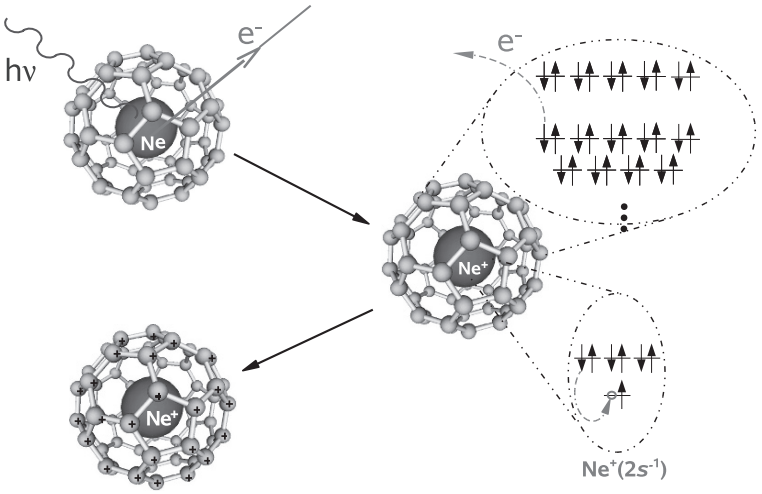

Fig. 4 A schematic drawing of the ICD process in $(2s^{-1})$ Ne@C_{60}: a photon causes inner-valence ionization of the endohedral Ne atom, an outer-valence electron of Ne recombines into the $2s$ vacancy with the released energy being utilized for fullerene ionization

in endohedral fullerenes. A detailed consideration of the possible decay pathways reveals that the relatively low multiple ionization energies of the fullerenes give rise to a number of intriguing new processes, such as double ICD (DICD) (being interatomic analog of double Auger decay [62]), double electron transfer-mediated decay (DETMD), and a two-step cascade of interatomic decay [16]. A combination of ultrafast ICD with the rich pattern of the possible decay channels makes endohedral fullerenes particularly attractive for future theoretical and experimental studies.

4 ICD in Doubly Ionized Clusters

As pointed out in Sect. 1, Auger decay of core vacancies often produces highly excited states of the corresponding doubly ionized species which can, in full analogy with the case of single inner-valence vacancy, undergo interatomic (intermolecular) decay of the ICD type in clusters. Despite the recent progress in the experimental investigation of ICD following Auger decay [25, 27–29, 63], the theoretical description of the phenomenon is much less advanced than that of ICD in single ionized clusters, mainly due to unavailability of accurate data on the interatomic decay widths. However, the success of the Fano–ADC–Stieltjes method, described in Section 3, motivated extension of the approach to the description of the interatomic decay of excited doubly ionized states in clusters [64].

4.1 Fano–ADC–Stieltjes Method for Interatomic Decay Widths in $(N-2)$-Electron Systems

Most computational aspects of the method are fully analogous to the single vacancy case and will not be repeated here. Instead, we will focus only on the few points of difference. Obviously, the principal difference is that the wave function Ψ_E of Eq. (4) represents now doubly ionized ($N-2$-electron) cluster. Therefore, double ionization ADC technique has to be used to construct the bound (Φ) and continuum ($\chi_{\beta,\varepsilon}$) ($N-2$)-electron states. Suitable ADC scheme for the pp-propagator has been derived by Schirmer and Barth [65]. To describe the bound component (Φ, initial state of the decay) of the wave function Ψ_E within the ADC(n) approach, it is necessary to restrict the physical excitation operators generating the CESs Ψ_J^0 (and, in turn, the intermediate states $\tilde{\Psi}_J$) in such a way that open channels of the interatomic decay are not included in the resulting basis.

The intraatomic nature of the Auger decay makes it possible to follow similar strategy as in Sect. 3.2, based on the spatial localization properties of the occupied spin orbitals. Indeed, the initial state of the decay is characterized by two vacancies being localized on a single cluster constituent A, while in the triply ionized final states of Auger–ICD cascade, one or more vacancies reside on another cluster subunit. Therefore, in analogy with Eq. (13), the CESs for the initial state expansion are generated with the restriction that all the holes reside on the subunit A only:

$$\begin{aligned} \Psi_J^0 &= \hat{C}_J \Psi_0^N, \\ \{\hat{C}_J\} &\equiv \{c_i c_j, i<j, \varphi_{i,j} \in A;\, c_a^\dagger c_i c_j c_k, i<j<k, \varphi_{i,j,k} \in A;\, \ldots\}, \end{aligned} \tag{19}$$

where $\varphi_i \in A$ is an occupied spin orbital of the neutral cluster localized on the subunit A. Note that we are now working with two-hole (2h, $J=1$), three-hole, one-particle (3h1p, $J=2$), …excitation classes. Upon diagonalization of the Hamiltonian constructed in the restricted basis of intermediate states generated from the CESs of Eq. (19), the approximation to the initial state is identified as the eigenstate of the desired symmetry with the largest overlap with the 2h configuration describing the initial two vacancies. The approximate continuum components, $\chi_{\beta\varepsilon}$, corresponding to the possible final states of the interatomic decay, are obtained in a separate ADC(n) calculation as the eigenstates of the 3h1p character:

$$\chi_{\beta,\varepsilon} \sim \Psi_q^{3\mathrm{h1p}} = \sum_i \sum_{[J]=i} Y_{q,J} \tilde{\Psi}_J\,, \quad 1 - \sum_{[J]=2} |Y_{q,J}|^2 \ll 1\,. \tag{20}$$

Once the ADC(n) approximations for the bound and continuum components of the wave function (4) are constructed, one can use the Stieltjes imaging procedure of Sect. 3.3 to renormalize the matrix elements computed with the $\mathcal{L}^2$ wave functions, $\Psi_q^{3\mathrm{h1p}}$, and interpolate them in energy as necessary for the computation of the decay widths.

4.2 ICD After Auger Decay in Rare Gas–Alkaline Earth Clusters

To demonstrate the similarities and differences between ICD in singly and doubly ionized clusters, let us investigate the non-radiative decay widths of doubly ionized $Ne^{2+}(2s^{-1}2p^{-1})$ in MgNe diatomic. In the first order of perturbation theory picture, the decay process proceeds in the same way as ICD of the single Ne $2s$ vacancy, since the initial Ne $2p$ vacancy is only a spectator. Higher orders of perturbation theory involve also pathways in which the initial Ne $2p$ vacancy participates actively, but partial width analysis shows that these processes account only for about 5% of the total decay width. The qualitative similarity of the two decay processes is confirmed in Fig. 5, which shows the total non-radiative decay widths of different symmetries of $MgNe^{2+}(2s^{-1}2p^{-1})$ as functions of internuclear distance R. The decay width of $MgNe^{+}(2s^{-1})$ is shown as the full line for reference. At large distances all the widths follow the $\Gamma(R) \propto R^{-6}$ law, predicted by the virtual photon model for dipole–dipole interatomic decay processes. At smaller distances around the equilibrium geometry the overlap between atomic orbitals of the two involved atoms leads to significant enhancement of ICD widths as in the case of ICD of singly ionized cluster. Note, however, that the overlap enhancement is less pronounced, in particular in the case of triplet initial states.

It turns out that, although the spectator Ne $2p$ vacancy does not affect significantly the qualitative behavior of the interatomic decay rates, it has very strong impact on the magnitude of the widths. For example, at $R = 12$ Å, the decay width

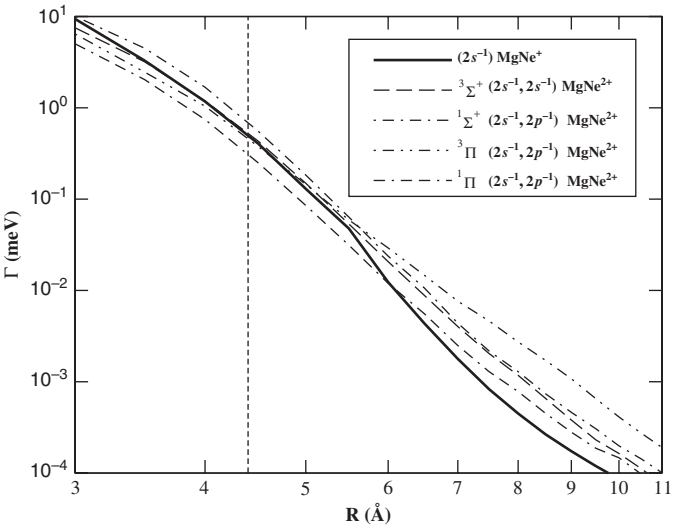

Fig. 5 Doubly logarithmic plot of the total non-radiative decay width of $MgNe^{2+}(2s^{-1}2p^{-1})$-excited state of different spatial symmetries and spin multiplicities. For reference, the *full line* shows the ICD width of the single Ne $2s$ vacancy. The equilibrium distance of MgNe in the ground state is shown by *vertical dashed line*

of the $^1\Sigma^+$ state of $MgNe^{2+}(2s^{-1}2p^{-1})$ is about 2 times larger than the width of the singly ionized cluster and the width of the $^3\Pi$ state is even 3.5 times larger. The change in the magnitude in the presence of additional vacancy is caused mainly by two factors. First, the electron missing in the $2p$ shell reduces the number of decay pathways, which increases the lifetime of the decaying state. On the other hand, spatial orbitals of multiple ionized atom or molecule are more compact, which increase their Coulombic coupling and in turn also the efficiency of the energy-transfer-dominated pathways of the interatomic decay process. The competition of these two effect explains why, at large distances where the energy-transfer character of the decay prevails, the excited doubly ionized states decay faster. In the orbital overlap-dominated region, on the other hand, the compactness of the atomic orbitals leads to reduction of the overlap enhancement, in particular for the triplet initial states.

To understand more deeply the diverse magnitudes of the total decay widths of various doubly ionized states of different spatial symmetry and spin multiplicity, particular decay pathways and corresponding partial decay widths have to be analyzed. It appears that, for the $^3\Sigma^+$ initial state in particular, the vacancy in the $2p$ shell can impede certain very important decay pathways. For a thorough discussion the reader is referred to Ref. [64].

5 Decay Widths of Inner-Shell-Excited Systems by Fano–ADC–Stieltjes Method

ADC(n) schemes for the excited states of many-electron systems can be described within the ISR approach analogously to how it was done in Sect. 3.2 for the singly ionized states. The main difference between the ADC(n) approximations for N-electron and $(N-1)$-electron systems is the necessary inclusion of the N-electron ground state into the ISR orthonormalization procedure (see Sect. 3.2), where it plays the role of zeroth excitation class. ADC(1) scheme represents the excited N-electron states in the basis of one-hole, one-particle (1h1p) intermediate states and can be shown to be related to the well-known random phase approximation (RPA) [66]. N-electron ADC(2) uses second-order perturbation theory for the correlated ground state and expands the excited states in 1h1p and 2h2p excitation classes. ADC(2) treats the 1h1p–1h1p and 1h1p–2h2p couplings in second and first order, respectively, and neglects the coupling between different 2h2p intermediate states. The extended ADC(2) scheme, or ADC(2)x, takes into account the 2h2p–2h2p interactions to first order. The details of the ISR–ADC schemes for the calculation of the excited states can be found in Ref. [67] and references therein.

As it was emphasized in Sect. 1.2.1, RICD is always accompanied by intraatomic autoionization. Practically, this means that any computational scheme for the decay widths of inner-valence-excited states in clusters must be capable of taking the intraatomic autoionization into account. Let us concentrate for the moment on the problem of computation of autoionization widths of isolated atoms within the

Fano–ADC–Stieltjes method and construct the appropriate selection scheme for the 1h1p and 2h2p ADC intermediate states. Suppose, we are interested to compute the decay rates of excited noble gas atoms (Ne, Ar, and Kr), where the excited states belong to the ms^{-1}np Rydberg series ($m = 2,\ n \geq 3$ for Ne; $m = 3,\ n \geq 4$ for Ar; $m = 4,\ n \geq 5$ for Kr) [68]. We see that, due to energy conservation, no singly excited configuration with a hole on the ms orbital or a deeper shell can represent an open decay channel. Therefore, all such configurations should be used in constructing the bound-like state Φ [see Eq. (4)]. Similar considerations can be applied to the doubly excited configurations with one or both of the holes residing on the ms or deeper lying orbitals. We offer the following mathematical formulation of these conditions. The intermediate states $\Psi_J = \hat{C}_J \Psi_0^N$ with

$$\begin{aligned} &\{\hat{C}_J\} \in \{c_a^\dagger c_k,\ \ -\varepsilon_k > -\varepsilon_{ms}\ ; \\ &c_a^\dagger c_b^\dagger c_j c_k, a < b,\, j < k,\ \ -\varepsilon_j - \varepsilon_k > -\varepsilon_{ms}\} \end{aligned} \tag{21}$$

represent closed decay channels and should be used to expand the bound component ϕ. The quantity ε_i is the HF energy of the ith orbital, or, according to the Koopmans' theorem, the first-order approximation to the respective ionization potential.

The doubly excited configurations m$p^{-2}ab$ with both holes on the outer-valence mp orbital and a, b standing for virtual orbitals of appropriate symmetry do not appear among the states in Eq. (21). In order to decide whether to include them in the expansion of Φ or not, we need to answer the following question.

Is a *spectator* resonant Auger decay possible in the systems under study?

If the answer is positive, then excited singly ionized species with two holes in an outer-shell are allowed final states and, therefore, the configurations m$p^{-2}ab$ cannot be used to expand Φ. Since *spectator* resonant Auger decay is forbidden in Ne, Ar, and Kr, we can include the configurations m$p^{-2}ab$ among those in Eq. (21). These intermediate states are used to set up an ADC(n) matrix, which is diagonalized, and one of its eigenvectors is identified as the bound-like component Φ.

Let us now consider which configurations contribute to the continuum-like part $\chi_{\beta,\varepsilon}$. It is obvious that any singly excited configuration with a hole on an orbital higher than ms represents a valid open channel. Mathematically this condition can be written as $-\varepsilon_i < -\varepsilon_{ms}$. The allowed final states are of predominantly singly excited character, which might suggest that only singly excited configurations should be used in constructing them. However, m$p^{-2}ab$ states are necessary to describe the electronic correlation in the final state. Thus, they should be included in the expansion of the final states. Since the formulation of the Fano method which we use does not call for the orthogonality between the bound and continuum parts, we proceed as follows. The singly excited configurations obeying $-\varepsilon_i < -\varepsilon_{ms}$ together with m$p^{-2}ab$ states are used to set up another ADC(n) matrix. It is diagonalized and a number of its eigenvectors having the largest weight of singly excited configurations are taken to be the continuum states $\chi_{\beta,\varepsilon}$. Using this procedure, we

improve the description of the final states while avoiding the inclusion of spurious open channels.

We applied the selection scheme described above to compute the decay rates of the excited inner-valence states in Ne, Ar, and Kr atoms by Fano–ADC–Stieltjes method [68]. For all three atoms, we calculated the decay widths Γ of the first three inner-valence-excited states, i.e., $2s^{-1}np$ ($n = 3, 4, 5, \dots$) for Ne, $3s^{-1}np$ ($n = 4, 5, 6$) states for Ar, and $4s^{-1}\mathrm{n}p$ ($n = 5, 6, 7$) for Kr. The results are shown in Tables 1, 2, and 3.

Table 1 Experimental [69] and theoretical decay widths Γ for the autoionizing $2s^{-1}\mathrm{n}p$ ($n = 3, 4, 5$) states of Ne. The results of time-dependent density functional theory in the local density approximation (TDLDA) are taken from Ref. [70]. R-matrix (RM) theoretical results are taken from Ref. [71]

	$n = 3$	$n = 4$	$n = 5$
Γ_{exp} (meV)	13 (±2)	4.5 (±1.5)	2 (±1)
$\Gamma_{\mathrm{ADC(1)}}$ (meV)	30.48	9.31	5.59
$\Gamma_{\mathrm{ADC(2)}}$ (meV)	8.93	2.86	1.72
$\Gamma_{\mathrm{ADC(2)x}}$ (meV)	11.46	3.78	1.94
Γ_{TDLDA} (meV)	13. 90	3.86	1.62
Γ_{RM} (meV)	34.9	6.65	2.47

Table 2 Experimental [72] and theoretical decay widths Γ for the autoionizing $3s^{-1}\mathrm{n}p$ ($n = 4, 5, 6$) states of Ar. The TDLDA results are taken from Ref. [70]

	$n = 4$	$n = 5$	$n = 6$
Γ_{exp} (meV)	76 (±5)	25 (±7)	16 (±7) 111
$\Gamma_{\mathrm{ADC(1)}}$ (meV)	50.61	13.52	5.59
$\Gamma_{\mathrm{ADC(2)}}$ (meV)	61.5	18.42	8.05
$\Gamma_{\mathrm{ADC(2)x}}$ (meV)	67.76	25.85	12.14
Γ_{TDLDA} (meV)	183.4	42.8	18.2

Table 3 Experimental [73] and theoretical decay widths Γ for the autoionizing $4s^{-1}\mathrm{n}p$ ($n = 5, 6, 7$) states of Kr. The TDLDA results are taken from Ref. [70]

	$n = 5$	$n = 6$	$n = 7$
Γ_{exp} (meV)	22.8 (±0.8)	13.2 (±0.5)	7.8 (±0.6)
$\Gamma_{\mathrm{ADC(1)}}$ (meV)	34.26	9.4	3.97
$\Gamma_{\mathrm{ADC(2)}}$ (meV)	42.37	12.13	5.1
$\Gamma_{\mathrm{ADC(2)x}}$ (meV)	54.69	16.14	7.16
Γ_{TDLDA} (meV)	130.4	27.8	11.6

The Fano–ADC–Stieltjes autoionization widths for inner-valence-excited states of Ne and Ar (see Tables 1 and 2) lie within the experimental error for all n's. The results in the case of Kr (Table 3) exhibit a comparatively large deviation for the lowest Rydberg term and improve greatly toward higher excitation energies. This is explained by the prevalence of electronic correlation effects in Kr which can only

partly be taken into account by the ADC(2)x technique [68]. Theoretical results obtained by TDLDA are comparable to those of Fano–ADC(2)x–Stieltjes data in the case of Ne but become worse than those for Ar and Kr. The R-matrix results, unlike the TDLDA and the present method, fail to reproduce the experimental decay width of the lowest Rydberg $2s^{-1}3p$ term in Ne.

The success of the Fano–ADC–Stieltjes method to describe the intraatomic autoionization calls for the generalization of this technique to the case of interatomic decay of inner-valence-excited states, i.e., RICD. At present, only lowest-order perturbation-theoretical (Wigner–Weisskopf) estimations of the RICD widths are available [22]. The much more accurate Fano–ADC–Stieltjes method cannot be readily applied to the RICD problem because of the full diagonalization bottleneck of the Stieltjes imaging procedure (see discussion in sect. 3.3). At present, work is in progress on the implementation of the new scheme for the Fano–ADC–Stieltjes calculation of the RICD widths.

6 Outlook

The preceding sections outlined a remarkable activity, both theoretical and experimental, aiming at in-depth study of interatomic decay processes. A manifold of new physical processes have been observed and still more new phenomena have been predicted theoretically. The first demonstration-of-principle experiment has been performed showing the potential of ICD electron spectroscopy as an analytical technique for the study of interfaces [17]. All these developments clearly point at the study of interatomic decay in clusters as at an emerging field of research. Key to theoretical progress in this new field is the ability to obtain reliable estimations of the rates of the various interatomic decay processes. The Fano–ADC–Stieltjes approach described in this chapter seems to be the method of choice. While established fairly well for singly and doubly ionized systems, the Fano–ADC–Stieltjes technique is yet to be generalized to the case of RICD of inner-valence-excited states. This goal appears to be well within reach as the full diagonalization bottleneck of the Stieltjes imaging technique has been already overcome successfully for the related problem of calculation of photoionization cross-section [57]. Furthermore, it would be desirable to extend the existing Fano–ADC–Stieltjes approaches for singly ionized states to the ADC(3) and ADC(4) levels of the ab initio theory. Indeed, going to the ADC(3) level of approximation of the many-electron states will help to describe the decay of inner-valence-ionized states more accurately than it is done on the currently implemented ADC(2)x level. This could be very important for the vacancy states of elements beyond the second row of periodic table (e.g., $3s^{-1}$ Ar^{+}). ADC(4) level of theory would provide a quantitative description of double decay processes (e.g., DICD) as well as highly accurate results for the decay of core-ionized states. As plausible applications of the envisaged ab initio theory, one could cite, for example, the rich pattern of interatomic decay processes in endohedral fullerenes. Of particular interest is the question of the relative time

scale of the various single and double decay processes as well as the possible interrelation between ultrafast character of ICD in these systems and the fullerene plasmon.

While the experiment has so far targeted rare gas clusters, a solid theoretical evidence for interatomic decay in other systems, such as hydrogen-bonded clusters and endohedral fullerenes, represents an excellent motivation for bringing some chemical diversity into the experimental studies. First steps along this direction have been taken by Hergenhahn and co-workers who have been able to measure ICD in inner-valence-ionized water clusters [74], Dörner, Jahnke, and co-workers who performed coincidence measurements on ICD in water dimer [75], and by Aziz et al. who have identified an ICD process involving a 1*s*-ionized OH^- ion and a water molecule in NaOH solution [76]. Relevance of interatomic decay processes for water and water solutions naturally leads to the question of the relevance of ICD for biochemical environment, e.g., in the processes leading to radiation damage. At present, this direction is only very little explored and certainly has a high potential for future studies.

A separate chapter in the experimental study of electronic decay has been opened with the advent of new high-frequency radiation sources: attosecond lasers [77] and X-ray free electron lasers (XFELs) [78]. Attosecond lasers operating in the XUV domain provide a unique opportunity to study the electronic decay processes in time domain using the so-called streaking probe [79]. The moderate photon energies needed to initiate interatomic decay, together with the characteristic time scales of 1–100 fs make interatomic decay processes natural candidates for the application of the attosecond pump–probe techniques. The first step toward the time-dependent theoretical description of electronic dynamics in the course of interatomic decay has been already taken [80].

While the intensities of the presently available attosecond pulses do not reach strong field regime (the laser field acting on the electrons is much weaker than the one due to atomic or molecular core), XFELs are expected to produce unprecedented field strengths of up to tens of atomic units [78]. Certainly, at such field strengths, the process of creation of a vacancy state can no longer be described perturbatively, as it is done in Sect. 2. New theoretical approaches treating the inner-shell ionization and/or excitation non-perturbatively will have to be found.

In this chapter, we have outlined the major successes and challenges of the study of interatomic decay with the particular emphasis on the development of ab initio theoretical methodology. It is our hope that more theoreticians and experimentalists will enter the new fascinating world of interatomic decay and contribute to turning the new basic concepts into a powerful spectroscopic tool.

Acknowledgments The authors would like to thank Jochen Schirmer for many fruitful discussions in the course of the work described in the present review. V. A. would like to acknowledge financial support of the Max Planck Society through the distinguished PKS postdoctoral fellowship. P. K. acknowledges financial support from the Grant GAČR 202/09/0786 of the Czech Science Foundation. Financial support of Deutsche Forschungsgemeinschaft is gratefully acknowledged.

References

1. P. Auger, J. de Phys. **6**, 205 (1925)
2. E.H.S. Burhop, W.N. Asaad, Adv. At. Mol. Phys. **8**, 163 (1972); W. Mehlhorn, *Atomic Inner-Shell Physics*, ed. by B. Crasemann (Plenum, New York, 1985)
3. N.H. Turner, J.A. Schreifels, Anal. Chem. **72**, 99R (2000)
4. C.D. Wagner, A. Joshi, J. Elec. Spectr. Rel. Phen. **47**, 283 (1988)
5. L.S. Cederbaum, J. Zobeley, F. Tarantelli, Phys. Rev. Lett. **79**, 4778 (1997)
6. R. Santra, J. Zobeley, L.S. Cederbaum, N. Moiseyev, Phys. Rev. Lett. **85**, 4490 (2000)
7. M.S. Deleuze, J.-P. Francois, E.S. Kryachko, J. Am. Chem. Soc. **127**, 16824 (2005)
8. S. Marburger, O. Kugeler, U. Hergenhahn, T. Möller, Phys. Rev. Lett. **90**, 203401 (2003)
9. T. Jahnke, A. Czasch, M.S. Schöffler, S. Schössler, A. Knapp, M. Käsz, J. Titze, C. Wimmer, K. Kreidi, R.E. Grisenti, A. Staudte, O. Jagutzki, U. Hergenhahn, H. Schmidt-Böcking, R. Dörner, Phys. Rev. Lett. **93**, 163401 (2004)
10. R. Dörner, V. Mergel, O. Jagutzki, L. Spielberger, J. Ullrich, R. Moshammer, H. Schmidt-Böcking, Physics Reports **330**, 95 (2000)
11. S. Scheit, V. Averbukh, H.-D. Meyer, N. Moiseyev, R. Santra, T. Sommerfeld, J. Zobeley, L. S. Cederbaum, J. Chem. Phys. **121**, 8393 (2004)
12. G. Öhrwall, M. Tchaplygine, M. Lundwall, R. Feifel, H. Bergersen, T. Rander, A. Lindblad, J. Schulz, S. Peredkov, S. Barth, S. Marburger, U. Hergenhahn, S. Svensson, O. Björneholm, Phys. Rev. Lett. **93**, 173401 (2004)
13. R. Santra, J. Zobeley, L.S. Cederbaum, Phys. Rev. B **64**, 245104 (2001)
14. N. Vaval, L.S. Cederbaum, J. Chem. Phys. **126**, 164110 (2007)
15. I.B. Müller, L.S. Cederbaum, J. Chem. Phys. **122**, 094305 (2005)
16. V. Averbukh, L.S. Cederbaum, Phys. Rev. Lett. **96**, 053401 (2006)
17. S. Barth, S. Marburger, S. Joshi, V. Ulrich, O. Kugeler, U. Hergenhahn, PCCP **8**, 3218 (2006)
18. S. Barth, S. Joshi, S. Marburger, V. Ulrich, A. Lindblad, G. Öhrwall, O. Björneholm, U. Hergenhahn, J. Chem. Phys. **122**, 241102 (2005)
19. T. Aoto, K. Ito, Y. Hikosaka, F. Penent, P. Lablanquie, Phys. Rev. Lett. **97**, 243401 (2006)
20. W. Eberhardt, G. Kalkoffen, C. Kunz, Phys. Rev. Lett. **41**, 156 (1978); G.C. Brown, M.H. Chen, B. Crasemann, G.E. Ice, Phys. Rev. Lett. **45**, 1937 (1980)
21. F. Gel'mukhanov, H. Ågren, Phys. Rep. **312**, 87 (1999)
22. K. Gokhberg, V. Averbukh, L.S. Cederbaum, J. Chem. Phys. **124**, 144315 (2006)
23. R. Santra, L.S. Cederbaum, Phys. Rev. Lett. **90**, 153401 (2003)
24. S. D. Stoychev, A.I. Kuleff, F. Tarantelli, L.S. Cederbaum, J. Chem. Phys. **129**, 074307 (2008)
25. Y. Morishita, X.-J. Liu, N. Saito, T. Lischke, M. Kato, G. Prümper, M. Oura, H. Yamaoka, Y. Tamenori, I.H. Suzuki, K. Ueda, Phys. Rev. Lett. **96**, 243402 (2006)
26. S.D. Stoychev, A.I. Kuleff, F. Tarantelli, L.S. Cederbaum, J. Chem. Phys. **128**, 014307 (2008)
27. K. Kreidi, T Jahnke, Th. Weber, T. Havermeier, R.E. Grisenti, X. Liu, Y. Morisita, S. Schössler, L.Ph.H. Schmidt, M. Schöffler, M. Odenweller, N. Neumann, L. Foucar, J. Titze, B. Ulrich, F. Sturm, C. Stuck, R. Wallauer, S. Voss, I. Lauter, H.K. Kim, M. Rudloff, H. Fukuzawa, G. Prümper, N. Saito, K. Ueda, A. Czasch, O. Jagutzki, H. Schmidt-Böcking, S.K. Semenov, N.A. Cherepkov, R. Dörner, J. Phys. B **41**, 101002 (2008)
28. K. Kreidi, T. Jahnke, Th. Weber, T. Havermeier, X. Liu, Y. Morisita, S. Schössler, L.Ph.H. Schmidt, M. Schöffler, M. Odenweller, N. Neumann, L. Foucar, J. Titze, B. Ulrich, F. Sturm, C. Stuck, R. Wallauer, S. Voss, I. Lauter, H.K. Kim, M. Rudloff, H. Fukuzawa, G. Prümper, N. Saito, K. Ueda, A. Czasch, O. Jagutzki, H. Schmidt-Böcking, S. Stoychev, Ph. V. Demekhin, R. Dörner, Phys. Rev. A **78**, 043422 (2008)
29. M. Yamazaki, J. Adachi, Y. Kimura, A. Yagishita, M. Stener, P. Decleva, N. Kosugi, H. Iwayama, K. Nagaya, M. Yao, Phys. Rev. Lett. **101**, 043004 (2008)
30. K. Ueda, private communication.
31. L.S. Cederbaum, F. Tarantelli, J. Chem. Phys. **98**, 9691 (1993)
32. S. Scheit, L.S. Cederbaum, H.-D. Meyer, J. Chem. Phys. **118**, 2092 (2003)

33. S. Scheit, V. Averbukh, H.-D. Meyer, J. Zobeley, L.S. Cederbaum, J. Chem. Phys. **124**, 154305 (2006)
34. U.V. Riss, H.-D. Meyer, J. Phys. B **26**, 4593 (1993)
35. J.G. Muga, J.P. Palao, B. Navarro, I.L. Egusquiza, Phys. Rep. **395**, 357 (2004)
36. R. Santra, L.S. Cederbaum, H.-D. Meyer, Chem. Phys. Lett. **303**, 413 (1999)
37. N. Moiseyev, J. Phys. B **31**, 1431 (1998); U.V. Riss, H.-D. Meyer, J. Phys. B **31**, 2279 (1998)
38. J. Schirmer, L.S. Cederbaum, O. Walter, Phys. Rev. A **28**, 1237 (1983); L.S. Cederbaum, in *Encyclopedia of Computational Chemistry*, eds. by P.v.R. Schleyer, P.R. Schreiner, N.A. Allinger, T. Clark, J. Gasteiger, P. Kollman, H.F. Schaefer III (Wiley, New York, 1998)
39. J. Schirmer, Phys. Rev. A **43**, 4647 (1991); F. Mertins, J. Schirmer, Phys. Rev. A **53**, 2140 (1996); A. B. Trofimov, J. Schirmer, J. Chem. Phys. **123**, 144115 (2005) J. Schirmer and F. Mertins, Int. J. Quant. Chem. **58**, 329 (1996).
40. R. Santra, L.S. Cederbaum, Phys. Rep. **368**, 1 (2002)
41. A.B. Trofimov, J. Schirmer, J. Chem. Phys. **123**, 144115 (2005)
42. I.B. Müller, Ph.D. thesis, Universität Heidelberg, 2006, in German
43. H. Hennig, Diploma thesis, Universität Heidelberg, 2004, in German
44. V. Averbukh, L.S. Cederbaum, J. Chem. Phys. **123**, 204107 (2005)
45. U. Fano, Phys. Rev. **124**, 1866 (1961)
46. P.W. Langhoff, in *Electron-Molecule and Photon-Molecule Collisions*, eds. by T. Rescigno, V. McKoy, B. Schneider (Plenum, New York, 1979); A. U. Hazi, *ibid.*
47. G. Howat, T. Åberg, O. Goscinski, J. Phys. B **11**, 1575 (1978)
48. T. Åberg, G. Howat, in *Handbuch der Physik*, Vol 31, ed. by W. Mehlhorn (Springer, Berlin, 1982)
49. A. Szabo, A.S. Ostlund, *Modern Quantum Chemistry: Introduction to Advanced Electronic Structure Theory* (Dover, New York, 1996)
50. J. Schirmer, A.B. Trofimov, G. Stelter, J. Chem. Phys. **109**, 4734 (1998)
51. E. Davidson, J. Comp. Phys. **17**, 87 (1975)
52. V. Averbukh, L.S. Cederbaum, J. Chem. Phys. **125**, 094107 (2006)
53. F. Müller-Plathe, G.H.F. Diercksen, in *Electronic Structure of Atoms, Molecules and Solids*, eds. by S. Canuto, J. D'Albuquerque e Castro, F.J. Paixão (World Scientific, Singapore, 1990); F. Müller-Plathe, G.H.F. Diercksen, Phys. Rev. A **40**, 696 (1989)
54. I. Cacelli, V. Caravetta, R. Moccia, Mol. Phys. **59**, 385 (1986)
55. R.K. Nesbet, Phys. Rev. A **14**, 1065 (1976)
56. K. Gokhberg, V. Visotskiy, L.S. Cederbaum, V. Averbukh, J. Chem. Phys. **130**, 064104 (2009)
57. B.N. Parlett, *The Symmetric Eigenvalue Problem* (Prentice-Hall, Englewood Cliffs, 1980)
58. J.A.D. Matthew, Y. Komninos, Surf. Sci. **63**, 716 (1975)
59. T.D. Thomas, C. Miron, K. Wiesner, P. Morin, T.X. Carroll, L.J. Sæthre, Phys. Rev. Lett. **89**, 223001 (2002)
60. D.C. Griffin, D.M. Mitnick, N.R. Randell, J. Phys. B **34**, 4401 (2001)
61. V. Averbukh, I.B. Müller, L.S. Cederbaum, Phys. Rev. Lett. **93**, 263002 (2004)
62. T.A. Carlson, M.O. Krause, Phys. Rev. Lett. **14**, 390 (1965); Phys. Rev. Lett. **17**, 1079 (1966)
63. Y. Morishita, N. Saito, I.H. Suzuki, H. Fukuzawa, X.-J. Liu, K. Sakai, G. Prümper, K. Ueda, H. Iwayama, K. Nagaya, M. Yao, K. Kreidi, M. Schöffler, T. Jahnke, S. Schössler, R. Dörner, T. Weber, J. Harries, Y. Tamenori, J. Phys. B **41**, 025101 (2008)
64. P. Kolorenč, V. Averbukh, K. Gokhberg, L.S. Cederbaum, J. Chem. Phys. **129**, 244102 (2008)
65. J. Schirmer, A. Barth, Z. Phys. A **317**, 267 (1984)
66. J. Schirmer, F. Mertins, J. Phys. B **29**, 3559 (1996)
67. J. Schirmer, A. Trofimov, J. Chem. Phys. **120**, 11449 (2004)
68. K. Gokhberg, V. Averbukh, L.S. Cederbaum, J. Chem. Phys. **126**, 154107 (2007)
69. K. Codling, R. Madden, D. Ederer, Phys. Rev. **155**, 26 (1967)
70. M. Stener, P. Decleva, A. Lisini, J. Phys. B **28**, 4973 (1995)
71. K. Schulz, M. Domke, R. Püttner, A. Gutierrez, G. Kaindl, G. Miecznik, C. Greene, Phys. Rev. A **54**, 3095 (1996)

72. S. Sorensen, T. Åberg, J. Tulkki, E. Rachlew-Kälne, G. Sundström, M. Kirm, Phys. Rev. A **50**, 1218 (1994)
73. D.L. Ederer, Phys. Rev. A **4**, 2263 (1971)
74. U. Hergenhahn, private communication.
75. T. Jahnke, R. Dörner, private communication.
76. E.F. Aziz, N. Ottoson, M. Faubel, I.V. Hertel, B. Winter, Nature **455**, 89 (2008)
77. M. Hentschel, R. Kienberger, Ch. Spielmann, G. A. Reider, N. Milosevic, T. Brabec, P. Corkum, U. Heinzmann, M. Drescher, F. Krausz, Nature **414**, 509 (2001); G. Sansone, E. Benedetti, F. Calegari, C. Vozzi, L. Avaldi, R. Flammini, L. Poletto, P. Villoresi, C. Altucci, R. Velotta, S. Stagira, S. De Silvestri, M. Nisoli, Science **314**, 443 (2006)
78. M.A. Kornberg, A.L. Godunov, S. Itza-Ortiz, D.L. Ederer, J.H. McGuire, L. Young, J. Synchrotron Rad. **9**, 298 (2002)
79. M. Drescher, M. Hentschel, R. Kienberger, M. Uiberacker, V. Yakovlev, A. Scrinzi, Th. Westerwalbesloh, U. Kleineberg, U. Heinzmann, F. Krausz, *Nature* **419**, 803 (2002)
80. A.I. Kuleff, L.S. Cederbaum, *Phys. Rev. Lett.* **98**, 083201 (2007)

Spectroscopy of Atoms in Liquid Helium Environment: A Theoretical Perspective

Kaline Coutinho, Sylvio Canuto, Prasanta K. Mukherjee, and Burkhard Fricke

Abstract This brief review is dedicated to provide possible interpretations of spectral properties such as the energy levels, spectral line positions and line profiles of atoms embedded in a liquid helium environment from a theoretical standpoint, keeping in view the wide range of availability of highly precise laser spectroscopic data in this field. Different models adopted for the interpretation of the experimental data as well as current quantum mechanical viewpoints in this regard have been described. Possible future direction for the interpretation of the available experimental data is suggested.

Keywords: Confined atomic systems · Atoms in liquid helium · Atomic Spectroscopy · Liquid simulation

1 Introduction

Liquid helium has been the subject of intense investigation for many years. Of particular interest are the extraordinary properties of the superfluid phase below the critical temperature at $\sim 2.17\,\mathrm{K}$. In more recent years there has also been an

P. K. Mukherjee (✉)
Department of Spectroscopy, Indian Association for the Cultivation of Science, Jadavpur, Kolkata 700 032, India and Department of Physics, Ramakrishna Mission Vivekananda University, Belur Math, Howrah, India,
e-mail: profpkmukherjee@gmail.com

K. Coutinho
Instituto de Física, Universidade de São Paulo, CP 66318 São Paulo, SP 05315-970, Brazil,
e-mail: kaline@if.usp.br

S. Canuto
Instituto de Física, Universidade de São Paulo, CP 66318 São Paulo, SP 05315-970, Brazil,
e-mail: canuto@if.usp.br

B. Fricke
Institute of Physics, University of Kassel, D-34109 Kassel, Germany,
e-mail: fricke@physik.uni-kassel.de

P. Piecuch et al. (eds.), *Advances in the Theory of Atomic and Molecular Systems*, Progress in Theoretical Chemistry and Physics 20, DOI 10.1007/978-90-481-2985-0_9,

increased interest in the study of the properties of foreign particles embedded in a liquid helium environment. Early investigations on the quantum fluid properties were performed by using electrons and positively charged He^+ ions as external probes [1]. A large number of experimental investigations have already been performed for the study of the properties of impurities implanted in liquid helium by different means [2–36]. A good review on the experimental investigations on this subject is now available [37]. Understanding the details of the interaction of foreign particles embedded in liquid helium is important because it provides a motivation for studying quantum fluid properties using foreign particles as external microprobes [37, 38]. Experiments have generated a wealth of data on the spectroscopic properties of the embedded particles like the spectral line shifts compared to the free system, changes in line profiles, and other spectroscopic parameters. The earlier successful implantation by injecting charge carriers into the liquid [39] and also by using field emission [40] and field ionization techniques [41] is replaced by an electric field driven mechanism [42], condensation of atomic beam methods [2–5] [43–45] and laser sputtering and laser ablation methods [1, 4, 6, 7, 11–13, 15, 16, 46]. The theoretical understanding of the geometrical structure of foreign particles embedded in liquid helium originated from the experimentally observed fact that ortho-positronium in liquid helium has a relatively long lifetime of $\sim 10^{-9}$ sec [47, 48]. Ferrel [49, 50] explained this as a consequence of the repulsive exchange force between the positronium atom and helium. The positronium atom repels the neighbouring He atoms and creates a cavity or bubble in the liquid, thereby avoiding contact with the liquid surface and increasing the lifetime. Ionic mobility measurements in liquid helium and solid helium [51–53] give an indication of the picture of a bubble and the snowball structure that was confirmed by Atkin's electrostriction theory [54]. Optical absorption spectra of electrons and metastable He atoms and also molecules in liquid helium [55–58] provide an impressive confirmation of the bubble structure of the impurities. The measurements by different techniques of the spectroscopic properties of foreign atoms in liquid helium yield data for a wide variety of atoms, the details of which may be obtained from Ref. [37]. The basic observations resulting from the series of experiments are the spectral line shifts compared to the free atomic system, broadening of emission and absorption lines, change in line shapes, lowering of the ionization potentials, different characteristics of absorption and emission lines, splitting of absorption lines, absence of resonance radiation from $\sim$ 200 to 800 nm for light alkali atoms and the presence of lines which are forbidden in the free systems. The details of the individual observations are given by Tabbert et al. [37]. Current experimental observations aim at understanding the spectroscopy and dynamics of atoms and molecules not in bulk liquid helium but attached to helium nanodroplets and the subject is well reviewed by Stienkemeier and Lehmann [59]. In this short review we will try to address the problem of the spectral properties of foreign atoms embedded in liquid helium purely from a theoretical point of view. A survey of the theoretical methods applied for the investigations on the various properties of the atomic systems confined under liquid helium will be given together with their viability for such descriptions. We give a summary and possible future direction in this line in a final section.

2 Theoretical Developments

Although spectroscopic data available from the experimental observations on foreign atoms embedded in liquid helium are substantial (In Table 1 we display several such experimental results [3–5, 8, 17]), theoretical investigations which interpret these data are rather limited in number. This is possibly due to the complexity of the problem. Because the He atom interacts weakly with other atomic systems through long-range interactions, dealing with a large number of interacting He atoms in the liquid with an embedded foreign atom and the consequent bubble structure is a complex problem from the molecular point of view. Table 2 shows some of the available data on the bubble radius for different systems embedded in liquid helium [3, 10, 49, 50, 56, 60–69]. For systems where more than one bubble radius exists, the spread in the values is given.

The first attempt to find the energy levels of an electron and atoms embedded within a bubble is what is known as the standard bubble model (SBM) [5, 56] [70–72]. This is described in the next section.

Table 1 Typical spectral line shifts and broadening of atomic transitions embedded in liquid helium

Wavelength (nm)				
Atom	Transition	Free	Shift	FWHM (nm)
Be[a]	$2p:{}^1P_1 \rightarrow 2s:{}^1S_0$	234.86	+0.99±0.1	0.97±0.1
Al[a]	$4s:{}^2S_{1/2} \rightarrow 3p:{}^2P_{3/2}$	394.40	+0.22±0.49	0.54±0.049
Mg[a]	$3p:{}^1P_1 \rightarrow 3s:{}^1S_0$	285.17	+3.60±0.1	1.50±0.20
Ca[b]	$4s:{}^1S_0 \rightarrow 4p:{}^1P_1$	422.67	−2.65±0.5	4.75±0.6
Ca[c]	$4p:{}^1P_1 \rightarrow 4s:{}^1S_0$	422.67	+0.63±0.07	0.81±0.04
Sr[b]	$5s:{}^1S_0 \rightarrow 5p:{}^1P_1$	460.73	−3.3±0.05	5.95±0.5
Sr[c]	$5p:{}^1P_0 \rightarrow 5s:{}^1S_0$	460.73	+0.60±0.16	0.9±0.2
Ba[b]	$6s:{}^1S_0 \rightarrow 6p:{}^1P_1$	553.55	−4.3±0.5	8.5±0.5
Ba[c]	$6p:{}^1P_1 \rightarrow 6s:{}^1S_0$	553.55	−0.23±0.06	0.80±0.20
Ba^{+}[b]	$6s:{}^2S_{1/2} \rightarrow 6p:{}^2P_{3/2}$	493.4	−11.4±0.5	4.4±0.5
Ba^{+}[d]	$6p:{}^2P \rightarrow 6s:{}^2S$	493.4	−2.4±0.5	2.0±0.5
Cu[a]	$5s:{}^2S_{1/2} \rightarrow 4p:{}^2P_{3/2}$	809.26	+0.29±0.2	2.60±0.40
Ag[a]	$5p:{}^2P_{1/2} \rightarrow 5s:{}^1S_{1/2}$	338.29	−0.11±0.01	0.35±0.04
Zn[a]	$4p:{}^1P_1 \rightarrow 4s:{}^1S_0$	213.86	+5.50±0.1	3.50±0.3
Cd[a]	$5p:{}^1P_1 \rightarrow 5s:{}^1S_0$	228.80	+4.43±0.1	2.80±0.3
Rb[e]	$5s:{}^1S_{1/2} \rightarrow 5p:{}^2P_{1/2}$	794.76	−16.8±0.5	4.0±0.5
	$5s:{}^2S_{1/2} \rightarrow 5p:{}^1P_{3/2}$	780.03	−16.0±0.5	3.0±0.5
	$5p:{}^2P_{1/2} \rightarrow 5s:{}^2S_{1/2}$	794.76	−1.2±0.2	0.9±0.2
Cs[e]	$6s:{}^2S_{1/2} \rightarrow 6p:{}^2P_{1/2}$	894.35	−18.4±0.5	5.5±0.5
	$6s:{}^2S_{1/2} \rightarrow 6p:{}^2P_{3/2}$	852.11	−18.1±0.5	2.8±0.5
	$6p:{}^2P_{1/2} \rightarrow 6s:{}^2S_{1/2}$	894.35	−2.1±0.2	1.2±0.2
	$6p:{}^2P_{3/2} \rightarrow 6s:{}^2S_{1/2}$	852.11	6±2	12±2

[a] Ref.[8]; [b] Ref.[5]; [c] Ref.[4]; [d] Ref.[3]; [e] Ref.[17]. For Rb and Cs the width values are HWHM.

Table 2 Bubble radii (in nm) of atoms in liquid helium

Atom/ion	State	Bubble radius
$e-$[a,b]	^2S	1.75–2.0
Ps[c]	^3S	2.0
He[d]	2^3S, 2^3P	0.476–0.53
He[d]	3^1S	1.323
He[d]	3^3S	1.111
Li[e]	^2S	0.491
Na[e,f,g,h,i,j]	^2S	0.44–0.59
K[e,f]	^2S	0.56–0.60
Rb[e,f,k]	^2S	0.515–0.61
Cs[e,f,j]	^2S	0.57–0.64
Ba^{+}[l]	^2S	0.450
Ca[m]	^1S	~ 0.585
Ba[n]	^1S	0.650

[a] Ref.[56]; [b] Ref.[60]; [c] Ref.[49, 50]; [d] Ref.[61]; [e] Ref.[62]; [f] Ref.[63]; [g] Ref.[64]; [h] Ref.[65]; [i] Ref.[66]; [j] Ref.[67]; [k] Ref.[68]; [l] Ref.[3]; [m] Ref.[10]; [n] Ref.[69].

2.1 The Standard Bubble Model

The consequence of the formation of a cavity or bubble inside liquid helium with a foreign atom at the centre is apparent from the experimentally observed line shifts and changes in line profiles. Liquid He atoms interact with the central impurity atom and modify the effective potential of the free system. The altered potential is responsible for the change in the ground as well as the excited state wavefunctions of the impurity, resulting in a change of the spectroscopic properties. In order to obtain the energy eigenvalues we have to solve the Schrödinger equation (we use a.u. unless otherwise stated),

$$H\Psi = E\Psi, \tag{1}$$

subject to the normalization

$$\langle \Psi | \Psi \rangle = 1, \tag{2}$$

where H is the total Hamiltonian and Ψ is the total wavefunction. The total Hamiltonian can be partitioned into [37]

$$H = H_{\text{Liq}} + H_{\text{A}} + H_{\text{int}}, \tag{3}$$

where H_{Liq} is the Hamiltonian of the liquid helium consisting of the kinetic energy of the He atoms and the potential energy arising out of the pair interactions,

$$H_{\text{Liq}} = -\frac{1}{2M}\sum_k \nabla_k^2 + \sum_{k<l} V\left(\mathbf{R}_k, \mathbf{R}_l\right), \tag{4}$$

where M is the mass of the He atom and the indices run over the number of He atoms whose coordinates are specified by $\mathbf{R}$.

The atomic Hamiltonian is given by the usual kinetic energy of the electrons and Coulomb interactions between the charges,

$$H_{\mathrm{A}} = -\frac{1}{2}\sum_i \nabla_i^2 - \sum_i \frac{Z}{r_i} + \sum_{i<j} \frac{1}{r_{ij}}, \tag{5}$$

where the indices run over the number of electrons in the system.

The interaction term is represented as a linear sum of pair potentials between the impurity atom and He and using the density profile of liquid helium $\rho(\mathbf{R})$ can be expressed as [61]

$$H_{\mathrm{int}} = \sum_k V_{\mathrm{int}}(\mathbf{R}_k, \mathbf{r}) = \int \rho(\mathbf{R}) V_{\mathrm{int}}(\mathbf{R}, \mathbf{r})\, d\mathbf{R}. \tag{6}$$

In Eq. (6), $\mathbf{r}$ represents collectively the coordinates of the electrons.

The radial liquid helium density profile is represented as [61, 73]

$$\rho(R) = \begin{cases} 0; & R \le R_0 \\ \rho_0 \left\{1 - [1 + \delta(R - R_0)]\, \mathrm{e}^{-\delta(R-R_0)}\right\}; & R > R_0 \end{cases}, \tag{7}$$

in which ρ_0 is the normal liquid helium density. The quantities δ and R_0 are the parameters related to the bubble profile and size with respect to which the total energy of the bubble is optimized. Such a representation for ρ was first given by Jortner et al. [73] for the electron bubble problem and subsequently used by Dennis et al. [74] and others [61, 75–79] for the energy levels and line profiles for excited atoms in liquid helium. The density of liquid helium vanishes at the centre of the bubble and remains so up to a point R_0 determined by the pair potential and reaches the bulk density asymptotically. The centre of mass of the density distribution at the radius $R = R_{\mathrm{b}}$ is defined as the effective bubble radius and is determined from the relation

$$\int_0^{R_{\mathrm{b}}} \rho(\mathbf{R})\, d\mathbf{R} = \int_{R_{\mathrm{b}}}^{\infty} [\rho_0 - \rho(\mathbf{R})]\, d\mathbf{R}. \tag{8}$$

The liquid energy in the SBM model is approximated by the corresponding classical pressure volume energy, surface energy and the additional term arising from the enhanced kinetic energy of the liquid at the bubble margin [70],

$$E_{\mathrm{Liq}} = \frac{4}{3}\pi R_{\mathrm{b}}^3 P + 4\pi R_{\mathrm{b}}^2 \gamma + \frac{1}{8M}\int \frac{(\nabla\rho)^2}{\rho}\, d\mathbf{R}. \tag{9}$$

In the equation above P is the liquid pressure and γ is the surface tension. Usually, the liquid is assumed incompressible. During a fast optical transition the liquid

configuration does not change and one can calculate the effect of the interaction on atomic system using perturbation theory. In the SBM first-order perturbation theory is used and the energy of the atom is given by the energy of the atom in the absence of interaction and the first-order correction to the energy due to the interaction term,

$$E_{\mathrm{A}} = E_{\mathrm{A0}} + \langle \Psi_{\mathrm{A0}} | H_{\mathrm{int}} | \Psi_{\mathrm{A0}} \rangle. \tag{10}$$

The equilibrium configuration of the bubble can be determined by minimizing the total energy including the liquid energy with respect to the parameters in the density expression. Using accurate estimates of the existing pair potentials between helium and other atoms, the first-order energy shift of the atom can be calculated for both the initial and the final states of the impurity. This determines the transition energy and the spectral line shift. Due to the incompressible nature of the liquid, this simple procedure gives the line shifts and a configuration coordinate diagram [37] gives the asymmetry in the line shapes during absorption and emission. The SBM can be utilized with the static line-broadening theory to estimate the spectral line profiles with reasonable success [61, 75–78]. The SBM is a somewhat crude approximation to the actual situation. It ignores the influence of the angular momentum of the excitation on the shape of the bubble, considers liquid helium as incompressible and the liquid energy is described only by classical means. Optical spectra of alkaline earths can be explained with reasonable success with this method [5, 8, 72]. The details about the spectral line shapes and broadenings for both the emission and the absorption lines have been discussed by Tabbert et al. [37]. It is important to note that experiments do not reveal any particular change in the line positions due to the superfluid nature of the liquid [8]. In other words, the spectral shift is insensitive when crossing the critical temperature. In Table 3 we compare the results for alkaline earth and alkali atoms in liquid helium [10, 64, 80–82] calculated using the SBM [5] with existing experimental data [5].

Table 3 Comparison of SBM calculated and experimental data of the spectral shift in liquid helium

	Transition		Expt.[a]	Pseudopot.[b]	Configuration Coord.[c]
Ca	$4s:^1S \rightarrow 4p:^1P$	Shift (nm)	−2.65±0.5	−21.5	−9.40[d], −2.80[f]
		FWHM(nm)	4.75±0.5	5.6	3.20[d], 1.75[f]
Sr	$5s:^1S \rightarrow 5p:^1P$	Shift (nm)	−3.30±0.5	−25.0	
		FWHM(nm)	5.95±0.5	6.3	
Ba	$6s:^1S \rightarrow 6p:^1P$	Shift (nm)	−4.30±0.5	−33.5	−19.30[e]
		FWHM(nm)	8.50±0.5	7.6	6.6[e]
Ba^+	$6s:^2S \rightarrow 4p:^2P$	Shift (nm)	−11.40±0.5	−6.8	
		FWHM(nm)	4.40±0.5	2.7	

[a] Ref.[5]; [b] Theoretical estimates in Ref.[5, 10]; [c] Ref.[64] in which the pair potentials of
[d] Ref.[80]; [e] Ref.[82]; [f] Ref.[81] have been used.

2.2 Refinements of the Standard Bubble Model

The SBM fails to predict the emission spectra of light alkali atoms in liquid helium. Takahashi et al. [17] pointed out that for light alkali atoms like Li, Na and K inside liquid helium, no fluorescent emission occurs, but the SBM predicts the existence of emission lines. For Na, the model predicts an emission $3p \rightarrow 3s$ at 620 nm [79]. Kanorski et al. [79] pointed out that the excited pair potential for Na [83] has a rotational symmetry about the z axis if the p function has Y_{10} character. A finite number of He atoms can be localized within a ring of 0.2–0.3 nm in the nodal plane of the electronic wavefunction forming a $Na^*(3p)He_n$ exciplex. The density of He atoms in this complex can exceed the bulk density of liquid helium. A variational calculation of the exciplex indicates a near-degeneracy of the $3s$ and $3p$ levels with a quenching of the $3p$ state, indicating the absence of the resonant radiation. This was confirmed by the calculation of Dupont-Roc [84] who showed that excited states in light alkali atoms have the possibility of non-radiative decay. It was further pointed out by Dupont-Roc [84] that the liquid helium configurations around the foreign atoms in the s and p states are different. The total energy, in which the interaction energy is taken as the sum of pair potentials between He and an alkali atom like Na in ground and excited states, is optimized with respect to both the electronic wavefunction and the shape of the cavity to get the surface structure [84]. According to Hickman et al. [61], the effect of the non-spherical nature of the bubble radius can be treated by expanding the bubble radius in terms of Legendre polynomials keeping only the quadrupolar term in the expansion,

$$R_b(\Theta) = R_b \left[1 + \zeta P_2(\cos\Theta)\right], \tag{11}$$

where Θ is the polar angle between the atomic state described by the angular momentum orientation (z axis in this case) and the radius vector of the He atoms and ζ is the anisotropy parameter. It has been found that in the excited p state of Na in liquid helium approximately $5-6$ He atoms surround the nodal plane with a radius of ~ 0.25 nm [79, 84]. This is because of an attractive dipolar interaction between the ion core and the He atoms. The red shift of the $3p$ energy level due to this effect can be of the order of the $3s$-$3p$ energy difference. The $3p$ state can have a resonance coupling with the ground state with a non-radiative de-excitation possibility. This may be the reason for the absence of fluorescent emission in light alkali atoms. The mechanism of recombination of electrons and positive ions has been explained by Beau et al. [64] using a tunnelling model. The model has been successful in predicting the lowering of the ionization potential and the subsequent $\sim$ 1.8 eV population gap in alkaline earth atoms. The recombination process is considered as a tunnelling of the electron from the bubble into the Coulombic potential of the positive ion and subsequent relaxation of the recombined atom and the environment as a consequence of neutralization. This tunnelling probability has been calculated using the WKB approximation. Using the SBM with improved pair potentials [80–82] for

the ground as well as the excited states between He and Ca and Ba, the equilibrium configuration of the bubble structure is determined by minimizing the total energy with respect to the size and shape of the bubble, and the optical transitions have been analyzed [64]. The optical excitation takes place in a much shorter time than that required for the readjustment of the bubble shape, and consequently, the atomic excitation takes place in the same spherical cavity of the ground state. Hence, the excitation properties from the ground state of alkali, alkaline earth and group Ib and IIb atoms can be analyzed using a spherical bubble structure. The excitation line is usually blue shifted because the excited state wavefunction, having a larger extent, experiences stronger repulsion at the liquid helium boundary, thereby placing the excited state at a higher energy level than that for the free system. The lifetime of the excited state is longer than the relaxation time characterizing the transformation of the bubble into a new shape, which results in a cavity greater than that of the ground state and not necessarily spherical. The de-excitation takes place from a relaxed bubble shape of wider cavity. For example, the excited p states of such atoms have the defect structure modified compared with that of the ground state because of the non-spherical nature of the excited wavefunctions. To deal with such a situation, the bubble radius is taken as in Eq. (11) with the anisotropy parameter introduced within. Optical excitation pumps energy into the system, resulting in excitations of the bubble and the subsequent breathing oscillation and quadrupolar oscillation modes [85, 86] involving the bubble size and the anisotropy parameter. Pascale [83] has studied in detail the pair potential of the Na-He system using a pseudopotential approach. Beau et al. [64] used the pseudopotential of Pascale [83] for making the configuration coordinate analysis, i.e., the energy versus the bubble structure parameter for Na embedded in liquid helium. According to Beau et al. [64], the $3s$ ground state of Na resides in a bubble of radius ~ 0.54 nm. The spectral shift of this state with a bubble shape parameter $\delta = 23\,\mathrm{nm}^{-1}$ is found to be $+5.4$ meV compared with free Na. In the $3p$ excited state, the Na atom forms a non-spherical bubble with anisotropic structure given by $\zeta = 0.58$, $\delta = 20\,\mathrm{nm}^{-1}$ and $R = 0.65$ nm. The energy of this state is shifted by $+12.4$ meV. This results in the shift of the absorption line centre by -16.7 nm and the emission line centre by $+1.0$ nm.

2.3 Density Functional Approach

Following the phenomenological density functional approach by Dupont-Roc *et al.* [87] for liquid helium, De Toffol et al. [88] estimated the spectral line shifts in the absorption and emission from the first excited states of Na and Cs atoms. The alkali–He pair potentials have been calculated from the SCF charge density of the alkali atom and the van der Waals coefficients for the ground and excited states. In this method the total energy is assumed to be a sum of the liquid energy, the energy of the free atom and the interaction energy between the atom and the liquid helium. According to Dupont-Roc et al. [87] the liquid energy is written as

$$E_{He}[\rho] = \frac{1}{2M}\int \left[\nabla \rho^{1/2}(\mathbf{r})\right]^2 d\,\mathbf{r} + \frac{1}{2}\int\int \rho(\mathbf{r})\rho(\mathbf{r}')V_l\left(|\mathbf{r}-\mathbf{r}'|\right) d\,\mathbf{r}\, d\,\mathbf{r}' + \frac{g}{2}\int \rho(\mathbf{r})\overline{\rho_r}^{1+\nu} d\,\mathbf{r}, \tag{12}$$

where $\rho(\mathbf{r})$ is the liquid helium density. The first term on the right-hand side of eq. (12) is the kinetic energy of the liquid, the second term is a two-body He–He pair potential $V_l(r)$ screened at a distance shorter than a characteristic length R_l, and the third term accounts for the internal kinetic energy and the increasing contribution of the hard-core He–He repulsion when the density is increased. $\overline{\rho}_r$ is the average of the He density over a sphere of radius R_l [87]. The parameters R_l, g and ν are adjusted to reproduce the experimental energy per He atom for the liquid, the compressibility of the bulk liquid at the saturation density and the surface tension. The alkali atom is treated within the density functional scheme of Kohn and Sham [89] in which the valence electron wavefunction $\Psi(\mathbf{r})$, interacting with the frozen alkali ion core via ab initio pseudopotentials [90], is obtained by minimizing the total energy

$$E_A[\Psi] = \frac{1}{2}\int [\nabla\Psi(\mathbf{r})]^2\, d\,\mathbf{r} + \int \hat{V}_{\rm ps}(\mathbf{r})\rho_{\rm e}(\mathbf{r})\, d\,\mathbf{r} + \frac{1}{2}\int\int \frac{\rho_{\rm e}(\mathbf{r})\rho_{\rm e}(\mathbf{r}')}{|\mathbf{r}-\mathbf{r}'|} d\,\mathbf{r}\, d\,\mathbf{r}' + E_{\rm xc}[\rho_{\rm e}], \tag{13}$$

where $\rho_{\rm e}(\mathbf{r}) = |\Psi(\mathbf{r})|^2$ is the valence electron charge density and $\hat{V}_{\rm ps}$ is a norm-conserving angular momentum-dependent pseudopotential. The exchange correlation part used is

$$E_{\rm xc}[\rho_{\rm e}] = \int \mathcal{E}_{\rm xc}[\rho_{\rm e}(\mathbf{r})]\,\rho_{\rm e}(\mathbf{r})\, d\mathbf{r}, \tag{14}$$

$\mathcal{E}_{\rm xc}$ being the exchange correlation energy density of a homogeneous electron gas of density $\rho_{\rm e}(\mathbf{r})$. The effect of the fine structure splitting has been taken into consideration for constructing the pseudopotential. The alkali– liquid interaction energy has been represented by [88]

$$E_{A-He}[\rho, \Psi] = \int\int \rho(\mathbf{r})\left[\rho_{\rm e}\left(\mathbf{r}'-\mathbf{r}_{\rm c}\right) + \rho_{\rm c}\left(\mathbf{r}'-\mathbf{r}_{\rm c}\right)\right] w\left(\mathbf{r}-\mathbf{r}'\right) d\,\mathbf{r}\, d\,\mathbf{r}' + \int \rho(\mathbf{r})\, U\left(\mathbf{r}-\mathbf{r}_{\rm c}\right) d\,\mathbf{r}, \tag{15}$$

where $\rho_{\rm e}$ and $\rho_{\rm c}$ are, respectively, the valence and core electron charge density of the alkali atom and $\mathbf{r}_{\rm c}$ is the vector position of the alkali core. The valence charge density $\rho_{\rm e}$ is obtained self-consistently from a minimization of the total energy. $w(\mathbf{r})$ is a short-range repulsive potential arising from the overlap of the He and the alkali wavefunctions, and U is the van der Waals interatomic attraction between the alkali atom and He. The details of this procedure may be found in Ref. [88]. The van

der Waals coefficients C_6 are to be properly obtained both for the ground and for the excited states. Minimization of the total energy subjected to constraints yields the liquid helium density $\rho(\mathbf{r})$ and the wavefunction $\Psi(\mathbf{r})$. De Toffol et al. [88] calculated the spectral line shifts of Na and Cs atoms for excitation and emission with reasonable success as we will show later. With this method they have been able to find qualitatively the splitting of the absorption profile of the Cs atom in liquid helium, which is explained by introducing the dynamic Jahn–Teller distortion [17].

2.4 Ab Initio Quantum Chemical Approach

Very few theoretical attempts have been made to study the spectroscopic properties of atoms embedded in liquid helium environment using ab initio quantum chemical methods. Recent attempts in this direction are aimed at the spectral line shift calculations for alkali atoms, for which experimental line shifts [17] are relatively larger.

2.4.1 Combined Quantum Mechanics and Monte Carlo Simulation

The theoretical results reported earlier referred to applications of the SBM or its refinements in suitable ways. The density functional approach of De Toffol et al. [88] utilizes existing pseudopotentials and van der Waals coefficients with adjustable parameters in the formulation. However, an ab initio quantum chemical approach to the problem is worth investigating. Such an attempt was first made by Ludwig et al. [65] for estimating both the excitation line shift and the line width of the principal resonance line of an Na atom embedded in liquid helium. In this method the liquid structure surrounding the central Na atom was generated by Monte Carlo simulation [91, 92] using accurate interatomic potentials available in the literature [93]. The Monte Carlo simulation was performed using the DICE program [92] in the NPT ensemble with the number of He atoms N, its temperature T and pressure P fixed. Correspondingly, the simulation included one Na atom surrounded by $1,000$ He atoms with $P = 1\,\text{atm}$ and $T = 2\,\text{K}$. The simulation process generates a large number of configurations, and only the statistically relevant configurations are sampled using the autocorrelation function of the energy [65] for subsequent quantum chemical calculations using time-dependent density functional theory (TDDFT). The quantum mechanical calculations have been performed by Ludwig et al. [65] with 50 statistically uncorrelated configurations. The density distribution shows clearly that the He atoms are well structured around the central Na atom with more than one solvation shell, which is clearly different from that obtained using the SBM. Figure 1 shows a plot of the radial distribution function against the distance of He atoms from the central Na atom. Because of the weak intermolecular potential between Na and He, only the He atoms within the first solvation shell are considered for subsequent calculation for the absorption spectrum and the line shift. The first solvation shell corresponds to the peak located

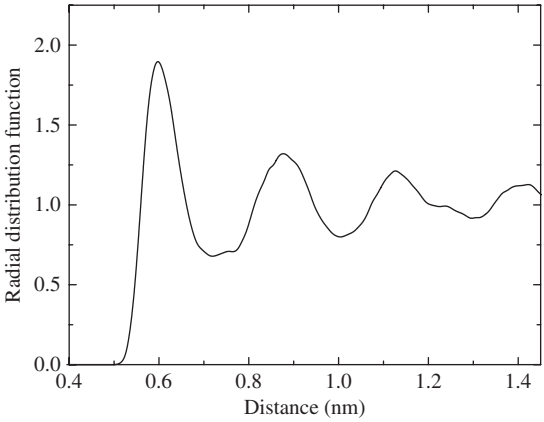

Fig. 1 The radial distribution function between Na and He

at 0.59 nm but starts at 0.50 nm and ends at 0.72 nm. Integration of this peak gives the coordination number of 42 He atoms surrounding the Na atom. Figure 2 illustrates this solvation shell. For the calculation of the spectral line shift the TDDFT method was used as implemented in the Gaussian 03 program. Different exchange functionals have been explored. The gaussian basis set employed was 6-311++G(d, p), which includes both polarization and diffuse functions in Na and He. This leads to a total of 324 basis functions. Using the PBE1PBE functional [94], a shift of 14.7 nm was obtained for the excitation corresponding to the D line of Na. This is in good agreement with other existing theoretical results. Estimates with other exchange functionals have also been made. Statistical distribution of the calculated transitions yields the line width. This particular calculation furnishes a statistical representation of the structure of the liquid helium cavity surrounding the Na atom. Using the B3LYP, PBE1PBE and B3P86 exchange correlation functionals in different basis sets, Ludwig et al. [65] estimated the spectral blue shift of Na in liquid helium within the interval of 14.7–18.9 nm and the line width between 6 and

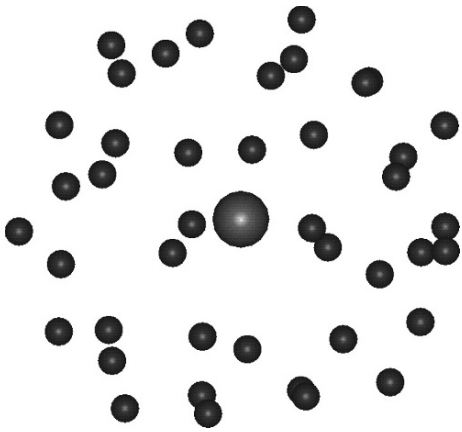

Fig. 2 Monte Carlo simulation of Na in liquid helium. One configuration illustrating the first solvation shell composed of 42 He atoms surrounding Na

8 nm. An interesting contribution to the calculated line width comes from the natural splitting of the 3p orbital in the inhomogeneous liquid environment.

2.4.2 Non-Relativistic Cluster Model Calculation

The symmetry-adapted cluster configuration interaction (SAC-CI) method, which has been well tested for studying excitation energies for extended systems [95–98], has also been applied for the calculation of the excitation line shift of the D line of Na atom embedded in liquid helium by Saha et al. [66]. In this method, the effect of the surrounding liquid helium was taken care of by considering only the nearest neighbour interactions using several model clusters. The number of He atoms in the model clusters was chosen to be 12, 20 and 24 so that an approximately spherically symmetric structure could be obtained. The excitation energy of the $3s \rightarrow 3p$ transition for the free Na atom was first determined using the SAC-CI method with a contracted $6s5p3d1f$ Gaussian basis of Mclean and Chandler including diffuse s- and p-type functions [99]. For He, the $5s$ basis developed by Dunning and Hay [100] augmented with an additional diffuse s function was adopted. The radius of the cluster was then varied in each case and the $3s \rightarrow 3p$ excitation energies were determined. The shift of the spectral lines in the presence of the He clusters could then be calculated. In this calculation, two points are to be satisfied, namely, (i) the Na – He distance should be in conformity with the Na – He interatomic distance at equilibrium and (ii) the He – He distance in the cluster should be approximately the He – He interatomic distance. Since the cluster geometry was not optimized, amongst various choices of the cluster radius, Saha et al. [66] selected two specific radii, calculated from a formula due to Gspann [101],

$$N_{\text{neigh}} = \frac{4^{4/3}\pi}{\sqrt{3}}\, r^2\, \rho^{2/3}, \tag{16}$$

using two different densities for liquid helium. In Eq. (16), N_{neigh} is the coordination number, i.e., the number of He atoms finding a place on the sphere of radius r, and ρ is the number density of liquid helium. For a given coordination number, i.e., the number of nearest neighbours, the first radius is obtained by assuming the normal density of liquid helium and the second radius is due to half of the normal density corresponding to the centre of mass of the bubble. Table 4 shows the transition wavelength for the resonance line of Na in different clusters along with those corresponding to these two radii. It is noted from this table that for the cluster with 20 He atoms surrounding the central Na, the shift at the realistic liquid density, $\rho/2 \sim 10.9/\text{nm}^3$, corresponding to the effective bubble radius of 0.594 nm, appears to be $\sim$ 16.6 nm, in good agreement with other available results. This distance is also in very good agreement with the Na–He peak maximum of 0.59 nm, obtained in the Monte Carlo simulation discussed in the previous section (see also Fig. 1). The He–He distance comes out to be $\sim$ 0.424 nm, in conformity with the result of $\sim$ 0.4 nm obtained from a closed pack plane of He atoms [101].

Table 4 $^2S \rightarrow {}^2P$ resonance line position of Na–He_n clusters [66]. All quantities in nm

Cavity radius	He–He distance	λ_{LHe}	$\Delta\lambda = \lambda_{\text{free}} - \lambda_{LHe}$
Na–He_{12}			
0.70	0.98995	596.4	0.4
0.60	0.84853	587.9	8.9
0.56	0.79196	580.7	16.1
0.52	0.73540	569.9	26.9
0.46038[a]	0.65107	545.0	51.8
0.36540[b]	0.51676	484.3	112.5
Na–He_{20}			
0.70	0.49955	594.6	2.2
0.60	0.42819	581.5	15.3
0.56	0.39964	571.0	25.8
0.52	0.37110	555.0	41.8
0.59434[a]	0.42415	580.2	16.6
0.47173[b]	0.33665	527.5	69.3
Na–He_{24}			
0.70	0.50037	592.9	3.9
0.60	0.42889	577.9	18.9
0.56	0.40030	565.5	31.3
0.52	0.37170	547.7	49.1
0.65172[a]	0.46586	587.7	9.1
0.51676[b]	0.36938	546.0	50.8

$\lambda_{\text{free}}(\text{Na}) = 589.6\,\text{nm}$; [a] Number density of He at half bulk density = $10.9\,\text{nm}^{-3}$;
[b] Number density of liquid helium = $21.8\,\text{nm}^{-3}$.

2.4.3 Relativistic Density Functional Approach

Anton et al. [67] first applied relativistic density functional theory (RDFT) to estimate the spectral line shifts of the principal resonance lines of alkali atoms such as Na and Cs. They used a cluster model, much along the same line as was done by Saha et al. [66], and subsequently extended the calculation to obtain the spectral line shift of the Rb atom in liquid helium [68]. Instead of taking different clusters, a model cluster of 14 He atoms surrounding the central alkali atom was chosen such that eight He atoms are located at the corners of a cube and six additional He atoms are located above each surface of the cube, maintaining a constant distance from the centre. This model is reasonably tractable and maintains a near-spherically symmetric structure. In making the structure, one has to be in conformity with the fact that the average distance between He atoms in a closed pack structure is $\sim 0.4\,\text{nm}$ [101] with a normal liquid helium density of $21.8/\text{nm}^3$. The alkali-He distance is approximated by the interatomic distance. Such distances were previously given by Ancilotto et al. [62]. In the relativistic density functional approach, the total energy of a system with N nuclei and M electrons is given by [102–104]

$$E = \sum_{i=1}^{M} n_i \langle \Psi_i | \hat{T} | \Psi_i \rangle + \int \left(V_{\text{nuc}} + \frac{1}{2} V_{\text{H}} \right) \rho_{\text{e}}(\mathbf{r})\, d\,\mathbf{r} + E_{\text{xc}}[\rho_{\text{e}}] + \sum_{k<k'}^{N} \frac{Z_k Z_{k'}}{|\mathbf{R}_k - \mathbf{R}_{k'}|}, \tag{17}$$

where $\hat{T} = c\alpha \cdot \mathbf{p} + (\beta - 1)mc^2$ is the Dirac kinetic energy operator, V_{nuc} is the interaction between the electron and the nuclei and V_H is the Hartree potential. The symbols in the definition of $\hat{T}$ have their usual meaning. In the non-pair approximation, the electronic density is constructed as

$$\rho_{\text{e}}(\mathbf{r}) = \sum_{i=1}^{M} n_i \, \Psi_i^{\dagger}(\mathbf{r})\Psi_i(\mathbf{r}), \tag{18}$$

where n_i is the occupation number of the molecular orbital $\Psi_i(\mathbf{r})$. The variation of the total energy leads to the relativistic Kohn–Sham equation,

$$\left(\hat{T} + V_{\text{nuc}} + V_{\text{H}} + V_{\text{xc}}\right) \Psi_i(\mathbf{r}) = \varepsilon_i \Psi_i(\mathbf{r}), \tag{19}$$

which is to be solved self-consistently. The LCAO-MO method has been adopted to solve the Kohn–Sham equations in which the molecular orbital $\Psi_i(\mathbf{r})$ is expanded in a series of symmetry-adapted orbitals $\chi_j(\mathbf{r})$,

$$\Psi_i(\mathbf{r}) = \sum_j C_{ji} \chi_j(\mathbf{r}). \tag{20}$$

The symmetry-adapted orbitals are expanded as a linear combination of atomic orbitals, the expansion coefficients of which can be obtained from group theory [105],

$$\chi_j(\mathbf{r}) = \sum_{\nu} d_{\nu j} \phi_{\nu}(\mathbf{r}). \tag{21}$$

The energy eigenvalue and the molecular orbital coefficients can be obtained from the solution of the generalized eigenvalue equation

$$\mathbb{HC} = \mathbb{SCE}, \tag{22}$$

where $\mathbb{H}$ and $\mathbb{S}$ are the Fock and the overlap matrices, respectively, $\mathbb{C}$ is the coefficient matrix and $\mathbb{E}$ is the diagonal eigenvalue matrix of ε_i. Details may be found elsewhere [102–104]. The geometry of the cluster is optimized with respect to the alkali – He distance. The RDFT applied here utilizes the relativistic local density functional (RLDA) for this optimized geometry to obtain the energies of the lowest excited $^2P_{1/2}$ and $^2P_{3/2}$ states. The results for the free atom case and also those in the cluster condition are shown in Table 5 and compared with existing experimental and theoretical data. For Na, the non-relativistic results do not account for spin–orbit interaction and hence represent the shifts for the $3s \rightarrow 3p$ level, while for Cs, the reported results account for the spin–orbit interaction. From this table it appears that the RDFT is quite successful in predicting the experimental spectral line shifts in Rb and Cs, although for Na it predicts a relatively larger shift. However, for

Table 5 Spectral line shifts (nm) of alkali atoms in helium environment

	Free atom		Atom in He cluster		Shift		
	λ	Δλ	λ	Δλ	Theory		Experiment
Transition					Relativistic	Non-relativistic	
Na							
$S_{1/2} \rightarrow P_{1/2}$	533.30	0.70	510.40[a]	0.52	−22.90[a]	−16.70[b], −15.0[c]	
$S_{1/2} \rightarrow P_{3/2}$	532.60		509.88[a]		−22.72[a]	−14.7[d] ∼ −18.9[d]	
						−16.6[e]	
Rb							
$S_{1/2} \rightarrow P_{1/2}$	794.76	14.73	780.74[f]	17.52	−14.02[f]		−16.8±0.5[g]
$S_{1/2} \rightarrow P_{3/2}$	780.03		763.22[f]		−16.81[f]		−16.0±0.5[g]
Cs							
$S_{1/2} \rightarrow P_{1/2}$	811.15	42.60	795.63[a]	44.91	−15.52[a]	−26.0[c]	−18.4±0.5[g]
$S_{1/2} \rightarrow P_{3/2}$	768.55		750.72[a]		−17.83[a]	−27.0[c]	−18.1±0.5[g]

[a] Ref.[67]; [b] Ref.[64]; [c] Ref.[88]; [d] Ref.[65]; [e] Ref.[66]; [f] Ref.[68]; [g] Ref.[17].

Na the experimental excitation spectra in liquid helium is unavailable. For Cs, the relativistic effect appears to be more important, as expected.

2.5 Summary and Future Directions

In this brief review we discussed the few theoretical attempts towards understanding the spectral line shifts and other spectroscopic properties of foreign atoms embedded in a liquid helium environment. It appears that only little of the vast experimental data could be interpreted using the theoretical methodologies discussed above and the majority of the experimental data needs to be properly interpreted. Monte Carlo simulation of the liquid structure followed by quantum chemical calculations seems to be a viable method, but it has to be carried out systematically to predict the experimentally observed line shifts and line profiles. This methodology is presently used for the case of Rb in liquid helium with promising results [106]. Quantum chemical calculations for the interpretation of emission spectra based on distorted liquid structure are a necessity. Finally, theoretical attempts are necessary for understanding the details of the liquid properties based on interactions with foreign atoms.

Acknowledgments The author PKM expresses his sincere gratitude to Professor G. zu Putlitz for his constant encouragement in pursuing the research on the spectroscopic properties of atoms in liquid helium. He also acknowledges the financial support received from Department of Science and Technology and also Department of Atomic Energy, Government of India under Grant Nos: SR/S2/LOP-05/2005, 2007/37/59/ BRNS/436. The financial support from AvH Foundation, Germany, FAPESP, Brazil and JSPS, Japan, where parts of this work have been performed in collaboration, are gratefully acknowledged. PKM also acknowledges the encouragement from his parent Institution IACS, Kolkata, for allowing him all facilities necessary for sustaining research work. K. Coutinho and S. Canuto acknowledge continuous support of the Brazilian agencies CNPq, CAPES and FAPESP. The authors are thankful to Jesse Lutz for his critical examination of the manuscript.

References

1. A.L. Fetter, in *The Physics of Liquid and Solid Helium*, Part I, eds. by K.H. Bennemann, J.B. Ketterson (Wiley, New York, 1976)
2. H. Bauer, M. Haussmann, R. Mayer, H.J. Reyher, E. Weber, A. Winnacker, Phys. Lett. A **1**10, 279 (1985)
3. H.J. Reyher, H. Bauer, C. Huber, R. Mayer, A. Sch, A. Winnacker, Phys. Lett. A **1**15, 238 (1986)
4. H. Bauer, M. Beau, A. Bernhardt, B. Friedl, H.J. Reyher, Phys. Lett. A **1**37, 217 (1989)
5. H. Bauer, M. Beau, B. Friedl, C. Marchand, K. Miltner, H.J. Reyher, Phys. Lett. A **1**46, 134 (1990)
6. H. Bauer, M. Beau, J. Fisher, H.J. Reyher, J. Rosenkranz, K. Venter, Physica B **1**65 & 166, 137 (1990)
7. M. Arndt, S.I. Kanorski, A. Weis, T.W. Hänsch, Phys. Lett. A **1**74, 298 (1993)
8. B. Tabbert, M. Beau. H. Günther, W. Häussler, C. Hönninger, K. Meyer, B. Plagemann, G. zuPutlitz, Z. Phys. B **9**7, 425 (1995)
9. H. Günther, M. Foerste, M. Kunze, G. zuPutlitz, Z. Phys. B **1**01, 613 (1996)
10. J.H.A. Beijersbergen, Q. Hui, M. Takami, Phys. Lett. A **1**81, 393 (1993)
11. B. Tabbert, M. Beau, J. Fischer, G. zuPutlitz, H.Schreck, Physica B **1**94, 731 (1994)
12. A. Fuzisaki, K. Sano, T. Kinoshita, Y. Takahashi, T. Yabuzaki, Phys. Rev. Lett. **7**1, 1039 (1993).
13. S.I. Kanorski, M. Arndt, R. Dziewior, A. Weis, T.W. Hänsch, Phys. Rev. B **5**0, 6296 (1994)
14. M. Arndt, R. Dziewior, S.I. Kanorski, A. Weis, T.W. Hänsch, Z. Phys. B **9**8, 377 (1995)
15. T. Kinoshita, K. Fukuda, Y. Takahashi, T. Yabuzaki, Z. Phys. B **9**8, 387 (1995)
16. T. Kinoshita, K. Fukuda, Y. Takahashi, T. Yabuzaki, Phys. Rev. A **5**2, 2707 (1995)
17. Y. Takahashi, K. Sano, T. Kinoshita, T. Yabuzaki, Phys. Rev. Lett. **7**1, 1035 (1993)
18. T. Kinoshita, K. Fukuda, T. Yabuzaki, Phys. Rev. B **5**4, 6600 (1996)
19. T. Yabuzaki, T. Kinoshita, K. Fukuda, Y. Takahashi, Z. Phys. B **9**8, 367 (1995)
20. S.I. Kanorski, M. Arndt, R. Dziewior, A. Weis, T.W. Hänsch, Phys. Rev. B **4**9, 3645 (1994)
21. Q. Hui, J.L. Persson, J.H.M. Beijersbergen, M. Takami, Z. Phys. B **9**8, 353 (1995)
22. J.L. Persson, Q. Hui, J. Jakubek, M. Nakamura, M. Takami, Phys. Rev. Lett. **7**6, 1501 (1996)
23. H. Günther, M. Foerste, C. Hönninger, G. zuPutlitz, B Tabbert, Z. Phys. **9**8, 395 (1995)
24. E.B. Gordon, L.P. Mezhov-Deglin, O.F. Pugachev, V.V. Khmelenko, Chem. Phys. Lett. **5**4, 282 (1978)
25. E.B. Gordon, V.V. Khmelenko, A.A. Pelmenev, E.A. Popov, O.F. Pugachev, Chem. Phys. Lett. **1**55, 301 (1989)
26. E.B. Gordon, V.V. Khmelenko, A.A. Pelmenev, O.F. Pugachev, Physica B **1**08, 1311 (1981)
27. E.B. Gordon, E. A.A. Pelmenev, O.F. Pugachev, V.V. Khmelenko, Chem. Phys. 1981, **6**1, 35 (1981)
28. R.E. Boltnev, E.B. Gordon, I.N. Krushinskaya, A.A. Pelmenev, E.A. Popov, O.F. Pugachev, V.V. Khmelenko, Sov. J. Low. Temp. Phys. **1**6, 576 (1992)
29. R.E. Boltnev, E.B. Gordon, V.V. Khmelenko, I.N. Krushinskaya, M.V. Martinenko, A.A. Pelmenev, E.A. Popov, O.F. Pugachev, A.F. Shestakov, Sov. Chem. Phys. **1**89, 367 (1994)
30. J.L. Persson, Q. Hui, M. Nakamura, M. Takami, Phys. Rev. A **5**2, 2011 (1995)
31. T. Kinoshita, Y. Takahashi, T. Yabuzaki, Phys. Rev. B **4**9, 3648 (1994)
32. M. Arndt, S.I. Kanorski, A. Weis, T.W. Hänsch, Phys. Rev. A **7**4, 1359 (1995)
33. S.I. Kanorski, S. Lang, S. Lucke, S.B. Ross, T.W. Hänsch, A. Weis, Phys. Rev. A **5**4, R1010 (1996)
34. M. Foerste, H. Günther, O. Riediger, J. Wiebe, G. zuPutlitz, Z. Phys. B **1**04, 317 (1997)
35. B. Tabbert, M. Beau, M. Foerste, H. Günther, C. Hönninger, H. Hust, K. Layer, G. zuPutlitz, T. Schumacher, Z. Phys. B **9**8, 399 (1995)
36. Y. Takahashi, K. Fukuda, T. Kinoshita, T. Yabuzaki, Z. Phys. B **9**8, 391 (1995)

37. B. Tabbert, H. Günther, G. zuPutlitz, J. Low. Temp. Phys. **1**09, 653 (1997)
38. Z. Phys. B **9**8 (1995) (Special Issue dedicated to Atoms in Superfluid Helium)
39. A.N. Gerritsen, Physica **1**4, 407 (1948)
40. P.V.E. McClintock, Phys. Lett. A **2**9, 453 (1969)
41. A. Phillips, P.V.E. McClintock, Phil. Trans. Roy. Soc. **2**78, 271 (1975)
42. G.G. Ihas, T.M. Saunders Jr., Phys. Lett. A **3**1, 502 (1970)
43. E.B. Gordon, L.P. Mezhov-Deglin, O.F. Pugachev, JETP. Lett. **1**9, 63 (1974)
44. E.B. Gordon, A.A. Pelmenev, O.F. Pugachev, V.V. Khmelenko, JETP. Lett. **3**7, 283 (1983)
45. E.B. Gordon, V.V. Khmelenko, A.A. Pelmenev, E.A. Popov, O.F. Pugachev, A.F. Shestakov, Chem. Phys. **1**70, 411 (1993)
46. T. Yabuzaki, A. Fujisaki, K. Sano, T. Kinoshita, Y. Takahashi, in *Atomic Physics*, Vol. 13, eds. by H. Walther, T.W. Hänsch (North Holland, New York, 1992)
47. D.A.L. Paul, R.L. Graham, Phys. Rev. **1**06, 16 (1957)
48. J. Wackerle, R. Stump, Phys. Rev. **1**06, 18 (1957)
49. R.A. Ferrel, Rev. Mod. Phys. **2**8, 308 (1956)
50. R.A. Ferrel, Phys. Rev. **1**08, 167 (1957)
51. R.L. Williams, Can. J. Phys **3**5, 134 (1957)
52. L. Meyer, F. Reif, Phys. Rev. **1**10, 279 (1958)
53. G. Careri, F. Scaramuzzi, J.O. Thomson, Nuovo Cimento **1**3, 186 (1959)
54. K.R. Atkins, Phys. Rev. **1**16, 1339 (1959)
55. J.A. Northby, T.M. Sanders Jr., Phys. Rev. Lett. **1**8, 1184 (1967)
56. W.B. Fowler, D.L. Dexter, Phys. Rev. **1**76, 337 (1968)
57. W.A. Fitzsimmons, in *Atomic Physics*, Vol. 3, ed. by E.J. Smith (Plenum, New York, 1973)
58. J.C. Hill, O. Heybey, G.K. Walthers, Phys. Rev. Lett. **2**4, 657 (1970)
59. F. Stienkemeier, K.K. Lehmann, J. Phys. B : At. Mol. Opt. Phys, **3**9, R127 (2006), and references therein
60. B.E. Springett, R.J. Donnelly, Phys. Rev. Lett. **1**7, 364 (1966)
61. A.P. Hickman, W. Steets, N.F. Lane, Phys. Rev. B **1**2, 3705 (1975)
62. F. Ancilotto, E. Cheng, M.W. Cole, F. Toigo, Z. Phys. B **9**8, 323 (1995)
63. F. Dalfovo, Z. Phys. D **2**9, 61 (1994)
64. M. Beau, H. Günther, G. zuPutlitz, B. Tabbert, Z. Phys. B **1**01, 253 (1996)
65. V. Ludwig, P.K. Mukherjee. K. Coutinho, S. Canuto, Phys. Rev. A **7**2, 062714 (2005)
66. B. Saha, R. Fukuda, H. Nakatsuji, P.K. Mukherjee, Theor. Chem. Acc. **1**18, 437 (2007)
67. J. Anton, P.K. Mukherjee, B. Fricke, S. Fritzsche, J. Phys. B At. Mol. Opt. Phys **4**0, 2453 (2007)
68. J. Anton, B. Fricke, P.K. Mukherjee, S. Fritzsche, Phys. Lett. **3**72, 4462 (2008)
69. K. Ueda. H. Sotome, Y. Sato, J. Chem. Phys. **9**4, 1903 (1991)
70. K. Hiroike, N.R. Kestner, S.A. Rice, J. Jortner, J. Chem. Phys. **4**3, 2625 (1965)
71. W.T. Sommer, Phys. Rev. Lett. **1**2 271 (1964)
72. M.W. Cole, R.A. Bachman, Phys. Rev. B **1**5, 1388 (1977)
73. J. Jortner, N.R. Kestner, S.A. Rice, M.H. Cohen, J. Chem. Phys. **4**3, 2614 (1965)
74. W.S. Dennis, E. Durbin Jr., W.A. Fitzsimmons, O. Heybey, G.K. Walthers, Phys. Rev. Lett. **2**3, 1083 (1969)
75. A.P. Hickmann, N.F. Lane, Phys. Rev. Lett. **2**6, 1216 (1971)
76. J.P. Hansen, E.L. Pollock, Phys. Rev. A **5**, 2214 (1972)
77. W. Steets, A.P. Hickman, N.F. Lane, Chem. Phys. Lett, **2**8, 31 (1974)
78. J. Wisdom, T.W. Hartquist, N.F. Lane, Phys. Rev. B **1**4, 4205 (1976)
79. S.I. Kanorski, A. Weis, M. Arndt, R. Dziewior, T.W. Hänsch, Z. Phys. B **9**8, 371 (1995)
80. E. Czuchaj, F. Rebentrost, H. Stoll, H. Preuss, Chem. Phys. **1**38, 303 (1989)
81. E. Czuchaj, F. Rebentrost, H. Stoll, H. Preuss, Chem. Phys. Lett. **1**82, 191 (1991)
82. E. Czuchaj, F. Rebentrost, H. Stoll, H. Preuss, Chem. Phys. **1**77, 107 (1993)
83. J. Pascale, Phys. Rev. A, **2**8, 632 (1983)
84. J. Dupont-Roc, Z. Phys. B **9**8, 383 (1995)

85. E.P. Gross, H. Tung-Li, Phys. Rev. **1**70, 190 (1968)
86. P.B. Lerner, M.B. Chadwick, I.M. Sokolov, J. Low. Temp. Phys. **9**0, 319 (1993)
87. J. Dupont-Roc, M. Himbert, N. Pavloff, J. Treiner, J. Low. Temp. Phys. **8**1, 31 (1990)
88. G. De Toffol, F. Ancilloto, F. Toigo, J. Low. Temp. Phys. **1**02, 381 (1996)
89. W. Kohn, L.J. Sham, Phys. Rev. A **1**40, 1133 (1965)
90. G.B. Bachelet, D.R. Hamann, M. Schluter, Phys. Rev. B **2**6, 4199 (1982)
91. K. Coutinho, S. Canuto, Adv. Quantum Chem. **2**8, 89 (1997)
92. K. Coutinho. S. Canuto, DICE (version 2.8): A general Monte Carlo program for liquid simulation (University of São Paulo, 2002)
93. S.H. Patil, J. Chem. Phys. **9**4, 8089 (1991)
94. J.P. Perdew, K. Burke, M. Ernzerhof, Phys. Rev. Lett. **7**8, 1396 (1997)
95. H. Nakatsuji, Chem. Phys. Lett. **5**9, 362 (1978)
96. H. Nakatsuji, Chem. Phys. Lett. **6**7, 334 (1979)
97. H. Nakatsuji, K. Hirao, J. Chem. Phys. **6**8, 2053 (1978)
98. J. Hasegawa, K. Ohkawa, H. Nakatsuji, J. Phys. Chem. B **1**02, 10410 (1998)
99. A.D. Mclean, G.S. Chandler, J. Chem. Phys. **7**2, 5639 (1980)
100. T.H. Dunning. Jr, P.J. Hay, in *Modern Theoretical Chemistry*, Vol. 3, ed. by H.F. Schaefer, III, (Plenum, New York, 1976), p. 1
101. J. Gspann, Z. Phys. B **9**8, 405 (1995)
102. D. Geschke, S. Fritzsche, W.D. Sepp, B. Fricke, S. Varga, J. Anton, Phys. Rev. B **6**2, 15439 (2000)
103. S. Varga, E. Engel, W.D. Sepp, B. Fricke, Phys. Rev. A, **5**9,4288 (1999)
104. S. Varga, B. Fricke, H. Nakamatsu, T. Mukoyama, J. Anton, D. Geschke, A. Heitmann, E. Engel, T. Bastug, J. Chem. Phys. **1**12, 3499 (2000)
105. W. Ludwig, C. Falter, *Symmetries in Physics* (Springer, Berlin, 1988)
106. L. Modesto, K. Coutinho, P.K. Mukherjee. S. Canuto (private communication)

Level-Structure and Magnetic Properties from One-Electron Atoms to Clusters with Delocalized Electronic Orbitals: Shell Models for Alkali Trimers

Andreas W. Hauser, Carlo Callegari, and Wolfgang E. Ernst

Abstract The triatomic alkali–metal clusters we investigate here are still accessible via molecular-orbital-based ab initio computation, but do already show some features characteristic of extended many-electron systems. Experimental observation of both the low-spin multiplicity (doublet) and the high-spin multiplicity (quartet) presents us with two species with very different binding mechanisms (covalent vs. van der Waals). The Complete Active Space Self Consistent Field method in combination with Multi Reference Rayleigh Schrödinger Perturbation Theory of second order is applied to the high-spin (quartet) states of all possible homonuclear and heteronuclear trimers of K and Rb. We calculate the first few electronically excited states and compare the results with the doublet system of K_3 and Rb_3. The classical shell model for metal trimers is briefly reviewed in relation to the low-spin configuration and compared with a new model we introduce to rationalize the significantly different level structure we observe for the high-spin. This structure turns out to be related to the eigenstates of the harmonic oscillator, a feature known from the description of single-particle states in quantum dots.

Keywords: Ab initio · Alkali-metal clusters · Trimers · Shell model · Quantum dots · Electronically excited states · CASSCF · CASPT2 · High-spin

1 Introduction

Much experimental effort has been devoted to the investigation of small alkali–metal clusters ($N < 10$), as these objects offer a model system to overview the evolution of the properties of matter when moving from a single atom to larger aggregates [1–6]. Clusters in general are investigated predominantly by mass spectroscopy; alkali–metal clusters have strong, fluorescing electronic excitations conveniently accessible with visible lasers.

A.W. Hauser (✉), C. Callegari, W.E. Ernst
Institute of Experimental Physics, Graz University of Technology, Petersgasse 16, A-8010 Graz, Austria, e-mail: ahauser@sbox.tugraz.at, carlo.callegari@tugraz.at, wolfgang.ernst@tugraz.at

P. Piecuch et al. (eds.), *Advances in the Theory of Atomic and Molecular Systems*, Progress in Theoretical Chemistry and Physics 20, DOI 10.1007/978-90-481-2985-0_10,

As for the onset of metallic properties, group Ia atoms are preferred as a model system, because of their simple one-electron valence structure; other elements are studied in relation to magnetic properties, and are gaining attention because of the importance of themes such as spintronics, magnetic storage, superconductivity.

Popular production techniques for low-spin group Ia clusters are the condensation of alkali atoms on cold surfaces [7], or the adiabatic expansion of alkali vapor seeded in a rare gas [8, 9]. In a more recent technique, high-spin aggregates are obtained by doping a supersonic beam of large helium droplets with alkali atoms [10–13]. In our group, by depositing alkali atoms on rare gas clusters of argon or helium, we have observed the formation of cold trimers in doublet [14] and quartet [15] states, and recorded many of their laser-induced-fluorescence (LIF) electronic excitation spectra.

In this chapter we focus on the spectroscopic properties, and underlying level structure, of the alkali trimers from a theoretical point of view. These objects are small enough to be calculated with standard techniques of highly correlated quantum chemistry; their electronically excited states provide, depending on their spin multiplicity, benchmark systems for a basic understanding of metallic cluster spectroscopy, or for the spectroscopy of van der Waals-type species.

Available theoretical data on alkali trimers are generally scarce. Ab initio calculations were performed mostly for the doublet state: Li_3 [16, 17], Na_3 [17–20], K_3 [17]; fewer calculations exist for quartet states altogether [11, 12, 21–23]. Cocchini et al. [19] rationalize the level structure of the first few electronically excited states of doublet Na_3 in terms of a shell model which we have adapted to the doublet system of K_3 [24]. These calculations helped also with the assignment of experimental spectra of potassium-doped argon clusters [14]. Upon observation of new high-spin alkali trimers ($K_xRb_{3-x}, x = 0, 1, 2, 3$) on superfluid helium nanodroplets our group has worked to extend ab initio calculations to the quartet systems. In Ref. [15] we reported the measurement and calculation-backed assignment of LIF spectra of K_xRb_{3-x}, and we suggested a new shell model description, based on the interpretation of the ab initio results, in terms of harmonic oscillator (HO) eigenstates in a quantum-dot-like confining potential. A detailed discussion of this model can be found in Sect. 3.2.

The first part of this work is dedicated to the computational aspects of our ab initio approach. It summarizes the work we published so far, then presents its extensions and refinements. We account for the choice of an augmented, uncontracted version of the relativistic small-core ECP basis sets "ECP10MDF" and "ECP28MDF" of the Stuttgart/Köln group. With these basis sets we optimize the geometries of all possible homo- and heteronuclear quartet trimers of K and Rb, and calculate the first few electronically excited states at the CASSCF (Complete Active Space Self Consistent Field)/CASPT2 (CAS-Perturbation Theory of second order). The obtained level patterns are then compared with the structures of doublet K_3 [24] and Rb_3 [25].

In Sect. 3, we introduce different shell models to rationalize the calculated level structures. We first look at the doublet states of the trimers in the picture of atomic-like eigenenergies, reducing the Coulomb interactions between electrons and atomic nuclei to a single effective potential of spherical symmetry, with its origin at the

center of mass. Secondly, we try to rationalize the level structure of the quartet trimers in terms of HO states of the three valence electrons in a quantum-dot-like confining potential.

2 Computational Details

For all calculations we choose uncontracted and augmented versions of the ECP10MDF (K) and ECP28MDF (Rb) basis sets [26]. We add one diffuse function each of *s, p*, and *d* type to the standard basis sets, using the even-tempered scheme implemented in the MOLPRO program [27], which was used throughout this article.[1] This leads to the basis set schemes $(12s, 12p, 6d, 3f)$ and $(14s, 11p, 6d, 3f, 1g)$ for potassium and rubidium, respectively. No core polarization potentials (CPP) are included.

2.1 Symmetries

The natural symmetry of the problem is that of the equilateral triangle geometry of the homonuclear trimers, D_{3h}, with the high-symmetry axis C_3 perpendicular to the molecular plane. This symmetry is lowered to C_{2v} for the heteronuclear trimers, although the close chemical similarity between K and Rb is such that a description in terms of a slightly distorted D_{3h} symmetry is still appropriate. The above holds for quartet trimers: the ground state of doublet trimers is affected by a significant, and well-known, Jahn–Teller distortion [17, 19, 24, 25] and C_{2v} is the appropriate symmetry; all the extrema of the energy are associated to a symmetric distortion (isosceles triangle), so the isosceles bond length b and apical angle θ suffice to span the geometry space of interest.

For the analysis of small distortions away from equilateral geometry, as related to vibronic coupling, a convenient alternative are the symmetry-adapted internal coordinates Q_s, Q_x, and Q_y (breathing mode, symmetric and fully asymmetric bend mode, respectively), which describe the planar vibrational modes of systems in D_{3h} symmetry. The transformation matrix between classical two-dimensional Cartesian coordinates and symmetry-adapted internal coordinates can be found elsewhere [24]. Since all geometries presented in Table 1 are of C_{2v} symmetry, Q_y is identically zero. For homonuclear quartet ground states Q_x is also zero, in conformity with their equilateral geometry. In Sect. 2.3, which is dedicated to the calculation of electronically excited states, we investigate distortion patterns by scanning over the Q_x coordinate, with Q_s fixed at the value it has at the global-minimum of the energy.

For the analysis of level patterns, it is convenient to neglect the azimuthal modulation present in D_{3h} symmetry and increase the symmetry to cylindrical ($D_{\infty h}$),

[1] The additional exponents are 0.0035 (0.0050) for the *s*-type 0.0014 (0.0031) for the *p*-type and 0.0108 (0.0092) for the *d*-type function of potassium (rubidium).

Table 1 Comparison of doublet K_3 and Rb_3 ground states with the quartet ground states of K_xRb_{x-3}, $x = \{0, \ldots, 3\}$

	K_3		Rb_3		K_2Rb	KRb_2
symmetry	C_{2v}	D_{3h}	C_{2v}	D_{3h}	C_{2v}	C_{2v}
species	$^2B_2$	$^4A_2'$	$^2B_2$	$^4A_2'$	$^4B_2$	$^4B_2$
b (Å)	4.096	5.049	4.387	5.500	5.284	5.263
θ (°)	77.13	60.0	78.90	60.0	57.78	62.30
Q_x (Å)	−0.704	0.000	−0.832	0.000	0.118	−0.122
Q_y (Å)	0.000	0.000	0.000	0.000	0.000	0.000
Q_s (Å)	4.403	5.049	4.743	5.500	5.224	5.323
E (hartree)	−84.899273	−84.87617	−72.146543	−72.127286	−80.626590	−76.376964
ΔE^a (cm^{-1})	6330	1260	5170	939	1160	1060

[a] Formation energy: difference between minimum energy and the sum of the atomic energies calculated at the same level of theory.

around the C_3 axis. This amounts to assuming that shielding effects, and the diffuseness of the valence electrons, smooth out the influence of the strong Coulomb singularities in the vicinity of each atomic core. In both symmetries, the most important symmetry element in relation to our problem is the reflection by the molecular plane, indicated with $'$ (symmetric) and $''$ (antisymmetric) in D_{3h}; for the corresponding labels in $D_{\infty h}$, as well as the correlation of molecular level labels, see Table 3. In C_{2v}, A_1 and B_2 states are symmetric, A_2 and B_1 antisymmetric. Let us note that internally MOLPRO handles the D_{3h} symmetry as C_{2v}: E states have to be recognized "by hand" as a degenerate pair of A_1, B_2 ($= E'$) and A_2, B_1 ($= E''$).

2.2 Geometry Optimizations

We optimize all trimer geometries at the coupled cluster (CC) level of theory, employing for the doublet a partially spin-restricted single-reference open-shell variant with single and double excitations plus perturbative triples [RHF-RCCSD(T)], and for the quartet a spin-unrestricted variant [28, 29]. The geometry of doublet K_3 has been published in Ref. [24], and a detailed discussion of ground state Rb_3 will be published separately [25]. Results are listed in Table 1.

For the doublet ground states the CR-CCSD(T) method may give better results [30, 31]. As stated in Ref. [30], a noniterative single-reference CC aproach like CCSD(T) fails to describe quasidegenerate states, when the restricted Hartree–Fock configuration is used as a reference. Let us note, however, that the CCSD(T) energy difference between the 1^2A_1 and the 1^2B_2 states at equilateral geometry is already less than 6 cm^{-1}.

The quartet geometries deviate a little from the ones we published in Ref. [15], since in the present improved calculations no shells were kept frozen.

We see from Table 1 that only the quartet ground states are of equilateral geometry (the homonuclear exactly, the heteronuclear very nearly); in the low-spin case we recognize the above-mentioned Jahn–Teller distortion. As expected, bond lengths increase slightly with increasing atomic radius, and formation energies essentially

reflect the change of bond type from covalent (bond order 1.5) to van der Waals (bond order 0) when going from doublet to quartet.

The formation energies are of special interest for the helium-nanodroplet community: Alkali atoms, which are unique in that they are the only species remaining on the surface of the helium droplets [32], attract each other and form covalent or van der Waals-bond clusters depending on their, presumably random, relative spin orientation. The formation energies have to be dissipated by the helium nanodroplet. Hence, nanodroplet isolation spectroscopy is spin-selective: The dissipation of covalently bound trimers usually destroys the nanodroplet (binding energy per He atom is about $5\,\mathrm{cm}^{-1}$ [33]) or leads to the ejection of the dopant. In any case, the low-spin alkali clusters are lost for further experimental investigations. We can say that thermodynamic stability has the opposite effect as in all other production methods mentioned above. For this reason a variety of electronic transitions of high-spin alkali dimers and trimers to date have been measured exclusively on He nanodroplets [10–13].

2.3 Excited States

We now review a selected area of the ab initio potential energy surfaces of electronically excited states, to have a better insight into the level structure, in particular regarding degeneracy and its lifting upon geometric distortions. The shell models we introduce in Sects. 3.1 and 3.2 seek to rationalize this structure in terms of general symmetry arguments. The models are at the moment restricted to the global minimum geometries of the trimers, but we count on being able, with suitable parametrization, to correctly reproduce the patterns observed in the ab initio calculations upon slight distortions away from equilibrium.

First we apply the CASSCF method of Werner and Knowles [34–37] to scan over the first few electronically excited quartet states as functions of the Q_x coordinate. To improve the quality of the state-averaged wavefunctions we run separate calculations for states of opposite symmetry with respect to reflection by the molecular plane. The active space size varies with symmetry and species between 16 and 24 molecular orbitals (MOs), three of them singly occupied by the atomic valence electrons ($4s^1$ for K_3, $5s^1$ for Rb_3). According to the internal orbital ordering for the C_{2v} point group in MOLPRO ($A_1/B_1/B_2/A_2$), the occupation scheme for the $^4B_2$ (A_2' at $Q_x = 0$) ground states was 5/2/4/1 for the doubly occupied MOs and 2/0/1/0 for the singly occupied MOs. Doubly occupied MOs are fully optimized but do not form part of the active space. For all trimer species, the state-averaged CASSCF wavefunctions comprise up to 260 configuration state functions (CSFs) of A_1/B_2 and up to 506 CSFs of A_2/B_1 symmetry. The larger active space for the latter group of states was necessary to obtain a degenerate $2^4E''$ excited state in the case of Rb_3.

The asymptotic energy level separations, at very large internuclear distances, compare poorly with the well-known atomic values, specifically the 4S-4P level separation of K and the 5S-5P level separation of Rb [38]. In our previous

calculation on the doublet states of K_3 [14] we applied ad hoc shifts to force asymptotic consistency. It is known that these significant deviations are a systematic error due to the finite-sized space in the CASSCF approach, which does not account for dynamic correlation. To overcome this limitation, we further apply a modified version of CASPT2 (Complete Active Space with Second-order Perturbation Theory, developed by Celani and Werner [39], referred to as "RS2C" in MOLPRO), using the CASSCF wavefunctions as references in the RS2C calculation. The subsequent R2SC wavefunctions consist of 3.858 to 4.58×10^6 contracted (181 to 213×10^3 uncontracted) CSFs of A_1/B_2 symmetry. For the A_2/B_1 states 3.50 to 5.48×10^6 contracted (153 to 263×10^3 uncontracted) CSFs are used. The MOs 2/0/1/0, corresponding in K (Rb) to the 3*s* (4*s*) atomic orbitals (AOs), are kept frozen in the RS2C approach. To avoid intruder state problems [40] we apply an energy shift of 0.2 hartree. All reported energies are internally corrected for this shift by MOLPRO. The calculated electronically excited quartet states for all discussed trimer species are printed in Fig. 2. For the sake of comparison we also provide the doublet states of K_3 and Rb_3 obtained from earlier calculations [24, 25] in Fig. 1.

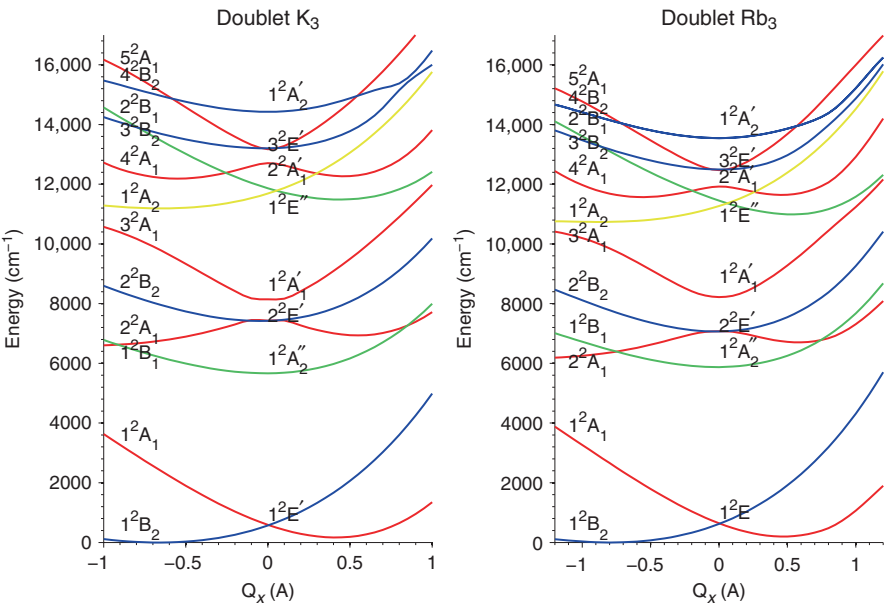

Fig. 1 Potential energy curves for the doublet states of K_3 and Rb_3, scanned along the Q_x coordinate at $\{Q_s, Q_y\} = \{4.40, 0\}$ and $\{4.74, 0\}$, respectively. The curves are labeled according to the C_{2v} point group except at Q_x=0, where D_{3h} applies

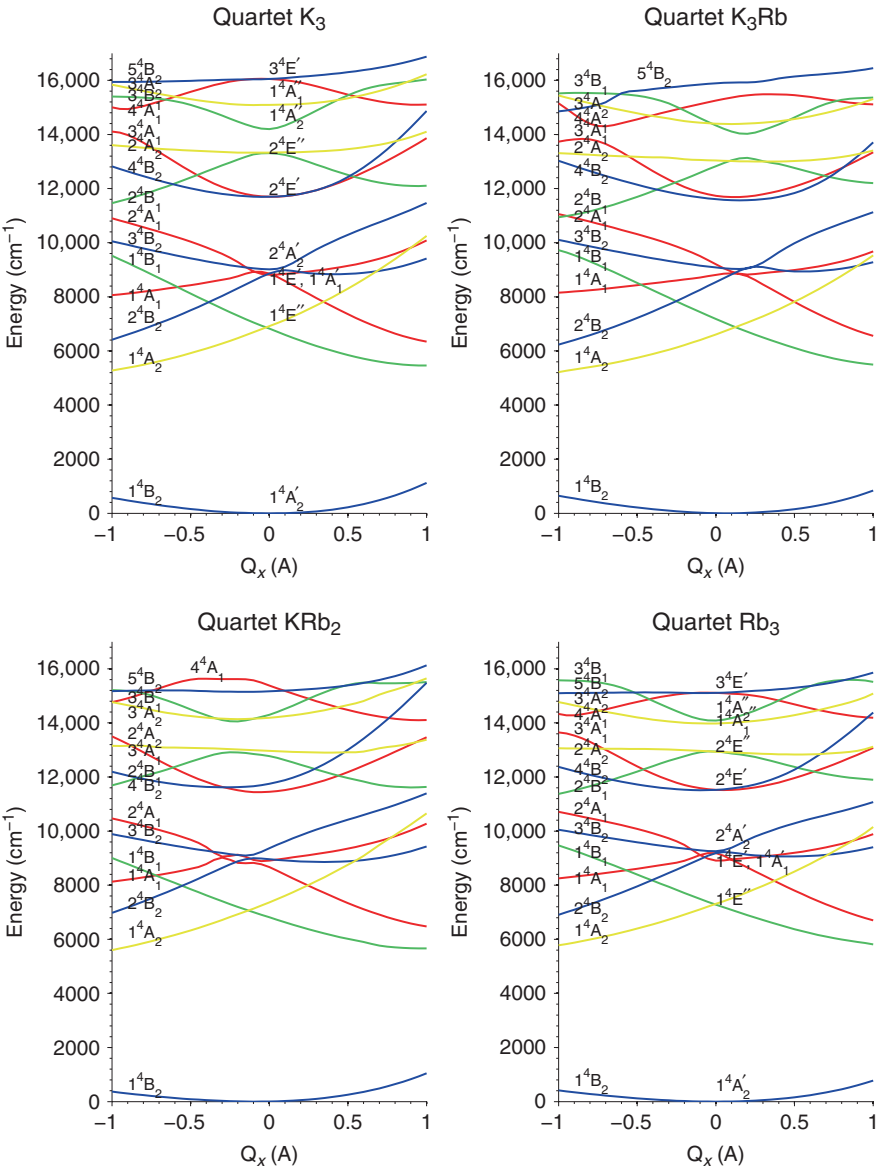

Fig. 2 Potential energy curves for the quartet states of K_3, K_2Rb, KRb_2, and Rb_3, scanned along the Q_x coordinate at $\{Q_x, Q_y\} = \{5.05, 0\}, \{5.22, 0\}, \{5.32, 0\}, \{5.50, 0\}$ respectively. The curves are labeled according to the C_{2v} point group except for the homonuclear trimers at Q_x=0, where D_{3h} applies

3 Shell Models

Shell models are an attempt to capture the fundamental physics of an electronic-structure problem based on simple symmetry arguments. Ideally, electron shells are diffuse over the whole molecule, well separated in energy and with a clearly defined nodal structure. Note that symmetry arguments alone will always correctly predict the presence of degenerate states, and the removal of degeneracy upon lowering of the symmetry (the latter may be due to a true distortion of the molecule but also to a mere refinement of the model). To correctly predict the energy ordering, however, one has to make in addition a reasonable guess of the mean field potential experienced by the valence electrons.

In our case, there are essentially three approaches to classifying the ab initio level structures. All three are based on singly occupied MOs and differ in the zeroth-order description of the orbitals. The freezing of doubly occupied MOs immediately leads to the picture of single-electron excitations as explanation for the doublet state structures. In the case of quartet states, with valence electrons forbidden to occupy the same orbital, the product of three singly occupied orbitals must be considered.

3.1 A Shell Model for the Doublet States

The first approach, which Herzberg calls the *united atom* limit [41], describes shells in terms of atomic levels. For simple molecules, where the level structure is similar to that of the united atom (e.g., CH_4; united atom: Ne), it makes sense to consider all electrons. In the case of metal clusters, only the valence electrons are considered; the united atom is a fictitious one, and the alternative designation *electron droplet model* is used. One just borrows from the united-atom limit the idea of a single effective potential of spherical symmetry, with its origin at the center of mass, to find atomic-like eigenenergies as functions of two quantum numbers n, l. As a refinement of this zeroth-order approach, to better describe the doublet states of the alkali trimers, one applies an oblate distortion in the z direction (the C_3 axis of the trimers) that lifts the degeneracy of the quantum number m_l. A detailed study of ellipsoidal distortions in free-electron metal clusters was performed by Clemenger [42] who introduced a modified Nilsson Hamiltonian with parameters U, δ. To a certain extent this distortion mimics the planar geometry: electronic eigenfunctions with significant extension out of the molecular plane experience a significant rise of their energy. Cocchini *et al.* successfully applied this method to the doublet states of Na_3 [19], and we did the same for the doublet states of K_3 [24].

In Fig. 3 the obtained shell model energies are compared with the K_3 doublet state structure of Fig. 1 at equilateral (D_{3h}) and global minimum (C_{2v}) geometry. By adjustment of the two model parameters ($U = 0.04$, $\delta = -0.56$) we match the shell-model states with those of K_3 at equilateral geometry. Further reduction

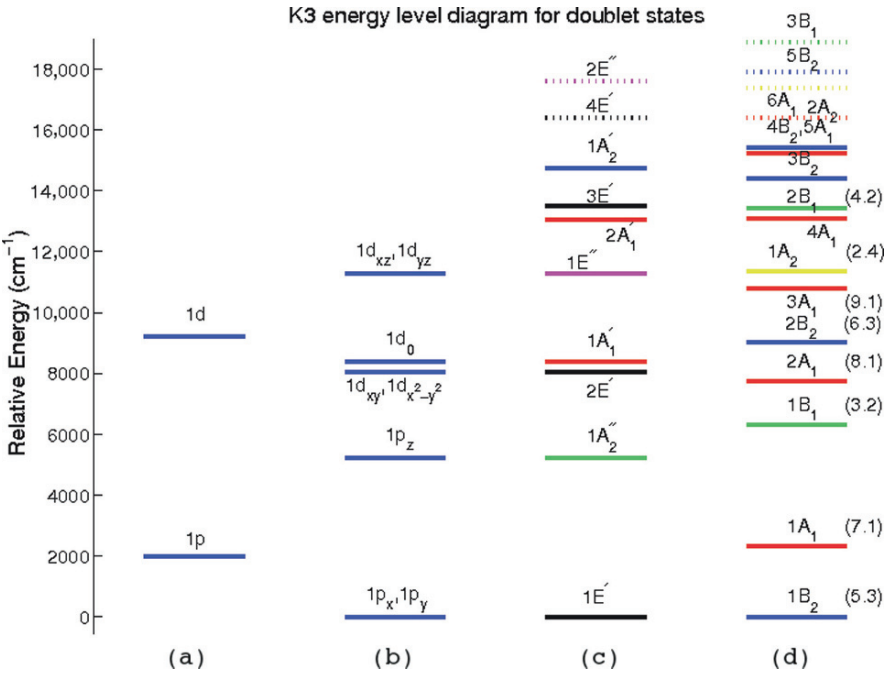

Fig. 3 Correlation diagram showing the progressive lifting of electronic state degeneracies as the applied MO theory becomes more sophisticated. From left to right: (**a**) spherical symmetric shell model, (**b**) oblate distortion added, (**c**) ab initio calculation at equilateral geometry, (**d**) ab initio calculation at the equilibrium geometry for the B_2 ground state.The color code in (d) corresponds to the one used in Fig. 1. The singly occupied MOs, which were assigned to the corresponding state in the shell-model interpretation, are given in brackets. The labeling $(x.y)$ means xth orbital of symmetry y, with respect to the internal symmetry order of MOLPRO for the point group C_{2v} ($A_1/B_1/B_2/A_2$)

of the molecular symmetry from D_{3h} to C_{2v} finally lifts the degeneracy in the xy plane.

In Ref. [24] we gave arguments for the applicability of this choice of a shell model for the doublet states. Here we explain why it is poorly suited to describe the quartet states structure.

The following conditions must be satisfied for this shell model to be applicable to trimers:

1. The MOs are strongly delocalized. Their spatial part is well described by functions with origin at the center of mass.
2. The observed electronically excited states are single-electron excitations without strong mixing, i.e., the CI-expansion of each state is predominantly composed of a singly excited determinant.
3. All MOs are doubly occupied, except for one. The latter is singly occupied and determines the state energy and the symmetry of the corresponding electronic wavefunction.

For the quartet system, however, condition 3 is no longer valid: the Pauli exclusion principle dictates that the three valence electrons occupy three distinct orbitals, all of which must be considered for a proper description of the excited states.

3.2 A Shell Model for the Quartet States

In contrast to the shell model for the doublet system, a description of the quartet level structure requires a more complex multi-electron picture. Nevertheless, the observed level structure, in particular the existence of quadruply degenerate states (pairs of E') can be clarified in terms of singly occupied MOs for the three valence electrons. To gain insight, we look at two simplifications: first we assume the correct D_{3h} symmetry for the quartet trimer, but we only consider a minimum-sized set of AOs. We then map these orbitals, according to their nodal structure, onto the solutions of a problem with cylindrical symmetry around the C_3 axis: this is the same symmetry as the oblate spheroid model, but we do not use atomic states for classification. The advantage of cylindrical symmetry is that orbitals can be classified in terms of the angular momentum projection along the C_3 axis, so that their mutual interaction, or lack thereof, and the reason for their degeneracy are easily recognized. At last we deduce their energy ordering by mapping them onto the canonical orbitals of the ab initio calculation, and we look for a cylindrically symmetric potential reproducing this energy ordering. This leads rather naturally to the HO model.

Let us then start with D_{3h} symmetry: we look at the possible ways of distributing the three valence electrons within the twelve MOs formed by linear combination of the atomic orbitals (LCAO) s_i, p_i^x, p_i^y, p_i^z ($i = 1 \ldots 3$ is an index for the three atoms). Following Herzberg, the x and y axes are local, i.e., on each atom the x axis coincides with the C_2 axis going through the atom, and the y axis is perpendicular to it. In a more general notation we denote AOs as ϕ_i. For each of the above choices of ϕ there are one symmetric combination $\phi_1 + \phi_2 + \phi_3$ and two degenerate anti-symmetric combinations ($2\phi_1 - \phi_2 - \phi_3$ and $\phi_2 - \phi_3$). The respective symmetries of these combinations are a_2'', e'' for $\phi = p^z$; a_1', e' for $\phi = \{s, p^x\}$; a_2', e' for $\phi = p^y$. It is convenient to already think of these LCAOs as having cylindrical symmetry and label them with a triplet of integers (n, ℓ, n_z) counting the nodes in the in-plane-radial, azimuthal, and out-of plane direction; if a $\pm$ sign is added to indicate the double degeneracy of orbitals with azimuthal nodes, ℓ will be the projection of the electronic angular momentum for the HO orbitals. The three LCAOs from $\phi = s$ are those occupied in the ground quartet state, which has then the symmetry of the product $a_1' e'^2 = A_2'$ ground state; they correspond to the $(0, 0, 0)$ and $(0, \pm 1, 0)$ orbitals. The excited states are formed by promoting one of the e' electrons. The p^z generate the $(0, 0, 1)$ and $(0, \pm 1, 1)$ orbitals which are responsible for the doubly primed molecular states ($a_1' e' a_2'' = E''$; $a_1' e' e'' = A_1'' + A_2'' + E''$); a_1' and a_2' orbitals give each an isolated E' molecular level; an e' orbital gives a set of $A_1' + A_2' + E'$. From inspection of the ab initio orbitals, the lowest E' state comes from the a_1' orbital $(1, 0, 0)$; the pair of $A_1' + A_2'$ along with the higher E' derives from the e' orbital $(0, \pm 2, 0)$; higher states are a mix of more than one configuration.

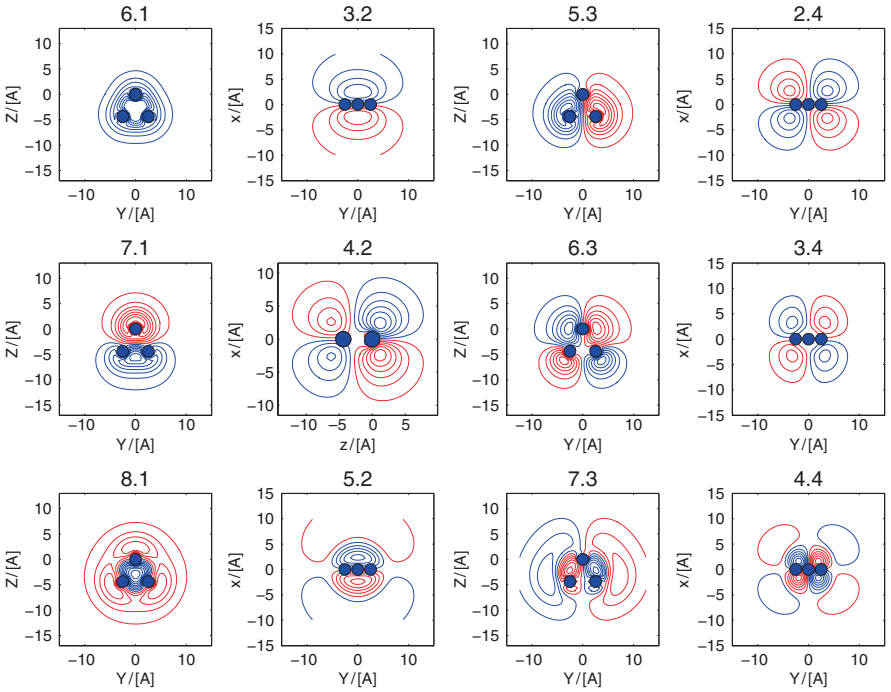

Fig. 4 Contour plots of the canonical orbitals of K_3 obtained at the CASSCF level of theory. The labeling $x.y$ means xth orbital of symmetry y, with respect to the internal symmetry order of MOLPRO for the point group C_{2v} ($A_1/B_1/B_2/A_2$). *Red* lines show positive, *blue* lines negative amplitudes. The strongly delocalized MOs are clearly resembling harmonic oscillator eigenfunctions

We conclude that a minimal basis set is sufficient to capture the quartet orbital structure; we cannot yet say something about level energies. As an alternative to the full ab initio calculations of Sect. 2, we introduce a new shell model description which is based on two observations we made for the quartet systems.

Firstly, the canonical MOs we calculate at the CASSCF level, are still delocalized. As can be seen from the contour plots of the canonical orbitals in Fig. 4, the MOs closely resemble HO eigenfunctions. This is a well-known feature of single-particle states in quantum dots, where the electronic structure is emphasized over the geometric structure [43]. Secondly, the pattern of orbital energies in the quartet system is closer to that of an HO than to that of a fictitious united atom.

We seek to describe the MOs, according to their nodal structure, as a product of two-dimensional HO eigenfunctions (Fock-Darwin orbitals) in the molecular plane times a separate one-dimensional HO eigenfunction for the z-direction (the C_3 axis). This is done to account for the different strength of the potential in-plane and off-plane. The energy of the Fock–Darwin orbitals depends on the quantum numbers (n, ℓ) through the oscillator frequency (here expressed as wavenumber $\tilde{\nu}_\rho$):

$$E = hc\tilde{\nu}_\rho(2n + |\ell| + 1) = hc\tilde{\nu}_\rho(n_\rho + 1) \tag{1}$$

where we have defined a quantum number $n_\rho = 2n+|\ell|$. The energy for an off-plane HO depends on a different frequency, $\tilde{\nu}_z$, and on the associated quantum number n_z:

$$E = hc\tilde{\nu}_z(n_z + 1/2) \tag{2}$$

The easiest way to account for discrepancies between the HO model and the ab initio orbital energies is to include anharmonic terms (x_ρ,x_z) and a cross term ($x_{\rho z}$). The zero of the energy is of no particular significance, so we only consider energy differences measured from the (0, 0, 0) state:

$$\Delta E = hc(n_\rho\tilde{\nu}_\rho + n_z\tilde{\nu}_z - x_\rho n_\rho^2\tilde{\nu}_\rho - x_z n_z^2\tilde{\nu}_z - x_{\rho z}n_\rho n_z\sqrt{\tilde{\nu}_\rho\tilde{\nu}_z}) \tag{3}$$

The energies of the first 13 MOs fit well to this 5-parameter formula. In Table 2 the best-fit parameters and RMS are reported for all four trimer species. Note that for all MOs considered here, n_z only assumes the values 0 or 1, so x_z is redundant and can be set to zero. The rather large value of the cross term tells us that at large orbital energies the distinction between in-plane and out-of-plane oscillator tends to vanish, and a three-dimensional HO model may be more appropriate. Let us note that for higher yet excitation energies, near the ionization limit, the best description will realistically be in terms of Rydberg-atom orbitals.

Let us look at the possible occupation schemes for the set of HO eigenstates. The expected degeneracy at D_{3h} symmetry, and the symmetry of the molecular levels are made particularly obvious by the azimuthal quantum number ℓ. The useful relationships between the HO quantum numbers and the orbital symmetry are summarized in Table 3. For the sake of completeness we also provide the labels in the united atom picture, the LCAO approach and the corresponding molecular levels of Fig. 2.

As already stated, in a high-spin configuration, each orbital can accommodate only one of the three electrons; the ground state corresponds to occupied (0, 0, 0) orbital and (0, ±1, 0) orbital pair (symmetry $\sigma_g^+\pi_u\pi_u = \Sigma_g^-$, correlating to $a_1'e'e' = A_2'$).

As the ground state corresponds to a complete $|\ell| = 1$ shell, we infer that the trimers should be a magic number for planar geometries: Unless the internuclear separation changes strongly upon adding a further atom, we should reasonably

Table 2 Parameters obtained from fits of Eq. (3) to the calculated orbital energies

	$\tilde{\nu}_\rho$	$\tilde{\nu}_z$	x_ρ	x_z	$x_{\rho z}$	res. rms
	(cm^{-1})	(cm^{-1})				(cm^{-1})
K_3	14,963	19,589	0.1237	0	0.3571	930
K_2Rb	14,269	18,747	0.1201	0	0.3353	1100
KRb_2	13,975	18,104	0.1161	0	0.2963	1210
Rb_3	13,312	17,329	0.1136	0	0.2754	1070

Table 3 Orbital labels in the united atom model, LCAO model and harmonic oscillator model (n, ℓ, n_z). The ground state configuration is $a_1' e' e'$ $(\sigma_g^+ \pi_u \pi_u)$, corresponding to the A_2' (Σ_g^-) molecular level; other molecular levels are calculated assuming promotion of one of the two e' electrons into the tabulated one-electron orbital

Orbitals			Symmetry		Molecular levels	
United atom	LCAO	Harmonic osc.	D_{3h}	$D_{\infty h}$	D_{3h}	$D_{\infty h}$
$1s$	$s_1 + s_2 + s_3$	(0,0,0)	a_1'	σ_g^+	—	—
$2p_x$	$2s_1 - s_2 - s_3$	$(0, \pm 1, 0)$	e'	π_u	A_2'	Σ_g^-
$2p_y$	$s_2 - s_3$					
$2p_z$	$p_1^z + p_2^z + p_3^z$	(0,0,1)	a_2''	σ_u^+	E''	Π_g
$2s$	$p_1^x + p_2^x + p_3^x$	(1,0,0)	a_1'	σ_g^+	E'	Π_u
$3d_{xy}$	$p_2^x - p_3^x$	$(0, \pm 2, 0)$	e'	δ_g	$A_1' + A_2' + E'$	$\Phi_u + \Pi_u$
$3d_{x^2-y^2}$	$2p_1^x - p_2^x - p_3^x$					
$3d_{xz}$	$p_2^z - p_3^z$	$(0, \pm 1, 1)$	e''	π_g	$A_1'' + A_2'' + E''$	$\Sigma_u^\pm + \Delta_u$
$3d_{yz}$	$2p_1^z - p_2^z - p_3^z$					
$4f_{x(x^2-3y^2)}$	$p_1^y + p_2^y + p_3^y$	$(0, \pm 3, 0)$	a_2'	ϕ_u	E'	$\Delta_g + \Gamma_g$
$4f_{y(3x^2-y^2)}$	—		a_1'		E'	
$3p_x$	$p_2^y - p_3^y$	$(1, \pm 1, 0)$	e'	π_u	$A_1' + A_2' + E'$	$\Sigma_g^\pm + \Delta_g$
$3p_y$	$2p_1^y - p_2^y - p_3^y$					

expect that the binding energy per atom of the trimer be larger than that of the planar tetramer.

We note that because of symmetry, few HO orbitals will mix, meaning that a single one should be a decent description of the true MO or, conversely, that a small basis set of HO orbitals should be sufficient for accurate calculations. Let us also note that for the same symmetry reasons, most of the low-lying configurations do not interact with each other, meaning that the level structure should be reasonably reproduced already at the Hartree–Fock level. Although we have not tried yet, it seems reasonable that a parametrized distortion from $D_{\infty h}$ to C_{2v} should be able to capture the level structure at $Q_x \neq 0$ (Fig. 2).

Upon inspection of the CI vectors from the ab initio calculations, we have already noted in the LCAO model that the first three pairs of excited states of $'$ symmetry and the first two pairs of $''$ symmetry are indeed dominated by a single configuration. The $''$ states are better isolated, thus easier to rationalize: the first E'' is obtained by promoting one electron from the degenerate $(0, \pm 1, 0)$ orbital pair to the (0,0,1) orbital ($a_1' e' a_2'' = E''$); the next group of 4 states corresponds to promotion to the $(0, \pm 1, 1)$ orbital ($a_1' e' e'' = A_1'' + A_2'' + E''$). The energy order and approximate separation, which was not part of the LCAO model is neatly captured by the HO model. For the $'$ states, the HO model predicts an accidental degeneracy between the orbital pair $(0, \pm 2, 0)$ and $(1, 0, 0)$ orbital. Promotion of one of the $(0, \pm 1, 0)$ electrons into this set of three orbitals should produce a sixfold degeneracy ($2\ \Pi_u$ states, $1\ \Phi_u$ state). Inspection of the CI vectors reveals that the Π_u pair from the $(1, 0, 0)$ orbital remains degenerate with the Φ_u pair, while the Π_u pair from the $(0, \pm 2, 0)$ is shifted to a higher energy.

4 Conclusion

We calculated the optimized ground state geometries of all possible homo- and heteronuclear trimers of K and Rb. The calculation of the first few electronically excited quartet states as a function of the fully symmetric vibrational mode Q_x revealed similar level patterns with a significant structure of degeneracies at D_{3h} symmetry for the homonuclear species. We showed that the classical approach of an atomic-like shell structure provided a sufficient description for the doublet states only. Hence we introduced a new shell model based on HO eigenfunctions in a quantum-dot-like confining potential. The existence of a shell structure shows that despite the larger interatomic distances in quartet states, the valence electrons should be considered as diffuse. Based on the rather close similarities between HO orbitals and high-level ab initio MOs, and on the high symmetry of the model, which restricts the interaction between different configurations, we anticipate that a minimal basis set of these orbitals should have good predictive power, already at a low level of theory (Hartree–Fock). The model is not limited to trimers and should become even more competitive for larger aggregates.

Acknowledgments AWH gratefully acknowledges support from the Graz Advanced School of Science, a cooperation project between TU Graz and the University of Graz. The authors thank Pavel Soldán for helpful discussions on the ab initio calculations. This research is supported by the Austrian Science Fund (FWF, Grant No. P18053-N02).

References

1. H. Haberland (ed.), *Clusters of Atoms and Molecules I*, vol. 52 (Springer Series in Chemical Physics, Berlin, 1993)
2. A.W. Castleman, K.H. Bowen, J. Phys. Chem. **100**, 12911 (1996)
3. W.A. de Heer, Rev. Mod. Phys. **65**, 611 (1993)
4. W.D. Knight, K. Clemenger, W.A. de Heer, W.A. Saunders, Phys. Rev. B **31**(4), 2539 (1985)
5. W.D. Knight, W.A. Saunders, M.Y. Chou, M. Cohen, Phys. Rev. Lett. **52**(24), 2141 (1984)
6. W.A. Saunders, W.A. de Heer, W.D. Knight, Phys. Rev. B **32**(2), 1366 (1985)
7. H.P. Bonzel, A.M. Bradshaw, G. Ertl (eds.), *Physics and Chemistry of Alkali Metal Adsorption* (Elsevier, Amsterdam, 1989)
8. G. Delacrétaz, L. Wöste, Surf. Sci. **156**(2), 770 (1985)
9. W.E. Ernst, S. Rakowsky, Ber. Bunsenges. Phys. Chem. **99**, 441 (1995)
10. J. Higgins, C. Callegari, J. Reho, F. Stienkemeier, W.E. Ernst, M. Gutowski, G. Scoles, J. Phys. Chem. A **102**(26), 4952 (1998)
11. J. Higgins, C. Callegari, J. Reho, F. Stienkemeier, W. E. Ernst, K. K. Lehmann, M. Gutowski, G. Scoles, Science **273**, 629 (1996)
12. J. Higgins, W.E. Ernst, C. Callegari, J. Reho, K.K. Lehmann, G. Scoles, M. Gutowski, Phys. Rev. Lett. **77**(22), 4532 (1996)
13. J.H. Reho, J. Higgins, M. Nooijen, K.K. Lehmann, G. Scoles, M. Gutowski, J. Chem. Phys. **115**, 10265 (2001)
14. J. Nagl, A.W. Hauser, G. Auböck, C. Callegari, W.E. Ernst, J. Phys. Chem. **111**(49), 12386 (2007)

15. J. Nagl, G. Auböck, A.W. Hauser, O. Allard, C. Callegari, W.E. Ernst, Phys. Rev. Lett. **100**(6), 063001 (2008)
16. W.H. Gerber, Theorie des dynamischen Jahn-Teller-Effektes in Li_3 und Untersuchung von Lithium-Molekularstrahlen. Ph.D. thesis, Bern University (1981)
17. J.L. Martins, R. Car, J. Buttet, J. Chem. Phys. **78**(9), 5646 (1983)
18. J. Gaus, Strukturelle und elektronische Eigenschaften kleiner reiner, gemischter und dotierter Alkalimetall-Cluster. Ph.D. thesis, Freie Universität Berlin (1995)
19. F. Cocchini, T.H. Upton, W. Andreoni, J. Chem. Phys. **88**, 6068 (1988)
20. P.H. Zhang, J.M. Li, Phys. Rev. A **54**, 665 (1995)
21. M.T. Cvitaš, P. Soldán, J.M. Hutson, Phys. Rev. Lett. **94**, 33201 (2005)
22. P. Soldán, M.T. Cvitaš, J.M. Hutson, Phys. Rev. A **67**, 054702 (2003)
23. G. Quéméner, P. Honvault, J.M. Launay, P. Soldán, D.E. Potter, J.M. Hutson, Phys. Rev. A **71**, 032722 (2005)
24. A.W. Hauser, C. Callegari, P. Soldán, W.E. Ernst, J. Chem. Phys. **129**, 044307 (2008)
25. A.W. Hauser, C. Callegari, P. Soldán, W.E. Ernst, J. Chem. Phys., submitted (2009)
26. I.S. Lim, P. Schwerdtfeger, B. Metz, H. Stoll, J. Chem. Phys. **122**, 104103 (2005)
27. H.J. Werner, P.J. Knowles, R. Lindh, F.R. Manby, M. Schütz, P. Celani, T. Korona, G. Rauhut, R.D. Amos, A. Bernhardsson, A. Berning, D.L. Cooper, M.J.O. Deegan, A.J. Dobbyn, F. Eckert, C. Hampel, G. Hetzer, A.W. Lloyd, S.J. McNicholas, W. Meyer, M.E. Mura, A. Nicklass, P. Palmieri, R. Pitzer, U. Schumann, H. Stoll, A.J. Stone, R. Tarroni, T. Thorsteinsson. Molpro, version 2006.1, a package of ab initio programs (2006). See http://www.molpro.net
28. J.D. Watts, J. Gauss, R.J. Bartlett, J. Chem. Phys. **98**(11), 8718 (1993)
29. M. Urban, P. Neogrády, I. Hubač, in *Recent Advances in Coupled Cluster Methods*, *Recent Adcances in Computational Chemistry*, vol. 3, ed. by R.J. Bartlett (World Scientific, 1997), pp. 275–306
30. K. Kowalski, P. Piecuch, J. Chem. Phys. **113**(1), 18 (2000)
31. P. Piecuch, K. Kowalski, I.S.O. Pimienta, M.J. McGuire, Int. Rev. Phys. Chem. **21**(4), 527 (2002)
32. F. Stienkemeier, J. Higgins, C. Callegari, S.I. Kanorsky, W.E. Ernst, G. Scoles, Z. Phys. D: At., Mol. Clusters **38**, 253 (1996)
33. V.R. Pandharipande, J.G. Zabolitzky, S.C. Pieper, R.B. Wiringa, U. Helmbrecht, Phys. Rev. Lett. **50**(21), 1676 (1983)
34. H.J. Werner, W. Meyer, J. Chem. Phys. **73**(5), 2342 (1980)
35. H.J. Werner, W. Meyer, J. Chem. Phys. **74**(10), 5794 (1981)
36. H.J. Werner, P.J. Knowles, J. Chem. Phys. **82**(11), 5053 (1985)
37. P.J. Knowles, H.J. Werner, Chem. Phys. Lett. **115**(3), 259 (1985)
38. Ralchenko, Yu., Kramida, A.E., Reader, J., and NIST ASD Team (2008). NIST Atomic Spectra Database (version 3.1.5), [Online]. Available: http://physics.nist.gov/asd3 [2008, September 12]. National Institute of Standards and Technology, Gaithersburg, MD.
39. P. Celani, H.J. Werner, J. Chem. Phys. **112**, 5546 (2000)
40. B. Roos, K. Andersson, Chem. Phys. Lett. **245**, 215 (1995)
41. G. Herzberg, *Electronic Spectra of Polyatomic Molecules* (Van Nostrand Reinhold Company, New York, 1966)
42. K. Clemenger, Phys. Rev. B **32**(2), 1359 (1985)
43. S.M. Reimann, M. Manninen, Rev. Mod. Phys. **74**(4), 1283 (2002)

Part III
Nanostructures and Complex Systems

Influence of the Level of Protonation on the Geometry and the Electronic Structure of Emeraldine Oligomers

Jasmina Petrova, Julia Romanova, Galia Madjarova, Anela Ivanova, Alia Tadjer, and Natalia Gospodinova

Abstract A number of studies prove the existence of magnetically active states in polyaniline and claim polaronic nature of conductivity, but the molecular structure of polarons and bipolarons with account of the solvent effect has not been exhausted. Alongside with conductivity, the optical and magnetic properties of the polymer related to its practical application could be rationalized by the elucidation of this problem. The purpose of this chapter is the assessment of the degree of protonation on the spatial and electronic structure of hydrated polyaniline oligomers. Neutral and protonated emeraldine octamers are modeled to this end. UHF, UBLYP, and UB3LYP with 6-31G* basis set were employed for optimization of the geometry in aqueous medium (PCM). Various structural parameters: bond lengths, valence, and torsion angles, were analyzed and compared. The distribution of Mulliken and NBO charge density and Mulliken atomic spin density was discussed.

A. Tadjer (✉)
Laboratory of Quantum and Computational Chemistry, Department of Physical Chemistry, Faculty of Chemistry, University of Sofia, 1 J. Bourchier Ave, 1164 Sofia, Bulgaria,
e-mail: tadjer@chem.uni-sofia.bg

J. Petrova
Laboratory of Quantum and Computational Chemistry, Department of Physical Chemistry, Faculty of Chemistry, University of Sofia, 1 J. Bourchier Ave, 1164 Sofia, Bulgaria

J. Romanova
Laboratory of Quantum and Computational Chemistry, Department of Physical Chemistry, Faculty of Chemistry, University of Sofia, 1 J. Bourchier Ave, 1164 Sofia, Bulgaria

G. Madjarova
Laboratory of Quantum and Computational Chemistry, Department of Physical Chemistry, Faculty of Chemistry, University of Sofia, 1 J. Bourchier Ave, 1164 Sofia, Bulgaria

A. Ivanova
Laboratory of Quantum and Computational Chemistry, Department of Physical Chemistry, Faculty of Chemistry, University of Sofia, 1 J. Bourchier Ave, 1164 Sofia, Bulgaria

N. Gospodinova
Laboratoire de Chimie Macromoleculaire, Ecole Nationale Superieure de Chimie de Mulhouse, 3 rue Alfred Werner, 68093 Mulhouse Cedex, France, and Institut de Science des Matériaux de Mulhouse, 15, rue Jean Starcky, BP 2488, 68057 Mulhouse Cedex, France

P. Piecuch et al. (eds.), *Advances in the Theory of Atomic and Molecular Systems*, Progress in Theoretical Chemistry and Physics 20, DOI 10.1007/978-90-481-2985-0_11,

Keywords: Polyaniline (PANI) · Protonation · Solvent effect · Polarons vs. bipolarons · DFT

1 Introduction

In the past two decades polyaniline (PANI) was among the most extensively investigated polymer systems. Nevertheless, the nature of its most attractive electric, optical, magnetic, and mechanical properties is not fully understood yet.

The continued interest toward PANI is due to a combination of sought-after characteristics: thermal stability, solubility and fusibility, chemically controllable conductivity preserved up to 200°C which spans a wide range of magnitudes ($10^{-10}/10^{2}$ S/cm) [1–3], etc. The possibility for wet processing allows the production of PANI-based electro-active dyes, inks, and other adhesives, electrochromic "smart" windows, electro-conducting and antistatic transparent coatings, and fibers of different cross sections and high mechanical robustness [4]. Some uncommon color-related phenomena [5] make PANI applicable in microelectronics and optics [6, 7]. In modern nanotechnology PANI can be implemented in integrated circuits, in the construction of numerous electro-optical devices, e.g., FETs [8, 9] and flexible light-emitting diodes (LEDs) [10, 11], as materials for nonlinear optics, as optical storage medium.

Various spectroscopic techniques: TEM, AFM, UV/vis, and Raman spectra, etc. [12–16] have been used in the study of structure and organization of PANI chains.

A number of spectral studies [1, 2, 17–20] demonstrate the presence of magnetically active states in protonated emeraldine [21–24]. However, the ground state structure-multiplicity correlation is not clarified yet. Protonated emeraldine may contain polaronic and bipolaronic domains. Some authors believe that in shorter ES oligomers spins pair and no polaronic form is feasible therein [25]. Other publications [26, 27] relate PANI conductivity to the polaronic form. The occurrence of the latter has been confirmed by in situ electron spin resonance (ESR) [17, 18]. It has been demonstrated that the fully protonated ES octamers may exist in ground states of different multiplicities [28, 29].

In the recent years the number of theoretical investigations on conjugated polymers in general [30], and specifically on PANI, employing ab initio/DFT quantum chemistry methods grows steadily. These studies consider mainly structural and electronic characteristics quantified by means of different functionals and/or basis sets [24, 31–33]. PBE/6-31G* has been used to assess the electronic structure of PANI oligomers (4–16 monomer units) in the presence of inorganic (HCl) and organic (HCSA) doping agents [34]. Neutral and protonated emeraldine chains modeled with a tetramer repeating block (consisting of one quinoid and three aromatic rings) have been calculated. It has been shown that protonation softens the bond alternation and enhances coplanarity of conjugated rings, the changes being most

prominent in the vicinity of the protonated nitrogens. It has been demonstrated that structural changes in a single chain are insensitive to the size and type of doping agent. The role of hydrogen-bond formation in the interaction between PANI and the doping acid has been discussed. Tighter coupling between PANI and the organic dopant has been established, where the H-bonding provides an avenue for charge transfer between oligomer and organic dopant, thus increasing conductivity. The formation of polaronic (magnetically active) and bipolaronic (nonmagnetic) states upon protonation has been addressed and stronger π-conjugation has been established in the former state. However, the PBE functional has been reported [35, 36] to be inappropriate for description of magnetic properties in organic conjugated systems.

To our knowledge, direct correlation between electron structure and macroscopic features of PANI has not been derived. PANI properties are sensitive to both bond length alternation and degree of deplanarization. The latter is represented by the torsion angles, which are important characteristics of the polymer chain, influencing its optical spectrum. This structural descriptor is related to the π-delocalization in the system, responsible for charge mobility along the chains. Environment (comprising solvent, monomer excess, oxidizing and protonating agents, neighboring polymer chains) also has an impact on PANI geometry.

The effects of solvent, counterions, aggregation, and monomer excess on the structure, energetics, optical and vibrational spectra of PANI tetramers in different oxidation states and protonation degree were estimated earlier [37]. Monte Carlo/molecular mechanics protocol was used for sampling of single and stacked hydrated structures of different multiplicity. Averaged structural parameters and AM1-calculated electron spectra were comprehensively summarized. RHF/6-31G* and B3LYP/6-31G* vibrational (Raman) spectra of isolated partially and fully protonated PANI tetramers in vacuum were simulated. The simulations reproduced well the experimental spectra and proved the existence of more than one spin states both in water and in film [37].

The clarification of electron density distribution is of prime importance and requires further detailed analysis. The high/low-spin energy splitting was estimated semiempirically to be of the order of 10^{-2} eV [37]. Such negligible difference in the energy implies the possibility of coexistence of spin states. This hypothesis calls for calculations at the higher first-principles (UHF and DFT) level of theory aiming at validation of the semiempirical findings, which is the goal of the present communication. Special attention is paid to the structural study of emeraldine base (EB) octamers and their partly (doubly) protonated forms.

2 Computational Details

Octamers of PANI in the emeraldine oxidation state were chosen as models for this study as their length is sufficient to allow simulation of both polaronic and bipolaronic forms. In addition, the size of the octamers permits extensive ab initio calculations at reasonable computational cost.

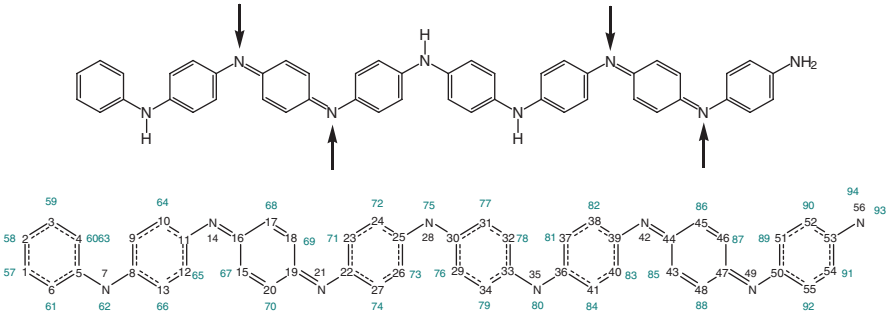

Fig. 1 Chemical formula of the studied emeraldine base octamer (*top panel*) and numbering of the atoms of EB and protonated oligomers (*bottom panel*); arrows indicate the protonation sites; hydrogen atoms designated by green numbers; protons have numbers 95 and 96 and chloride anions – 97 and 98

An emeraldine octamer contains four amine and four imine nitrogen atoms. In principle, the four imine sites are potential candidates for protonation in the emeraldine salt (ES) form of PANI (Fig. 1). However, due to their inequivalent position along the chain – two are in the middle of the octamer and the other pair is closer to the NH_2-end of the molecule (Fig. 1) – the separate imine nitrogens may not be equally prone to protonation.

In line with this, the first stage of the study was geometry optimization of the neutral form of emeraldine – the EB (Fig. 1). In order to test whether different ab initio methods will give dissimilar results with respect to geometry of the molecules and electron density distribution, the following set of methods was employed for the study of the neutral octamers: UHF, UB3LYP, and UBLYP. Preliminary results for protonated emeraldine tetramers (data not shown) indicated that the optimized structure of the molecules is not sensitive to increase of the basis set size above 6-31G*. Therefore, this set of atomic orbitals was used for geometry optimization of all octamers.

The initial molecular models consisted of idealized aromatic and quinoid rings ordered according to the formal chemical formula of the octamer sketched in Fig. 1.

The second topic of study was aimed at elucidating the factors which govern the charge transport in the conducting form of polyaniline (PANI) and consisted of geometry optimization of protonated emeraldine octamers as models of ES. A series of singly protonated (SPE) and doubly protonated (DPE) emeraldine oligomers were considered (Fig. 2).

Calculation of Mulliken and NBO atomic charges for the geometry of EB octamers optimized with UHF, UB3LYP, and UBLYP employing 6-31G* basis set showed (see *Results and Discussion*) that within a certain type of nitrogen atoms (imine or amine), there is no marked asymmetry of the atomic charges related to the position of the atom along the chain. The four imine nitrogens have very similar charges calculated with all methods, all of them being much more negative than the atomic (group) charges on the amine nitrogen atoms. The two wavefunction

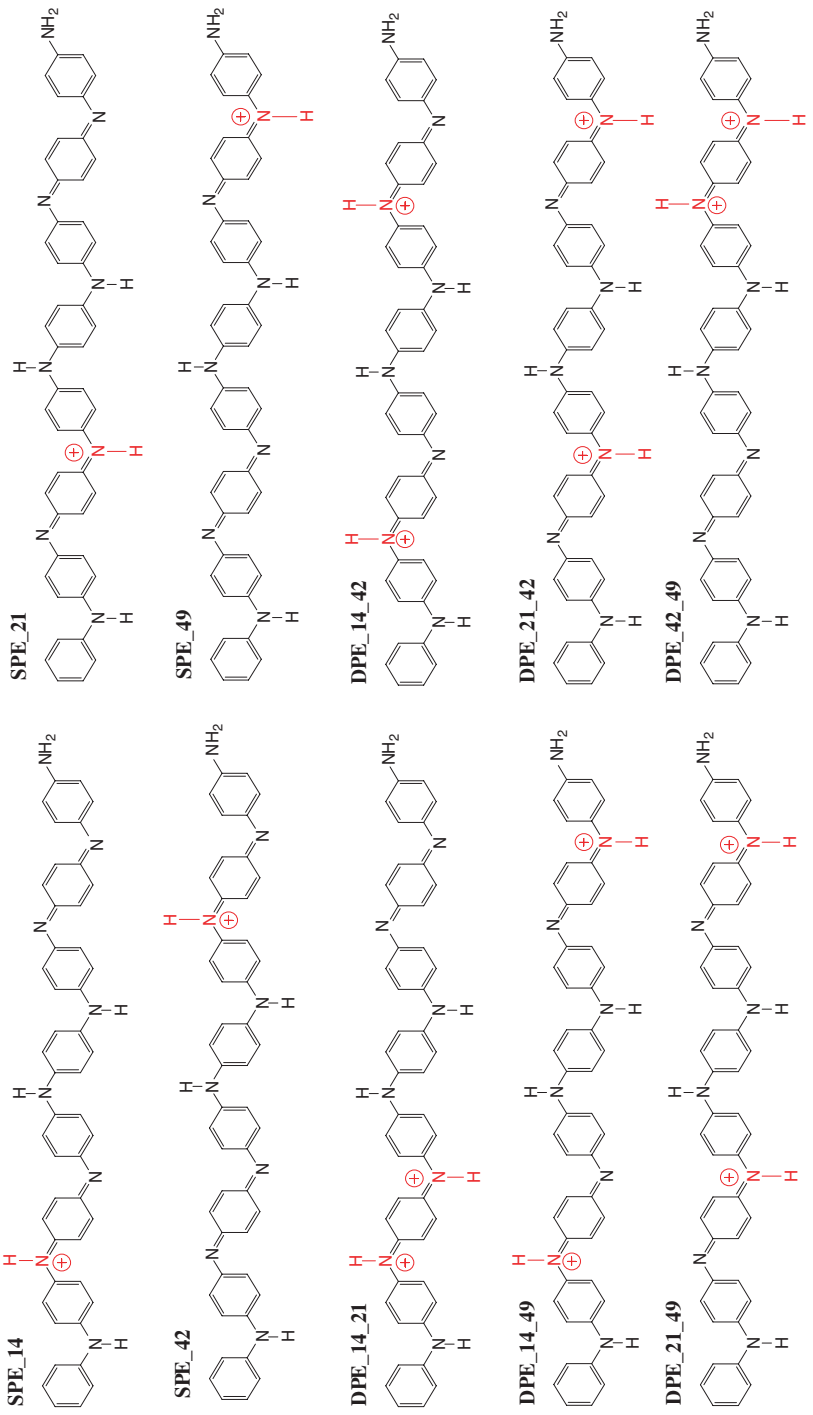

Fig. 2 Chemical formulae of the modeled singly and doubly protonated emeraldine octamers; hydrogen atoms bound to carbons and chloride counterions are omitted for clarity; abbreviated oligomer names used throughout the text are also shown (numbers in the acronyms designate the protonated nitrogen atoms in compliance with the atom numbering shown in Fig. 1)

partitioning schemes also yield very similar charges of the four imine nitrogens with all methods. This means that there will be no preferred position for protonation when the emeraldine chain is accessed by a protonic acid. Therefore, all variants of protonated emeraldine octamers were considered. A set of four singly protonated and six doubly protonated molecules was prepared by attaching proton(s) to the respective imine atom(s) of the UBLYP/6-31G* optimized EB octamer. Chloride anions balanced the positive charges. These were chosen since hydrochloric acid is often used as a protonating agent in experimental studies [1, 19]. In our initial structures the chloride counterions were placed at a distance of 3 Å from the proton along the direction of the N—H bond. The chemical formulae of the modeled oligomers are shown in Fig. 2.

UBLYP/6-31G* was used further for geometry optimization of the series of protonated oligomers. The other details of the simulation procedure were preserved as for the study of EB. The unrestricted version of the method was chosen because it allows equal-footed treatment of both the polaronic (magnetic) and the bipolaronic (nonmagnetic) form of the doubly protonated octamers (Fig. 3). An additional merit of the functional is the negligible spin contamination of the wavefunctions for both multiplicities.

In order to simulate bipolaronic or polaronic state of DPE, the respective octamers were optimized assigning unrestricted singlet or triplet multiplicity. All geometry optimizations were carried out with standard PCM solvation [38] (with relative dielectric constant of water equal to 78.39) without explicit treatment of the hydrogen atoms. Both Mulliken and NBO atomic charges of the optimized hydrated (PCM) tetramers were calculated. Whenever atomic charges are discussed, these are always the condensed ones, i.e., with hydrogen atom charges summed up to those of the heavy atoms they are bound to. Group charges of the rings were obtained by summing the atomic charges of the six carbon atoms from the cycle and those of the four (five in the leftmost ring, Fig. 1) hydrogens bound to them. These group charges are a measure of the local electrostatic properties of the separate rings – whether they are partially positive or partially negative. In addition, the Mulliken atomic spin densities were calculated for the triplets. The singlet–triplet energy splitting ($\Delta E_{ST} = E_S - E_T$) was evaluated as a measure of the relative stability of the two different ES forms.

All calculations were done with the program package Gaussian 03 [39].

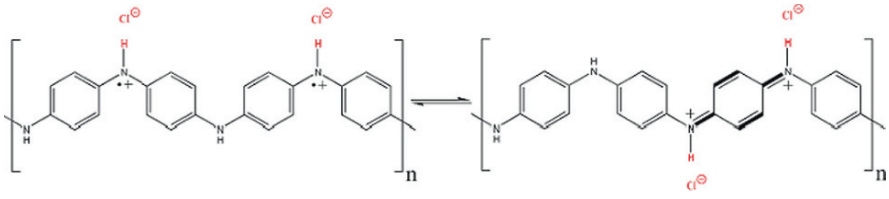

Fig. 3 Polaronic (*left*) and bipolaronic (*right*) states of ES [1, 19]; hydrogen atoms bound to carbons are omitted for clarity

3 Results and Discussion

3.1 Emeraldine Base

One of the most important structural characteristics of the EB octamers is the length of chemical bonds. Some representative examples are shown in Figs. 4, 5, 6, and 7. Average values of the various types of bond lengths are collected in Table 1.

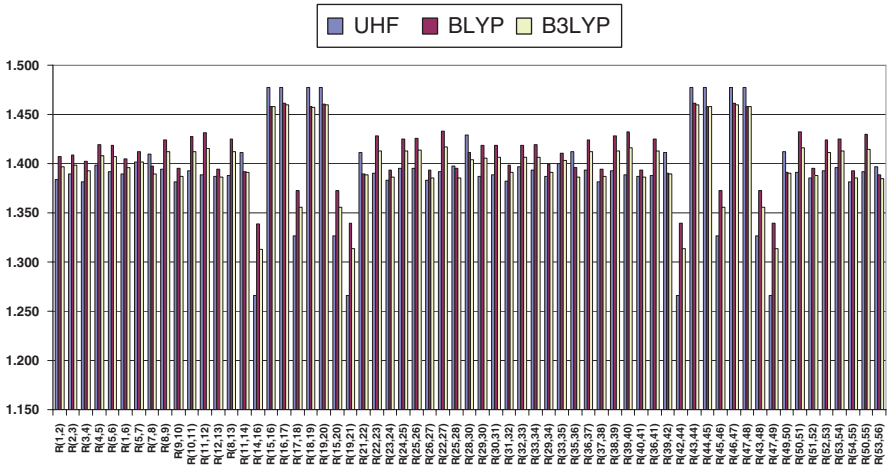

Fig. 4 Optimized C=---=C, C—C, and C—N bond lengths (in Å) of EB in water obtained with UHF/6-31G* (*blue bars*), B3LYP/6-31G* (*yellow bars*), and BLYP/6-31G* (*brown bars*)

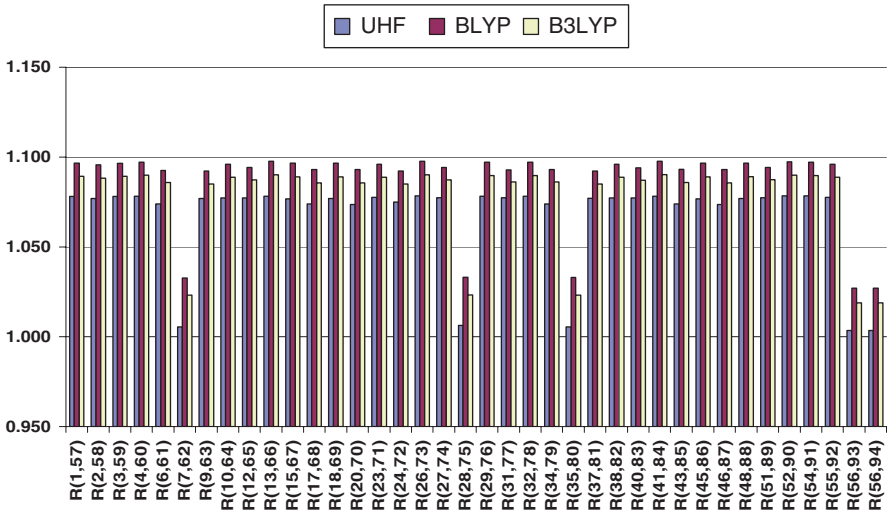

Fig. 5 Optimized C—H and N—H bond lengths (in Å) of EB in water obtained with UHF/6-31G* (*blue bars*), B3LYP/6-31G* (*yellow bars*), and BLYP/6-31G* (*brown bars*)

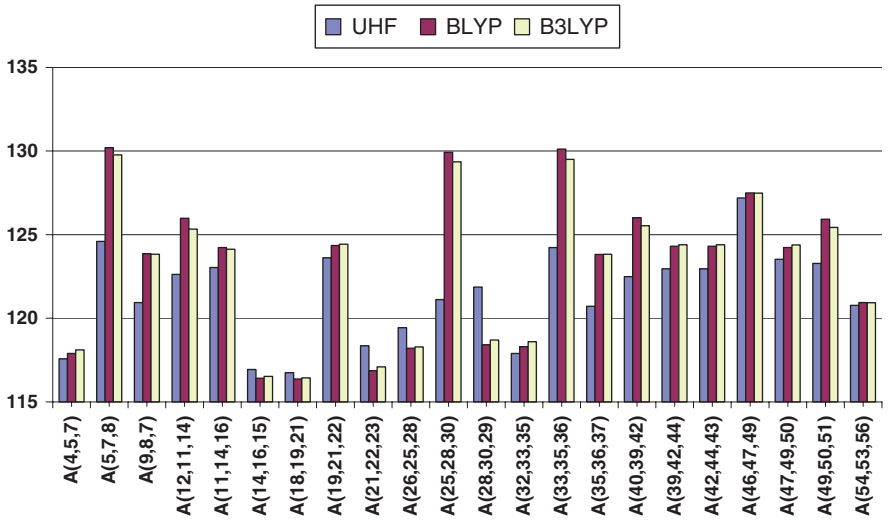

Fig. 6 Optimized C—C—N and C—N—C valence angles (in °) of EB obtained with UHF/6-31G* (*blue bars*), B3LYP/6-31G* (*yellow bars*), and BLYP/6-31G* (*brown bars*) in water

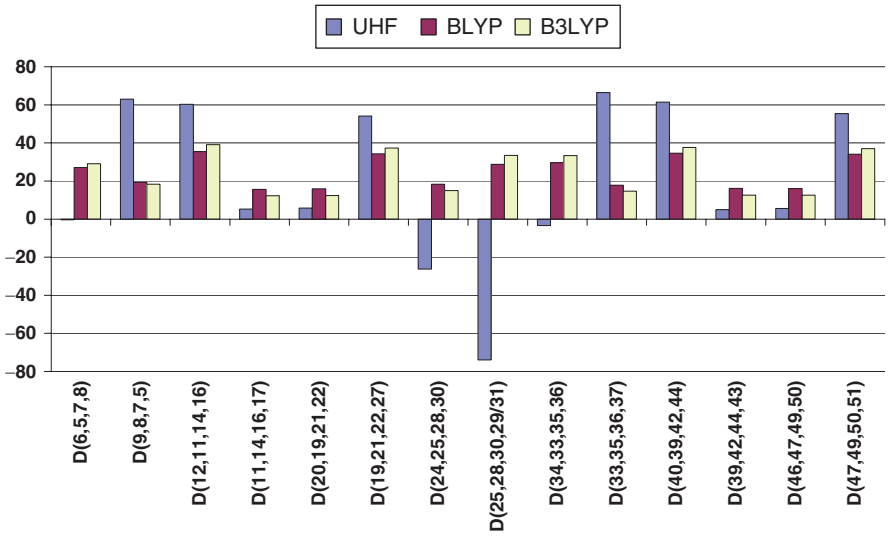

Fig. 7 Optimized C—C—N—C and C—N—C—C torsion angles (in °) of EB in water obtained with UHF/6-31G* (*blue bars*), B3LYP/6-31G* (*yellow bars*) and BLYP/6-31G* (*brown bars*)

The bond lengths of single C—C and double C═C bonds in the EB molecule (Fig. 4) optimized with UHF do not change significantly from their value in the initial model. This corresponds to clear distinction of aromatic and quinoid rings along the octamer chain. No redistribution of electron density between the various bonds is observed.

Table 1 Average values with standard deviations of the optimized bond lengths (in Å), valence and torsion angles (in °) of EB in water obtained with the three theoretical methods

Type	UHF/6-31G*	UB3LYP/6-31G*	UBLYP/6-31G*
Bonds			
C-·-·-C	1.389 ± 0.005	1.403 ± 0.011	1.415 ± 0.014
C—C	1.477 ± 0.000	1.459 ± 0.001	1.459 ± 0.002
C═C	1.327 ± 0.000	1.356 ± 0.000	1.373 ± 0.000
C—N	1.408 ± 0.009	1.392 ± 0.007	1.398 ± 0.009
C═N	1.266 ± 0.000	1.313 ± 0.000	1.339 ± 0.000
C—H	1.077 ± 0.002	1.088 ± 0.002	1.095 ± 0.002
N—H	1.005 ± 0.001	1.021 ± 0.002	1.031 ± 0.003
Valence angles			
C—C—N	120.5 ± 2.0	121.4 ± 3.4	121.5 ± 3.7
C—N—C	123.3 ± 1.9	129.5 ± 0.2	130.1 ± 0.1
C—N═C	123.3 ± 0.3	124.3 ± 0.1	124.3 ± 0.1
N═C—C	122.0 ± 5.9	122.0 ± 6.4	121.9 ± 6.4
Torsion angles			
C—C—N═C	57.8 ± 3.6	37.8 ± 0.9	34.6 ± 0.6
C—N═C—C	5.4 ± 0.4	12.4 ± 0.1	15.9 ± 0.2
C—C—N—C	4.2 ± 53.7	24.0 ± 9.0	23.5 ± 5.6

The results for the carbon–carbon single and double bonds yielded by UBLYP differ considerably from the UHF ones. All bonds in the octamer deviate substantially from the initial model. No aromatic or quinoid rings can be defined in the optimized structure. Significant electron density redistribution takes place through the bond lengths – a process of dearomatization/dequinoidization is observed.

The data obtained with the hybrid B3LYP functional have the expected intermediate values between those of the other two methods. The lengths of all bonds are closer to these given by UBLYP.

The UHF calculated bond lengths of the bonds C—N, C═N, and C—N again do not show any essential variation from the initial values. UBLYP, however, strongly lengthens the C═N bonds and shortens less markedly the C—N ones. A kind of alternation is observed for the bonds of the amine nitrogen atoms – one of them is lengthened by UBLYP while the other one of the same nitrogen center is shortened. This trend is preserved for all amine atoms within the chain.

The propensity of UHF to preserve the initial bond lengths remains almost unchanged, that of UBLYP to lengthen the single bonds and the fact that UB3LYP gives intermediate values are preserved also within the set of hydrogen-containing bonds in EB (Fig. 5).

Concerning the absolute values of these bond lengths, the N—H ones are always shorter than the C—H ones, in line with the relative electronegativity of carbon and nitrogen. The average values are in the normal range for hydrogen atoms bound to sp^2 carbon or nitrogen. All bonds of a given type (C—H or N—H) provided by a certain method are very similar along the octamer chain. This means that their length is insensitive to the type of carbon (quinoid or aromatic) to which hydrogen is bound.

Valence angles are the next structural characteristic of the EB octamers. The values of selected angles optimized with the three theoretical methods are shown in Fig. 6. Only the angles C—C—N and C—N—C are discussed because they are important for the overall dimensions of the oligomer. The remaining valence angles have magnitude close to the standard value of 120° typical for sp^2 hybridization.

The three methods give quite different C—N—C valence angles after geometry optimization. UBLYP yields larger angles compared with UHF. This means that the oligomer chain obtained with UBLYP is more stretched, which implies easier access of solvent molecules and better hydration. Opening the C—N—C angles is also a way to reduce the steric hindrance between the ortho-positioned hydrogens of two adjacent rings.

The largest values of the angles C—N═C are obtained with UB3LYP, intermediate magnitude gives UBLYP, and the smallest angles result from UHF. In contrast, comparable values of the angles C═N—C are produced with the three methods.

Probably the most important structural parameters of PANI are the torsion angles between each pair of adjacent rings. Torsion angles characterize the overall conformation of the molecule. They determine the degree of nonplanarity of the oligomer which is directly related to the extent of electron or spin density (de)localization. The more planar a structure is, the easier the electron delocalization should be. Moreover, planarity facilitates tighter packing and higher crystallinity of the PANI material. Again, only the pairs of torsion angles between the atoms connecting two rings were analyzed and their values are shown in Fig. 7.

UBLYP and UB3LYP give close values for the dihedral angles C—C—N—C and C—N—C—C (ca. 25°). Somewhat larger (ca. 35°) are the torsions C—C═N—C at the two quinoid rings. The angles of a given type have similar values along the entire chain although at the central part of the oligomer there is a tendency toward uniform torsion angles of the two kinds. On the whole, the DFT functionals tend to keep the deplanarization of the molecule as limited as possible. This is combined with the more open valence angles between each pair of rings. Thus, the structure preserves maximum planarity and at the same time the steric repulsion between the closely situated hydrogen atoms is minimized.

On the contrary, UHF produces a significantly deformed geometry of the emeraldine octamer after optimization. A well-expressed alternation of large and small torsion angles along the chain is observed. In the middle of the chain – at torsions D(24,25,28,30) and D(25,28,30,29) – even a change of conformation takes place. This leads to the formation of a kink of the molecule, i.e., in substantial deviation from linearity. Such helical conformations of PANI are known [40], but they are not studied so extensively as the traditional linear models and it is not clear whether they are populated in the conducting ES state of PANI. The highly nonplanar and asymmetric structure given by UHF is apparently due to the neglect of electron correlation. The poor planarity also explains the preserved aromatic-quinoid structure of the molecules. The large dihedral angles ($\sim 60°$) prevent electron delocalization between the rings and thus no dequinoidization of the structure can be observed.

From structural point of view, the pure DFT functional UBLYP seems to provide the most accurate description of the emeraldine oligomers while UHF cannot

reproduce properly the convergence of the ring structure in the emeraldine form. For the latter exist experimental indications too [1, 19].

As a next step, the atomic charges of the nitrogen atoms and the group charges of the rings of the optimized EB octamers were analyzed. The atomic charges of the nitrogen atoms computed with the Mulliken and NBO schemes from the optimized wavefunctions of the three methods are shown in Fig. 8. The corresponding ring group charges are plotted in Fig. 9. The numerical values are provided in Tables 2 and 3, respectively.

The three methods give more negative charges of the imine nitrogen atoms in the octamer than of the amine ones, both with the Mulliken and with the NBO scheme. This difference is large enough (varying from ca. 0.130 a.u. with UHF to ca. 0.230 with UBLYP) to ensure that imine nitrogens will be the only ones protonated, irrespective of the strength of the protonating agent. Within a certain type of nitrogen atoms (imine or amine), there is no marked asymmetry of the atomic charges related to the position of the atom along the chain.

Among the amine sites, only the terminal atom has much higher charge. However, its terminal position attributes a special role to this atom because it is

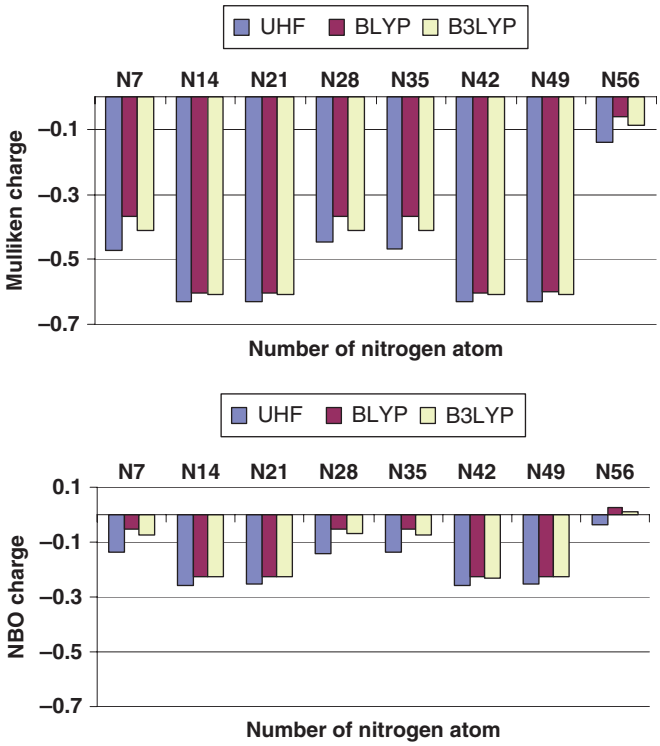

Fig. 8 Mulliken (*top panel*) and NBO (*bottom panel*) condensed atomic charges of the nitrogen atoms of EB in water obtained with UHF/6-31G* (*blue bars*), B3LYP/6-31G* (*yellow bars*) and BLYP/6-31G* (*brown bars*)

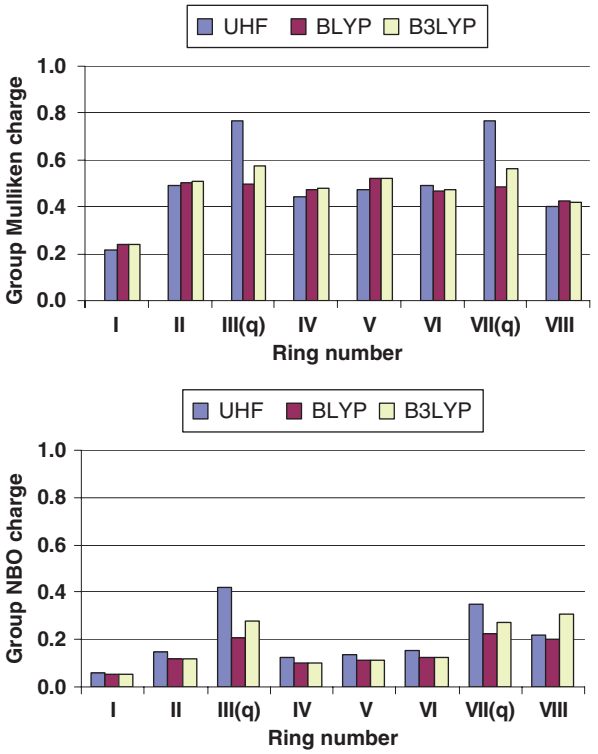

Fig. 9 Mulliken (*top panel*) and NBO (*bottom panel*) group charges of the rings of EB in water obtained with UHF/6-31G* (*blue bars*), B3LYP/6-31G* (*yellow bars*), and BLYP/6-31G* (*brown bars*); rings numbering starts from left to right along the chain of the molecule as shown in Fig. 1. The two quinoid rings have an additional index (q)

responsible for the chain elongation during polymerization. Therefore, it is expected to bear the least negative or even slightly positive atomic charge. Among the three remaining amine nitrogen atoms, only UHF, and solely with the Mulliken scheme, gives some preference in terms of negative charges to atoms N7 and N35. The four imine nitrogens have very similar charges calculated with all methods. The two wavefunction partitioning schemes also yield very similar charges of four imine nitrogens with all three methods. This means that there will be no preferred position for protonation when the emeraldine chain is accessed by the protonic acid.

If one looks at the absolute values, the calculated NBO charges are much smaller than the Mulliken ones for all atoms. The former renders a more realistic representation of the electron density distribution, and Mulliken gives a somewhat overpolarized description of the atomic charges. Nevertheless, the qualitative agreement between the two schemes is very good. The three computational methods yield quite similar charges for a given type of nitrogen atoms.

In order to compensate the partially negative nitrogen sites, all rings carry partial positive charges. Their relative magnitudes differ depending on the theoretical

Table 2 Mulliken and NBO condensed atomic charges of the nitrogen atoms of EB in water obtained with the three theoretical methods

	UHF/6-31G*	UBLYP/6-31G*	UB3LYP/6-31G*
Mulliken			
N_7	−0.472	−0.369	−0.410
N_{14}	−0.632	−0.603	−0.608
N_{21}	−0.629	−0.602	−0.607
N_{28}	−0.446	−0.367	−0.409
N_{35}	−0.470	−0.369	−0.411
N_{42}	−0.631	−0.604	−0.609
N_{49}	−0.628	−0.600	−0.606
N_{56}	−0.141	−0.059	−0.087
NBO			
N_7	−0.136	−0.055	−0.072
N_{14}	−0.260	−0.227	−0.229
N_{21}	−0.253	−0.226	−0.227
N_{28}	−0.144	−0.050	−0.070
N_{35}	−0.136	−0.052	−0.072
N_{42}	−0.260	−0.228	−0.229
N_{49}	−0.253	−0.225	−0.227
N_{56}	−0.039	0.027	0.008

method or partitioning scheme used. Similar to the atomic charges of the nitrogen atoms, NBO gives much smaller excess (half of the Mulliken values) of positive charge on the rings. However, there is again qualitative coincidence with the results of the Mulliken approach. This qualitative picture is as follows: UHF predicts much

Table 3 Mulliken and NBO group charges of the rings of EB in water obtained with the three theoretical methods

	UHF/6-31G*	UBLYP/6-31G*	UB3LYP/6-31G*
Mulliken			
I	0.213	0.239	0.240
II	0.491	0.502	0.511
III(q)	0.766	0.495	0.574
IV	0.444	0.474	0.478
V	0.471	0.521	0.523
VI	0.493	0.464	0.471
VII(q)	0.768	0.488	0.566
VIII	0.402	0.426	0.418
NBO			
I	0.062	0.055	0.054
II	0.147	0.116	0.121
III(q)	0.418	0.205	0.279
IV	0.122	0.103	0.103
V	0.135	0.111	0.111
VI	0.155	0.126	0.126
VII(q)	0.352	0.226	0.275
VIII	0.218	0.202	0.308

higher partial positive charges of the two quinoid rings than those of the aromatic ones. These high positive charges are counterbalanced by lower values of the group charge for the two terminal aromatic rings. On the contrary, the DFT methods predict much more equivalent distribution of the partial positive charges on all rings, which is in line with the more homogeneous structure given by the correlation-accounting approach. This also provides more realistic description of emeraldine.

3.2 Singly and Doubly Protonated Emeraldine Octamers

3.2.1 Singly Protonated Emeraldine Octamers (SPEs)

Among the geometry optimizations of all singly protonated octamers shown in Fig. 2, only that of SPE_42 converged successfully. The remaining calculations encountered severe convergence problems. The difficult convergence may be an indication for instability of oligomers with a single protonated site. A possible reason may be the local structural changes deforming in an unbalanced way the molecule around the protonated nitrogen atom, which may result in an overall geometrical instability. The Gaussian optimization settings may be another source of error, although most of the options were tested without success.

The optimized structure of SPE_42 is shown in Fig. 10.

The specific structural changes of this SPE octamer with respect to the neutral EB can be summarized as follows (Table 4):

On average, all bonds in the singly protonated octamer become longer than in the neutral base. Bond lengths are changed more substantially only in a fragment of the molecule close to the protonation site. As a result rings VI and VIII become more quinoid-like, while ring VII gains in aromatic character. The only pronounced quinoid structure is that of ring III and the only strictly aromatic is ring I. All other cycles are characterized by semi-quinoid/semi-aromatic nature, which is evidenced by the significantly increased standard deviations from the average bond lengths. If one makes two separate averages of the carbon–carbon bonds of rings III–VIII which are below and above 1.4 Å, the respective average values are 1.391 ± 0.006 Å and 1.430 ± 0.009 Å. This is a clear illustration of the uniformity of the structure caused by protonation, which propagates 4–5 rings away from the protonated nitrogen atom. Similar trends but less expressed are observed also for the carbon–nitrogen bonds.

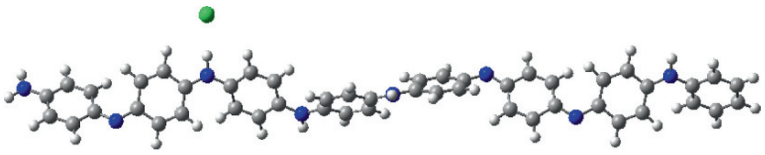

Fig. 10 UBLYP/6-31G*-optimized geometry of the hydrated singly protonated emeraldine octamer SPE_42

Table 4 Average values with standard deviations of the optimized bond lengths (in Å), valence and torsion angles (in °) of EB and SPE_42 octamers in water obtained with UBLYP/6-31G*. The values of EB are repeated for easier reference

Type	EB	SPE_42
Bonds		
C-~~---~~C	1.415 ± 0.014	1.415 ± 0.016
C—C	1.459 ± 0.002	1.451 ± 0.010
C=C	1.373 ± 0.000	1.377 ± 0.005
C—N	1.398 ± 0.009	1.394 ± 0.017
C=N	1.339 ± 0.000	1.352 ± 0.016
C—H	1.095 ± 0.002	1.095 ± 0.002
N—H	1.031 ± 0.003	1.033 ± 0.008
Valence angles		
C—C—N	121.5 ± 3.7	124.1 ± 1.7
C—N—C	130.1 ± 0.1	130.3 ± 0.2
C—N=C	124.3 ± 0.1	126.0 ± 2.7
N=C—C	121.9 ± 6.4	126.6 ± 1.7
Dihedral angles		
C—C—N=C	34.6 ± 0.6	30.8 ± 5.0
C—N=C—C	15.9 ± 0.2	16.8 ± 2.7
C—C—N—C	23.5 ± 5.6	22.8 ± 5.4

The only type of bond which is not affected by protonation is C—H. Their average value increases slightly with respect to EB but the standard deviation remains extremely small. The valence angles increase by up to 5° compared with EB but the standard deviations become almost negligible, which indicates a more rigid structure of the protonated oligomer. The torsion angles decrease slightly, the effect being most prominent in the vicinity of the protonated nitrogen atom. There is asymmetry even in the C—C—N—C angles around a given amine nitrogen atom – one of the dihedrals becomes much larger than the other one. This is in line with the trend toward dearomatization/dequinoidization of the molecule. Thus, the more correct average values of the angles would be 29.3 ± 4.1° for the larger ones and 17.3 ± 2.4° for the smaller ones. The overall change of the angles illustrates a lesser deplanarization of the molecule compared with that of EB.

Concerning the electron density distribution, the charges of the nitrogen atoms are changed locally (Figs. 21, 25) whereas the benzene rings charges are altered along the entire oligomer chain (Figs. 23, 27). The latter is an indication of significant charge transfer through the π-conjugated system.

3.2.2 Geometry of Doubly Protonated Emeraldine Octamers (DPEs)

The geometry optimization of five singlet and of three of the triplet DPE oligomers has converged successfully. The optimized structures of singlet and triplet DPE_21_49 and DPE_14_21 are shown in Figs. 11 and 12, respectively. These two octamers

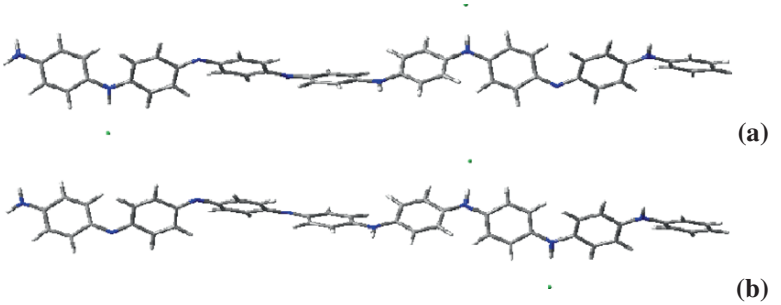

Fig. 11 Illustration of UBLYP/6-31G*-optimized singlet hydrated DPE structures: (**a**) DPE_21_49; (**b**) DPE_14_21

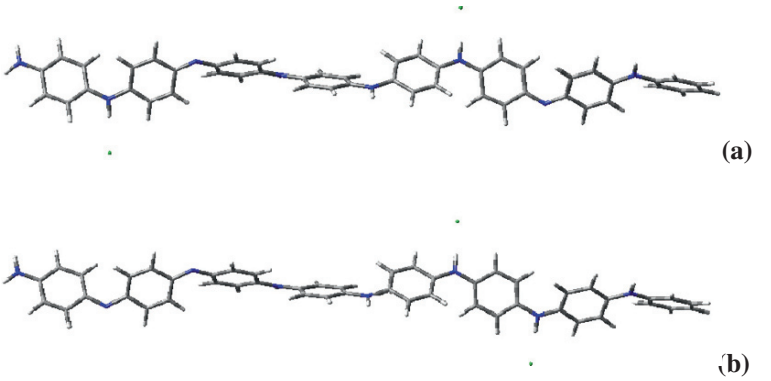

Fig. 12 Illustration of UBLYP/6-31G*-optimized hydrated triplet DPE structures: (**a**) DPE_21_49; (**b**) DPE_14_21

differ in pattern of protonation – in DPE_14_21 two adjacent imine nitrogens are protonated, while in DPE_21_49 two non-neighboring nitrogen atoms bear positive charges.

Overall rod-like shape is observed for all optimized DPE octamers, irrespective of the protonation site. There are no visible conformational differences between the singlet and the triplet state of a given DPE octamer. No significant differences are detected in the bond lengths of the various DPEs. The bond lengths of the $\overset{+}{\text{N}}$—H bonds, together with the distances from a proton to its counterion, are collected in Table 5 for description of the singlet optimized structures. Figures 13, 14, and 15 also contain optimized structural parameters of the singlets.

The $\overset{+}{\text{N}}$—H bond lengths are equal both within a given DPE and for all DPEs. This means that the length of these bonds is insensitive to the location of the protonation sites along the oligomer chain.

The proton–counterion distance changes in a small range between the various DPEs. This distance can serve as a measure of the degree of hydration of the

Table 5 UBLYP/6-31G* $\overset{+}{N}$—H bond lengths and distances between the proton and the Cl^- (in Å) of the singlet DPEs; for numbering see Figs. 1 and 2

	DPE_14_21	DPE_14_42	DPE_21_42	DPE_21_49	DPE_42_49
$\mathbf{R_{N\text{-}H95}}$	1.048	1.048	1.048	1.049	1.049
$\mathbf{R_{N\text{-}H96}}$	1.049	1.048	1.048	1.048	1.049
$\mathbf{R_{H95\text{-}Cl97}}$	2.204	2.209	2.204	2.200	2.194
$\mathbf{R_{H96\text{-}Cl98}}$	2.195	2.199	2.206	2.212	2.193

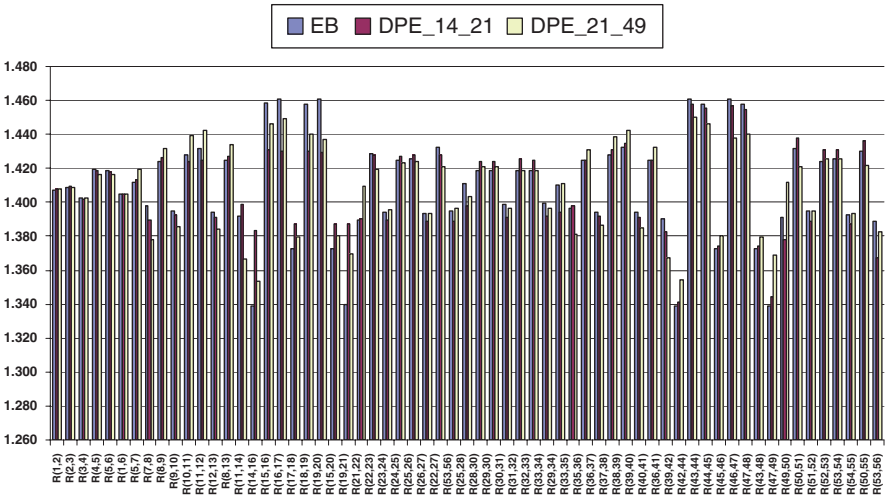

Fig. 13 UBLYP/6-31G*-optimized C—C, C=C, C=N, and C—N bond lengths (in Å) of hydrated EB (*blue bars*), singlet DPE_14_21 (*brown bars*) and singlet DPE_21_49 (*yellow bars*)

molecule. The more detached from the proton the chloride anion, the better hydrated the octamer. DPE_42_49 has its counterions at the closest distance and DPE_21_49 has the farthest anions. In some of the octamers, the two distances within the molecule are non-equal but the variations are insignificant.

Naturally, the most substantial geometrical perturbation of all DPEs can be expected in the vicinity of the protonated nitrogen atoms. The degree of this perturbation is comparable for all DPEs. Therefore, each of the six octamers can be used as representative for comparison with the neutral base. Figure 13 offers a comparison of the length of bonds C—C, C=C, C—N, and C=N of the neutral EB and of two doubly protonated singlet structures – DPE_14_21 (protonation at the same quinoid ring) and DPE_21_49 (protonation at different quinoid rings).

Indeed, the most substantial changes in the structure of the DPEs with respect to the neutral base are observed around the protonated sites. The C=$\overset{+}{N}$ and C—$\overset{+}{N}$ bond lengths of both ES forms are sizably lengthened compared with those of EB. The bond C=$\overset{+}{N}$ containing the protonated N_{21}, which is common for the two structures, is longer for DPE_14_21.

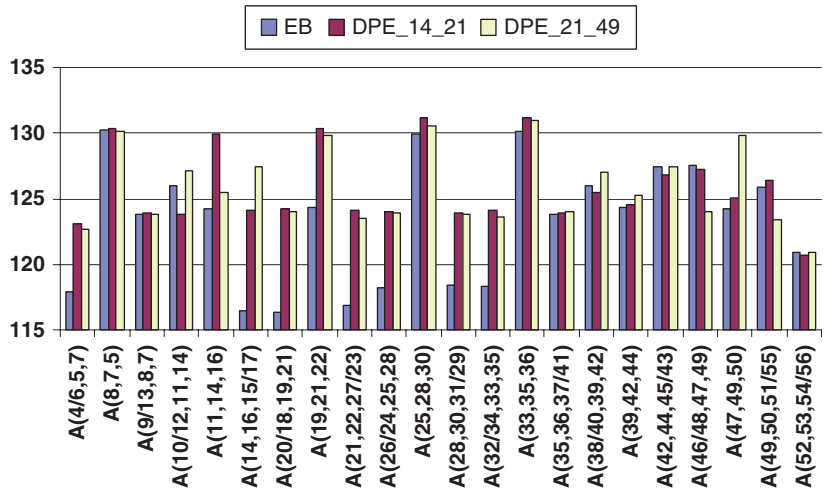

Fig. 14 UBLYP/6-31G*-optimized valence angles (in °) of hydrated EB (*blue bars*), singlet DPE_14_21 (*brown bars*), and singlet DPE_21_49 (*yellow bars*)

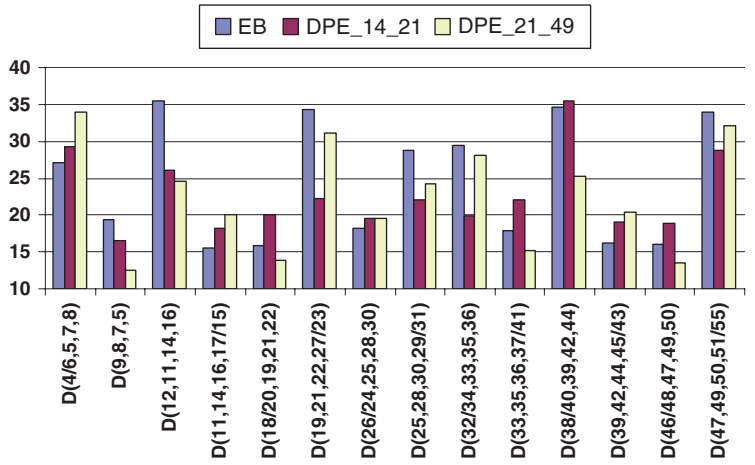

Fig. 15 UBLYP/6-31G*-optimized dihedral angles (in °) of hydrated EB (*blue bars*), singlet DPE_14_21 (*brown bars*), and singlet DPE_21_49 (*yellow bars*)

The lengths of the analyzed bonds for a particular structure around the two protonated atoms are very similar. The respective lengths of $\overset{+}{N}_{14}=C_{16}$ and $C_{19}=\overset{+}{N}_{21}$ of DPE_14_21 are 1.383 and 1.387 Å.

The two bonds C—$\overset{+}{N}$ differ less when the protonation affects imine nitrogen atoms in separate quinoid rings (the structure DPE_21_49).

The asymmetry in the lengths of the bonds C—N at the same amine nitrogen atom found for EB is observed also in the two DPEs. This change is more

noticeable for DPE_21_49. The same bond in DPE_14_21 is slightly stretched. The bonds of the amine N_{28} are the shortest in DPE_14_21. Compared to EB, this region of DPE_14_21 changes most markedly. In DPE_21_49 the bond C_{25}–N_{28} is unchanged in comparison to the neutral base. The bond length of N_{28}–C_{30} has a value between these of the other two structures. The shown asymmetry of the two carbon–nitrogen bonds at the amine nitrogen with N_{35} is retained for EB and DPE_21_49, while in the chain of DPE_14_21 they have very similar values (the difference is 0.004 Å).

Shortening of C—C and lengthening of C═C bonds in the quinoid nuclei relative to neutral emeraldine are observed in all doubly protonated structures. This effect takes place most strongly in DPE_14_21. In this chain C−C are the shortest and C═C are the longest bonds compared with the other two octamers considered. In this respect DPE_21_49 occupies an intermediate position. Of the three structures discussed DPE_21_49 features the major changes in bond lengths in the region of the quinoid nuclei.

In the first aromatic nucleus (from left to right along the chain, Fig. 1) the bonds of both DPEs (Fig. 13) change in the same direction and by the same degree – some of the bonds are lengthened with respect to EB and others are shortened. Their values are almost identical in the chains of the two doubly protonated structures. In the core of the chain the following trend of changes of the C---C bonds of DPE relative to EB is observed – those which are stretched in DPE_14_21 are shortened in DPE_21_49 and vice versa. The longest C---C bonds of all aromatic nuclei of the three structures are those in which one of the carbon atoms is bound to imine nitrogen, protonated or not.

Figure 14 contains the valence angles of EB and the two doubly protonated structures: DPE_14_21 and DPE_21_49.

Valence angles C—N—C of the three structures have very similar values. One of the angles C—C—N of a given amine? nitrogen atom remains unchanged after doping and the other one becomes significantly larger. Compared to EB, that opening of the angle is equal for both DPEs. Exceptions are the two angles at the oligomer core around N_{28}, which are considerably larger in the protonated structures.

The largest values of the angles C—N═C and C—C═N are found in the vicinity of the protonated nitrogen. The angle C_{18}—C_{19}═$\overset{+}{N}_{21}$ has equal values for DPE_14_21 and DPE_21_49, exceeding significantly that of EB. Both doped structures have the same magnitude of C—N═C including the common protonated imine nitrogen. The angles C—C—N= are smaller in the region in which the protonated nitrogen atom is located. An exception is again the angle at N_{21} of the chain – it is opened markedly after protonation and is approximately the same in DPE_14_21 and DPE_21_49.

Figure 15 presents the dihedral angles of EB, DPE_14_21, and DPE_21_49. Again an asymmetric increase/decrease is observed for each pair of C—C—N—C dihedral angles at the same amine atom.

Similarly, around the protonated imine nitrogens one of the dihedrals opens and the other one closes with respect to those of the base (in DPE_21_49 both angles

decrease, but one of them more markedly). Around the common protonated nitrogen atom (N_{21}) the more deformed structure is DPE_21_49. At the non-protonated imine nitrogen in both DPEs (N_{42}), the largest changes are observed in DPE_21_49. These torsion angles remain almost unchanged for DPE_14_21 with respect to the EB. The core of DPE_14_21 is least deformed compared with that of DPE_21_49 and the neutral base.

In all cases the dihedral angles encompassing the protonated nitrogen atoms are smaller than the rest. This increase of planarization is more significant for the region of the nitrogen atom, which is closer to the octamer core. The average degree of deformation of the protonated molecules, however, is very similar and comparable to that of EB. The summed dihedral angles at the protonated nitrogens decrease slightly compared with that of the neutral oligomer. The same angles involving the non-protonated imine nitrogens, however, increase by approximately the same value.

While the quinoid rings adjacent to the protonated imines are aromatized, the aromatic rings are affected in correspondence with the size of the dihedrals: the one on the side of the larger torsion increases its aromatic character, whereas the one on the side of the smaller torsion features deteriorated bond delocalization. In general, the carbon–carbon bonds remain almost unchanged compared with EB, especially the ones at the core of the oligomer. The combination of all effects corresponds to overall structural equalization of the protonated molecules.

Similar to the optimized singlet structures, the triplets do not feature substantial variation of a given type of bond length as a function of the location along the chains. The respective $\overset{+}{N}$—H bond lengths and the proton–counterion distances are summarized in Table 6.

The $\overset{+}{N}$—H bond lengths have very similar (yet lower than in the singlets) values both within one triplet octamer and in the various DPEs. Nevertheless, the differences are a bit larger than in the singlet molecules (Table 7). The trend for insensitivity of these bond lengths toward the location of the protonated nitrogen along the chain is preserved. In the triplets, however, the asymmetry of the proton–counterion distances within a given DPE is observed in all three structures. The two distances vary by ca. 0.02–0.03 Å, the distance of the protonated site closer to the oligomer core being always the larger. All optimized distances are greater than the corresponding ones of the singlet molecules, which is an indication that the triplets are more prone to hydration.

Table 6 UBLYP/6-31G* $\overset{+}{N}$—H bond lengths and proton–Cl^- distances (in Å) of the optimized hydrated triplet oligomers; for atom numbering refer to Fig. 1

	DPE_14_21	DPE_21_49	DPE_42_49
$\mathbf{R_{N\text{-}H95}}$	1.046	1.045	1.043
$\mathbf{R_{N\text{-}H96}}$	1.043	1.047	1.046
$\mathbf{R_{H95\text{-}Cl97}}$	2.228	2.235	2.241
$\mathbf{R_{H96\text{-}Cl98}}$	2.244	2.207	2.218

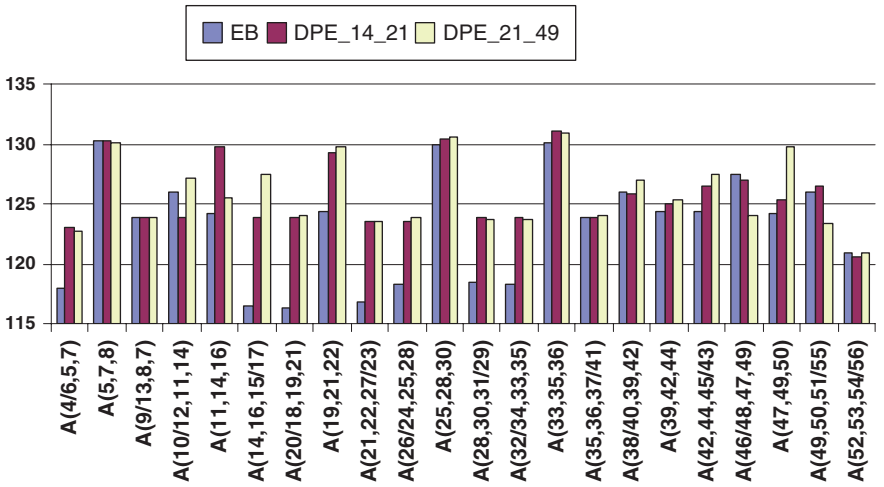

Fig. 16 UBLYP/6-31G*-optimized valence angles (in °) of hydrated EB (*blue bars*), triplet DPE_14_21 (*brown bars*), and triplet DPE_21_49 (*yellow bars*)

Figure 16 allows comparison of the EB valence angles to those of the optimized triplet structures DPE_14_21 and DPE_21_49.

Protonation leaves almost intact the valence angles C—N—C in both triplet DPEs. Angle C_5—N_7—C_8 in EB is equal to its analog in triplet DPE_14_21 while the same one in DPE_21_49 is smaller by 0.1°; the angles at amine nitrogens N_{28} and N_{35} increase in both triplet DPEs by ca. 0.18° – an infinitesimal doping effect. It is noteworthy that angles C—C—N exhibit tendency to open to identical extent upon protonation. Exceptions are the angles 9-8-7 and 37-36-35 which remain unchanged in all three species represented in Fig. 16.

Angles C—N═C are wider in the triplets than in EB no matter whether they are protonated or not. Similarly to the above singlet DPEs, angles C—N═C in triplet DPEs have the largest value at the protonation site. For a certain triplet the angles at the position of protonation are alike in magnitude and are substantially larger than those at the non-protonated imine nitrogens. Protonation opens appreciably the C—C—N= angles.

The torsion angles of EB and the two triplet DPEs are presented in Fig. 17.

Angles C—C—N—C and C—C—N═C at the same amine or imine atom deviate from the respective ones in EB in the same manner for both triplets considered: one of them increases and the other decreases. These changes are more pronounced in DPE_21_49. At N_{42}, the atom "unaffected" by protonation, DPE_21_49 (protonated at the ring containing N_{42}) exhibits the largest deviation from EB: marked decrease in the one and increase in the second torsion angle.

Least divergence from EB reveal dihedral angles at N_{21}: weak disproportion of the two constituent torsions most marked in DPE_21_49. Unlike in the singlets, the deformation in the chain core is more pronounced in the triplet DPE_14_21.

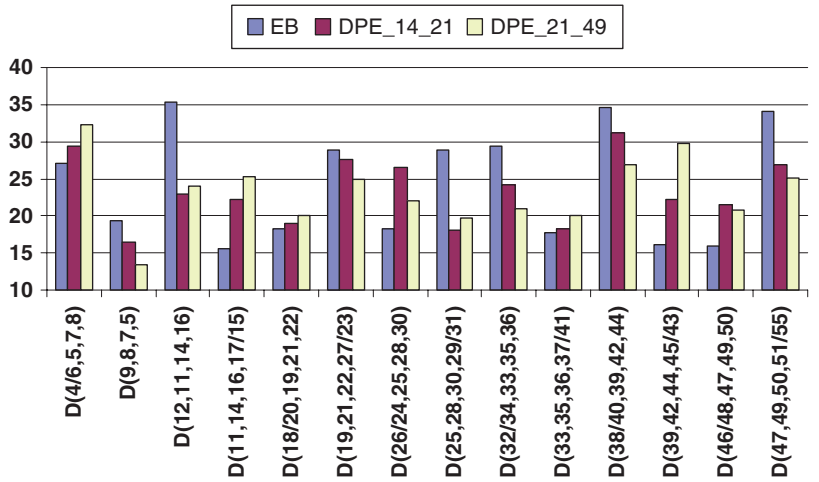

Fig. 17 UBLYP/6-31G*-optimized dihedral angles (in °) of hydrated EB (*blue bars*), triplet DPE_14_21 (*brown bars*), and triplet DPE_21_49 (*yellow bars*)

In summary, when the protonation is at the same quinoid ring, the valence angle centered at the N-atom opens at the expense of the two neighboring ones. When the protonation is at imine atoms from different rings, the effect is transferred to the angle involving the imine N-atom closer to the chain end. In all cases the largest valence angles remain those centered at amine nitrogens.

The overall degree of deformation of the three structures compared in Fig. 17 is very similar. Changes of the dihedral angles are seen again only in the vicinity of the protonated nitrogen atoms, where the angles become smaller compared with EB. The asymmetry of the two angles C—C—N—C around the same amine nitrogen atom is enhanced. The torsion angles C—C—N=C of two DPEs having the same nitrogen protonated (for instance N_{49}) are pretty much alike. In brief, the geometry of the various DPEs differs mainly around the protonated sites. Therefore, each of the three could be used for comparison with the neutral base and with the corresponding singlet structure.

Figure 18 contains the bond lengths of the neutral EB and of singlet and triplet DPE_21_49.

The tendencies described above when comparing the bonds C—C, C=C, C=N, and C—N of the neutral to those of the singlet DPE molecule remain valid also for comparison of the triplet to EB. All changes, namely the dearomatization/dequinoidization of the benzene rings, are just more expressed in the triplet structures than in the singlet ones.

Table 7 represents a comparison of the $\overset{+}{N}$—H bond lengths and of the proton–counterion distances for a singlet and triplet geometry of one and the same DPE.

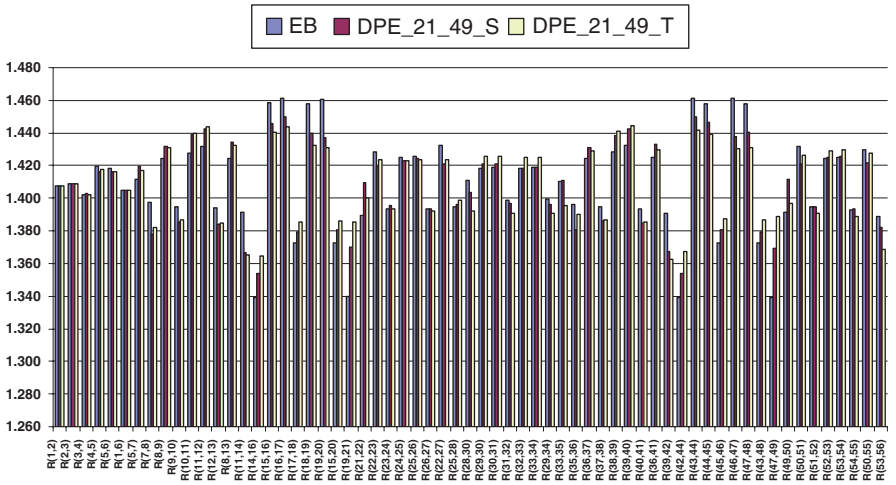

Fig. 18 UBLYP/6-31G*-optimized C—C, C=C, C=N, and C—N bond lengths (in Å) of hydrated EB (*blue bars*), singlet DPE_21_49 (*brown bars*), and triplet DPE_21_49 (*yellow bars*)

Table 7 UBLYP/6-31G* $\overset{+}{\text{N}}$—H bond lengths and proton–counterion distances (in Å) of the singlet (DPE_21_49_S) and the triplet (DPE_21_49_T) state of DPE_21_49

	DPE_21_49_S	DPE_21_49_T
$\mathbf{R_{N21\text{-}H95}}$	1.049	1.045
$\mathbf{R_{N49\text{-}H96}}$	1.048	1.047
$\mathbf{R_{H95\text{-}Cl97}}$	2.200	2.235
$\mathbf{R_{H96\text{-}Cl98}}$	2.212	2.207

The $\overset{+}{\text{N}}$—H bond lengths of the singlet and the triplet do not differ significantly. There is a larger difference in the proton–counterion distances – they are always longer for the triplet, both states featuring asymmetry of the two distances.

A comparison of the valence and the torsion angles of EB, a singlet DPE, and a triplet DPE is provided in Figs. 19 and 20.

The two types of angles of the triplet structures change in a similar fashion to the singlets with respect to the neutral base. The valence angles for both states of the protonated molecule are mostly identical and are appreciably larger than in the EB form.

Triplet geometries are characterized with larger torsion angles around the protonated atoms than the singlets (especially the angles around core N_{21}). The chain of DPE_21_49_T is more open also at the C—C—N—C angles (N_{35}). In general, the asymmetry of the two dihedrals at the same nitrogen is reduced in the triplet state. However, the overall degree of deformation of the singlets and the triplets is alike. This structural information implies that coexistence of polaronic and bipolaronic forms of the polymer would not result in steric strain.

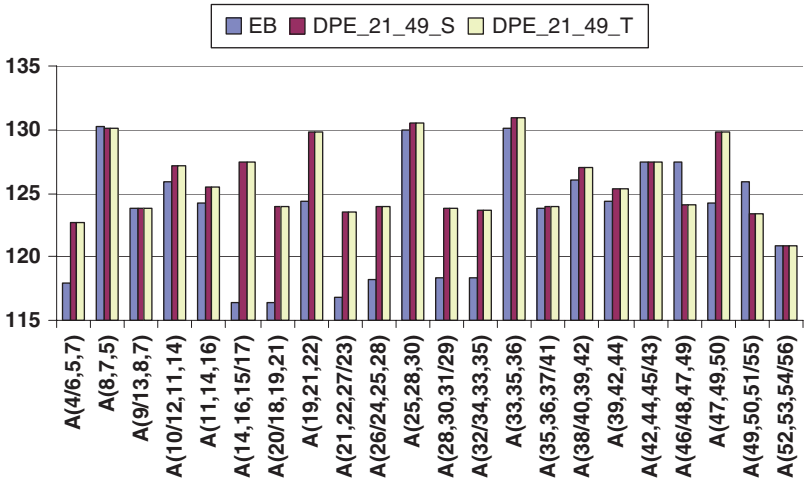

Fig. 19 UBLYP/6-31G*-optimized valence angles (in °) of hydrated EB (*blue bars*), DPE_21_49_S (*brown bars*), and DPE_21_49_T (*yellow bars*)

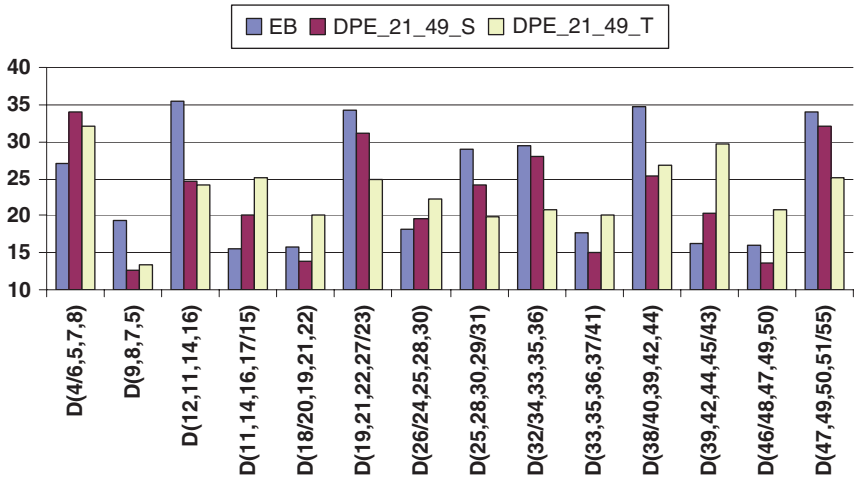

Fig. 20 UBLYP/6-31G*-optimized dihedral angles (in °) of hydrated EB (*blue bars*), DPE_21_49_S (*brown bars*), and DPE_21_49_T (*yellow bars*)

3.2.3 Electron Density of DPE

Mulliken and NBO atomic charges distribution was used for description of the electronic structure of the doubly protonated singlet and triplet oligomers. The results are presented in Figs. 21, 22, 23, 24, 25, 26, 27, and 28.

The Mulliken charges of the amine nitrogen atoms in the chains of all studied singlet compounds have very similar values (Fig. 21). As a rule, any protonation pattern results in moderate reduction of their negative charge. The chain-ending amine

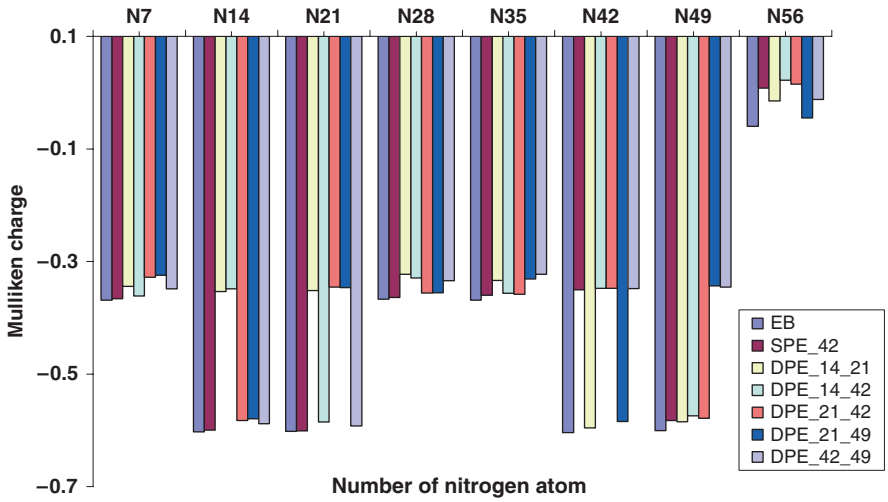

Fig. 21 Mulliken charges on the nitrogen atoms along the chain of hydrated EB, SPE_42, and all singlet DPEs

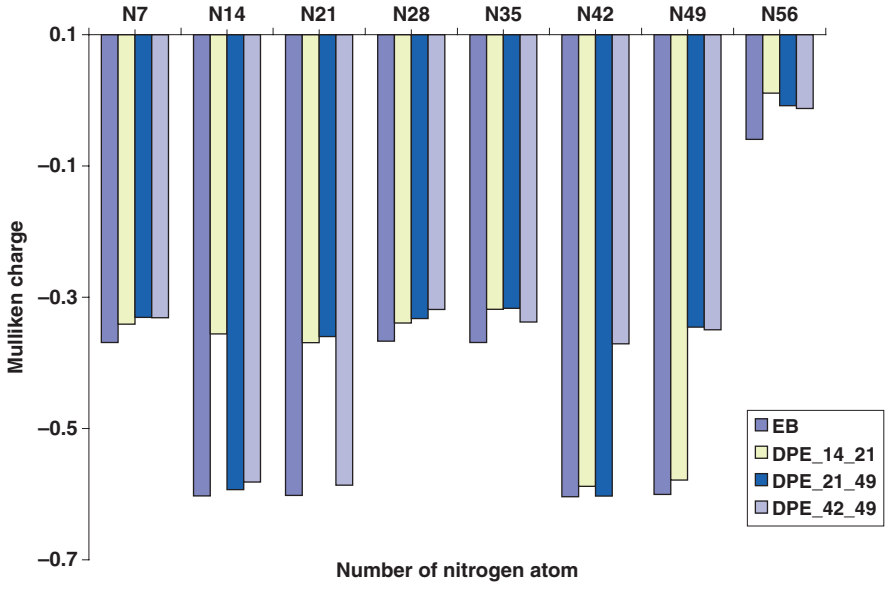

Fig. 22 Mulliken charges on the nitrogen atoms along the chain of hydrated EB and all optimized triplet DPEs

nitrogen has always a higher (positive) charge whenever imine N_{42} is protonated. The most negative imine nitrogen of EB is N_{42}; however, the charge distribution in SPE_42 implies that the next candidate for protonation is not the neighboring N_{49} but rather the farthest N_{14} and N_{21}. The expected trend of less negative charges

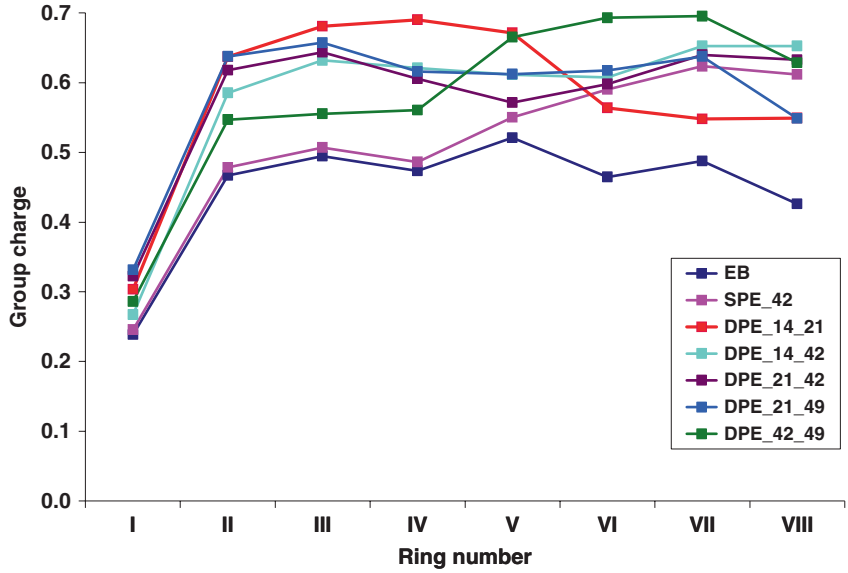

Fig. 23 Mulliken group charges of the rings of hydrated EB, SPE_42, and all singlet DPEs

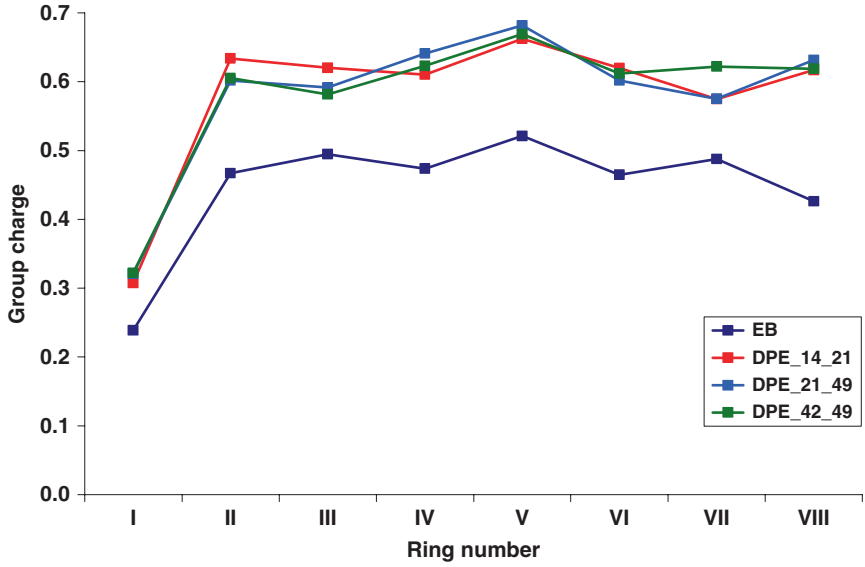

Fig. 24 Mulliken group charges of the rings of hydrated EB and all optimized triplet DPEs

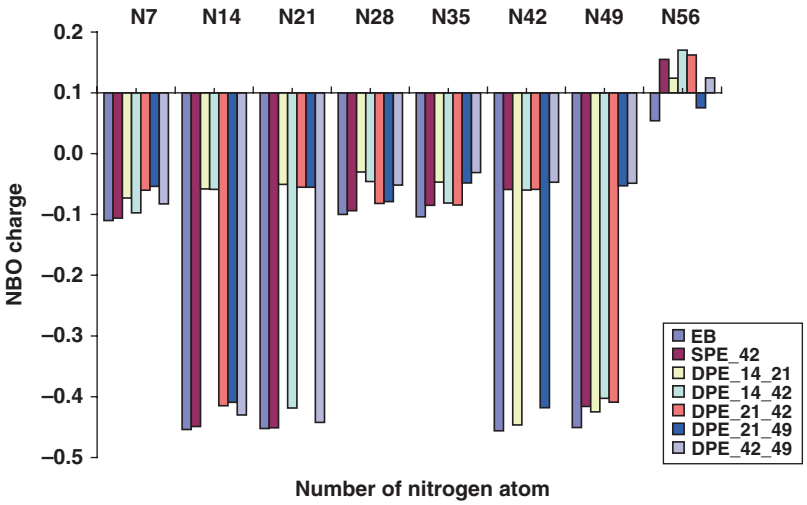

Fig. 25 NBO group charges on the nitrogen atoms of hydrated EB, SPE_42, and all singlet DPEs

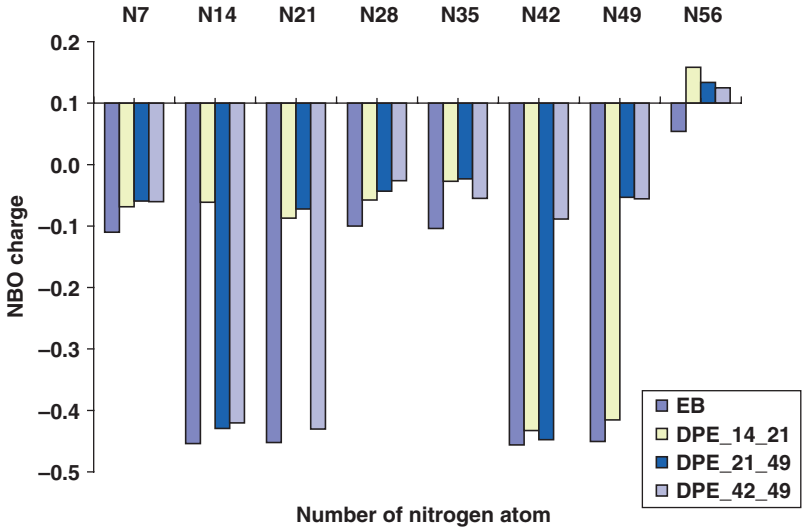

Fig. 26 NBO group charges on the nitrogen atoms of hydrated EB and all optimized triplet DPEs

on the protonated centers and more negative (yet lesser than in EB) ones on the non-protonated imine nitrogens is preserved throughout.

This tendency is observed also in the atomic charges distribution of the triplet structures (Fig. 22). The Mulliken charges of the corresponding protonated or non-protonated nitrogen atoms of the singlets and the triplets are very close.

In Figs. 23 and 24 we have summarized the data of the group charges on the rings for EB, the singlet SPE, and the singlet and triplet DPEs. The numbers of the rings denoted on the abscissa correspond to counting from left to right along the oligomer as drawn on Fig. 1.

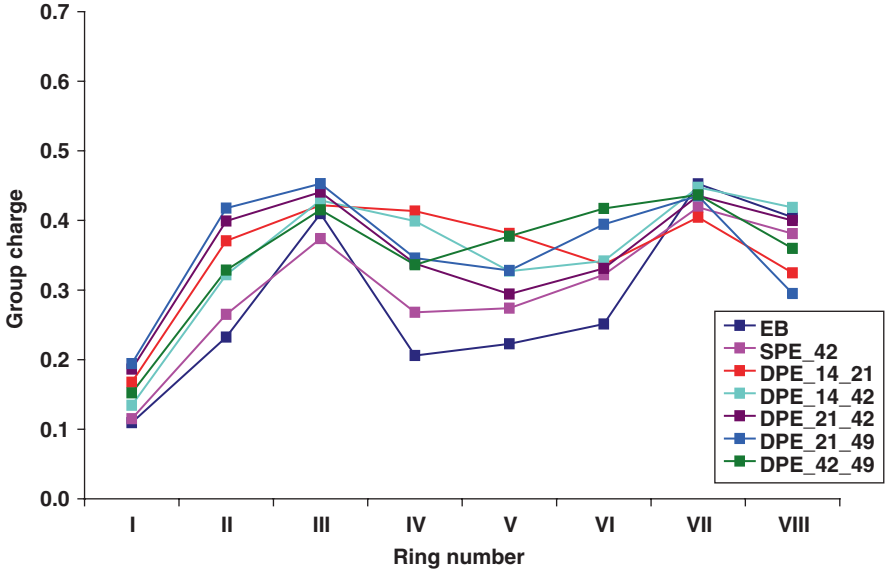

Fig. 27 NBO group ring charges of hydrated EB, SPE_42, and all singlet DPEs

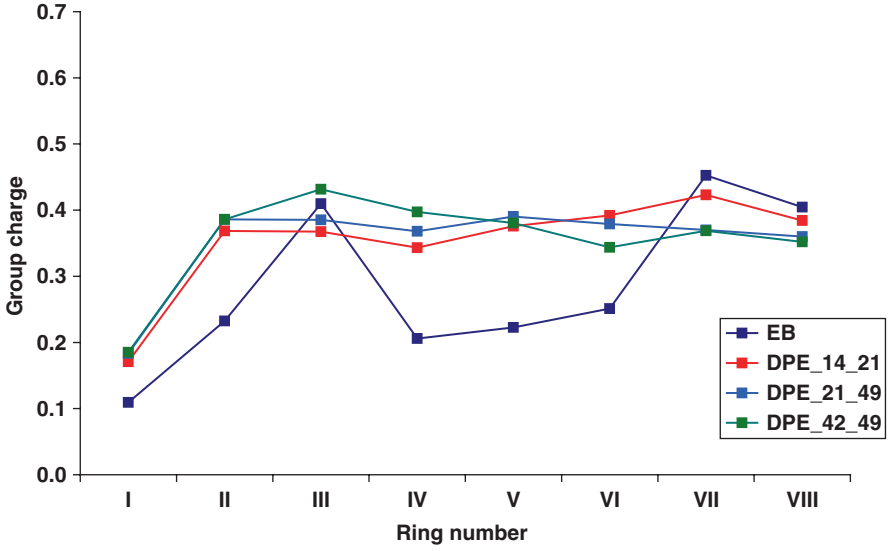

Fig. 28 NBO group ring charges of hydrated EB and all optimized triplet DPEs

In the neutral emeraldine oligomer there is regular alternation of rings with higher and lower positive charge, all group charges on the rings being positive. The first ring is the only outlier having always a very low positive charge. Nevertheless, even its charge is higher in the protonated structures than in the neutral EB.

Both in singlet and in triplet DPEs the Mulliken ring charges become more positive compared with the base. However, the regularity of alternation is broken in the protonated molecules depending on the pattern of protonation. As expected, the rings around the protonated nitrogens always possess a higher positive charge than the remaining ones, but when the protonated sites are well separated the alternation is milder and the delocalization of charge more prominent. Excluding the first ring which maintains constant charge values, the charge alternation of rings is within 0.1 for both singlets and triplets.

In order to obtain a more quantitative picture of the charge distribution along the chains of the protonated octamers, the NBO atomic charges were calculated too. The respective values of the nitrogen group charges of the singlets and the triplets are shown on Figs. 25 and 26, respectively.

Once again, as for the neutral bases, the values of the NBO charges are substantially reduced with respect to the ones yielded by the Mulliken analysis. Within a given octamer, the charges of the two subgroups of nitrogen atoms (amine and imine) remain relatively constant. These charges are highest for the DPEs, intermediate for SPE_42, and lowest for EB, as should be expected.

The tendency of the protonated imine nitrogens having much higher charges than the non-protonated ones is preserved. Interestingly, the atomic charges of the protonated imine nitrogens almost coincide with those of the amine atoms. Such a picture corresponds to the formal representation of the polaronic structure of PANI.

The highest charge of all nitrogens possesses the end-amine nitrogen atom (N_{56}), which even becomes positively charged in all studied forms of EB and ES octamers.

The trends in the charge distribution of the triplet structures (Fig. 26) are completely identical to those discussed above. Even the absolute values of the charges on the same atoms are quite alike.

Figures 24 and 28 contain the group charges of the rings in the singlet and the triplet molecules. The numbering of the rings is identical to the one described above.

In all studied oligomers the first ring remains with the lowest positive charge, its values being equal for the pair EB and SPE_42 and for the pair DPE_21_42 and DPE_21_49, even though the charge is a bit larger for the latter pair of molecules. More substantial changes of the group charges undergo the rings in the vicinity of the protonation site. There the ring charge becomes higher than that of EB if the protonation affects the first quinoid ring (III). When the second quinoid ring is protonated, however, the group charge of ring III may become lower than in EB (SPE_42) or remain unchanged (DPE_42_49). The charge of the second quinoid ring (VII) has very similar value, almost equal to that in EB, for all protonated oligomers.

All aromatic rings, however, have higher charges than they do in EB. This is an indication of an effective charge transfer from the quinoid to the aromatic rings during protonation.

In the triplet structures the fluctuation of the ring charges is more moderate, which means that the electron density is distributed more uniformly (within ca. 0.05) along the chain than in the singlet octamers (within ∼0.15).

3.2.4 Magnetic Characteristics of DPE

The total energy of the singlet (E_S) and triplet (E_T) DPEs and the energy of the singlet–triplet splitting (ΔE_{ST}) calculated with UBLYP/6-31G* in PCM are summarized in Table 8.

The presented data show that in all species the singlet state is more stable than the triplet one. Among the three singlets, the most stable is DPE_21_49 and among the triplets, the two DPEs protonated at the same ring are preferred. The energies of singlet–triplet splitting have very close values for the two octamers with protonated imine nitrogens at the same ring (DPE_14_21 and DPE_42_49). ΔE_{ST} of these two DPEs is much smaller than that of DPE_21_49, where the two protonated nitrogens are separated in space. At first glance, this contradicts the formal representation of polaronic and bipolaronic forms of PANI. According to the latter, the singlet state should be more stable when the two protonated sites are at the same quinoid rings, while the triplet should be favored by separation of the protonated centers. However, when one takes a look at the spin density distribution of the triplet oligomers (Fig. 29), an explanation of this "contradiction" can be suggested.

The spin density distribution in Fig. 29 shows that enhanced spin density is observed not only close to the protonated centers but that it is also transferred along the chain (at maximum distance of two nitrogen atoms away from the protonated one). The highest spin density in some of the DPEs is not on the protonated but rather on the neighboring nitrogen atom. In DPE_21_49 the spin has even migrated completely from the protonated position (N_{21}) to the adjacent imine nitrogen (N_{14}). It should be noted that an appreciable amount of spin density is localized also on some of the amine nitrogens. This contradicts the expectation of localized spin density of the bipolaronic form. Another unexpected result is that stabilization of the high spin state when two adjacent nitrogen atoms are protonated is achieved through spin delocalization. On the other hand, spin polarization facilitates the migration of spin along the chain, when a neighboring protonated imine site is missing (DPE_21_49). Such migration, however, can take place at a relatively limited length, which allows us to conclude that polaron length in PANI may not exceed a distance corresponding to about 3–4 aniline units, similar to analogous estimates

Table 8 Total energy (a.u.) of the singlet (E_S) and triplet (E_T) DPE octamers and singlet−triplet splitting (ΔE_{ST}, kcal/mol) calculated with UBLYP/6-31G* in PCM

Oligomer	ES	ET	EST
DPE_14_21	−3210.680374	−3210.674922	−3.421
DPE_21_49	−3210.684427	−3210.667171	−10.828
DPE_42_49	−3210.680188	−3210.674439	−3.608

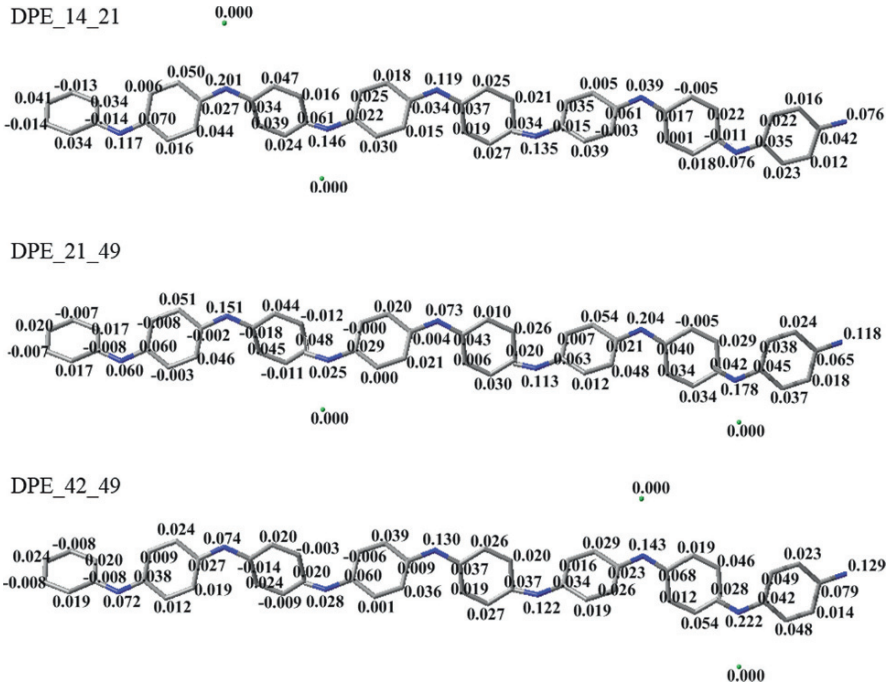

Fig. 29 Mulliken atomic spin densities of the triplet DPE octamers DPE_14_21 (*top panel*), DPE_21_49 (*middle panel*), and DPE_42_49 (*bottom panel*); hydrogen atoms are omitted as their spin densities do not exceed 0.005

for doped polyacetylene [30], where solitons span ca. 28 methine units. Around the atoms with large excess of spin, there is always spin delocalization, which stabilizes the polaron.

4 Summary

Inclusion of a continuum solvent in the modeling of PANI oligomers does not affect considerably their structural characteristics but enhances the effect of dearomatization/dequinoidization of protonated emeraldine. PCM increases slightly the polarization along the chain.

Protonation influences the electron density distribution most markedly in the vicinity of the protonated site but propagates along the chain as well. In doubly protonated structures the atomic charges of protonated imine nitrogen atoms are substantially less negative than those of non-protonated imine atoms and almost equal to the charges of the amine nitrogens. The group ring charges of the singlets are more sensitive to the protonation position, while the electron density of the triplets is relatively uniformly distributed.

The stability of the spin states is also affected by the position of protonation. The spin density distribution suggests stabilization of the high spin structures by local spin delocalization or spin polarization.

Acknowledgments This research is supported by Projects BYX-202/2006 and DO-02-136/2008 of the Bulgarian National Science Fund. An equipment grant from the Alexander von Humboldt Foundation is highly appreciated. A. I. is grateful to the Alexander von Humboldt Foundation for a return fellowship.

References

1. Z. Wang, E. Scherr, A. MacDiarmid, A. Epstein, Phys. Rev. B **45**, 4190 (1992)
2. K. Mizoguchi, M. Nechtschein, J. Travers, Synth. Metals **41**, 113 (1991)
3. J. Rouleau, J. Goyette, T. Bose, R. Singh, R. Tandon, Phys. Rev. B **52**, 4801 (1995)
4. (a) W.J.M. Naber, S. Faez, W.G. van der Wiel, J. Phys. D: Appl. Phys. **40**, R205 (2007); (b) G. Paasch, J. Electroanal. Chem. **600**, 131 (2007); (c) F.M. Kelly, J.H. Johnston, T. Borrmann, M.J. Richardson, J. Nanosci. Nanotechnol. **8**, 1965 (2008); (d) H.P. Huang, X.M. Feng, J.J. Zhu, Nanotechnology **19**, 145607 (2008); (e) C.C. Wang, J.F. Song, H.M. Bao, Q.D. Shen, C.Z. Yang, Adv. Func, Mater. **18**, 1299 (2008); (f) B.N. Grgur, V. Ristic, M.M. Gvozdenovic, M.D. Maksimovic, B.Z. Jugovic, J. Power Sources. **180**, 635 (2008)
5. A.G. MacDiarmid, A.J. Epst?in, Faraday Discuss Chem. Soc. **88**, 317 (1989)
6. D.V. Petrov, A.S. Gomes, Cid B. de Araujo, J.M. de Souza, W.M. de Azevedo, J.V. de Melo, F.B. Diniz, Optics. Lett. **20**, 554 (1995)
7. S. Chen, G. Hwang, Macromolecules **29**, 3950 (1996)
8. D. Bloor, Nature **335**, 115 (1988)
9. A.G. MacDiarmid, Synth. Metals **84**, 27 (1997)
10. G. Gustafsson, Y. Cao, G.M. Treacy, F. Klavetter, N. Colaneri, A.J. Heeger, Nature **357**, 477 (1992)
11. G.M. Tsivgoulis, J.M. Lehn, Adv. Mater. **9**, 627 (1997)
12. P. McManus, R. Cushman, S. Yang, J. Phys. Chem. **9**, 744 (1987)
13. (a) O. Aksimentyeva, O. Konopelnik, Mol. Cryst. Liq. Cryst. **427**, 429 (2005); (b) D. Sarno, S. Manohar, A. MacDiarmid, Synth. Metals **148**, 237 (2005); (c) C.G. Wu, S.S. Chang, J. Phys. Chem. B **109**, 825 (2005)
14. M. Kulkarni, A. Viswanath, R. Marimuthu, T. Seth, Polym. Eng. Sci. **44**, 1676 (2004)
15. S. Sahoo, R. Nagarajan, S. Roy, L.A. Samuelson, J. Kumar, A.L. Cholli, Macromolecules **37**, 4130 (2004)
16. M.C. Bernard, A. Hugot-Le Goff, Electrochim. Acta **52**, 595 (2006)
17. V. Krinichnyi, S. Chemerisov, Y. Lebedev, Phys. Rev. B **55**, 16233 (1997)
18. A. Kon'kin, V. Shtyrlin, R. Garipov, A. Aganov, A. Zakharov, V. Krinichnyi, P. Adams, A. Monkman, Phys. Rev. B **66**, 075203 (2002)
19. A. Petr, A. Neudeck, L. Dunsch, Chem. Phys. Lett. **401**, 130 (2005)
20. (a) L. Ge, S. Li, T.F. George, X. Sun, Phys. Lett. A **372**, 3375 (2008); (b) Y. Harima, F. Ogawa, R. Patil, X. Jiang, Electrochim. Acta **52**, 3615 (2007)
21. P.K. Kahol, A. Raghunathan, B.J. McCormick, Synth. Metals **140**, 261 (2004)
22. (a) V. Prigodin, A. Samukhin, A. Epstein, Synth. Metals **141**, 155 (2004); (b) J. Joo, S. Long, J. Pouget, E.J. Oh, A. MacDiarmid, A. Epstein, Phys. Rev. B **57**, 9567 (1998); (c) R. Kohlman, A. Zibold, D. Tanner, G. Ihas, T. Ishiguro, Y. Min, A. MacDiarmid, A. Epstein, Phys. Rev. Lett. **78**, 3915 (1997); (d) M. Angelopoulos, A. Ray, A. MacDiarmid, A. Epstein, Synth. Metals **21**, 21 (1987)
23. Z.T. Oliveira Jr., M. dos Santos, Chem. Phys. **260**, 95 (2000)

24. J.P. Foreman, A.P. Monkman, J. Phys. Chem. A **107**, 7604 (2003)
25. (a) R.H. Baughman, J.F. Wolf, H. Eckhardt, L.W. Shaklette, Synth. Metals **25**, 121 (1989); (b) L.W. Shaklette, J.F. Wolf, S. Gould, R.H. Baughman, J. Chem. Phys. **88**, 3955 (1988); (c) M.P. Lima, G.M. Silva, J. Molec. Struct THEOCHEM **852**, 15 (2008); (d) A. Varela-Álvarez, J.A. Sordo, J. Chem. Phys. **128**, 174706 (2008)
26. M. Schreiber, K. Tenelsenb, T. Vojta, J. Luminescence **66–67**, 521 (1996)
27. (a) J.L. Bredas, C. Quattrocchi, J. Libert, A.G. MacDiarmid, J.M. Ginder, A.J. Epstein, Phys. Rev. B **44**, 6002 (1991); (b) A.G. MacDiarmid, A.J. Epstein, Synth. Metals **69**, 85 (1995); (c) S. Stafstroem, J.L. Bredas, A.J. Epstein, H.S. Woo, D.B. Tanner, W.S. Huang, A.G. MacDiarmid, Phys. Rev. Lett. **59**, 1464 (1987)
28. D. Djurado, M. Bee, M. Gonzalez, C. Mondelli, B. Dufour, P. Rannou, A. Pron, J.P. Travers Chem. Phys. **292**, 355 (2003)
29. (a) A. Kulikov, A. Komissarova, A. Ryabenko, L. Fokeeva, I. Shunina, O. Belonogova, Russ. Chem. Bull. **12**, 2794 (2005); (b) A. Kulikov, V. Bogatyrenko, O. Belonogova, L. Fokeeva, A. Lebedev, T. Echmaeva, I. Shunina, Russ. Chem. Bull. **51**, 2216 (2002)
30. B. Champagne, M. Spassova, Phys. Chem. Chem. Phys. **6**, 3167 (2004)
31. B. Grossmann, J. Heinze, T. Moll, C. Palivan, C. Ivan, G. Gescheidt, J. Phys. Chem. B **108**, 4669 (2004)
32. (a) C. Aleman, C.A. Ferreira, J. Torras, A. Meneguzzi, M. Canales, M.A.S. Rodrigues, J. Casanovas, Polymer **49**, 5169 (2008); (b) S.L. Lim, K.L. Tan, E.T. Kang, W.S. Chin, J. Chem. Phys. **112**, 10648 (2000)
33. J. Libert, J.L. Bredas, Synth. Metals **69**, 121 (1995)
34. G. Yang, W. Hou, X. Feng, X. Jiang, J. Guo, Int. J. Quant. Chem. **108**, 1156 (2008)
35. A. Pecchia, A. Di Carlo, Rep. Prog. Phys. **67**, 1497 (2004)
36. E.A.A. Noh, J. Zhang, Chem. Phys. **330**, 82 (2006)
37. (a) H. Zhekova, A. Tadjer, A. Ivanova, J. Petrova, N. Gospodinova, Int. J. Quant. Chem. **107**, 1688 (2007); (b) N. Gospodinova, S. Dorey, A. Ivanova, H. Zhekova, A. Tadjer, Int. J. Polym. Anal. Charact. **12**, 251 (2007); (c) A. Ivanova, A. Tadjer, N. Gospodinova, J. Phys. Chem. B, **110**, 2555 (2006); (d) A. Ivanova, G. Madjarova, A. Tadjer, N. Gospodinova, Int. J. Quant. Chem. **106**, 1383 (2006)
38. (a) J. Tomasi, B. Mennucci, R. Cammi, Chem. Rev. **105**, 2999 (2005); (b) S. Miertus, E. Scrocco, J. Tomasi, Chem. Phys. **55**, 117, (1981)
39. M.J. Frisch, G.W. Trucks, H.B. Schlegel, G.E. Scuseria, M.A. Robb, J.R. Cheeseman, J.A. Montgomery, Jr., T. Vreven, K.N. Kudin, J.C. Burant, J.M. Millam, S.S. Iyengar, J. Tomasi, V. Barone, B. Mennucci, M. Cossi, G. Scalmani, N. Rega, G.A. Petersson, H. Nakatsuji, M. Hada, M. Ehara, K. Toyota, R. Fukuda, J. Hasegawa, M. Ishida, T. Nakajima, Y. Honda, O. Kitao, H. Nakai, M. Klene, X. Li, J.E. Knox, H.P. Hratchian, J.B. Cross, C. Adamo, J. Jaramillo, R. Gomperts, R.E. Stratmann, O. Yazyev, A.J. Austin, R. Cammi, C. Pomelli, J.W. Ochterski, P.Y. Ayala, K. Morokuma, G.A. Voth, P. Salvador, J.J. Dannenberg, V.G. Zakrzewski, S. Dapprich, A.D. Daniels, M.C. Strain, O. Farkas, D.K. Malick, A.D. Rabuck, K. Raghavachari, J.B. Foresman, J.V. Ortiz, Q. Cui, A.G. Baboul, S. Clifford, J. Cioslowski, B.B. Stefanov, G. Liu, A. Liashenko, P. Piskorz, I. Komaromi, R.L. Martin, D.J. Fox, T. Keith, M.A. Al-Laham, C.Y. Peng, A. Nanayakkara, M. Challacombe, P.M.W. Gill, B. Johnson, W. Chen, M.W. Wong, C. Gonzalez, and J.A. Pople, Gaussian 03, revision D.01 (Gaussian Inc., Pittsburgh PA, 2004)
40. (a) Y. Yan, Z. Yu, Y.W. Huang, W.X. Yuan, Z.X. Wei, Adv. Mater. **19**, 3353 (2007); (b) B. Jia, T, Hino, N. Kuramoto, Reactive Func. Polym. **67**, 836 (2007); (c) J. Li, L.H. Zhu, W. Luo, Y. Liu, H.Q. Tang, J. Phys. Chem. C **111**, 8383 (2007)

Quantum Mechanical Examination of Optical Absorption Spectra of Silver Nanorod Dimers

Jérémy Vincenot and Christine M. Aikens

Abstract Time-dependent density functional theory calculations are employed to examine the optical absorption spectra of dimers of the pentagonal silver nanorods Ag_{19}^{+1}, Ag_{25}^{+1}, and Ag_{31}^{+1}. The qualitative features of the spectra agree well with the exciton-coupling model and with previous experimental and theoretical results. In the end-to-end orientation, longitudinal peak red-shifts with decreasing distance. For side-by-side dimers, the transverse peak splits as the interparticle distance decreases due to symmetry-breaking, and the longitudinal peak blue-shifts slightly with decreasing distance. Quantum mechanical calculations are required for the calculation of absorption spectra at very short interparticle distances where the electron densities of the two subsystems overlap. At short distances, the energies and intensities of the monomer peaks change substantially and new excitation peaks emerge.

Keywords: Density functional theory · TDDFT · Optical absorption · Silver nanorods · Nanoparticle dimers · Plasmon resonance · Plasmon coupling · Plasmon shifts

1 Introduction

Quantum confinement of electrons in nanoscale materials leads to physical properties that differ from those of the bulk. For noble metal nanoparticles, strong surface plasmon absorption leads to one or more sharp peaks in the visible region of the optical spectrum, and the exact characteristics depend sensitively on the nanoparticle size and shape [1, 2]. Due to their anisotropic structure, nanorods possess more

C.M. Aikens (✉)
Department of Chemistry, Kansas State University, Manhattan, KS 66506-0401, USA,
e-mail: cmaikens@ksu.edu

J. Vincenot
Department of Chemistry, Kansas State University, Manhattan, KS 66506-0401, USA, and Department of Physics Engineering, Polytech Clermont-Ferrand, 24 Avenue des Landais, BP 206, 63174 Aubière Cedex, France

P. Piecuch et al. (eds.), *Advances in the Theory of Atomic and Molecular Systems*, Progress in Theoretical Chemistry and Physics 20, DOI 10.1007/978-90-481-2985-0_12,

complex optical absorption properties than nanospheres. Nanorods display two optical absorption bands that correspond to excitation along the long and short axes of the particle, where the wavelength of the strong longitudinal plasmon resonance band depends linearly on aspect (length-to-diameter) ratio [3, 4]. The aspect ratios of these systems are very tunable; for example, a seed-mediated synthesis can be used to prepare silver nanorods and nanowires with aspect ratios of 2.5–10 and 50–350, respectively [5]. Gold nanorods are finding application in cancer diagnostics and therapy due to their controllable aspect ratios, which yields tunable absorption in the near-infrared region of the electromagnetic spectrum [6, 7].

Single molecule detection using techniques such as surface-enhanced Raman scattering (SERS) [8–10] is facilitated by large local electric fields located at the junction of two nanoparticles, which has stimulated a strong interest in understanding plasmon coupling in metal nanostructure assemblies. These assemblies could also find use in optoelectronic applications such as photonic wave-guiding [11–13]. As a result, nanoparticle dimers have been widely studied experimentally and theoretically (for a recent review, see Ref. [14]). Of note, El-Sayed et al. examined the end-to-end and side-by-side orientations of gold nanorods using the discrete dipole approximation (DDA) model and found predictions that agree with experimental observations that the longitudinal plasmon resonance red-shifts when the nanorods are arranged in an end-to-end fashion, whereas the longitudinal band blue-shifts and the transverse band red-shifts when the nanorods aggregate in a side-by-side orientation [15]. Most theoretical investigations to date have employed classical approaches such as the DDA method. However, these methods cannot account for quantum phenomena such as electron tunneling that become important at very small interparticle distances. Quantum mechanical effects significantly influence the plasmonic response of the dimer for short interparticle distances and must be treated using methods such as the time-dependent local density approximation [16].

At long distances, the exciton-coupling model provides a convenient method for understanding nanoparticle dimer interactions. The interaction between two identical two-level systems A and B can be treated with Heitler – London perturbation theory provided the perturbation is weak. Neglecting dispersion, the energies of the excited states are $\Delta E \pm V_{AB}$, where ΔE is the energy difference between the ground and the excited states in the isolated particle A and V_{AB} is the interaction matrix element $V_{AB} = \left\langle \Psi_0^A \Psi_1^B \right| V \left| \Psi_1^A \Psi_0^B \right\rangle = \left\langle \Psi_1^A \Psi_0^B \right| V \left| \Psi_0^A \Psi_1^B \right\rangle$, where Ψ_0^A and Ψ_1^A are the ground and excited state wavefunctions, respectively, of the isolated system [17]. The corresponding eigenfunctions for the excited states of dimer AB are $\Psi_\pm = \frac{1}{\sqrt{2}} \left\{ \Psi_1^A \Psi_0^B \pm \Psi_0^A \Psi_1^B \right\}$. Recently, a "plasmon hybridization" theory has shown that the plasmon resonances of metallic nanostructures can be treated analogously to atomic and molecular wavefunctions [18], so the discussion in this section applies to metal nanoparticles in addition to molecular systems. Due to the interaction of the two systems the excitation is not localized in A or B, and this is the origin of *excitation (exciton) transfer*. At long interparticle distances where electronic overlap between A and B can be neglected, the perturbation is often represented by the dipole – dipole interaction $V = \left[\vec{\mu}_A \cdot \vec{\mu}_B - \left(3/R^2\right) \left(\vec{\mu}_A \cdot \vec{R} \right) \left(\vec{\mu}_B \cdot \vec{R} \right) \right] \Big/ R^3$

where $\vec{\mu}_A$ is the dipole moment of A and $\vec{R}$ is the relative position vector of A and B. The magnitude of the perturbation increases with decreasing interparticle distance.

Two important cases arise where the transition dipole moments of A and B are either perpendicular or parallel to $\vec{R}$. For the case where the transition dipole moments are parallel to each other and are both perpendicular to $\vec{R}$ (denoted H aggregates), V_{AB} reduces to $|\mu_{10}|^2 / R^3$ where $\mu_{10} \equiv \langle \Psi_1 | \vec{\mu} | \Psi_0 \rangle$. Then, the eigenvalues and wavefunctions of the two states are

$$\Delta E - |\mu_{10}|^2/R^3 \; ; \; \Psi_- = 1/\sqrt{2} \left\{ \Psi_1^A \Psi_0^B - \Psi_0^A \Psi_1^B \right\}$$
$$\Delta E + |\mu_{10}|^2/R^3 \; ; \; \Psi_+ = 1/\sqrt{2} \left\{ \Psi_1^A \Psi_0^B + \Psi_0^A \Psi_1^B \right\}.$$

For the case where both transition dipole moments are parallel to $\vec{R}$ and arranged in a head-to-tail fashion (J aggregates), the eigenvalues and wavefunctions of the two excited states are

$$\Delta E - 2|\mu_{10}|^2/R^3 \; ; \; \Psi_+ = 1/\sqrt{2} \left\{ \Psi_1^A \Psi_0^B + \Psi_0^A \Psi_1^B \right\}$$
$$\Delta E + 2|\mu_{10}|^2/R^3 \; ; \; \Psi_- = 1/\sqrt{2} \left\{ \Psi_1^A \Psi_0^B - \Psi_0^A \Psi_1^B \right\}.$$

The transition moments between the ground state and the state Ψ_- are zero, so only transitions to the Ψ_+ state will be observed. When the transition dipole moments are perpendicular to $\vec{R}$, the observed excited state energy will increase with decreasing distance, whereas the excitation energy will decrease with decreasing distance when the transition dipole moments are arranged in a head-to-tail fashion.

At shorter distances R, the perturbation can be expanded as a series of multipole – multipole interactions. Higher-order multipole plasmon interactions have been employed to explain the appearance of new peaks in the absorption spectrum for nanoshell dimers [19]. When the interparticle distance is small enough that the electron clouds of A and B overlap, the system is in a conductive regime where states in which one electron is transferred from an occupied orbital of one subsystem to an unoccupied orbital of the other become important for a complete description of the manifold of excited states.

2 Computational Methods

All calculations performed in this work utilize the Amsterdam Density Functional (ADF) 2007.01 program [20]. The molecular structures of the $Ag_{19}{}^{+1}$, $Ag_{25}{}^{+1}$, and $Ag_{31}{}^{+1}$ silver nanorod monomers are optimized using the gradient-corrected Becke – Perdew (BP86) exchange-correlation functional [21, 22]. Nuclear coordinates for the dimer orientations are constructed by offsetting the coordinates of two identical monomers without further optimization. The basis set employed in the optimizations is a double-zeta (DZ) Slater-type basis set with a $[1s^2\text{–}4p^6]$ frozen core for Ag. Scalar relativistic effects are included by utilizing the zeroth-order regular approximation (ZORA) [23]. Time-dependent density functional theory

(TDDFT) is employed to determine energetics and compositions of excited states using the asymptotically correct statistical average of orbital potentials (SAOP) [24, 25] model potential. SAOP calculations employ an all-electron DZ basis set. The first 200 or 400 dipole-allowed states are evaluated for the optical absorption spectrum of monomers and dimers, respectively. The smoothed spectra shown in the figures are convoluted with a Lorentzian with a full width at half-maximum (FWHM) of 0.2 eV. Several computational parameters were adjusted to improve the numerical accuracy of the calculations as reported in Ref. [26]. In addition, an additional order of magnitude improvement in the self-consistent field convergence, tolerance, and orthonormality parameters was found to be necessary for precise determination of dimer peak energies.

3 Results and Discussion

3.1 Silver Nanorod Monomers

Pentagonal silver nanorods with 19, 25, and 31 atoms are examined in this work. These rods range from 1.1 to 1.7 nm in length (calculated from the nuclear coordinates of the tips plus the bulk nearest neighbor Ag– Ag distance of 0.289 nm as an estimate of twice the atomic radius). The diameters of these rods are approximately 0.8 nm, which leads to aspect ratios of 1.4–2.1. As discussed recently by Johnson and Aikens, the neutral nanorods have a single unpaired electron in the highest occupied molecular orbital, which is doubly degenerate for systems such as Ag_{31} [26]. Thus, nanorods in the +1 charge state are considered in this work.

The molecular geometries and TDDFT optical absorption spectra for $Ag_{19}{}^{+1}$, $Ag_{25}{}^{+1}$, and $Ag_{31}{}^{+1}$ are shown in Fig. 1. Each monomer spectrum consists of two peaks; the lower energy peak has A_1 symmetry corresponding to excitation along the *z*(long)-axis of the nanorod and relates to the longitudinal plasmon oscillation band observed experimentally [3, 4], while the higher energy peak arises from states with E_1 symmetry (*x,y*-axes) and is compatible with the transverse plasmon oscillation. The intensity of the transverse peak remains nearly constant as the length of the nanorod increases, whereas the intensity of the longitudinal peak depends linearly on the size of the system (Fig. 2). As the length of the nanorod increases, the position of the longitudinal peak red-shifts linearly with the number of atoms from 3.73 eV for $Ag_{19}{}^{+1}$ to 3.16 eV for $Ag_{31}{}^{+1}$ (Fig. 3(a)). The linear relationship between system size and longitudinal peak excitation wavelength has been explained using a particle-in-a-cylinder model [26]. The position of the transverse peak varies less than the position of the longitudinal peak; for the systems examined in this work, the maximum in the excitation energy varies from 4.26 to 4.36 eV (Fig. 3(b)). As discussed in earlier work, several states are responsible for the transverse excitation, and this peak is broader in general than the longitudinal excitation [26]. The longitudinal excitation can also involve several states; for $Ag_{19}{}^{+1}$, this peak arises from two different excitations at similar energies.

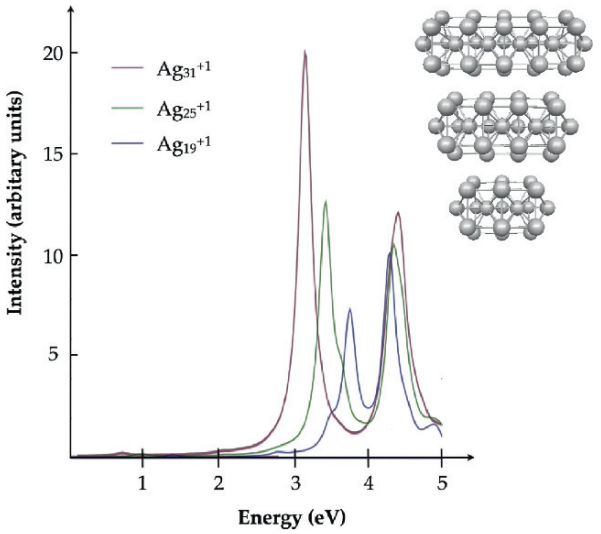

Fig. 1 TDDFT optical absorption spectra and molecular geometry of Ag_{31}^{+1}, Ag_{25}^{+1}, and Ag_{19}^{+1} silver nanorod monomers (shown in order of decreasing size)

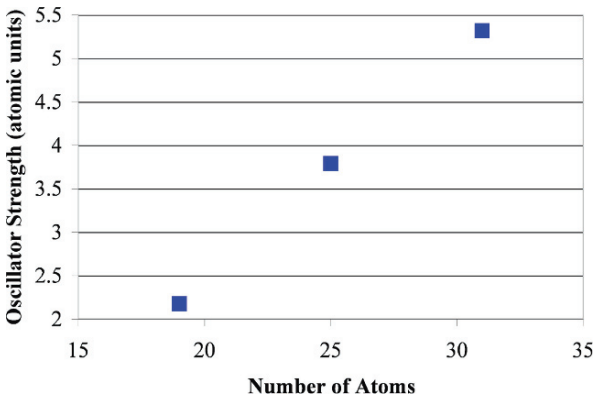

Fig. 2 Oscillator strength of longitudinal peak versus number of atoms

3.2 Silver Nanorod Dimer Orientations

The end-to-end (J aggregate) and side-by-side (H aggregate) orientations (Fig. 4) for nanorod dimers are examined in this work. The end-to-end orientation retains the fivefold symmetry of the monomer whereas this symmetry is broken in the side-by-side configuration, and this has implications in the optical absorption spectra as discussed below. In the next section, the absorption spectra for Ag_{19}^{+1} dimers at intermediate and long distances are considered. (The spectra for Ag_{25}^{+1} and Ag_{31}^{+1}

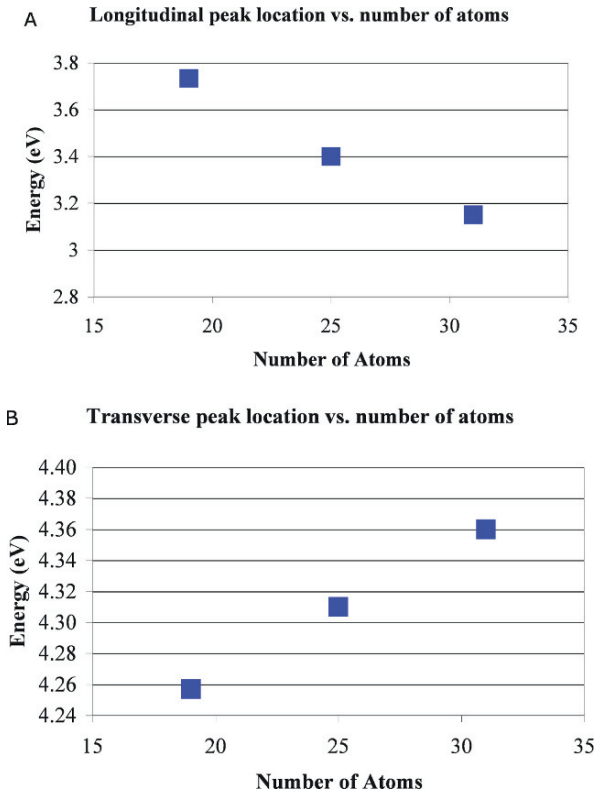

Fig. 3 Energy of (**a**) longitudinal and (**b**) transverse absorption peak versus number of atoms

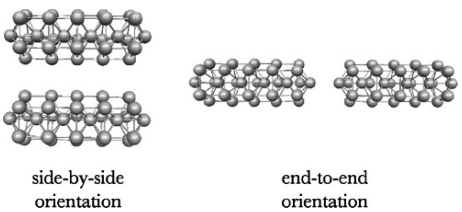

Fig. 4 Silver nanorod dimer orientations

dimers exhibit similar results.) Subsequently, the absorption spectra for dimers with very short interparticle distances are examined.

3.3 Ag_{19}^{+1} Dimer Absorption Spectra

For each monomer, dimers were constructed by fixing a second monomer at a given distance from the first. For the end-to-end orientation for Ag_{19}^{+1}, the longest

distance considered is 39 Å between the centers of mass. At this distance, the nanorods are essentially non-interacting. The absorption spectrum is identical to that of the monomer with the exception that the intensities are twice that of those in the monomer spectrum, which is a natural consequence of the doubling of the total number of electrons in the system. At shorter interparticle distances, the nanorods interact which leads to changes in the excitation peak locations and intensities. The absorption spectra for dimers with tip-to-tip distances of 5.659–9.659 Å (corresponding to center of mass separations of 14–18 Å) are shown in Fig. 5.

As the particles approach each other, the excitations responsible for the longitudinal peak slightly red-shift (Fig. 5(f), rectangular box), whereas the position of the transverse peak excitation is unchanged (Fig. 5(f), oval). The red-shift of the

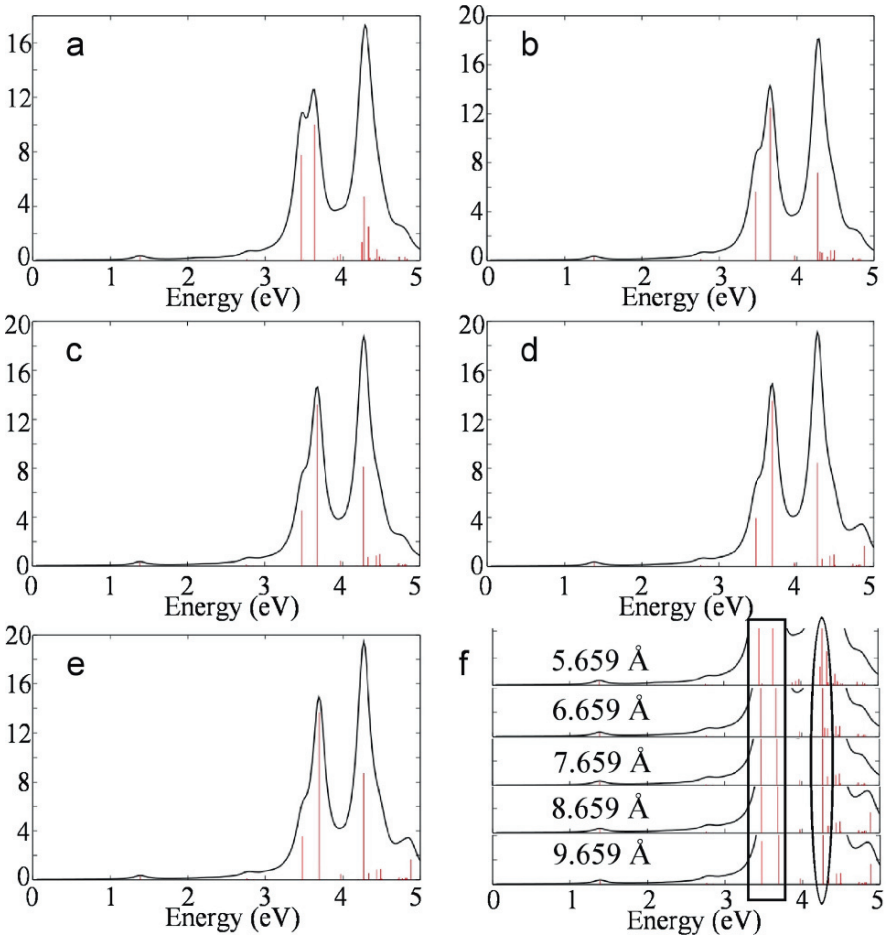

Fig. 5 Absorption spectra in arbitrary units (a.u.) for Ag_{19}^{+1} end-to-end dimers with tip-to-tip distances of (**a**) 5.659 Å, (**b**) 6.659 Å, (**c**) 7.659 Å, (**d**) 8.659 Å, and (**e**) 9.659 Å. (**f**) Spectra (**a–e**) offset on the same energy axis

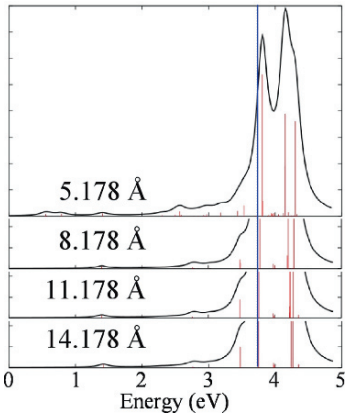

Fig. 6 Absorption spectra for Ag_{19}^{+1} side-by-side dimers with nearest interdimer distances shown. The *blue dotted line* at constant energy is intended as a guide for the eye

longitudinal peak agrees qualitatively with the exciton-coupling model for J aggregates, and the unchanged transverse peak is reasonable because there are no perturbations in the x and y directions. For side-by-side dimers, the transverse peak splits as the interparticle distance decreases (Fig. 6) because the E_1 symmetry of this transition in the monomer is split by the perturbation arising from the second nanorod. The longitudinal peak blue-shifts slightly with decreasing distance, in accord with the exciton-coupling model for H aggregates.

The change in the interparticle distance also affects the relative intensities of various excitations, such as the two excitations responsible for the longitudinal peak in the end-to-end dimer. When two Ag_{19}^{+1} monomers are separated by a tip-to-tip distance of 9.659 Å, the lower- and higher-energy longitudinal peaks have oscillator strengths of 1.12 and 4.29 a.u., respectively. At 5.659 Å, these oscillator strengths are predicted to be 2.44 and 3.15 a.u., respectively. The total oscillator strength does not change dramatically (5.41 vs. 5.59 a.u.), but the change effectively shifts the overall longitudinal peak position to lower energy. Other peaks also experience intensity changes; for example, the minor peak near 5 eV decreases in intensity as the interparticle distance decreases.

Numerous fitting functions for the relationship of the oscillator strength (f) to the tip-to-tip distance (R) have been examined in this work, and one of these is shown in Fig. 7. A functional form that depends on R^{-3} appears to reproduce the TDDFT calculations fairly well; however, it should be stressed that the fittings are very sensitive to the parameters employed. Fittings based on tip-to-tip and on center of mass distances have been considered, and neither is a clear choice. For other nanorods and peaks, functions that depend on R^{-2} are found to more closely reproduce the TDDFT-calculated oscillator strengths. Similar fittings have been examined in order to connect the interparticle distance with the red- or blue-shifts in the energy, and functions of R^{-6} and R^{-2} have been found. Based on a dipole – dipole perturbation, a function of the form R^{-3} may be expected. This discrepancy could be

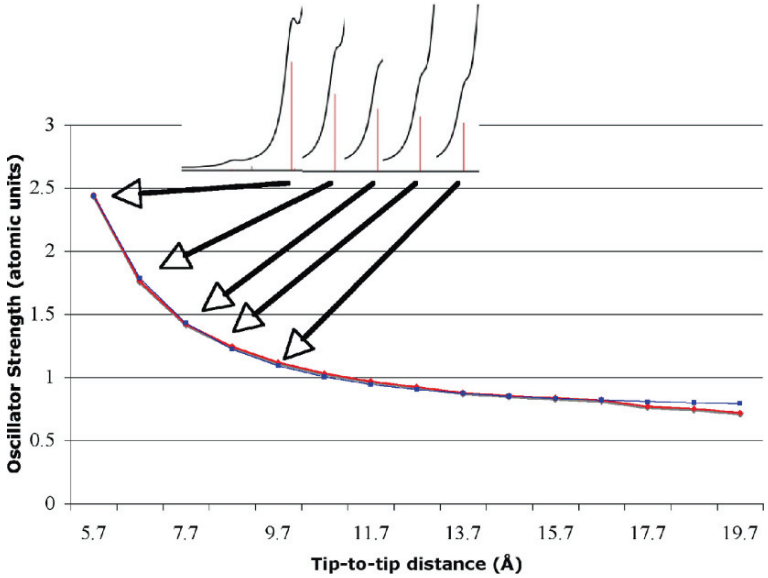

Fig. 7 Oscillator strength (f) of first longitudinal peak for $Ag_{19}{}^{+1}$ end-to-end dimers versus tip-to-tip distance (R). TDDFT-calculated data (*red*) shown with points fit using equation $f(R) = 305.55R^{-3} + 0.7513$ (*blue*)

due to several causes. Higher-order multipole interactions such as those considered in Ref. [19] could be important, especially since these distances are intermediate between the weak coupling and the conductive regimes. In addition the nanorod has a non-negligible size, and therefore models based on point dipoles may not yield quantitatively accurate predictions.

3.4 Dimer Absorption Spectra at Short Interparticle Distances

At very short interparticle distances, the electronic wavefunctions of the two subsystems overlap significantly and the dipolar exciton-coupling model does not provide a reasonable approximation for the system. The absorption spectra for $Ag_{25}{}^{+1}$ end-to-end dimers with interparticle distances of 2.8–4.5 Å are shown in Fig. 8. (In general, 2.8 Å is the closest silver – silver distance predicted in the monomer at this level of theory, so it is assumed that the two particles will maintain interparticle distances greater than 2.8 Å.) At 4.5 Å, the dimer absorption spectrum is dominated by two longitudinal excitations that are red-shifted and two transverse excitations that are slightly blue-shifted relative to the corresponding monomer peaks. As the interparticle distance decreases, the intensities of the two longitudinal peaks decrease. Simultaneously, amplified intensities of initially minor peaks such as the peak at 2.15 eV in the 4.5 Å spectrum are observed. This peak increases in intensity and blue-shifts; when the interparticle distance is reduced to 2.8 Å, this excitation falls

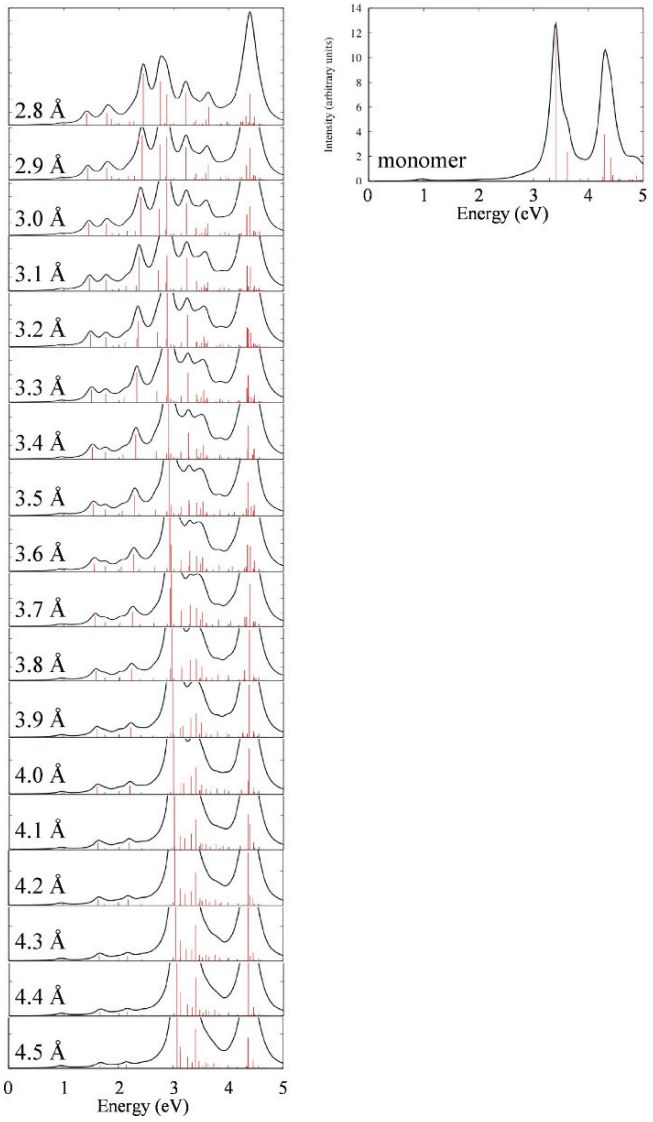

Fig. 8 Absorption spectra for Ag_{25}^{+1} end-to-end dimers with short tip-to-tip distances as shown. The monomer spectrum is shown for comparison

at 2.45 eV and is stronger than the originally dominant longitudinal peak. Similarly, the strong peak at 2.76 eV in the 2.8 Å spectrum grows out of a very weak excitation near 2.63 eV in the 3.8 Å spectrum. Thus, in addition to energy and intensity changes predicted for the original peaks, new excitations become important for a correct description of the absorption spectrum when the electron densities of the two subsystems overlap. This can be seen clearly in Fig. 9, which displays the evolution of the absorption spectra for Ag_{31}^{+1} dimers with decreasing interparticle distance.

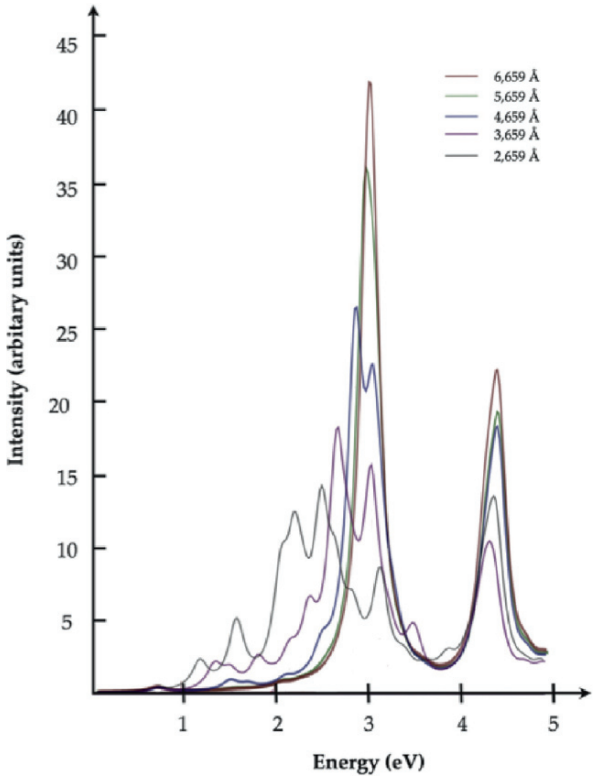

Fig. 9 Absorption spectrum for $Ag_{31}{}^{+1}$ dimers in end-to-end orientation

4 Conclusions

TDDFT correctly reproduces trends in silver nanorod absorption spectra determined experimentally or from other theoretical models. For silver nanorod monomers, the wavelength of the longitudinal excitation depends sensitively on the length of the monomer, whereas the transverse excitation is not greatly affected. In nanorod dimers, the red-shift of the longitudinal peak with decreasing distance for the end-to-end orientation agrees qualitatively with the exciton-coupling model. For side-by-side dimers, the transverse peak splits as the interparticle distance decreases due to symmetry-breaking, and the longitudinal peak blue-shifts slightly with decreasing distance. The TDDFT-predicted relationships of peak energies and oscillator strengths to the interparticle distance are in qualitative but not quantitative agreement with the exciton-coupling model using a point dipole – dipole perturbation, and this discrepancy may be due to the finite sizes of the nanorods or the higher multipole interactions that are neglected in the latter model. Quantum mechanical calculations are particularly critical for the calculation of absorption spectra at very short interparticle distances where the electron densities of the two subsystems

overlap. At short distances, the energies and intensities of the monomer peaks change substantially and new excitation peaks emerge.

Acknowledgments C.M.A. thanks Kansas State University for start-up funding. The authors thank Professor Peter Nordlander for sending a preprint of Ref. [16].

References

1. U. Kreibig, M. Vollmer, *Optical Properties of Metal Clusters* (Springer, Berlin, 1995)
2. K. L. Kelly, E. Coronado, L. L. Zhao, G. C. Schatz, J. Phys. Chem. B **107**, 668 (2003)
3. Y.-Y. Yu, S.-S. Chang, C.-L. Lee, C.R.C. Wang, J. Phys. Chem. B **101**, 6661 (1997)
4. S. Link, M.B. Mohamed, M.A. El-Sayed, J. Phys. Chem. B **103**, 3073 (1999)
5. N.R. Jana, L. Gearheart, C.J. Murphy, Chem. Commun. 617 (2001)
6. I. H. El-Sayed, X. Huang, M. A. El-Sayed, Nano Lett. **5**, 829 (2005)
7. X. Huang, I.H. El-Sayed, W. Qian, M.A. El-Sayed, J. Am. Chem. Soc. **128**, 2115 (2006)
8. K. Kneipp, Y. Wang, H. Kneipp, L.T. Perelman, I. Itzkan, R.R. Dasari, M.S. Feld, Phys. Rev. Lett. **78**, 1667 (1997)
9. S. Nie, S.R. Emory, Science **275**, 1102 (1997)
10. A.M. Michaels, M. Nirmal, L.E. Brus, J. Am. Chem. Soc. **121**, 9932 (1999)
11. M. Quinten, A. Leitner, J.R. Krenn, F.R. Aussenegg, Opt. Lett. **23**, 1331 (1998)
12. S.A. Maier, H.A. Atwater, J. Appl. Phys. **98**, 011101 (2005)
13. W.L. Barnes, A. Dereux, T.W. Ebbesen, Nature **424**, 824 (2003)
14. S.K. Ghosh, T. Pal, Chem. Rev. **107**, 4797 (2007)
15. P.K. Jain, S. Eustis, M.A. El-Sayed, J. Phys. Chem. B **110**, 18243 (2006)
16. J. Zuloaga, E. Prodan, P. Nordlander, Nano Lett. **9**, 887 (2009)
17. N. Mataga, T. Kubota, *Molecular Interactions and Electronic Spectra* (Marcel Dekker, New York, 1970)
18. H. Wang, D.W. Brandl, P. Nordlander, N.J. Halas, Acc. Chem. Res. **40**, 53 (2007)
19. J.B. Lassiter, J. Aizpurua, L.I. Hernandez, D.W. Brandl, I. Romero, S. Lal, J.H. Hafner, P. Nordlander, N.J. Halas, Nano Lett. **8**, 1212 (2008)
20. G. te Velde, F.M. Bickelhaupt, E.J. Baerends, C. Fonseca Guerra, S.J. A. van Gisbergen, J.G. Snijders, T. Ziegler, J. Comp. Chem. **22**, 931 (2001)
21. A.D. Becke, Phys. Rev. A **38**, 3098 (1988)
22. J.P. Perdew, Phys. Rev. B **33**, 8822 (1986)
23. E. van Lenthe, E.J. Baerends, J.G. Snijders, J. Chem. Phys. **99**, 4597 (1993)
24. O.V. Gritsenko, P.R.T. Schipper, E.J. Baerends, Chem. Phys. Lett. **302**, 199 (1999)
25. P.R.T. Schipper, O.V. Gritsenko, S.J.A. van Gisbergen, E.J. Baerends, J. Chem. Phys. **112**, 1344 (2000)
26. H.E. Johnson, C.M. Aikens, J. Phys. Chem. A **113**, 4445 (2009)

On the Electronic Spectra of a Molecular Bridge Under Non-Equilibrium Electric Potential Conditions

Alexander Prociuk and Barry D. Dunietz

Abstract The linear response of the electronic density of a molecular based junction under potential bias conditions to a probing polarizing perturbation is calculated to model the electronic spectra. It is shown that steady flux conditions lead to dramatic effects on the electronic spectra of the confined system. The non-equilibrium conditions enable electronic transitions that are otherwise forbidden. The implemented methodology uses the Keldysh contour formalism to express the electronic equations of motion. The related time correlation Green Functions are then solved for in the full frequency representation and at the linear response level.

Keywords: Non-equilibrium Green's function · Electronic spectra · Electron dynamics · Molecular conductance

1 Introduction

The modeling and experimenting of electron transport (ET) through nanoscale systems are the focus of intensive research efforts. Interest in such systems ranges from possible advances in technology to studies of interesting physical phenomena. The characterization of time-dependent (TD) ET is a challenge at the forefront of research efforts since most state-of-the-art computational treatments of ET are limited to describing the conductance under steady state conditions [1–8].

TD transport studies provide access to fascinating quantum effects related to the conductance. For example, a large body of research considers quantum interferences associated with photoassisted conductance in nanoscopic systems driving behaviors such as absolute negative conductance, Coulomb blockade, Kondo effects, and electron pumping [9–20]. The experimental study of the dynamics of ET related to electron pumping is complemented by important theoretical treatments [21–36].

Barry D. Dunietz (✉)
The University of Michigan, Ann Arbor, Michigan 48109, USA, e-mail: bdunietz@umich.edu

Alexander Prociuk
The University of Michigan, Ann Arbor, Michigan 48109, USA, e-mail: prociuk@umich.edu

P. Piecuch et al. (eds.), *Advances in the Theory of Atomic and Molecular Systems*, Progress in Theoretical Chemistry and Physics 20, DOI 10.1007/978-90-481-2985-0_13,

The challenges underlying molecular conductance studies include the atomic scale characterization of the junction and association of the measured conductance to single molecules. Typically, an elaborate experimental procedure involving large statistical sampling and control schemes is required for proper investigation of the conductance properties of single molecules. The combined measurement of both conductance and spectra of molecular junctions has been reported using Raman scattering [37–41]. Conductance enhancement in the junction has been correlated with changes of the in situ measured Raman spectra of the molecular junction. This is an exciting development that contributes to the characterization of molecular junctions under bias. The ability to obtain spectral information of the junction system under bias provides the needed probe to confirm that single molecules are indeed confined between the electrodes and carry the transport in the junction. It is, therefore, important to proceed and consider the effects of electronic flux due to the bias on the electronic spectra of the molecular junction that is mediating the ET.

In order to understand the dynamical effect of electron flux on the spectra or of any other photo-driven ET process proper treatment of the electronic structure of the open systems has to be achieved. For achieving analysis of the flux-affected electronic spectra, a TD approach that probes the response of the electronic density to a temporal delta function potential pulse can be used to generate the system's spectra as is performed in traditional widely used linear response implementations of TD-DFT. This is extended below to the analysis of electron flow effects on the optical excitations of a biased model system.

Our TD approach is based on solving the electronic equations of motion (e.o.m.) as expressed by the Kadanoff–Baym (K–B) equations derived from the Keldysh formalism. Most descriptions of dynamic transport that use many-body Green's Functions (GF)-based formalisms [36, 42–44] follow the seminal work of Jauho et al. [45]. More recent extensions of GFs approaches to treat the dynamics of ET implement a real time propagation scheme. Other approaches use a real time propagation of the electron density evaluated at the DFT level [42, 43, 46–54]. A major limitation or difficulty is related to treating the coupling of the propagated electronic density to electron reservoirs. Other schemes involve the projection of the electronic structure of the infinite system to the device region. Master equations and propagation of the projected system expressed by density matrix formulations have been used to analyze TD transport, where the periodicity of the time perturbation is used to derive Floquet-based expansions [36, 55–61]. Of these we note schemes which combine Floquet-based approaches with NEGF formalisms [36, 60, 61].

Recently we have reported the solution to the equation of motion (e.o.m.s) (K–B equations) of a model open system under the influence of a time-dependent perturbing potential bias applied across the junction. Our approach for treating the dynamics was based on a simplified first-order time-dependent perturbation treatment, where the electronic density of the electrodes is described by a wide-band limit (WBL) approximation [62]. The transient conduction of model electronic channels were analyzed. There we also analyzed the dependence of coherently driven transport on detuning induced by an electrostatic field. This effect was characterized by temporal propagation of the current energy density.

In this report we study the effects of non-equilibrium conditions on the electronic spectra of a model open channel system. We express the equations in the full-frequency domain and solve them at the linear response level. The full frequency-space expressions of the e.o.m.'s are used to eliminate the WBL approximation in treating the electronic structure of the bulk [62]. Instead the electrodes are treated exactly at the applied modeling level. Therefore, an energy-dependent DOS of the electrode evaluated by the relevant tight binding treatment is used. This is a powerful scheme to calculate the electronic spectra of an open system at non-equilibrium conditions. We use our methodology to demonstrate that the effect of flux due to bias conditions is to allow electronic transitions that are otherwise forbidden in the equilibrated system.

2 Modeling Spectra of Open Channels under Bias Conditions

2.1 Starting Point: Energy-Resolved Time-Dependent Density Matrix

In this study, the effect of non-equilibrium conditions on the electronic spectra of the coupled and biased system is analyzed at the most fundamental level. Under equilibrium conditions electronic transitions between states below the Fermi energy of the electrodes are inhibited due to their steady population. This is illustrated in Fig. 1 (left), where the effect of coupling to electrodes, whose electronic structures are characterized by bands, is depicted. The continuum of the electrodes' DOS is projected on the device region leading to broadening of the otherwise discrete energy levels. In this study we consider the transitions between these states at non-equilibrium condition, where the bias results in dynamical flux coupling the two electrodes through the broadened energy levels. This flux as discussed below affects the electronic spectrum of the system greatly. See the non-equilibrium system illustrated in the right side of the figure.

The electronic spectrum is calculated from the dynamic electronic density of a system responding to relevant perturbations. The time-dependent response of the electronic density $\rho(t)$ can be expressed in terms of a TD energy-resolved response:

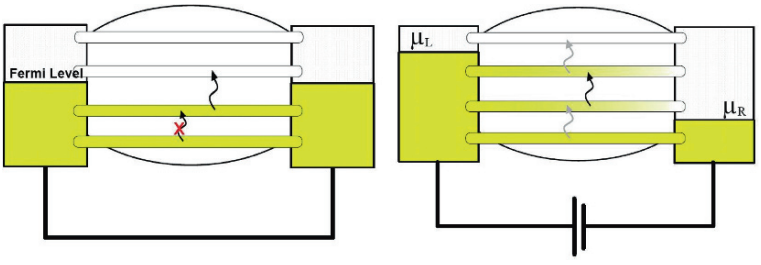

Fig. 1 Scheme of the electronic levels of a device model system coupled to the electron reservoir at (*left*) equilibrium (*right*) non-equilibrium conditions

$$\rho(t) = \int dE \rho(E, t), \tag{1}$$

where $\rho(E, t)$ is the energy-resolved density matrix projected onto the junction. The energy dependence reflects the band structure of the system coupled to electrodes, where scattering states that couple both electrodes contribute energy bands with a finite width. For example, in this distribution, a peak centered at E' with a ΔE width describes the effectively infinite number of states resulting from the projection. In general, $\rho(E, t)dE$ contributes states to the density matrix ($\rho(t)$) with energies in the range E to $E+dE$. This TD energy density can be used to describe the dynamics of any quantum mechanical operator ($\hat{O}$):

$$\langle O(t) \rangle = \int dE \mathrm{Tr}\left[\rho(E, t)\hat{O}\right]. \tag{2}$$

We consider next, in detail, the solution of the electronic equation of motion as obtained from Keldysh formalism-based expressions. It is, however, important to note the following change in notation. The density of state energy variable, E, will be replaced by $\bar{\omega}$ and the time variable, t, by $\bar{t}$, which corresponds to the notation used in the earlier study [62].

3 Linear Response of an Open System: Full-Frequency Space Electronic Equation of Motion

We now use the previously derived electronic e.o.m., in which the extended nature of the system is projected onto the electronic structure of the device region [62]:

$$\begin{aligned} i\frac{\partial}{\partial \bar{t}}\Delta G^{<}_{cc}(\bar{t}, \bar{\omega}) = &\left[\mathbf{h}_{cc}, \Delta G^{<}_{cc}(\bar{t}, \bar{\omega})\right] + \int d\omega' \mathbf{v_{cc}}(\bar{t}, \omega')\mathbf{G}^{<}_{cc}(\bar{t}, \bar{\omega} - \omega') \\ &-\mathbf{G}^{<}_{cc}(\bar{t}, \bar{\omega} + \omega')\mathbf{v_{cc}}(\bar{t}, \omega') \\ &+\int_{-\infty}^{\infty} dt' [\Sigma^{\mathbf{R}}(\bar{t} - t')\Delta G_{cc}{}^{<}(t', \bar{\omega})e^{-i\mathbf{h_{cc}}(\bar{t}-t')} \\ &-e^{i\mathbf{h}_{cc}(\bar{t}-t')}\Delta \mathbf{G}_{cc}(t', \bar{\omega})\Sigma^{A}(t' - \bar{t})]. \end{aligned} \tag{3}$$

In this equation h is the Hamiltonian, and $G^{<}$ is the GF from which the TD electronic density can be extracted. In the above equation, the subscript cc refers to the device central subspace and $G^{<}_{cc}(\bar{t}, \bar{\omega}) = G^{0,<}_{cc}(\bar{\omega}) + \Delta G^{<}_{cc}(\bar{t}, \bar{\omega})$. We note that this is written in atomic units, where $\hbar \equiv 1$. The projection is based on using the electrode's self-energy [62] expressed by Σ. Finally, $\mathbf{v_{cc}}(\bar{t}, \omega')$ is the energy-resolved TD perturbation expressed in terms of the actual perturbation, $v(t)$. In this representation $\mathbf{v_{cc}}(\bar{t}, \omega')$ is also unitless:

$$\mathbf{v}(\bar{t},\bar{\omega}) = \frac{1}{\pi} e^{-i2\bar{\omega}\bar{t}} \int_{-\infty}^{\infty} dt e^{i(2\bar{\omega})t} \mathbf{v}(t) = \frac{1}{\pi} e^{-i2\bar{\omega}\bar{t}} \tilde{\mathbf{v}}(2\bar{\omega}). \tag{4}$$

The full derivation of Eq. (3) is provided in Ref. [62].

To directly propagate the e.o.m.'s as expressed above in the mixed representation $(\bar{t},\bar{\omega})$ is computationally demanding at moderate to long times due to the memory kernel, which must be recalculated for every time and frequency. We, instead, solve the e.o.m. after expressing it in the full-frequency domain. This corresponds to a transformation from the mixed representation to:

$$G^{<}(\Delta\omega,\bar{\omega}) \equiv \int_{-\infty}^{\infty} d\bar{t} e^{i\Delta\omega\bar{t}} G^{<}(\bar{t},\bar{\omega}). \tag{5}$$

This transformation leads to the following form of the e.o.m. in the full-frequency domain:

$$\begin{aligned}
&\sum_{k,l} \mathcal{H}_{ijkl}(\Delta\omega)\Delta G^{<}_{CC,kl}(\Delta\omega,\bar{\omega}) = \\
&\frac{1}{2\pi}\left[\mathbf{v}_{CC}(\Delta\omega)\mathbf{G}^{0,<}_{CC}(\bar{\omega}-\Delta\omega/2) - \mathbf{G}^{0,<}_{CC}(\bar{\omega}+\Delta\omega/2)\mathbf{v}_{CC}(\Delta\omega)\right]_{ij} \\
&+\frac{1}{\pi}\int d\omega' \left[\mathbf{v}_{CC}(2\omega')\Delta G^{<}_{CC}(\Delta\omega-2\omega',\bar{\omega}-\omega')\right. \\
&\left.-\Delta G^{<}_{CC}(\Delta\omega-2\omega',\bar{\omega}+\omega')\mathbf{v}_{CC}(2\omega')\right]_{ij},
\end{aligned} \tag{6}$$

where

$$\mathcal{H}_{ijkl}(\Delta\omega) \equiv (\Delta\omega + i\eta - \Delta\epsilon_{ij})\Delta_{ik}\Delta_{jl} - \Gamma_{ijkl}(\Delta\omega) \tag{7}$$

and $\Delta\epsilon_{ij} \equiv \epsilon_i - \epsilon_j$ is the difference between the i-th and j-th eigenvalues (ϵ_i, ϵ_j) of H_{cc}. The implemented formalism includes a broadening factor (η) in defining the tensor $\mathcal{H}$. It is required that the factor be sufficiently small and that the temporal range of the calculation is large enough to include the system's return to equilibrium. Namely, that the turn off of the perturbation is included in the simulation.

For simplicity of both the notation and the computation, we now express the tensor and matrices in Eq. (6) by reduced rank representation (tetradic notation). In this representation, the rank four tensor is expressed as a rank two matrix and the matrices are represented as vectors. Thus, a tensor $\mathcal{H}$ with element $\mathcal{H}_{ijkl}$ is rewritten as an $n^2 \times n^2$ matrix $\mathbf{H}$, with elements $\mathbf{H}_{ni+j,nk+l}$. Likewise, an $n \times n$ matrix $\mathbf{A}$ with elements A_{ij} is rewritten as a vector $|A\rangle\rangle$ with elements $|A\rangle\rangle_{ni+j}$.

The resulting simpler expression of the equation of motion is inverted and solved by a perturbation expansion. After inverting $\mathbf{H}(\Delta\omega)$,

$$\mathbf{G}(\Delta\omega) \equiv \mathbf{H}^{-1}(\Delta\omega), \tag{8}$$

and using the reduced notation, the e.o.m. becomes

$$|\Delta G^{<}_{CC}(\Delta\omega, \bar{\omega})\rangle\rangle = \mathbf{G}(\Delta\omega)|B^{(1)}_{CC}(\Delta\omega, \bar{\omega})\rangle\rangle + \frac{1}{\pi}\mathbf{G}(\Delta\omega)\int d\omega' |B_{CC}(\omega', \Delta\omega, \bar{\omega})\rangle\rangle, \tag{9}$$

where

$$|B^{(1)}_{CC}(\Delta\omega, \bar{\omega})\rangle\rangle_{ni+j} \equiv \left[\mathbf{v}_{CC}(\Delta\omega)\mathbf{G}^{0,<}_{CC}(\bar{\omega} - \Delta\omega/2) - \mathbf{G}^{0,<}_{CC}(\bar{\omega} + \Delta\omega/2)\mathbf{v}_{CC}(\Delta\omega)\right]_{ij} \tag{10}$$

and

$$|B_{CC}(\omega', \Delta\omega, \bar{\omega})\rangle\rangle_{ni+j} \equiv [\mathbf{v}_{CC}(2\omega')\Delta G^{<}_{CC}(\bar{\omega} - \omega', \Delta\omega - 2\omega') - \Delta G^{<}_{CC}(\bar{\omega} + \omega', \Delta\omega - 2\omega')\mathbf{v}_{CC}(2\omega')]_{ij} \tag{11}$$

3.1 Models

The model system considered in this study is composed of a pair of sites aligned perpendicular to the direction of flow-coupling two one-dimensional wires. The graphical representation of this model system is provided in Fig. 2, where only the surface atom of the wire is depicted. The two central sites and the surface sites define the core region of the system. We use a simple tight binding model for the electronic structure, where each site is represented by a single s-type basis function. Relative to the center of a given atom A, this basis function is expressed in spherical coordinates as $\Phi(r_A, \theta_A, \phi_A) \sim e^{-\alpha r_A^2}$. The "tightness" parameter, α, is determined by setting $\langle r_A \rangle$ to the electronic radius of the given atom. The sites of the electrode have been parametrized to represent gold atoms and the device sites are each representing a single carbon atom. The corresponding region is designated below as AuC_2Au.

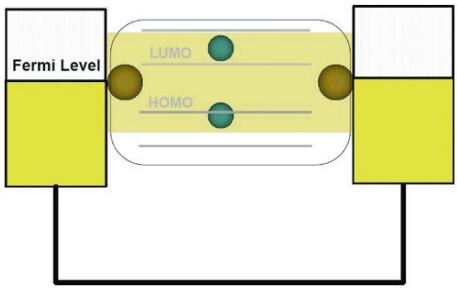

Fig. 2 Illustration of the model composed of two sites bridging two one-dimensional semi-infinite wires. Only the surface atom of each wire is depicted

The atomic orbital Hamiltonian matrix is parametrized based on the ionization potential and evaluated using the following Huckel-type expressions:

$$H_{A,A} = -I_A, \tag{12}$$

$$H_{A,B} = -\frac{1}{2}K(I_A + I_B)S_{A,B}, \tag{13}$$

where $S_{A,B}$ is the atomic orbital overlap between the s-electron basis functions centered on atoms A and B, I_A is the ionization potential for atom A, and K is a constant set to 1.75. The numerical values for these parameters are provided in Table 1. The Hamiltonian is then orthogonalized ($\mathbf{H} \rightarrow \mathbf{S}^{-1/2}\mathbf{H}\mathbf{S}^{-1/2}$) followed by the imposition of a tight-binding condition within the electrode regions, where only site and nearest-neighbor hopping elements are non-zero. All site and hopping elements are kept in the four-site region of the orthogonalized Hamiltonian that corresponds to the AuC_2Au region of the pre-orthogonalized Hamiltonian. This Hamiltonian is padded with electrode wires of nine Au atoms on each side of the perpendicular C_2 system to ensure that edge effects are minimized in the orthogonalization procedure.

Table 1 Radii, ionization potentials, I_A, and Gaussian basis set coefficients, α, for C and Au

Atom	radius Å	I_A (eV)	α (Å^{-2})
C	0.77	11.26	1.074
Au	1.44	9.22	0.307

We now calculate the electronic density and spectrum of this system, where we include the surface atoms in the confined device region. This defines the core device region as a four state space. The electronic DOS is generated from $G^{0,<}(\bar{\omega})$. The electrodes' effects on the electronic DOS of the junction are represented as usual by adding to the Hamiltonian the projection of the surface GF onto the central region using the TB coupling terms.

Next, we consider the system prior to probing its spectroscopy. In all cases, we note that for simplicity the Fermi energy is shifted to be zero and is located in the middle of the HOMO-LUMO gap. This is schematically illustrated in Fig. 1(left). The steady state description is derived from a time-independent perturbation perspective, where any bias has been turned on for a sufficiently long time to dissipate any transient or TD aspects.

The time-independent perturbation $\mathbf{v}(t) \equiv \mathbf{v}_\circ$ is Fourier transformed as in Eq. (5) to the frequency domain:

$$\mathbf{v}(\Delta\omega) = 2\pi\,\Delta(\Delta\omega)\mathbf{v}_\circ\,, \tag{14}$$

We use the two-frequency representation of the time-dependent e.o.m's to derive a time-independent correction to $G^{0,<}$. The resulting expression is

$$|\mathbf{G}^{0,<}_{CC}(\bar{\omega})\rangle\rangle \rightarrow |\mathbf{G}^{0,<}_{CC}(\bar{\omega})\rangle\rangle + \mathbf{G}(0)|B^{(1)}_{CC}(\bar{\omega})\rangle\rangle, \tag{15}$$

where $B_{CC}^{(1)}$ is reduced and simplified in the steady state limit to

$$|B_{CC}^{(1)}(\bar{\omega})\rangle\rangle_{ni+j} \equiv \left[\mathbf{v}_\circ \mathbf{G}_{CC}^{0,<}(\bar{\omega}) - \mathbf{G}_{CC}^{0,<}(\bar{\omega})\mathbf{v}_\circ\right]_{ij}. \tag{16}$$

Equation (15) is used as an initial guess for the steady state lesser Green function that introduces the effects of weak bias $\mathbf{v}_\circ$.

If $\mathbf{v}_\circ$ is energetically on the order of the transition energies in the Hamiltonian, a first-order expansion will not suffice. In this case we turn on the bias adiabatically (compared to the time evolution of the Hamiltonian) in n small increments. This amounts to applying Eq. (15) iteratively n times,

$$|\mathbf{G}_{CC}^{0,<,(m+1)}(\bar{\omega})\rangle\rangle \rightarrow |\mathbf{G}_{CC}^{0,<,(m)}(\bar{\omega})\rangle\rangle + \frac{1}{n}\mathbf{G}(0)|B_{CC}^{(1),(m)}(\bar{\omega})\rangle\rangle, \tag{17}$$

where

$$|B_{CC}^{(1),(m)}(\bar{\omega})\rangle\rangle_{ni+j} \equiv \left[\mathbf{v}_\circ \mathbf{G}_{CC}^{0,<,(m)}(\bar{\omega}) - \mathbf{G}_{CC}^{0,<,(m)}(\bar{\omega})\mathbf{v}_\circ\right]_{ij}. \tag{18}$$

This ensures that, for every iteration, the perturbing Hamiltonian $\mathbf{v}_\circ/n$ can be made small for large enough n.

3.2 Results

The electronic spectrum is obtained by tracing the dipole moment operator oriented along the device (C_2) axis (designated as z). This is aligned perpendicular to the gold wires axis:

$$Im\left[\langle\mu_z(\Delta\omega)\rangle\right] = \int d\bar{\omega} Tr\left[G^<(\bar{\omega}, \Delta\omega)\cdot\hat{\mu}_z\right], \tag{19}$$

where the dipole operator matrix representation ($\{\Phi\}$ are the basis functions) is

$$\mu_{z,ij} = \int d^3\mathbf{r}\Phi_i(\mathbf{r})\hat{z}\Phi_j(\mathbf{r}). \tag{20}$$

The projected electronic DOS of the device region is calculated for several related models. These models differ in the number of the wire gold atoms included in the device region. Following the tight-binding picture the most distant atom included in the device region from the core pair of atoms is assumed to represent well the surface site of the wire. The electronic DOS and the corresponding spectra are provided in Fig. 3.

We note that the DOS of the device region, which is shown on the right panel, converges with respect to the number of gold atoms included in the central region.

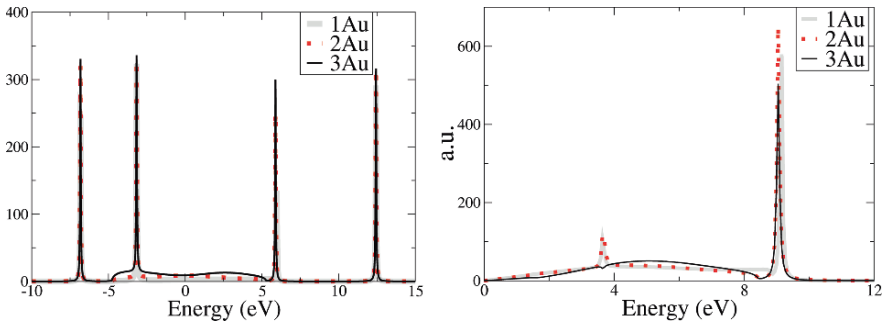

(a) Electronic DOS (b) Electronic spectra

Fig. 3 (**a**) The electronic density of states of the device region at **e**quilibrium conditions with models including 1, 2, and 3 wire sites in the central region. (**b**) The corresponding electronic spectra with the different inclusion of gold atoms in the central region (The spectra are given in atomic units as Bohr radius/Hartree)

Namely, adding gold atoms to the device region does not greatly affect the four major peaks in the distribution. These additional wire atoms mainly affect the DOS by further broadening the electronic density within the HOMO-LUMO gap. This is a reflection of the strongly delocalized nature of the electrode model used in our calculations. The effects of these broadening aspects on the modeled spectra are considered next.

Orbitals related to the main four bands of the core region are illustrated in Fig. 4. The core region includes the two carbon atoms and a gold atom from each wire which is most adjacent to the carbons. We have shifted the energies to be centered about the Fermi energy which has been chosen to be zero for simplicity. In the chosen geometry, we assign the lowest state (occ1) to a bonding interaction between the carbon atoms. The second state, which is also occupied (occ2 or HOMO), corresponds to an antibonding interaction between the carbon atoms. The next state is unoccupied (virt1 or LUMO), which at the considered equilibrium conditions involves antibonding interactions between the two carbon atoms and with additional bonding interaction between the two gold surface atoms across the device region. Finally the highest state (virt2) is dominated by electron density localized on the gold atoms with an antibonding node separating the two sites.

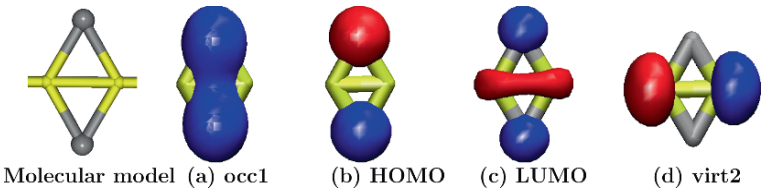

Fig. 4 Orbitals are plotted organized according to their energy levels from left to right in an increasing order. Left most panel illustrates the molecular model of the core system used in the calculations

The corresponding electronic spectra show a strong dependence on the model used. The models differ by the number of gold atoms included in the device region. First, we assign the dominant peak in all non-biased spectra to the HOMO-LUMO transition. We also note that there is no transition-noted coupling into state virt2 due to the symmetry of the involved orbitals. However, an unconverged response (peak) is generated for the limited model, where only a single gold atom is included in the junction's space. For this smaller model, a peak corresponding to the energy difference between states occ1 and occ2 is generated. These electronic states, however, which lie energetically below the Fermi energy, are both populated upon coupling to the two wires.

Clearly electronic transitions that couple two occupied states are forbidden at equilibrium conditions. This indicated forbidden transition is (almost completely) removed upon including additional wire sites in the device at equilibrium. It is shown that this peak in the spectra is gradually eliminated at the equilibrium conditions by expanding the central region to include one or two additional gold atoms from each wire. We also note that the differences in the broad bands between the different models result from the projection of the infinite electrodes onto the device region. This also leads to the broadening observed on the electronic spectra (see Fig. 3).

The appearance of the additional and unphysical transition at an equilibrium state is a reflection of using a too restrictive model in the response theory. This difficulty in converging the calculated spectra is due to the delocalized nature of the electronic states that participate in the considered transition. These states have a large gold atom component in their electronic DOS. The delocalized nature of the metal-related electronic density is represented by self energies and is associated with the broadening effects. For example, the strong delocalization of the HOMO results with an artifact as noted above due to the self energy used in the spectra calculation. We, therefore, use the model that includes three gold atom sites in analyzing the spectra under bias conditions to allow for proper treatment of the electrodes' effects on the electronic density of the confined system. Next, we analyze the spectra at non-zero bias-voltage conditions.

In Fig. 1(right) the effect of the potential bias is schematically represented. The bias is shifting the effective Fermi energies of the two electrodes. In the illustration the resulting energy window of non-equilibrium occupations between the two electrodes is large enough to include both bands of the HOMO and LUMO electronic states. In Figs. 5 and 6 the voltage dependent spectra are provided. In Fig. 5 we provide the spectra of the low (left) and high (right) bias regimes. In Fig. 6 we provide an overview of the overall bias effect. It is shown that for strong enough bias voltages the otherwise forbidden transition becomes allowed. This is a flux-induced transition. This is shown in the figure, where the peak corresponding to the transition between the two lowest states only starts to develop for strong enough applied voltages. It becomes a dominant peak in the spectra, when the non-equilibrium conditions are further enhanced by even higher applied potential biases.

We observe the opposite trend on the higher peak in the spectra. This peak corresponds to the transition of states occ2 to virt1 (HOMO-LUMO in the equilibrium

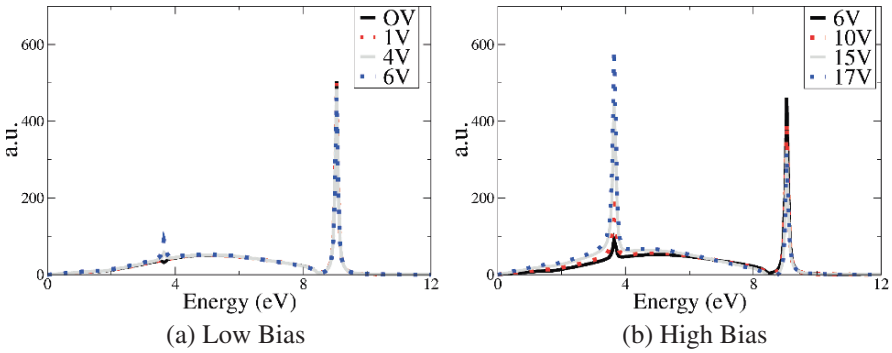

Fig. 5 The dependence of the electronic spectra on the voltage: (**a**) Low voltage (**b**) High voltage. The model used for these results includes three gold atoms in the device region for each electrode. (The spectra are given in atomic units as Bohr radius/Hartree)

Fig. 6 The dependence of the electronic spectra on the voltage: Overall bias range. The model used for these results includes three gold atoms in the device region for each electrode. (The spectra are given in atomic units as Bohr radius/Hartree)

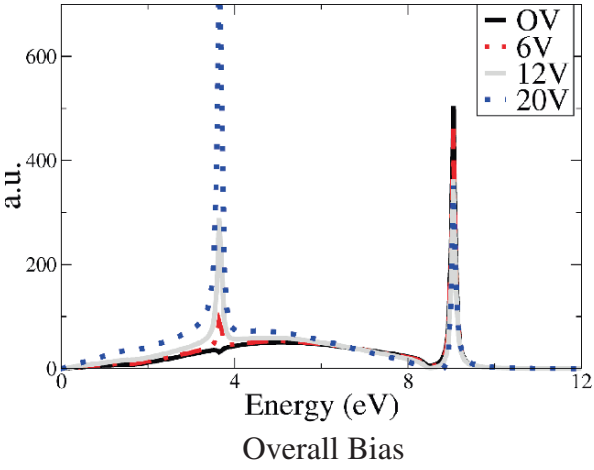

state). It becomes weaker as the two states experience stronger non-equilibrium conditions, where both bands are populated by the dynamic electron flux flowing through them. This is another important consequence of the spectra due to the non-equilibrium conditions that is nicely demonstrated by the implemented calculations.

4 Concluding Comments

A recently developed approach for the propagation of the electronic density of a system coupled to electron reservoirs under dynamic non-equilibrium conditions is used to study electrode biasing effects on the electronic spectra. The projected e.o.m.'s represent the effect of the electrodes on the dynamics expressed on the Keldysh contour, where the full time correlation is represented by two time variable

propagators, the Green functions. The projection is achieved by using self-energy expressions to represent the effect of electrode coupling. In this report, the general equation of motion is reexpressed in the full frequency domain and is solved at the linear response level to obtain the electronic response to electronic perturbations represented in the dipole approximation.

This method is implemented on a model system involving two carbon atoms sandwiched by and aligned perpendicular to two gold atom wires. Exposing the system to steady non-equilibrium conditions, where the potentials of the two electrodes are shifted, leads to electron flux that dynamically affects the electronic spectra. Electronic transitions between conducting electronic channels, which are fully populated at equilibrium, become allowed upon applying voltage bias. It is shown that a transition involving two occupied states (at equilibrium) becomes stronger with the increase of the voltage bias, whereas the electronic flux can lead to some reduction of the transition for a transition coupling an occupied level to a virtual level.

Acknowledgments We thank the reviewer for the thorough reading of the manuscript and providing an elaborate review and suggestions for improving the presentation. B.D.D. acknowledges the University of Michigan and the Petroleum Research Fund of the ACS through Grant No. 47118-G6 for financial support.

References

1. Y. Xue, S. Datta, M.A. Ratner, J. Chem. Phys. **115**, 4292 (2001)
2. P.S. Damle, A.W. Ghosh, S. Datta, Phys. Rev. B **64**, 201403(R) (2001)
3. J. Taylor, H. Guo, J. Wang, Phys. Rev. B **63**, 245407 (2001)
4. Y. Xue, S. Datta, M.A. Ratner, Chem. Phys **281**, 151 (2002)
5. P. Damle, A.W. Ghosh, F. Zahid, S. Datta, Chem. Phys. **171–187**, 225 (2002)
6. Y. Xue, M.A. Ratner, Phys. Rev. B **68**, 115406 (2003)
7. M. Brandbyge, J.L. Mozos, P. Ordejon, J. Taylor, K. Stokbro, Phys. Rev. B **65**, 165401 (2002)
8. M. Galperin, A. Nitzan, Ann. N.Y. Acad. Sci. **1006**, 48 (2003)
9. L.P. Kouwenhoven, A.T. Johnson, N.C. van der Vaart, C.J.P.M. Harmans, C.T. Foxon, Phys. Rev. Lett. **67**(12), 1626 (1991).
10. L.P. Kouwenhoven, S. Jauhar, K. McCormick, D. Dixon, P.L. McEuen, Y.V. Nazarov, N.C. van der Vaart, C.T. Foxon, Phys. Rev. B **50**, 2019 (1994)
11. B.J. Keay, S. Zeuner, S.J. Allen, K.D. Maranowski, A.C. Gossard, U. Bhattacharya, M.J.W. Rodwell, Phys. Rev. Lett. **75**(22), 4102 (1995).
12. T.H. Oosterkamp, L.P. Kouwenhoven, A.E.A. Koolen, N.C. van der Vaart, C.J.P.M. Harmans, Phys. Rev. Lett. **78**(8), 1536 (1997)
13. R. López, R. Aguado, G. Platero, C. Tejedor, Phys. Rev. Lett. **81**, 4688 (1998)
14. T.H. Oosterkamp, T. Fujisawa, W.G. van der Wiel, K. Ishibashi, R.V. Hijman, S. Tarucha, L.P. Kouwenhoven, Nature **395**, 873 (1998)
15. P. Nordlander, M. Pustilnik, Y. Meir, N.S. Wingreen, D.C. Langreth, Phys. Rev. Lett. **83**, 808 (1999)
16. L. DiCarlo, C.M. Marcus, J.S. Harris, Phys. Rev. Lett. **91**(24), 246804 (2003)
17. G. Platero, R. Aguado, Phys. Rep. **395**, 1 (2004)
18. M.G. Vavilov, L. DiCarlo, C.M. Marcus, Phys. Rev. B **71**(24), 241309 (2005)

19. P.J. Leek, M.R. Buitelaar, V.I. Talyanskii, C.G. Smith, D. Anderson, G.A.C. Jones, J. Wei, D.H. Cobden, Phys. Rev. Lett. **95**, 256802 (2005)
20. B.H. Wu, J.C. Cao, Phys. Rev. B **73**(20), 205318 (2006)
21. T.H. Stoof, Y.V. Nazarov, Phys. Rev. B **53**, 1050 (1996)
22. C.A. Stafford, N.S. Wingreen, Phys. Rev. Lett. **76**, 1916 (1996)
23. P. Brune, C. Bruder, H. Schoeller, Phys. Rev. B **56**, 4730 (1997)
24. P.W. Brouwer, Phys. Rev. B **58**(16), R10135 (1998)
25. M. Switkes, C.M. Marcus, K. Campman, A.C. Gossard, Science **283**, 1905 (1999)
26. F. Zhou, B. Spivak, B. Altshuler, Phys. Rev. Lett. **82**(3), 608 (1999)
27. P.W. Brouwer, Phys. Rev. B **63**(12), 121303 (2001)
28. B. Wang, J. Wang, H. Guo, Phys. Rev. B **65**(7), 073306 (2002)
29. M. Moskalets, M. Büttiker, Phys. Rev. B **69**, 205316 (2004)
30. L. Arrachea, Phys. Rev. B **72**, 121306 (2005)
31. L. Arrachea, Phys. Rev. B **72**, 125349 (2005)
32. L.E.F.F. Torres, Phys. Rev. B **72**, 245339 (2005)
33. S. Kohler, J. Lehmann, P. Hanggi, Phys. Rep. **406**, 379 (2005)
34. A. Agarwal, D. Sen, Phys. Rev. B **76**, 235316 (2007)
35. L. Arrachea, C. Naon, M. Salvay, Phys. Rev. B **76**, 165401 (2007)
36. G. Stefanucci, S. Kurth, A. Rubio, E.K.U. Gross, Phys. Rev. B **77**, 075339 (2008)
37. A.M. Nowak, R.L. McCreery, J. Am. Chem. Soc. **126**, 16621 (2004)
38. A.M. Nowak, R.L. McCreery, Anal. Chem. **76**, 1089 (2004)
39. A.P. Bonifas, R.L. McCreery, Chem. Mater. **20**, 3849 (2008)
40. D.R. Ward, N.J. Halas, J.W. Ciszek, J.M. Tour, Y. Wu, P. Nordlander, D. Natelson, Nano. Lett. **8**, 919 (2008)
41. D.R. Ward, G.D. Scott, Z.K. Keane, N.J. Halas, D. Natelson, J. Phys.-Cond. Mat. **20**, 374118 (2008)
42. G. Stefanucci, C.O. Almbladh, Phys. Rev. B **69**, 195318 (2004)
43. S. Kurth, G. Stefanucci, C.O. Almbladh, E.K.U. Rubio, A. Gross, Phys. Rev. B **72**, 035308 (2005)
44. J. Maciejko, J. Wang, H. Guo, Phys. Rev. B **74**, 085324 (2006)
45. A.P. Jauho, N.S. Wingreen, Y. Meir, Phys. Rev. B **50**, 5528 (1994)
46. R. Baer, D. Neuhauser, Int. J. Quantum Chem. **91**, 524 (2003)
47. R. Baer, T. Seidman, S. Ilani, D. Neuhauser, J. Chem. Phys. **120**, 3387 (2004)
48. R. Baer, D. Neuhauser, J. Chem. Phys. **121**, 9803 (2004)
49. D. Neuhauser, R. Baer, J. Chem. Phys. **123**, 204105 (2005)
50. N. Bushong, N. Sai, M. Di Ventra, Nano. Lett. **5**, 2569 (2005)
51. K. Burke, R. Car, R. Gebauer, Phys. Rev. Lett. **94**, 146803 (2005)
52. N. Sai, M. Zwolak, G. Vignale, M. Di Ventra, Phys. Rev. Lett. **94**, 186810 (2005)
53. C.L. Cheng, J.S. Evans, T. Van Voorhis, Phys. Rev. B **74**, 155112 (2006)
54. X. Qian, J. Ju Li, X. Lin, S. Yip, Phys. Rev. B **73**, 035408 (2006)
55. J. Lehmann, S. Kohler, P. Hänggi, A. Nitzan, Phys. Rev. Lett. **88**, 228305 (2002)
56. J. Lehmann, S. Kohler, P. Hanggi, A. Nitzan, J. Chem. Phys. **118**, 3283 (2003)
57. S. Camalet, J. Lehmann, S. Kohler, P. Hänggi, Phys. Rev. Lett. **90**, 210602 (2003)
58. M. Moskalets, M. Büttiker, Phys. Rev. B **69**, 205316 (2004)
59. S. Camalet, S. Kohler, P. Hänggi, Phys. Rev. B **70**, 155326 (2004)
60. L. Arrachea, Phys. Rev. B **72**, 125349 (2005)
61. L. Arrachea, M. Moskalets, Phys. Rev. B **74**, 245322 (2006)
62. A. Prociuk, B.D. Dunietz, Phys. Rev. B **78**, 165112 (2008)

Index

Note: The letters '*f*' and '*t*' following locators denote figures and tables, respectively.

T